Controlling Crystallization via Interfacial Engineering: Patterning, Fouling-inhibition, and Nutrient Recovery

by

Samantha McBride

B.S. Environmental Engineering, University of Nevada, Reno, 2013
M.S. Chemical Engineering, Rensselaer Polytechnic Institute, 2015

Submitted to the Department of Mechanical Engineering
in Partial Fulfillment of the Requirements for the Degree of

DOCTOR OF PHILOSOPHY

at the

MASSACHUSETTS INSTITUTE OF TECHNOLOGY

February 2020

Signature of Author:_____
Department of Mechanical Engineering
January 8th, 2020

Certified by:_____
Kripa K. Varanasi
Professor of Mechanical Engineering
Thesis Supervisor

Accepted by:_____
Nicolas Hadjiconstantinou
Professor of Mechanical Engineering
Chairman, Committee on Graduate Students

Controlling Crystallization via Interfacial Engineering: Patterning, Fouling-inhibition, and Nutrient Recovery

by

Samantha McBride

Submitted to the Department of Mechanical Engineering
on January 8th, 2020 in Partial Fulfillment of the
Requirements for the Degree of Doctor of Philosophy in
Mechanical Engineering

Abstract

Crystallization is ubiquitous in natural and anthropogenic environments; and can be detrimental or beneficial. For example, crystallization from sea-spray deposits is a leading contributor to rusting and fouling of coastal structures. However, crystallization can also be used as a purification technique for producing a variety of important chemicals. In this thesis, control of crystallization at interfaces is explored for improving sustainability across a variety of applications including pattering, anti-fouling, and as a separation process for recovery. Interfacial engineering is a natural starting point for controlling crystallization due to a propensity of many forms of crystals to form at phase boundaries. Control of crystallization on solid substrates is accomplished by modification of the surface morphology, length scale of surface features, surface chemistry, and surface energy. In this thesis I demonstrate that interfacial engineering can be used to prevent mineral fouling across salts and salt mixture, to develop microparticles which promote recovery of nutrients from waste water, and to design a micro-scale water-soluble crystalline masks with applications for the fabrication of microdevices.

Thesis Supervisor: Kripa K. Varanasi
Title: Professor of Mechanical Engineering

Acknowledgements

There are a great number of people whom I would like to acknowledge and thank for all of their support, wisdom, and guidance before and during my graduate education. I have been very fortunate throughout my education to have come into contact with a number of extraordinary educators and mentors who took a personal interest in helping me succeed. I have been similarly fortunate in my personal life to have a large and unconditionally supportive family, and to have met so many kind, fun, and wonderful friends over the years. I will attempt to do justice to how each of these individuals impacted my life and contributed to this dissertation.

First, I would like to sincerely thank all of the individuals and agencies who made this work possible via financial support. This dissertation was funded in part by a graduate research fellowship from the National Science Foundation (NSF), by an MIT Martin Family Sustainability Fellowship, and by Equinor via the MIT Energy Initiative.

I am deeply grateful to my thesis advisor, Professor Kripa Varanasi. Kripa allowed me a great amount of freedom in exploring different research paths, trying unusual experiments, and deciding which topics to pursue for my dissertation. I am extremely thankful for the great amount of trust and belief that he had in me and in our work. The experiments and analysis presented in this dissertation resulting from our collaboration are creative, fun, and impactful. Working with Kripa has taught me a great deal about how to communicate science and how to identify problems that are most impactful to work on. Kripa has actively supported my career by taking every opportunity presented to him to nominate me for awards, including the MIT Martin Family Sustainability Fellowship and the Meredith Kamm Memorial Award. He has also supported my academic ambitions by encouraging me to attend a large number of conferences and by arranging a teaching opportunity during my time at MIT. As a mentor, Kripa has been flexible, enthusiastic, and encouraging. For example, when I wanted to submit a proposal to a NASA research opportunity as a first-year student in his lab, he wholeheartedly agreed and guided that effort. Thank you, Kripa, for your openness to working in new areas and to forging new collaborations!

I have also had the great privilege of learning from, and being mentored by, a number of wonderful faculty at MIT. Of particular note is my thesis committee, composed of Professors Allan Myerson, Chris Love, and Xuanhe Zhao. I am grateful for all of the feedback, advice, and support that my committee has given me over the years. I would also like to sincerely thank Professors Irmgard Bischofberger and Asegun Henry, whom I have had the privilege of working with as a teaching assistant. I have learned a great deal by watching their examples as educators, and both have offered me important and helpful career advice. I would also like to thank Felice Frankel, who

taught me how to produce effective and beautiful figures for scientific papers and presentations. Her influence is clearly visible in this dissertation by comparing figures produced during the start and towards the end of my PhD work. Another professor of note is Susan Murcott, whose passion for water and sustainability and dedication to her students has helped me preserve my roots to environmental engineering. Finally, I would like to acknowledge Professor John Bush, who offered invaluable advice on some of the mathematical models presented in this work.

I would also like to thank Professor Amir Hirsa, my master's advisor at Rensselaer Polytechnic Institute. Amir has been exceptionally supportive of my graduate education and his influence has been vital in setting my trajectory. He was incredibly understanding and supportive when I realized that I wanted my PhD research to focus on water and was instrumental in my successful application to the PhD program at MIT and to the NSF graduate research fellowship program. He continues to be supportive of my career and is always quick to provide advice and recommendation letters whenever I ask. Amir was also the one who introduced me to microgravity science and encouraged me to get involved with the microgravity community. Through working with his group, I was also extremely fortunate to have the opportunity to help perform an experiment on a parabolic flight. This is a life experience that I will never forget. Thank you Amir! Other professors from RPI who have been excellent mentors/educators to me include professors Patrick Underhill, Peter Tessier, and Shekhar Garde. I thank them all for their mentorship.

Professors Edward Kolodziej, Eric Marchand, Keith Dennett, Dean Adams, Charles Coronella, and Amy Childress from my time at the University of Nevada, Reno have also been instrumental in starting me on the academic path. Each of them took a personal interest in my education and continued success, were happy to provide letters of recommendation, and were/are the reason why I am pursuing a career in higher education. Professor Childress took the time to meet with me when I was only a second-year undergraduate to encourage me to pursue undergraduate research and various scholarship opportunities. Professor Adams took it upon himself to go argue with the records department to convince them to drop an AP course I had taken in high school from my transcript so I could finish undergraduate with a 4.0. Professor Coronella reminded me that life is a marathon, not a sprint, when I was feeling frustrated with my progress. Professor Dennett was the faculty mentor for the Water Treatment Team that I was heavily involved in, and I aspire to be half as entertaining as he when teaching courses. Professor Marchand remembered my name the first day of class in a class of 70+ students, advised me in courses and in life, and continues to support my path towards academia. Professor Kolodziej, with whom I did research for two years, taught me how to be rigorous, precise, and independent in research. His mentorship in research has served me incredibly well throughout graduate school, and I deeply grateful to have had the opportunity to work with him and for his continued support.

I would also like to thank my many non-faculty mentors and collaborators. Susmita Dash, a post-doc (now faculty) who mentored me in research when I first started at MIT and who remains a wonderful friend and collaborator today. Srinivas Subramanyam, who introduced me to working with engineered surfaces for anti-fouling in the Varanasi Lab. Severine Atis, a post-doc whom I met through a course and who has become a mentor, friend, and collaborator on the patterning work in this thesis. I also want to thank the many mentors and friends whom I met through the American Society of Gravitational and Space Research (ASGSR), and regret that I cannot list each and every one by name here. Finally, I thank my friend and collaborator, Professor Luis Zea, for making Kripa and I a part of his Space Biofilms team and enabling us to send our materials to the space station.

I have also been very fortunate to work with an incredibly talented and motivated group of students at MIT. I would like to thank Henri-Louis Girard, who started in the Varanasi group with me and has always been available for brainstorming and collaboration. I would also like to thank Sami Khan, who worked with me on several projects and introduced me to the group. Vishnu Jayaprakash, who has worked with me on a number of course projects and whose sense of humor always improved my day. In addition to the group members who I have directly worked with and who have contributed to this dissertation, I cannot say enough about my other colleagues in the Varanasi lab and how these extraordinary people have contributed to my time at MIT. Nada Bjelobrk, Jack Lake, Caroline McCue, Sreedath Panet, Victor Leon, Ingrid Guha, Maher Damak, Karim Khalil, Divya Panchanathan, Taylor Farnham, Maxime Costalonga, David Kang, Leonid Rapoport, Dan Soto, Alvaro Soto, Somayajulu Dhulipala, and Valentina Negri; you have all made my time at MIT better! Finally, I would like to thank all of the talented and hardworking undergraduates who worked with me. Mohanned Elkholy, Janice Moya, and Karunya Sethurman all contributed to work presented in this thesis. I would also like to particularly thank Rachael Skye, who contributed greatly to the work presented in Chapter 5 and has been an exceptional collaborator.

I also wish to acknowledge all of the friends, and even acquaintances, I have met during my time at MIT. When I was first accepted to MIT, I was concerned that there would be a toxic/competitive culture at the school. However, I have never been in an environment with so many positive, kind, and supportive people, and I am grateful to everyone in the Mechanical Engineering Department and beyond who have made my PhD experience what it was. I am also grateful to everyone that I have worked with as part of the MIT Water Club; it amazes me how much we were able to accomplish working on relatively small teams, and I am grateful for all that I have learned from each of you.

On a personal note, I would like to thank my parents, Dr. Ellen McBride and Darren McBride. Growing up, I never considered studying any field that wasn't either science or engineering, and their influence had a lot to do with that. While they encouraged me to do well in school and to pursue extracurricular activities, they also let me quit activities/programs that I didn't like. Although quitting typically has a negative connotation, being able to try a large variety of activities and decide for myself whether or not I wanted to continue enabled me to find things that I was actually passionate about. The independence and motivation to keep working at something that they instilled in me has been vital throughout graduate school.

I also owe great thanks to my siblings: Meredith, Jaclyn, and Chris, who are my best friends and have been infinitely patient with my somewhat poor communication frequency throughout graduate school. Meredith is incredibly brave, fun, and has a strong sense of right/wrong. She has frequently encouraged me to leave my comfort zone which has made me a braver and better person. She is deeply committed to justice, and her continuous fight to make the world a better place inspires me to do the same. Jaclyn is incredibly perceptive, compassionate, and resilient. The depth of her compassion for others, whether human or animal, have also made me a more compassionate and understanding person. If I am fortunate enough to become a professor in the future, I have no doubt that my students will owe her great thanks for this. Her perseverance has also served as an example for me to keep going during the challenging periods of graduate school. Chris, with whom I have always shared the most common hobbies and interests, is imaginative, analytical, and kind. While neither of us are particularly good at reaching out regularly, I know he is and will always be there for me as a friend and as a brother. Thank you all for your support and friendship!

There are a number of other personal acknowledgements I would like to make. My friend Justin Lopez, who is much better than I am about periodically keeping touch despite being just as (actually, probably more) busy, and whose messages always make me laugh. My friend Emily Cole who helped me prepare for life on the east coast and has always been a kind and genuine friend. My roommates (Erin, Anastasiya, Max, Angelina, Alex, Chloe, and more), who have been both my friends and my family away from family. There are many more people that I would like to acknowledge here but will refrain from listing in the interest of brevity. You all know who you are; and thank you for everything!

Finally, I want to thank my fiancé/husband Sebastian Gehrmann, and dedicate this work to him. He has been incredibly patient and supportive throughout the duration of my PhD, has tolerated my late-night work schedule, prepared food when I was too busy, and has generally been the most supportive and understanding partner that I could ask for. Basti, thank you for making this work possible and for everything you have done to support me during this time. Ich liebe dich!

An meine neue deutsche familie: danke, dass sie mich in ihrer familie aufgenommen und sich bemüht haben, meine forschung zu verstehen!

Contents

List of Figures

FIGURE 5.2. Drop evaporation with time for the different solutions at 60°C. Contact angle measurements were terminated at the point at which the contact line became too distorted by particle/crystal accumulation to extract an angle.

FIGURE 5.3. Representative patterns from experiments for (top) particles, (second row) silver sulfate, (third row) calcium iodate, (fourth row) calcium sulfate. (a) 20°C, (b) 40°C, (c) 60°C, (d) 80°C. Length scale is the same for all images, and the diameter of the TOPS deposits is ~4mm.

FIGURE 5.4. Influence of surface energy on deposit morphology formed at 60°C for (top) calcium sulfate, (middle) silver sulfate, and (bottom) calcium iodate.

FIGURE 5.5. (a) Area localization (ratio of final contact area of deposit to contact area of initial drop) as a function of substrate surface area (where the more wettable substrates have a higher energy) across temperatures. (b) bar graph for OTS data outlined in blue in part "a," comparing temperature dependence of the particles and calcium iodate deposits. (c) Area localization as a function of the contact angle hysteresis (between the equilibrium angle and receding angle) at 60°C.

FIGURE 5.6. Data across five substrates and three temperatures (40°C, 60°C, 80°C) collapse onto a single trend based on the supersaturation at crystal nucleation. (a) squares = calcium sulfate, diamonds = silver sulfate, triangles = calcium iodate. (b) phase diagram of the pinning force against the supersaturation, where $F_{pin} = 2\pi R\,\gamma(T)(\cos\theta_R - \cos\theta_A)$, S_c is from experimental data, estimated as $S_c = V_o/V_c$, and data was classified according to the area localization. Data comes from experiments conducted at 40°C, 60°C, and 80°C.

FIGURE 6.1. Evaporative crystallization on a hydrophilic silicon surface. (A) Progression of drop evaporation and crystal deposition. (B) SEM images from one deposit, showing dendritic needle-shaped gypsum crystals in-plane with the substrate.

FIGURE 6.2. A) Representative examples of evaporative crystallization on superhydrophobic micropost surfaces with edge-to-edge post spacing of (i) 5, (ii) 25, and (iii) 50 μm. The images show the top and side views of drops at three different times instants: (left) experiment initiation, (middle) shortly after crystals at triple phase contact line have pinned the drop, and (right) end of evaporation. B) Contact angle as a function of time throughout evaporation (until crystal deposits obscure measurements) C) SEM images of crystalline deposits. Scale bars represent 100 μm.

FIGURE 6.3. Comparing the b40 and b50 Cassie to Wenzel transitions for water to those for calcium sulfate solution. SEM images show crystal growth on posts.

FIGURE 6.4. Room temperature vs. 60°C C for superhydrophobic surfaces (a) area of crystal deposit as a function of edge to edge post spacing, where filled triangles were conducted at ambient temperature, and empty circles are results from 60°C (b) SEM images of deposits formed at room temperature for b5, b10, b25, b40, and b75 surfaces. Scale is the same for all 5 images.

FIGURE 6.5. Deposits left on the b50 surface with different temperatures. Scale bars indicate 100 μm on all surfaces.

FIGURE 6.6. A) Progression of evaporative crystallization on liquid impregnated surfaces of (i) b5, (ii) b25, and (iii) b50. Top and side view images are shown for three time instants: (left) experiment onset (middle) shortly after crystals become apparent (right) end of evaporation. (B) Contact angle as a function of time for LIS surfaces, with measurements terminated after crystal deposits become too prominent for accurate measurement. (C) SEM images showing crystal deposits on the different LIS surfaces. Scale bar represents 100 μm and is the same for all images.

FIGURE 6.7. Comparison of evaporation behavior on the (○) superhydrophobic and (●) liquid impregnated surfaces as functions of substrate pitch.

FIGURE 7.1. Evaporation of a drop on a high advancing, low receding contact angle substrate ($\theta_A = 98°$, $\theta_R = 18°$, $T = 70°$C). First row shows a side view, second shows a top-down view of drop evaporation. Final row shows top-down view of the thin film rupture and contact line motion that leads to pattern formation on the drop interior. Scale bar is 0.5 mm.

FIGURE 7.2. Time series showing evaporation of a drop containing 0.1% latex nanospheres. Width of each image is 3mm.

FIGURE 7.3. Defining experimental timescales, where t_1 is the global evaporation time from start to finish, t_2 is the time between rupture and complete evaporation, t_3 is the time between rupture and pinning of the newly formed contact line, and t_4 is the timescale at which a given segment of a pattern remains pinned.

FIGURE 7.4. (a) Schematic of the geometry of the drop during the thin-film evaporation phase, where $R(t)$ is the position of the moving contact line, R_o is the radius between the center of the drop and the outer crystal ring, $h(r,t)$ is the height profile of the liquid, and J_o is the evaporative flux. At the moving contact line $R(t)$, the evaporative flux is at a maximum and the height profile can be approximated as a triangular wedge. (b) Schematic showing drop geometry from a top view. (c) SEM showing size of the crystalline needles, where the width of the needles serves as an estimate for the film thickness in the region of the moving contact line.

FIGURE 7.5 Experimental timescale of drop rupture plotted against predicted values from equation 7.7. Colored circles correspond to different temperatures (red = 85 ºC, orange = 75 ºC, yellow = 70 ºC, green = 65 ºC, light blue = 60 ºC, dark blue = 55 ºC, purple = 45 ºC). Line indicates a 1:1 ratio of experimental data to predicted values.

FIGURE 7.6. A selection of patterns formed on different substrates and temperatures. Different substrate colors are due to thickness and chemistry of the sputtered surface coating. Length scale is the same for all images and is 2.8mm wide.

FIGURE 7.7. The position of the moving contact line with time after rupture (where $R(t) = 0$ indicates the drop center) for a concentric ring (green dashed line) and for a spiral (purple continuous line). The concentric ring demonstrates a terraced dependence where the contact line sticks at the position of the ring over a period of time, while the spiral contact line demonstrates a smoother dependence.

FIGURE 7.8. Optical microscope images with overlaid Fermat's spiral to measure parameter "a".

FIGURE 7.9. (a) The radial position, n, as a function of normalized time ($t^*=t/t_2$, where t_2 is the burst time defined in Figure S1) (b) Fermat's equation overlaid on SEM image for the example tracked in part a. (c) Time series demonstrating the movement of the pinning and depinning points for the given sample.

FIGURE 7.10. Plot of normalized equations 7.6 and 7.14, showing the general shape of the radial position of the contact line with time predicted by the physical model (equation 7.6) and from the Fermat spiral equation (equation 7.14).

FIGURE 7.11. Proportionality constant a as a function of receding contact angle, where circle markers indicate experimental values (red = 75ºC, orange = 70ºC, green = 65ºC, blue =60ºC), and the grey line is the model presented in equation 2, with $\theta_{depin} = 10°$, R_o=1.2 mm, and $\theta_{pin} = \theta_R$. Scale bar indicates 0.5 mm.

FIGURE 7.12. Line plot of equation 7, where rings (blue circles) form at low values, patterns (purple triangles) form in the intermediate region, and random deposition (yellow squares) occurs at higher values. Selected images show examples of the patterns represented.

FIGURE 7.13. Deposits left on the substrates by different salt solutions on a substrate (θ_A=98°, θ_R=30°) heated to 70°C. (a) calcium carbonate, (b) sodium carbonate, (c) calcium sulfate, (d) calcium iodate, (e) sodium chloride (at 10% of saturation concentration), and (f) silver sulfate.

FIGURE 7.14. Deposits from different concentrations of sodium chloride on a substrate (θ_A=98°, θ_R=30°) heated to 70°C. (a) 1% of saturation (3.6 g/L), (b) 2% of saturation concentration, (c) 5% of saturation concentration, (d) 10% of saturation concentration.

FIGURE 8.1. Experiments and observations. (a) Schematic showing drop geometry from the side and defining the contact angle. (b) Schematic of temporal evolution of evaporation: A ring of crystals develops at the initial drop contact line, evaporation causes the contact line to retract with velocity $V_{CL}(r)$, and an interior crystalline pattern is left behind following complete evaporation. (c) SEM images of patterns left on the interior following evaporation: (i) dendrites with sawtooth pattern, (ii) aligned branches, (iii) hexagonal lattice of spherical calcium sulfate clusters. Scale bars are 20 μm. (d) Classification of patterns according to substrate temperature and substrate contact angle, where open circles (bottom right) indicate formation of an empty ring with no patterns, blue circles indicate a lattice pattern (c,iii), green squares indicate aligned dotted lines (c, ii), yellow triangles indicate the dendritic branches that form sawtooth patterns (c, i), and targets indicate formation of multiple concentric rings with no pattern (top left).

FIGURE 8.2. (a-d) shows AFM images, where the top row gives topographic image, and the second row shows amplitude image. (a) and (b) show different regions of dendrite triangles, where the thicker phase corresponds to the darker phases observed from SEM images. The thin, light regions are ~40nm thick, while the thicker regions are ~80 nm thick. (c) shows a magnified image of a single crystal cluster left from an array, and (d) shows a group of 5 clusters. Clusters are approximately 200 nm tall, 3 μm in diameter, and (for the array in (d)) are about 10 μm between cluster centers. (e) Tilted SEM image shows that the "darker" triangular phase is thicker than the "lighter" one.

FIGURE 8.3. Close up of triangle pinning points. (a) – (c) show nucleation of second phase triangle, where (a) and (b) were imaged using the SE2 detector, and (c) was imaged with the InLens. (d) shows a region where the lighter, thinner phase has nucleated from a bulk crystal that settled on the surface (InLens detector). Parts (e) and (f) show close up images of the same sample, with (e) showing the tip of the lighter, thinner phase, and (f) showing the tip of the darker, thicker phase. The thick phase nucleates from the thinner phase, grows in the vertical dimension until it meets another "thick" phase branch.

FIGURE 8.4. Triangles on other substrates. (a) plain silica wafer, (b), sputter-coated erbia (c) Sputter-coated titanium dioxide, (d) sputter- coated silicate. The universality of the patterning suggests that patterns can be formed on any substrate so long as the contact angle and temperature are within the regimes shown in Figure 8.1d.

FIGURE 8.5**.** Triangle patterns formed from other salt chemistries. (a) silver sulfate, and (b) calcium iodate.

FIGURE 8.6. Influence of surfactant. (a-c) show a branched network of triangles reminiscent of Sierpinski triangles. (d) close up of region of triangles, (e) altered morphology of calcium sulfate dendrites due to surfactant, (f) close up of boundary between two phases of crystal, where the left is a lighter sawtooth phase, and the right is a darker sawtooth phase.

FIGURE 8.7. Sawtooth patterns from other studies. (a) Sawtooth structures composed of mono- and double-layers of 0.1 μm particles from Deegan. Scale bar is 250 μm. (b) Calcium sulfate sawtooth structures formed on a drop in which the interface ruptured at the center, and propagated outward. Scale bar is 100 μm. (c) DPPC Langmuir-Blodgett film deposited onto curved mica. Scale bar is 5 μm. (d) Water drops deposited during rupture of a thin film at room temperature, which have features similar to the branching regime in the present work.

FIGURE 8.8. Radius with time for calcium sulfate solution. (a) for contact angle of 3°, (b) for contact angle 12°. Blue line indicates 40°C, green is 60°C, orange is 8°0C, red is 100°C.

FIGURE 8.9. Snapshot of increase in radius directly after drop deposition with time, on the substrate with contact angle 3° and temperature 60°C. The grey diamonds show the spreading of a drop of pure water, and white circles indicate experimental data for a crystallizing drop. The black line is a model for Tanner's law.

FIGURE 8.10. Fingering instability during drop spreading can lead to triangular formations at the crystalline coffee-ring.

FIGURE 8.11. High speed video frames showing patterning (a) growth of a thicker triangle phase from the mobile contact line. (b) deposition of aligned branches composed of small crystal clusters. (c) deposition of periodic arrays of crystal clusters.

FIGURE 8.12. Patterning Mechanisms. (a) Cartoon showing formation of arrays due to a Marangoni instability. (b) Array wavelength as a function of thin film height (c) distance between consecutive drops as a function of contact line velocity, (d) cartoon showing growth of sawtooth structures, where the curvature of the contact line is exaggerated. (4) wavelength between sawtooth peaks as a function of thin film height, (f) peak angle of sawtooth structures as a function of the height and contact line velocity.

FIGURE 8.13. Triangular phase boundary formation in the branching regime.

FIGURE 8.14. Demonstration of masking applications. (a) Creation of three-dimensional microstructures by placing patterned substrates directly in reactive ion etch, followed by removal of gypsum crystals using saline water. Scale bar is 5 μm. (b) Patterned gold/silica regions. A patterned sample was sputter-coated with gold to a depth of 20 nm. Crystals were then removed using saline water to create a substrate of patterned gold/silica region.

FIGURE 9.1. Growth of crystal critters. (a) Cartoon of experiment, where a drop of water containing dissolved salt is evaporated on a hot, superhydrophobic substrate. (b) SEM images showing nanotexture of superhydrophobic surface. Scale bar for both images is 3 μm. (c) growth of crystal critters with time, where substrate temperature is 90°C. Scale bar is 0.5 mm. (d) Time for evaporation as a function of temperature. Entire bar represents the total evaporation time, the blue segment is the first stage of evaporation prior to leg growth, and the orange segment is the second stage of evaporation during which legs grow. (e) Growth of legs with time as a function of temperature, where the lowest temperature (purple line) is 60°C and hottest (red line) is 110°C.

FIGURE 9.2. Crystalline legs are tubes grown from regions where fluid impinges in nanotexture. (a,b) Top view of a drop immediately after placement on a surface revealing areas where liquid has impinged within the texture. (c) Optical image of crystalline tubes where liquid is observed to be flowing through. (d) Optical image of tubes near surface, where a very thin tube still connected to the surface is outlined in green. (e) SEM image of the bottom of a tube. Scale bar is 20 μm. (f) SEM image of a region where salt stains reveal where critter legs previously grew. Scale bar is 100 μm. (g) SEM image showing details of a large salt stain. Diameter of this stain is about 70 μm, scale bar is 5 μm. (h) SEM image showing detail of a salt stain where the outer perimeter has also been left behind. Outer diameter is 30 μm, inner diameter is about 25 μm, and scale bar is 5 μm.

FIGURE 9.3. Critters only grow on Nanograss texture. From left to right, images show SEM of substrate texture, initial drop contact angle, intermediate step where crystals have begun to form, and final crystalline deposit formed during evaporation on substrates heated to 70°C for (a) hydrophobic flat silicon, (b)

superhydrophobic Nanograss (i.e., the same texture used in Figures 1 and 2), (c) superhydrophobic micro-posts, (d) superhydrophobic micro-holes, and (e) superhydrophobic micro-posts further textured with Nanograss. SEM images for (1-e) are 50 μm wide. (f) Cartoon examining how crystal intrusion into micro-textures leads to a Cassie-Wenzel Transition (e) SEM image of salt deposit inside the micro-texture of the superhydrophobic micro-posts + Nanograss substrate.

FIGURE 9.4. Changes to critter effect induced by other chemistries. (a) Saturated sodium chloride with 0.01% SDS (sodium dodecyl sulfate) grows critters, but alters the morphology of growth. (b) Sodium chloride at 10% saturation concentration with saturated calcium carbonate forms a ring deposit. (c) Sodium chloride at 50% saturation concentration with saturated calcium carbonate forms a bowl-deposit. (d) Sodium chloride at saturation concentration with saturated calcium carbonate successfully forms a critter.

FIGURE 9.5. Other salts and the critter effect. Leg growth is plotted against the difference in solubility concentrations for five different salts between room temperature and 90°C. Optical images show resultant critters formed for these salts at 90°C.

FIGURE 9.6. Growth mechanism and temperature dependence. (a) Images defining model parameters including h (length of the legs), J_o (evaporation rate), R_o, and R_i (outer and inner diameter of a given leg). (b) Average leg growth rate (mm/min) as a function of temperature, where purple circles indicate experimental values averaged from 5-6 trials, error bars show standard deviation, and solid line is model from equation 3 (where R_o=15 μm and R_i=12.5 μm). (c) Experiment showing critter growth on a substrate with an imposed temperature gradient. Legs grow longer on the side with a higher temperature, causing the crystal critter to become more and more unstable until it eventually tips over and rolls in the direction of the lower temperature. New legs begin to grow at the new position until evaporation is complete.

FIGURE 10.1. Merged phase diagram of calcium sulfate evaporative deposition patterns as a function of the wettability properties of a substrate heated to 60C.

List of Tables

Chapter 1.

Introduction

My interest in crystallization at interfaces first developed as an undergraduate while taking a thermodynamics course. Given my background in water and environmental engineering, I was surprised to learn that water is continuously vaporized in its capacity as a working fluid in thermoelectric plants. I reasoned that if water was being vaporized anyway, why wouldn't engineers use ocean water as a working fluid so that desalinated water is produced as a byproduct of energy generation? After exploring this question, I learned that crystallization (called scaling or mineral-fouling) is already a limiting factor in thermoelectric plants even when relatively pure water is used. This undergraduate curiosity combined with a passion for sustainable water resources ultimately led to my thesis topic: interfacial engineering for control of inorganic crystallization.

My thesis work begins by exploring how interfacial engineering can be applied to controlling fouling in water treatment and in desalination. However, this is not the only problem in which crystallization at interfaces can be applied towards water sustainability. There is growing interest in using crystallization as a separation technique to recover nutrients from waste water. Because crystallization is sensitive to the presence of heterogeneous surfaces, interfacial engineering is an ideal strategy to improve nutrient recovery ratios. By applying the lessons learned in the area of mineral-fouling prevention, I was able to design interfaces which enhance kinetics of nutrient crystal growth.

The final major theme of my thesis explores the patterning of inorganic salts from evaporating saline drops. Using techniques that I have developed, it is possible to generate a number of micro- and nano-scaled patterns from salt crystals including spirals, arrays of clusters, sawtooth structures, and more. These salt patterns can replace masks for some micro-systems engineering applications; which typically rely on multi-step processes which use large amounts of toxic solvents. Aside from significantly reducing the time required for device fabrication, the development of a water-soluble masking technique has the potentially to vastly improve the sustainability of fabrication.

1.1 Motivation

Crystal Fouling in Water Treatment & Industry

Scaling is a phase transition in which dissolved ions in aqueous solution nucleate and crystallize into solid mineral precipitates. Scale formation is a major unresolved problem in numerous industries including power generation,[1] water desalination,[2,3] oil and gas[4,5] and hydrometallurgy.[6] Scaling results in significant operational losses due to impaired heat transfer, flow blockage, and decreased equipment lifetime. The costs of heat exchanger fouling have been estimated to be on the order of 0.25% of the GDP of industrialized countries.[1,7] Another dramatic example involves the production loss from 30,000 barrels/day to zero in just 24 hours in one of the oil wells in the North Sea due to scale formation.[4] Scale deposits reduce process efficiency, increase production costs, and induce corrosion.

Scaling is also a significant limitation preventing widespread adaptation of commercial desalination processes. Research into desalination has become a global priority due to changing climates and growing scarcity of fresh water, with the UN predicting that over two thirds of the world's population will lack access to clean water by 2025.[8] Regardless of the process used for desalination (reverse osmosis, thermal desalination, electrodialysis, etc.), generation of fresh water requires that separated salts become concentrated elsewhere. This results in generation of a supersaturated waste brine that causes scale formation on pipes, membranes, and other equipment.[9]

In addition to monetary losses of replacing failed equipment, handling of supersaturated waste brines is environmentally challenging. Current technologies for managing scale typically involve addition of anti-precipitation agents.[10–12] However, reducing precipitation only serves to create brines that are supersaturated and further contaminated with anti-scalants. The resulting heavy brines sink to the ocean floor upon discharge and adversely impact marine life.[13,14] These technologies are also generally expensive, energy intensive, and in many cases inadequate in preventing scale formation.[1,4]

Previous work has sought to design scale-resistant surfaces by coating substrates with low surface energy materials.[15,16] Preliminary studies of $CaSO_4$ crystallization indicate a consistent trend of lowering of scale formation by decreasing polar and hydrophobic interactions.[17] Hence, understanding the effects of both surface chemistry (i.e. the effect of electronic and atomic structure) and morphology on scale formation can help in the development of durable materials that can be either scale-resistant or scale-promoting. The development of robust materials which control scaling phase transitions can lead to substantial benefits in a huge variety of energy and water systems.

Crystallization for Nutrient Recovery

Phosphorous is vital for nourishing crop growth; without its use in fertilizer, crop yields would decrease by 50% or more.[18] Global phosphate rock reserves are quickly being depleted by mining, with estimates suggesting that depletion will occur within 50-100 years.[19] Increasing global prices and decreasing phosphate exports reflect growing demand,[19] and yet, phosphate-containing waters are still largely treated as waste and much of the world's phosphorous is dumped into surface waters as agricultural run-off and wastewater.[20] Once in natural waters, phosphorous recovery is exceptionally difficult, and the nutrient can cause eutrophication and ecosystem destruction.[21]

Sustainable recovery and reuse of phosphate is a critical challenge for sustaining food for growing populations and for protecting water resources. One promising solution is incorporating dedicated recovery operations in wastewater treatment plants (WWTPs) and areas with voluminous run-off flows. Such an operation may even be thermodynamically favorable, as phosphate minerals naturally precipitate in many WWTPs.[22] A common phosphate mineral formed within WWTPs is struvite, an orthorhombic mineral composed of magnesium, ammonium, and phosphate ($MgNH_4PO_4 \cdot 6H_2O$); the latter two being present in excess in most municipal wastewaters:[23]

$$Mg^{2+} + NH_4^+ + H_nPO_4^{3-n} + 6H_2O \rightarrow MgNH_4PO_4 \cdot 6H_2O + nH^+ \qquad 1.1$$

Struvite scale has long been considered a nuisance in wastewater treatment, as precipitation fouling is a leading cause of deterioration and operational failures/losses.[1,24] However, its presence in wastewater near solubility presents unique opportunities for recovery by crystallization. One kg of struvite can fertilize 2.6 hectares of farmland per day, and use of a mineral avoids the safety concerns associated with other forms of sewage-fertilization.[25] Purchasing recovered struvite is far more cost effective for famers than mined rock, due to both rising costs of commercial fertilizers[19] and to slower dissolution of struvite, allowing struvite-fertilization to achieve similar crop yields with less waste.[25] Recovering struvite from wastewater is therefore attractive for: (1) reusing struvite as a low cost fertilizer (2) moving towards phosphate-neutral, sustainable waste treatment (3) removing nutrients from wastewater, and (4) reducing precipitation fouling).[23,26]

Because of the potential of struvite recovery from waste water, recovery processes are already being commercialized and implemented into existing wastewater treatment facilities. For example, the Pearl system by Ostara technologies uses chemical conditioning and two additional reactors to crystalize struvite in a WWTP. AirPrex by CNP also uses chemical conditioning combined with air stripping of CO_2 to enhance precipitation. A Swedish company EkoBalans and a Dutch company called Nuresys have designed systems for struvite crystallization in which continuous flow precipitation tanks are retrofitted to existing plants following aeration. Of the existing technologies, a handful (including Pearl and Phosphogreen) incorporate seed particles to increase kinetics of struvite crystallization through fluidized bed technologies.

Patterning and Self-Assembly

Patterning phenomena are ubiquitous in everyday life: zebra stripes, geological formations, butterfly wings, the symmetry exhibited by many species of plant, etc.[27] Patterning typically occurs as an effect of two or more competing forces. For example, reaction-diffusion patterns only occur when both reaction and diffusion significantly contribute to a certain process. If diffusion were much faster (more dominant) than reaction, reactants would disperse, and the resulting pattern would be chaotic. If reaction were faster than diffusion, the entire reaction would occur in one location and the result would be no pattern. Only when the two are balanced and in competition do we observe the beautiful, regular patterns first predicted by Turing.[28] Likewise, many fluid mechanics patterns are the result of an instability generated by two competing forces (Rayleigh-Benard convection cells, in which gravitational forces compete with viscous damping).[29–31]

Patterning and instability can be harnessed for low-effort self-assembly of ordered structures on the nano- and micro- scales for applications in sensor arrays, photonics, dielectric materials, materials of controlled porosity, scaffolds for bioengineering, and more.[32,33] Evaporative assembly is one method employed to for assembly of regular structures. to create patterned masks for these applications. One recently developed strategy is called evaporative lithography and involves a mask where the desired pattern is cut into a solid.[34] The mask is placed a few millimeters over an evaporating colloidal solution. The holes in the mask focus evaporation in a way that causes particles to assemble in the areas under the holes.

Devices on the micro- and nano- length scales are sometimes called microsystems technologies (MTS). These devices hold a great deal of promise for the applications previously mentioned; however, their widescale implementation is currently limited by a lack of sustainable, cost-effective scale-up procedures. Thus, methods which are able to produce organized micro-scale patterns with nano-scale resolution could be disruptive in this developing field.

1.2 Organization & Summary

In this thesis, I describe seven sets of experiments which explore how interfacial properties - namely substrate texture, chemistry, and wettability- influence the crystallization of inorganic salts in order to improve sustainability across several applications. Chapter 2 introduces a thorough background on crystallization science and the role of interfacial engineering in controlling the crystallization phase change process. Relevant theory and previous work that will be used throughout subsequent chapters is introduced there. Chapters 3 and 4 explore crystallization of salts from bulk solutions for specific applications in water treatment, where monitoring crystal mass and formation kinetics are of interest. Table 1.1 lists some of the salts that are used in these chapters along with some of their crystallization properties.

Chapters 5-8 focus on crystallization from evaporating drops and the different patterns that can arise due to changes in interfacial properties of the underlying substrates. In particular, Chapters 5 and 6 investigate the fundamentals of how crystalline deposits from evaporating drops differ from colloidal ones; while Chapters 7 and 8 cover specific contact line phenomena that leads to patterning. In Chapter 9, I combine concepts from drop evaporation and from anti-fouling in a project demonstrating self-ejection of salt crystals from superhydrophobic interfaces. Chapter 10 concludes with a wholistic view of all the experiments presented and an outlook on future work across these different areas.

TABLE 1.1 Summary of environmentally relevant salts used in subsequent chapters.

Salt	Sat. conc.	Temperature -solubility	Supersat level	MW	Problematic?	Crystal Habit	surface energy
$CaCO_3$	0.013 g/L	Peak at 10°C	2 to 20	100	water, desalination, heaters, etc.	trigonal, 3m	0.412 J/m^2 (mineral-water), 0.0605 mineral
$MgCO_3$	0.14 g/L	decreases to 0.06 g/Lat 100°C	3 to 10	84.3	Sometimes, but $CaCO_3$ precipitates first	trigonal 3m	0.078 J/m^2
$Mg(OH)_2$	0.0064 g/L	increases to 0.04 g/L at 100°C	2 to 10	58.3	alkaline water, desal, heaters	hexagonal, hP3	1 J/m^2
$CaSO_4$	2.1 g/L	peak at 4°C	1.5 to 6	136	desalination	orthorhombic	0.902 J/m^2 anhydrite
$Mg(NH_3)PO_4$	0.17 g/L	increases to 0.22 g/Lat 35°C			struvite, wastewater	orthorhombic, pyramidal, mm2	0.015 J/m^2
NaCl	360 g/L	increases to 390 g/L at 100°C	1.2	58.4	NA	Octahedral, fc-cubic	0.577 J/m^2
KCl	340 g/L	increases to 560 g/L at 100°C	1	74.6	NA	octahedral, fc-cubic	0.379 J/m^2

Chapter 3. In Chapter 3 I describe the foundational work for this thesis, which explores how the bulk crystallization of a variety of salts relevant for desalination is influenced by interfacial properties. Interfacial engineering is an ideal fouling-elimination strategy as thin coatings are often more cost-effective than bulk anti-fouling materials, are safer and more ecofriendly than chemical anti-foulants, and can produce long-term solutions. Interfacial engineering principles are routinely applied in crystallization engineering due to the large influence heterogeneous interfaces have on crystal nucleation and growth.

The number of ways in which a surface can control the growth kinetics and morphology of a crystal structure is enormous. Surfaces influence nucleation by serving either as sites for nucleation, or by providing a force to encourage alignment. Surfaces can also alter growth by introducing anisotropic forces that can result in different morphologies than those that are observed without surface effects. While certain surface properties, such as presence/size of pores or other nano/microstructures, lattice matching, and surface energy, and provide clues as to which crystal morphology may be preferred, understanding the influence of a given surface on crystallization is challenging due to the large number of factors which influence crystal morphologies.

In these experiments, I attempt to clarify some effects of different surface properties on crystallization and fouling propensity. The first set of experiments only investigates the role of surface energy on fouling across different salts. Sodium chloride and potassium chloride, two very similar salts, exhibit similar fouling-surface energy relationships. In contrast, calcium sulfate exhibits a non-linear fouling-surface energy relationship, with maximum scale formation occurring on substrates that are moderately hydrophobic.

The second set of experiments investigated the combined effects of substrate texture and wettability. In addition to testing single salts, the influence of the “common ion” and “uncommon ion” effects were tested for salt combinations important in desalination. The uncommon ion effect (for example, the mixture of sodium chloride and calcium sulfate) significantly reduces scale formation. This effect is well known amongst chemists, but so far has not translated into the field of anti-fouling. A final result of note from these experiments is that composite liquid/solid materials (liquid impregnated surfaces, LIS) are able to resist scale formation across salts and salt mixtures. The liquid phase of the LIS (usually oil) prevents crystals from adhering to the surface.

Chapter 4. In Chapter 4, engineered surfaces and particles were applied towards the improved recovery of nutrient minerals (struvite). Although the initial motivation for studying crystallization at interfaces was for the prevention of mineral precipitation, the same concepts can be applied towards developing interfaces that instead promote precipitation. Precipitating minerals will preferentially nucleate heterogeneously at solid interfaces, as opposed to homogeneously in bulk solution. This contributes to the troublesome tendency of scale to form on pipe and reactor interiors; however, it also presents a potential strategy for addressing scale formation and

controlling crystallization. Surfaces and their properties (energy, morphology, chemistry, etc.) have been well-established to exert considerable influence on both precipitation kinetics and on the morphology of crystals,[35–37] allowing for the possibility of designing substrates that control precipitation and outperform nucleation on homogeneous seeds.

Current struvite recovery technologies have demonstrated success in achieving these goals; however, the process is energy intensive due to the air stripping required for chemical conditioning to maximize crystallization kinetics. This project sought to develop technology that can reduce energy consumption in these reactors by nucleating struvite at sub-optimal chemical conditions on engineered seed particles. The first set of experiments explored the influence of surface pore size on struvite kinetics and final crystal morphology.

In the second set of experiments, I develop hydrogel-impregnated Janus particles which will alter the local solubility of a solution. Janus particles have two distinct regions with different chemical and physical properties. Here, one side of the particle was a micro-porous zeolite; while the other side was a hydrogel impregnated with sodium hydroxide. Because struvite nucleates better in the presence of nanopores and at higher pH levels, these particles are able to induce nucleation even in undersaturated conditions by altering the local solubility.

Chapter 5. In Chapter 5, I introduce the technique that will be used in the remaining experimental chapters and establish important differences between colloidal and crystalline solutions. This technique is the evaporative crystallization from drops, which can be used as a method to study fluid-substrate-crystal interactions. Evaporative deposition of particles from drops is also a surprisingly useful and simple tool for microscale self-assembly. In most reports, colloidal particles within evaporating drops assemble into three common patterns: rings,[38] concentric rings,[39] and filled deposits.[40] The preference of a system for one deposit pattern over another is dictated by the particle shape/size,[40,41] the substrate wettability,[42] temperature, etc.; and can be predicted by a balance between particle-substrate interactions, convection, and evaporation rate.[43] Evaporative deposition has found application in inkjet printing, size separations,[41] colloidal crystals,[44] diagnostics,[45] and more.[34]

Evaporation of a saline drop also results in deposition patterns. During evaporation, non-volatile solutes become concentrated beyond their solubility limit and precipitate as crystals. Crystallization from drops has additional complexity compared to the deposition of colloids from drops due to interdependence of the flow and emerging crystals.[46] Many crystals will preferentially nucleate at either the air/water interface, water/solid interface, or the three-phase contact line due to lowered energy barriers for nucleation,[37,47,48] and thus will form ring-deposits even on hydrophobic or superhydrophobic surfaces.[46,48] In addition, because crystalline structures will assemble into particular shapes depending on the internal lattice of the crystal, crystalline evaporative deposits may form three-dimensional structures,[49,50] depending on the crystal type and wettability of the surface.[46,48]

Crystalline evaporative deposits were directly compared to colloidal ones in order to determine how the change in solute will influence the final deposit morphology. Evaporative deposits are classified as ring-like or clump-like based on their area localization ratio, which describes the ratio between contact area of the initially deposited drop and the final area covered by the resultant deposit. This ratio is plotted as a function of temperature in Figure 1.1 for a colloidal solution (particles) and a salt solution ($Ca(IO_3)_2$), which shows that the two have inverse temperature relationships. The deviation of crystalline evaporative deposits from the well-established phase diagram for colloidal evaporative deposits can be explained by altered supersaturations with temperature.

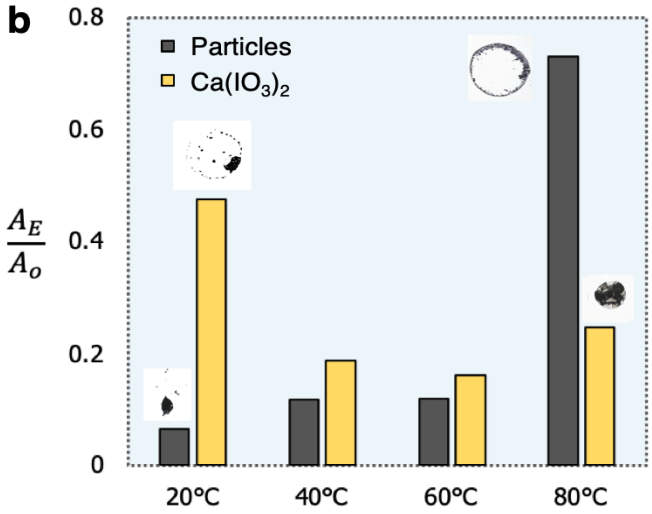

FIGURE 1.1. Temperature dependence of the final deposit size for crystalline and colloidal coffee rings. The two types of evaporative deposits exhibit an inverse temperature relationship.

Chapter 6. Chapter 6 explores how anti-fouling superhydrophobic surfaces perform when a drop of water containing dissolved gypsum, a common foulant, is evaporated on them. The goal of this work was to explore mechanisms of mineral-fouling induced corrosion/deterioration of marine vessels, aircraft, and coastal structures. Such corrosion is due in part from structural intrusion of crystals grown from ocean-generated saline drops. As such, much work has explored surface treatments that induce hydrophobicity or introduce barriers for anti-fouling and corrosion-prevention; however, I demonstrate that the efficacy of these strategies will be altered by the underlying substrate texture (the substrate solid fraction) for superhydrophobic surfaces.

I investigated evaporative gypsum crystallization from drops on superhydrophobic and liquid impregnated micropost surfaces as a function of edge-to-edge post spacing, as shown in Figure 1.2. Previous work has shown that geometric parameters of microposts have a strong influence on colloidal evaporative deposits.[51] For crystalline evaporative deposits on superhydrophobic

surfaces, four disparate regimes describing the behavior of a crystallizing solution of calcium sulfate are observed. These regimes are not observed for particle-laden drops and are a function of the substrate solid fraction. The regimes are: Cassie-pinning, Cassie-gliding, Cassie-Wenzel transition, and Wenzel. The superhydrophobic surfaces most effective at preventing ring-formation are those with low contact angle hysteresis that also remain stable in the Cassie state.

This work also validated the hypothesis that lubricant impregnation of the micropost surfaces can suppress ring-formation due to minimization of surface pinning (Figure 1.2c).[52,53] In contrast to the superhydrophobic surfaces, liquid impregnated surfaces demonstrate minimal influence of solid fraction on evaporative crystallization. The area, area localization, timescale of evaporation, and deposit morphology are all normalized by the presence of the lubricating layer, thus introducing an efficient method of eliminating crystal "coffee-rings" as well as reducing the potential for fouling and corrosion.

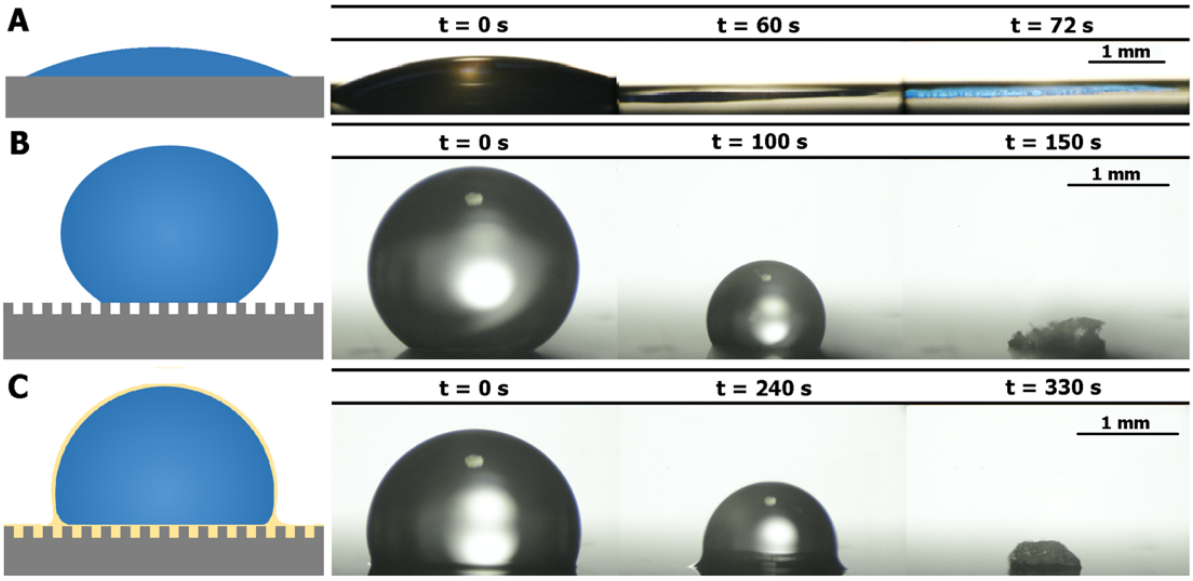

FIGURE 1.2. Schematics and images showing pinning behavior of evaporating calcium sulfate solution on A) hydrophilic silicon B) superhydrophobic microposts, and C) a spreading liquid impregnated surface. Images show the drops from both the top and side at three different times: (left) experiment initiation, (middle) shortly after crystallization has begun, and (right) end of evaporation.

Chapter 7. After observing behavior of hydrophilic, hydrophobic, and super hydrophobic surfaces, a remaining question was what would happen on a substrate of extreme contact angle hysteresis, which exhibits both hydrophobic and hydrophilic tendencies. Chapter 7 explores this question; with the result that an outer three-dimensional ring (hydrophobic tendency) emerges along with a two-dimensional (hydrophilic tendency) interior spiral or target pattern as shown in Figure 1.3. Spiral motifs are pervasive in nature, art, and technology due to their functional

property of providing compact length. Nature is particularly adept at spiral patterning, and yet, the spirals observed in seashells, hurricanes, rams' horns, flower petals, etc. all evolve via disparate physical mechanisms.

The self-guided formation of spirals from evaporating saline drops observed here occurs via a coupling of crystallization and contact line dynamics. These patterns are in contrast to commonly observed patterns from evaporation of colloidal drops which are discrete (rings, concentric rings) or continuous (clumps, uniform deposits) depending on the particle shape, contact line dynamics, and evaporation rate. Unlike the typical process of drop evaporation where the contact line moves radially inwards, here, a thin film pinned by a ring of crystals ruptures radially outwards. This motion is accompanied by a non-uniform pinning of the contact line due to crystallization which generates a continuous propagation of pinning and depinning events to form a spiral. By comparing the relevant timescales of evaporation and diffusion, I show that a single dimensionless number can predict the occurrence of these patterns. These insights on self-guided crystallization of spirals could be used to create compact length templates.

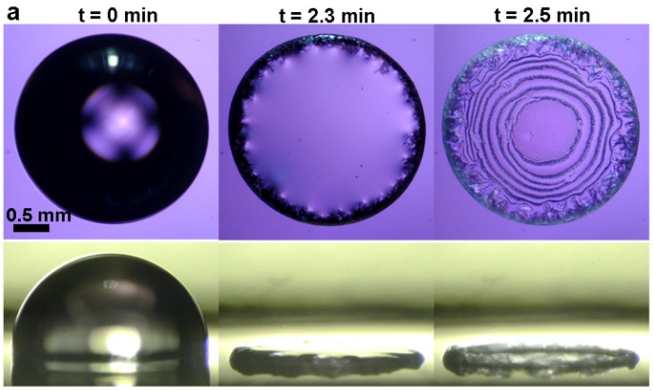

FIGURE 1.3. Spiral patterning on a substrate with extreme contact angle hysteresis. A drop of water containing dissolved calcium sulfate evaporates. Because the initial contact angle is hydrophobic, a three-dimensional outer crystalline ring forms. This ring pins the contact line and creates a thin film on the drop interior. This film ruptures at the drop center, and the newly formed contact line moves and deposits crystals in a spiral or concentric ring pattern.

Chapter 8. In Chapter 8, the theme of patterning from evaporation of drops containing a crystallizing solute is continued. Here, substrates with extremely high surface energies (low contact angles) are used. Like in the previous two chapters, a drop of calcium sulfate solution is placed on a heated surface. A crystalline ring forms at the contact line, as expected. However, patterns unexpectedly emerge at the drop interior, as shown in Figure 1.4.

Triangular sawtooth structures were the first to be observed; but by altering the experimental parameters (evaporation rate and substrate wettability), other patterns including aligned branches and hexagonal lattices of crystal clusters were discovered. The appearance of these patterns are highly repeatable so long as the evaporation rate and wettability are within specified values; which raises the question of why these patterns have not been previously observed by other investigators. I show that pinning from the initial crystalline coffee ring enables thin-film instabilities that are typically not observed in aqueous solutions.

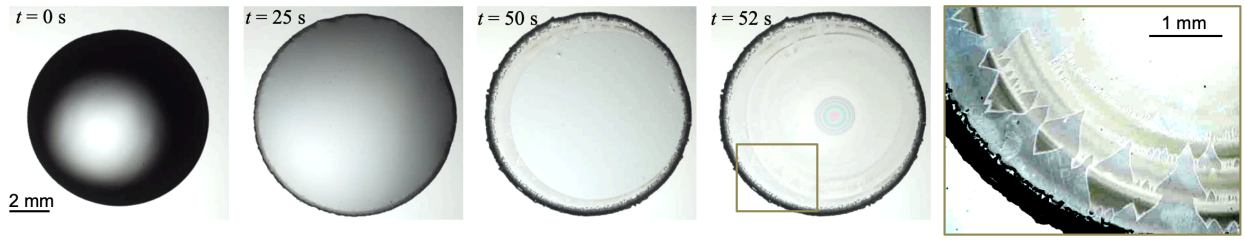

FIGURE 1.4. Evaporation of a drop on a wetting substrate leading to sawtooth patterns on the drop interior.

The patterning behavior can be explained by two different thin film instabilities. The sawtooth structures can be explained by a spinodal-like dewetting mechanism, in which Van der Waals forces in the region of the very thin (~50 nm) mobile contact line nucleates "holes" in the film. In these areas, the contact line will retract slightly faster in both the radial and azimuthal directions compared to other areas, leading to a sharp saw-tooth boundary between crystal structures of different heights. Periodic arrays, which form on the samples with largest contact angles and lowest evaporation rates, form due to a Marangoni instability. Usually calcium sulfate does not induce significant changes to surface tension on account of its low solubility, but on these length scales the anti-surfactant effect of the salt combined with evaporative cooling enable a Marangoni instability in which micro-scale drops periodically pinch off into patterned arrays. Branch patterns exist in a regime between the triangle and array regimes, and exhibit behaviors from both.

By placing a silica substrate patterned with a micro-scale array directly in a reactive ion etch, I was able to successfully etch a three-dimensional texture, as shown in Figure 1.5. The typical procedure for forming such a texture is a multi-step process involving many toxic chemicals including photo-resist, photo-developer, and acidic resist remover. Using crystalline patterns as a mask, I was able to completely skip all of those steps and remove the mask using salt water alone. This demonstration has huge implications for sustainable fabrication of micro-devices.

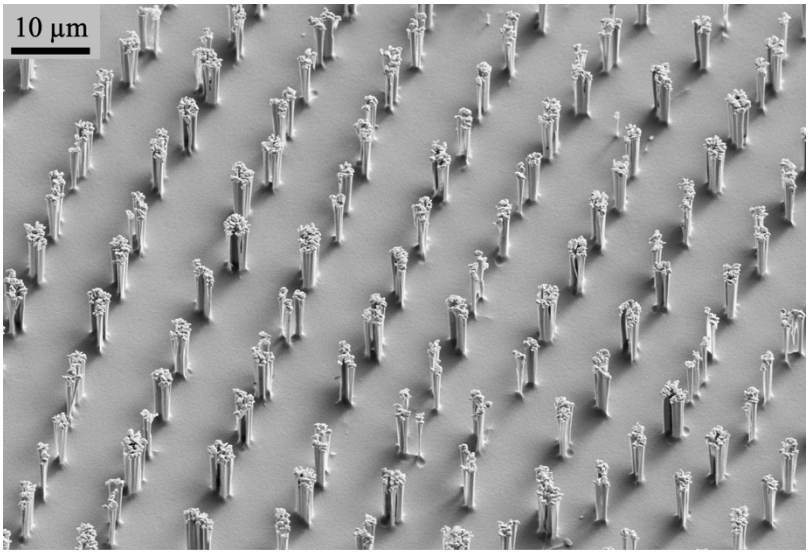

FIGURE 1.5. Three-dimensional microtexture etched into silica using array of calcium sulfate clusters as a mask.

Chapter 9. Chapter 9 reports on an unexpected and unusual phenomenon in which crystal structures formed from evaporating drops of water saturated with sodium chloride self-eject from heated, superhydrophobic surfaces (See Figure 1.6). This self-ejection occurs via the growth of crystalline "legs" during the end phase of evaporation, which results in upwards motion of a salt globe formed during the first phase of evaporation. The legs are hollow, crystalline tubes that transport vaporizing water from the sodium chloride structure towards the interface. I term the resulting structures composed of the salt globe and legs "crystal critters" due to the resemblance to biological organisms, and due to the often-erratic motions produced during growth.

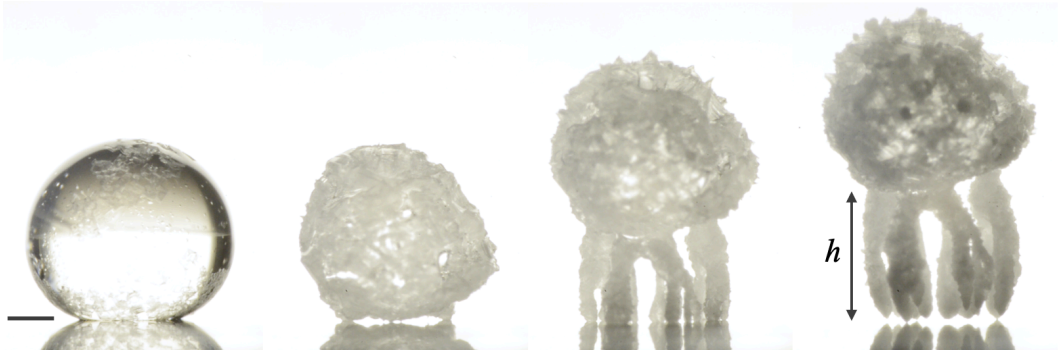

FIGURE 1.6. The crystal critter effect. A drop of salt water is placed on a heated, superhydrophobic surface. A crystalline globe forms, de-pins from the substrate, and grows legs. The final structure is easily removed due to minimal contact with the underlying substrate.

The critter phenomena does not occur for all superhydrophobic surfaces. The specific nanoscale texture of the substrate used here is vital in inducing leg growth due to "flow confinement" effects, in which routes for horizontal crystal growth across a surface are limited so that crystallization must instead grow in the vertical direction. New crystal growth between the structure and the substrate then pushes the entire salt globe up and off the surface. In contrast, on other superhydrophobic surfaces with micro-scale texture, crystals are able to grow in the vertical directions between texture features. This leads to a Cassie-Wenzel transition -similar to the transition explored in Chapter 6- where the drop falls into the texture, leading to contact line pinning and preventing the critter effect. Thus, the critter effect is dependent on the specific texture which prevents crystal intrusion and focuses flow.

Similarly, the critter effect can also be eliminated by introduction of "contaminant" salts which form at the substrate contact line and crystallize before sodium chloride. When sodium chloride is able to precipitate first, contaminant salts are unable to pin the contact line. Interestingly, addition of a surfactant does not disrupt the critter effect, and only modifies the crystal structure from a vaguely critter-like shape to a mushroom-like shape. The critter effect also works for salts that are not sodium chloride, although I show that the unique solubility properties of sodium chloride make it ideal for forming these structures.

The critter effect is controlled by the evaporation rate at the substrate surface, which controls both the rate of leg growth and the final height of the legs. Using a simple mass balance model comparing the crystallization and the fluid evaporation, it is possible to successfully predict the growth rate of legs as a function of temperature. Because of this temperature-dependent growth, it is possible to induce crystal rolling via application of a temperature gradient to the surface. Because crystals formed during this phenomenon are so easily removed from the substrate, the critter effect could provide a new method of extreme anti-fouling for spray-cooling using concentrated brines produced during desalination.

Chapter 10. Chapter 10 concludes this work by combining findings from all of the chapters. In particular, I compile a phase diagram for patterns formed from evaporating drops of calcium sulfate on substrates heated to 60°C. This phase diagram allows for prediction of patterns (single coffee-ring, spirals/concentric rings, clusters, arrays, or triangles) as a function of the substrate receding and advancing contact angles. Future possible directions for each of the three applications (anti-fouling, mineral recovery, and patterning) are discussed in conclusion of this dissertation.

References

1. Müller-Steinhagen, H., Malayeri, M. R. & Watkinson, a. P. Fouling of Heat Exchangers-New Approaches to Solve an Old Problem. *Heat Transf. Eng.* **26**, 1–4 (2005).
2. Al-Hadhrami, L. M., Quddus, A. & Al-Otaibi, D. A. Calcium sulfate scale deposition on coated carbon steel and titanium. *Desalin. Water Treat.* **51**, 2521–2528 (2013).
3. Zhao, Q., Liu, Y. & Wang, S. Surface modification of water treatment equipment for reducing CaSO4 scale formation. *Desalination* **180**, 133–138 (2005).
4. Crabtree, M. *et al.* Fighting Scale-Removal and Prevention. *Oilf. Rev.* 30–44 (1999).
5. Kan, A. & Tomson, M. Scale Prediction for Oil and Gas Production. *SPE J.* **17**, 362–378 (2012).
6. Dutrizac, J. E. & Kuiper, A. The solubility of calcium sulphate in simulated copper sulphate electrorefining solutions. *Hydrometallurgy* **92**, 54–68 (2008).
7. Zhao, X. & Chen, X. D. A Critical Review of Basic Crystallography to Salt Crystallization Fouling in Heat Exchangers. *Heat Transf. Eng.* **34**, 719–732 (2013).
8. The World Bank. Seawater and brackish water desalination in the Middle East, North Africa and Central Asia : A review of key issues and experience in six countries. 1–150 (2004).
9. Warsinger, D. M., Swaminathan, J., Guillen-Burrieza, E., Arafat, H. A. & Lienhard V, J. H. Scaling and fouling in membrane distillation for desalination applications: A review. *Desalination* **356**, 294–313 (2015).
10. Hasson, D., Drak, A. & Semiat, R. Induction times induced in an RO system by antiscalants delaying CaSO4 precipitation. *International Water Association. D. Hasson et al. / Desalination* **157**,
11. Yuan, P.-Q., Kong, N., Cheng, Z.-M. & Semiat, R. Electrostatic potential on anti-scalants modified CaCO 3 (104) surface: A molecular simulation study. *DES* **238**, 246–256 (2009).
12. and, R. P., Sumeath, C., and, F. H. B. & Fogler, H. S. Precipitation and Dissolution of Calcium−ATMP Precipitates for the Inhibition of Scale Formation in Porous Media. (1997).
13. Hodges, B. R., Furnans, J. E. & Kulis, P. S. Thin-Layer Gravity Current with Implications for Desalination Brine Disposal. *J. Hydraul. Eng.* **137**, 356–371 (2011).
14. Roberts, P. J. W., Taplin, J. & Zigas, E. Disposal of Seawater Desalination Brines and the CEQA/NEPA Process. in *World Environmental and Water Resources Congress 2017* 278–285 (American Society of Civil Engineers, 2017).
15. Müller-Steinhagen, H., Zhao, Q., Helali-Zadeh, A. & Ren, X.-G. The effect of surface properties on $CaSO_4$ scale formation during convective heat transfer and subcooled flow boiling. *Can. J. Chem. Eng.* **78**, 12–20 (2000).
16. Zhao, Q. & Wang, X. Heat transfer surfaces coated with fluorinated diamond-like carbon films to minimize scale formation. *Surf. Coatings Technol.* **192**, 77–80 (2005).
17. Azimi, G., Cui, Y., Sabanska, A. & Varanasi, K. K. Scale-resistant surfaces: Fundamental studies of the effect of surface energy on reducing scale formation. *Appl. Surf. Sci.* **313**, 591–599 (2014).
18. Cordell, D. & White, S. Peak Phosphorus: Clarifying the Key Issues of a Vigorous Debate about Long-Term Phosphorus Security. *Sustainability* **3**, 2027–2049 (2011).
19. Cordell, D., Drangert, J.-O. & White, S. The story of phosphorus: Global food security and food for thought. *Glob. Environ. Chang.* **19**, 292–305 (2009).
20. Hart, M. R., Quin, B. F. & Nguyen, M. L. Phosphorus Runoff from Agricultural Land and Direct Fertilizer Effects. *J. Environ. Qual.* **33**, 1954 (2004).
21. Conley, D. J. *et al.* Controlling Eutrophication: Nitrogen and Phosphorous. *Science (80-.).* **323**, 1014–1015 (2009).
22. Macadam, J. & Jarvis, P. Chapter 1 - Water-Formed Scales and Deposits: Types, Characteristics, and Relevant Industries. *Miner. Scales Depos.* 3–23 (2015).

23. Le Corre, K. S., Valsami-Jones, E., Hobbs, P. & Parsons, S. A. Phosphorus Recovery from Wastewater by Struvite Crystallization: A Review. *Critical Reviews in Environmental Science and Technology* (2009).
24. Bott, T. R. Aspects of Crystallization Fouling. (Oxford University Press, 1997).
25. Rahman, M. M. *et al.* Production of slow release crystal fertilizer from wastewaters through struvite crystallization – A review. *Arab. J. Chem.* **7**, 139–155 (2014).
26. Ye, X. *et al.* A comprehensive understanding of saturation index and upflow velocity in a pilot-scale fluidized bed reactor for struvite recovery from swine wastewater. *Powder Technol.* **295**, 16–26 (2016).
27. Ball, P. *Shapes: Nature's patterns: a tapestry in three parts*. (OUP Oxford, 2009).
28. Turing, A. M. *The Chemical Basis of Morphogenesis*. *Philosophical Transactions of the Royal Society of London. Series B, Biological Sciences* **237**, (1952).
29. Ball, P. *Flow*. (Oxford University Press, 2009).
30. Bergé, P. & Dubois, M. Rayleigh-bénard convection. *Contemp. Phys.* **25**, 535–582 (1984).
31. Assenheimer, M. & Steinberg, V. Transition between spiral and target states in Rayleigh–Bénard convection. *Nature* **367**, 345–347 (1994).
32. Ghosh, M. & Stebe, K. J. Convective Assembly of Patterned Media. in *Evaporative Self-Assembly of Ordered Complex Structures* (ed. Lin, Z.) 296 (World Scientific Publishing Co. Pte. Ltd, 2012).
33. Han, W. & Lin, Z. Learning from "Coffee Rings": Ordered Structures Enabled by Controlled Evaporative Self-Assembly. *Angew. Chemie Int. Ed.* **51**, 1534–1546 (2012).
34. Lin, Z. *Evaporative Self-Assembly of Ordered Complex Structures*. (WORLD SCIENTIFIC, 2012).
35. Page, A. J. & Sear, R. P. Crystallization Controlled by the Geometry of a Surface. *J. Am. Chem. Soc.* **131**, 17550–17551 (2009).
36. Diao, Y., Myerson, A. S., Hatton, T. A. & Trout, B. L. Surface Design for Controlled Crystallization: The Role of Surface Chemistry and Nanoscale Pores in Heterogeneous Nucleation. *Langmuir* **27**, 5324–5334 (2011).
37. Mullin, J. W. *Crystallization, 4th Edition*. (2001).
38. Deegan, R. D. *et al.* Capillary flow as the cause of ring stains from dried liquid drops. *Nature* **389**, 827–829 (1997).
39. Shmuylovich, L., Shen, A. Q. & Stone, H. A. Surface morphology of drying latex films: Multiple ring formation. *Langmuir* **18**, 3441–3445 (2002).
40. Yunker, P. J., Still, T., Lohr, M. A. & Yodh, A. G. Suppression of the coffee-ring effect by shape-dependent capillary interactions. *Nature* **476**, 308–11 (2011).
41. Wong, T.-S., Chen, T.-H., Shen, X. & Ho, C.-M. Nanochromatography Driven by the Coffee Ring Effect. *Anal. Chem.* **83**, 1871–1873 (2011).
42. Cui, L. *et al.* Avoiding coffee ring structure based on hydrophobic silicon pillar arrays during single-drop evaporation. *Soft Matter* **8**, 10448 (2012).
43. Bhardwaj, R., Fang, X., Somasundaran, P. & Attinger, D. Self-Assembly of Colloidal Particles from Evaporating Droplets: Role of DLVO Interactions and Proposition of a Phase Diagram. *Langmuir* **26**, 7833–7842 (2010).
44. Liu, L. *et al.* Regulation of the Deposition Morphology of Inkjet-Printed Crystalline Materials via Polydopamine Functional Coatings for Highly Uniform and Electrically Conductive Patterns. *ACS Appl. Mater. Interfaces* **8**, 21750–21761 (2016).
45. Gulka, C. P. *et al.* Coffee Rings as Low-Resource Diagnostics: Detection of the Malaria Biomarker *Plasmodium falciparum* Histidine-Rich Protein-II Using a Surface-Coupled Ring of Ni(II)NTA Gold-Plated Polystyrene Particles. *ACS Appl. Mater. Interfaces* **6**, 6257–6263 (2014).
46. McBride, S. A., Dash, S. & Varanasi, K. K. Evaporative Crystallization in Drops on Superhydrophobic and Liquid-Impregnated Surfaces. *Langmuir* **34**, (2018).
47. Shahidzadeh-Bonn, N., Rafai, S., Bonn, D. & Wegdam, G. Salt Crystallization during Evaporation: Impact of Interfacial Properties. *Langmuir* **24**, 8599–8605 (2008).
48. Shahidzadeh, N., Schut, M. F. L., Desarnaud, J., Prat, M. & Bonn, D. Salt stains from evaporating droplets. *Sci. Rep.* **5**, 10335 (2015).

49. Shin, B., Moon, M.-W. & Kim, H.-Y. Rings, Igloos, and Pebbles of Salt Formed by Drying Saline Drops. *Langmuir* **30**, 12837–12842 (2014).
50. Du, R. & Stone, H. A. Evaporatively controlled growth of salt trees. *Phys. Rev. E* **53**, 1994–1997 (1996).
51. Dicuangco, M., Dash, S., Weibel, J. A. & Garimella, S. V. Effect of superhydrophobic surface morphology on evaporative deposition patterns. *Appl. Phys. Lett.* **104**, 18–23 (2014).
52. Subramanyam, S. B., Azimi, G. & Varanasi, K. K. Designing Lubricant-Impregnated Textured Surfaces to Resist Scale Formation. *Adv. Mater. Interfaces* **1**, 1300068 (2014).
53. Smith, J. D. *et al.* Droplet mobility on lubricant-impregnated surfaces. *Soft Matter* **9**, 1772–1780 (2013).

Chapter 2.
Background

Crystallization is ubiquitous in both natural and artificial processes, and is a phase change process in which disordered units (which could be elements, ions, molecules, macromolecules, or even colloidal-scale particles) assemble into an organized, solid lattice structure called a crystal. Crystals differ from amorphous solids in that crystals demonstrate long-range order in their molecular structures,[1] and often exhibit unique properties as a result of this order. The best-known consequence of this is the optical properties of crystals, which often exhibit dramatic colors and/or glean due to birefringence (optical anisotropies) of the molecular lattice. Crystalline structures can be very simple, such as the cubic lattice of sodium chloride (NaCl) where anions and cations are arranged in an alternating sequence; or very complex, such as in macromolecular crystallization where multiple functional groups, geometries, and solute molecules intertwine to form a complex recurring pattern.

In industry, crystallization is used to prepare products such as table salt and chocolate, purify drugs, grow semiconductor materials from melts, and obtain commercial chemicals. Crystallization is also an important technique for drug discovery, as large and pure protein crystals are required for determination of structure via x-ray diffraction. Some natural crystallization processes include geologic mineral formation, development of kidney stones, and bio-mineralization of mollusk shells.[2] In each of these examples, crystallization occurs via different pathways. Chocolate crystals are formed from solidification of pure melted material, kidney stones and minerals grow from a solution containing dissolved pre-cursors, and thin polycrystalline films for semi-conductors may be crystallized from the vapor phase for precise control over structure.

Growth from solution (as opposed to from a melt or via the vapor phase) is the most common crystallization pathway in nature, and is also the most complex due to solute/solvent interactions. In nature, these interactions are often further complicated by the presence of additional solutal contaminants that may or may not contribute to crystal chemistry but nevertheless alter crystal formation. The present works focuses on crystallization of inorganic salts from aqueous solutions (i.e., water is the solvent), which is of importance in both natural and artificial systems. This chapter therefore introduces some essential concepts in solution crystallization and for predicting/understanding crystal morphology in section 2.1. Section 2.2 expands on how these principles can be applied and/or altered in the presence of an interface to demonstrate how interfacial engineering can applied to control crystallization. Finally, section 2.3 introduces the "coffee-ring effect" – the colloquial term for deposition of particles or solutes from an evaporating drop – and explains how observations of crystallization from an evaporating aqueous drop can yield information about crystal-interface interactions.

2.1 Crystallization Fundamentals

To understand crystallization, we first must understand the driving forces resulting in crystallization, the kinetics of the process, and the internal lattice structures that contribute to macroscopic crystal morphology. Thermodynamic principles explain why crystallization occurs, but say nothing about the rate. Kinetics is used to quantify the rate of the nucleation and growth of a crystal.

Thermodynamics

Thermodynamics is the study of changing energies, and the tools provided by equilibrium thermodynamics allow us to describe the spontaneity and rate of a phase change process such as crystallization of salts (minerals) from water. An equilibrium system is one that is in a state of minimum energy, and will therefore remain at that low energy state unless somehow perturbed. Although true thermodynamic equilibrium is rarely achieved in real systems, these approximations still provide valuable insight into the driving forces and direction of a reaction.

The driving force for crystallization from a solution is the supersaturation, which describes the amount of precipitant that is in excess of the solubility concentration. The supersaturation can be defined a number of different ways, including the ratio of the actual concentration to the saturation concentration (S), the difference between the two (Δc), or the normalized difference (σ, $\sigma = S-1$).[1] Supersaturation can be altered by great number of environmental factors, including temperature, pressure, chemistry, presence of impurities/interfaces, solvent quality, etc. Predicting how these environmental factors will influence the supersaturation is complex, as there is no general rule that can be applied across all crystal chemistries. For example, most salts have lowered solubilities at

decreased temperatures and will therefore crystallize more readily at lower temperatures. However, there are a handful of minerals which exhibit very little temperature dependence, and some that even have an inverse solubility-temperature relationship and become more likely to crystallize at higher temperatures.

The Gibb's energy of a reaction describes the driving force for that reaction to occur. For any chemical reaction, the change of free energy is:

$$\Delta G = \sum \Delta G_{products} - \sum \Delta G_{reactants} \quad 2.1$$

Where ΔG is the Gibb's free energy of the reaction. Gibb's energy is used to describe the direction of that a system moves towards, i.e., whether a process will occur spontaneously or not. Therefore, when the energy of products and reactants are known, we can predict whether or not a reaction is energetically favorable. When the net change in energy (ΔG) is negative, the associated process is thermodynamically favorable and will occur spontaneously (though, it should be noted that a spontaneous process may still be kinetically limited; aka slow). This concept can be applied to crystallization, where the reactants are the dissolved ionic building blocks and the product is the mineral of interest. For a phase change process, chemical potential describes the energy associated per mole of reactant:[3]

$$\mu_i = \left(\frac{\partial G}{\partial n_i}\right)_{T,P} \quad 2.2$$

Where μ_i is the chemical potential of species *i*, and n_i is the number of moles. The chemical potential as a function of the solution temperature and chemistry is:

$$\mu_i = \mu_i^o + RT \ln a_i \quad 2.3$$

where μ_i^o is the chemical potential of species *i* in the standard state, *R* is the ideal gas constant, *T* is the temperature in degrees Kelvin, and a_i is the activity of *i*. The activity is a dimensionless quantity that can be described as the molarity of species i (m_i) multiplied by an activity coefficient (γ_i). Rewriting equation 2.1 in terms of the chemical potential gives:

$$\Delta G = \sum_{products} \eta_i \mu_i - \sum_{reactants} \eta_i \mu_i \quad 2.4$$

Where η_i is the stoichiometric coefficient for species i. Combining equations 2.3 and 2.4 allows for derivation of the following:

$$\Delta G = \Delta G^o + RT \ln \left(\frac{\prod_{products} a_i^{\eta_i}}{\prod_{reactants} a_i^{\eta_i}}\right) \quad 2.5$$

Where ΔG^o is the standard free energy of the reaction, defining the change in energy for reaction when all components are at standard temperature and pressure. The term inside of the logarithm

of equation 2.5 is the definition of the equilibrium product $K_{eq.}$ For a precipitation reaction, this product is called the solubility product, and is notated as $K_{sp.}$ For a reasonably dilute aqueous solution, the activity of water is approximately 1. In addition, the activity of any standard state solid (crystal) is also 1.[3] With these two conditions, the equation for the solubility product for a crystallizing solution can be reduced to:

$$K_{sp} = \prod_{products} a_i^{\eta_i} \tag{2.6}$$

where the products are the dissolved ionic species that crystallize. Equation 2.6 does not depend on the amount of solid precipitant in the system, meaning that any amount of solid will be in equilibrium state with an aqueous solution at the saturation concentration. As previously noted, supersaturation and solubility are highly dependent on system conditions, and most notably on temperature. Adjustments to the solubility product (or other equilibrium product) to account for the influence of temperature is done using:

$$\ln K_1 - \ln K_2 = \frac{\Delta H_R^o}{R}\left(\frac{1}{T_1} - \frac{1}{T_2}\right) \tag{2.7}$$

Where ΔH_R^o is the difference between the standard state enthalpies of the reactants and products, also termed the standard enthalpy of formation, T_1 is the reference temperature, and T_2 is the temperature of interest.

For a dilute solution, the activity a_i of an ion is identical to its molar concentration. For non-dilute solutions, the activity is equal to the molar concentration multiplied by an activity coefficient, γ_i. For many environmental waters, salt concentrations are high enough that altered activities must be accounted for. The activity coefficient can be found using Debye-Hückel theory (valid for ionic strengths of to 0.001 M):

$$\log \gamma_i = -Az_i^2\sqrt{I} \tag{2.8}$$

Where A is a constant related to the pressure and temperature (0.5085 at STP), z_i is the charge on ion i, and I is the ionic strength of the solution:

$$I = \frac{1}{2}\sum m_i z_i^2 \tag{2.9}$$

For solutions of ionic strengths greater than 0.001 limit, equation 2.8 can be modified with additional chemistry-specific parameters.[3] When there are multiple salt species in solution, the ionic strength will be increased, the activity coefficients of all salts in solution will be lowered, and precipitation of a given salt will require a higher concentration than usual. Thus, the influence of other salts is typically to reduce precipitation rates. One exception to this rule is the common ion effect, in which addition of a chemistry sharing an ion with a salt already present (for example, $CaSO_4$ and $CaCO_3$ both contain calcium) will lead to decreased solubility of the original salt.

Nucleation

Nucleation refers to the initial formation of a crystal nuclei (also called seeds), and can be heterogeneous (at an interface/surface) or homogenous (in the bulk).[4] For nucleation to proceed, two things must occur.[5] First, the precursor units must group together either via random thermal fluxes or due to some attraction. Second, the units within the emerging nucleus must realign into the crystal lattice. The first process is inherently stochastic (random), and is far more likely to occur at concentrations at or above saturation. However, precursor seeds are capable of forming below saturation; but they are unstable and re-dissolve quickly. Following stable nucleation, growth of the crystal tends to proceed rapidly so that nucleation is typically the rate-limiting process in crystallization.

Crystals may begin to nucleate as soon as the conditions for supersaturation are met (i.e., once the concentration of dissolved reactants have reached or exceeded their solubility concentration). However, due to the energy barrier associated with nucleation, saturation may not be a sufficient condition for crystallization to begin. For some salts, homogeneous nucleation will not occur until the solution is well over the saturation point (5 to 10 times the solubility concentration). Addition of heterogeneous nucleation sites (for example, adding a porous material) to a supersaturated solution can induce precipitation at lower concentrations closer the solubility level.

Nucleation occurs as a result of competing processes: first, there is a negative (i.e., favorable) energy change associated with formation of the solid volume as a result of supersaturation or undercooling. Second, there is a positive energy associated with the formation of a new interface. Adding these two energies gives the free energy change of homogeneous nucleation as:[4]

$$\Delta G_n = -V_S \Delta G_{SL} + A_S \sigma_{SL} \tag{2.10}$$

Where V_S is the volume of the new solid particle, G_{SL} is the free energy change for the solid-liquid transformation (equation 2.5), A_S is the interfacial area of the solid particle, and σ_{SL} is the surface tension between the liquid solute and newly formed solid. Under the common assumption of a spherical nucleus this equation becomes:

$$\Delta G_n = -\frac{4}{3}\pi r^3 \Delta G_{SL} + 4\pi r^2 \sigma_{SL} \tag{2.11}$$

Where r is the radius of a spherical nucleus. Under the spherical nucleus assumption, it is then straightforward to derive a critical radius at which nucleation energy has a maximum:

$$r^* = \frac{2\sigma_{SL}}{\Delta G_{SL}} \tag{2.12}$$

where r^* is the critical nucleation radius, representing the smallest required size of a nucleus with favorable growth kinetics. Nuclei larger than this radius will continue to grow, while dissolution

is more favorable for nuclei smaller than this critical value. Because of the importance of nucleus size in determining growth, achieving a sufficiently large nucleation rate is fundamental to forming crystal nuclei that won't dissolve. The Gibb's energy at the critical radius gives the maximum energy barrier to crystallization. For a spherical nucleus, this has the form:

$$\Delta G_n^* = \frac{16\pi\sigma^3}{3(\Delta G_{SL})^2} \quad 2.13$$

The nucleation rate, J_N, is the product of the nuclei density times the rate that units are added. This broad definition of the nucleation rate can be related to the number of nucleation sites and to the energy barrier via classical nucleation theory.[6]

$$J_N = NZ\beta^* \exp\left(\frac{-\Delta G^*}{k_B T}\right) \quad 2.14$$

Where J_N is the steady-state nucleation rate [nuclei/volume-time] at temperature T, N is the number density of nucleation sites, Z is the Zeldovich factor, β^* is the rate at which units are added to the nucleus, ΔG^* is the Gibbs free energy of forming a critical nucleus (equation 2.13), and k_B is the Boltzmann constant ($1.38*10^{-23}$ J/K). This rate can also be written in more familiar terms as:

$$J_N = A \exp\left(\frac{-\Delta G^*}{RT}\right) \quad 2.15$$

Which is the Arrhenius equation for reaction kinetics, where A is a constant that depends on the reaction, and R is the ideal gas constant (8.314 J/mol-K). Note that the units of the energy barrier must be altered to match the units of either k_BT if using equation 2.14, and RT if using equation 2.15. The two are related by the Avogadro number, $6.022*10^{23}$ molecules/mole.

From classical nucleation theory (equation 2.14), we see that the nucleation rate is directly dependent on the energy barrier that must be overcome for stable nuclei to form. This energy barrier, in turn, is dependent on the concentrations/activities of chemical reactants in solution (equation 2.5). Thus, higher supersaturation levels will exponentially increase the rate of nucleation. In addition, any influences that change the interfacial energy term in equation 2.10 or add additional terms to this equation will profoundly influence nucleation rates. One important influence is the presence of solid surfaces, which will be discussed in section 2.2.

Growth

Following nucleation, a crystal seed continues to grow via addition of additional dissolved units into its lattice until a full-fledged crystal is grown. Unlike nucleation, whose rate is controlled by the likelihood of units gathering into a stable seed, crystal growth is typically diffusion-limited. Nucleation of new crystal seeds and growth of existing ones are competing processes, in which an overabundance of units in solution compared to sites on a growing crystal will result in new nucleation.[7] In contrast, for a solution that hovers near the saturation level with a sufficient number of existing crystal seeds will promote growth over new nucleation. The kinetics of crystal growth can be described as:[7]

$$-\frac{dc}{dt} = ks(c - c^*)^n \tag{2.16}$$

Where c is the molar concentration, c^* is the solubility concentration, k is the growth rate constant, n is the "order" of the crystal growth process, and s is a function of the number of growth sites available. A typical formulation for s is to estimate a site density multiplied by the surface area of the crystal. For salts crystallizing from aqueous solution, n typically ranges between 1 and 2.[1] This equation can be modified to separate the distinct steps of diffusion and reaction with an intermediate concentration in the vicinity of the interface.[1] For diffusion:

$$-\frac{dc}{dt} = k_d A(c - c_i) \tag{2.17}$$

Where k_d is the coefficient of mass transfer by diffusion, A is the surface area of the crystal, and c_i is the concentration of dissolved species at the crystal interface. For the incorporation reaction:

$$-\frac{dc}{dt} = k_r A(c_i - c^*) \tag{2.18}$$

With k_r being the reaction rate constant for the integration process. In practice, determination of the interfacial concentration is challenging and therefore the "overall" kinetic equation (equation 2.16) is used to describe the driving force for crystal growth. The diffusive transport is governed by Fick's law and mass conservation. For a spherical particle:[8]

$$\frac{dc}{dt} = D\left[\frac{1}{r^2}\frac{\partial}{\partial r}\left(r^2\frac{\partial c}{\partial r}\right)\right] \tag{2.19}$$

Where D is the diffusion coefficient, and r is the particle radius. This equation combined with boundary conditions that at the concentration goes to the bulk value at $r \to \infty$ and that the concentration is the saturation value c^* at the radius of the growing crystal allows us to solve for the growth rate of the crystal assuming the incorporation reaction is much faster than diffusion.

If we consider crystal growth to be a 2-dimensional nucleation problem (in which units adsorb to the 2D faces of the growing crystal), it is possible to describe growth in the same theoretical

framework as nucleation. The free energy of 2D nucleation is the sum of two competing processes: the favorable component driving equilibria towards the crystalline solid phase, and the unfavorable cost of creating new surface area. Starting with equation 2.10 and assuming a cylindrical 2D area of radius *r,* we find the energy of growth:

$$\frac{\Delta G_g}{h} = -\pi r^2 \Delta G_{SL} + 2\pi r \sigma_{SL} \quad 2.20$$

Where h is the height of 1 unit, and other values retain previous definitions from equation 2.10. The energy barrier to growth under the cylindrical disk assumption is then:

$$\Delta G_g^* = \frac{\pi h \sigma^2}{\Delta G_{SL}} \quad 2.21$$

The ratio of the energy barriers for nucleation (3D spherical) and growth (2D cylindrical) is therefore:

$$\frac{\Delta G_n}{\Delta G_g} = \frac{16\sigma h}{3\Delta G_{SL}} \quad 2.22$$

This ratio reveals that the energy barrier for nucleation will generally be larger than that for growth when the surface tension is large, or when the free energy of solidification is small. Both of these criteria are true at lower supersaturation conditions, where the free energy to be gained from rearrangement into a solid is small, and the surface tension barrier to creating new interface is high. At higher supersaturation conditions, the ratio becomes closer to 1, as increased salt concentration begins to "crowd" and precipitation is energetically favorable.[1]

While the growth theories presenting in equations 2.16-2.21 are simple in nature and application, true crystal growth is far from simple. There are multiple processes that might occur beyond the simple model of growth units diffusing towards, and then incorporating in, the growing face of crystal. Ions may migrate over the surface of the crystal, regions of local dissolution may occur, water may diffuse through the crystal matrix, etc. In addition, growth is hard to predict because it rarely proceeds the same way for any two crystals even when environmental conditions are identical. The growth rate of an individual face, or even just of a localized part of the face, will be ultimately determined by the dislocations.[9] Dislocations are regions of surface defects on the crystal that are energetically favorable for binding of new units. On a molecularly flat surface, an incorporating unit will only be able to bind with one other unit. At a step dislocation, it can bond with two; and at a kink, it can bond with three. Screw dislocations are of particular importance, as these spirals of new crystal growth constantly generate kink-type binding sites. The lattice structure and dislocations strongly influence the rate of growth, and anisotropy of growth rates of various crystal faces leads to the final crystal structure. These factors are difficult to understand and control, which is part of the reason that crystallization experiments show a wide amount of variability between trials.

Morphology

A crystal of the same chemistry can form different macroscopic structures, which are related to the microscopic packing structure of the atomic units. Despite having the same chemical formula, crystals of different morphologies can have very different solid and chemical properties in addition to simply having different shapes. For example, the crystal lattice structure can influence conductivity, thermal conductivity, and fracture strength. Depending on the application, alteration of these properties can have significant impact on the product quality.

The morphology of a crystal is strongly related to the packing of ions (or other growth unit) within the crystal lattice. The ions will arrange themselves in the crystal in a way that maximizes attractive forces while minimizing repulsive ones.[10] The resulting lattice structure depends strongly on the relative sizes of the cations and anions. When the two are similarly sized, a closest packing structure is typically resultant. For some species where the anion is much larger than the cation, for example cesium chloride, a cubic lattice of chloride ions is formed with the cesium anion in the center of the cube.[10] The seven crystal systems common to ionic compounds are shown in Figure 2.1.

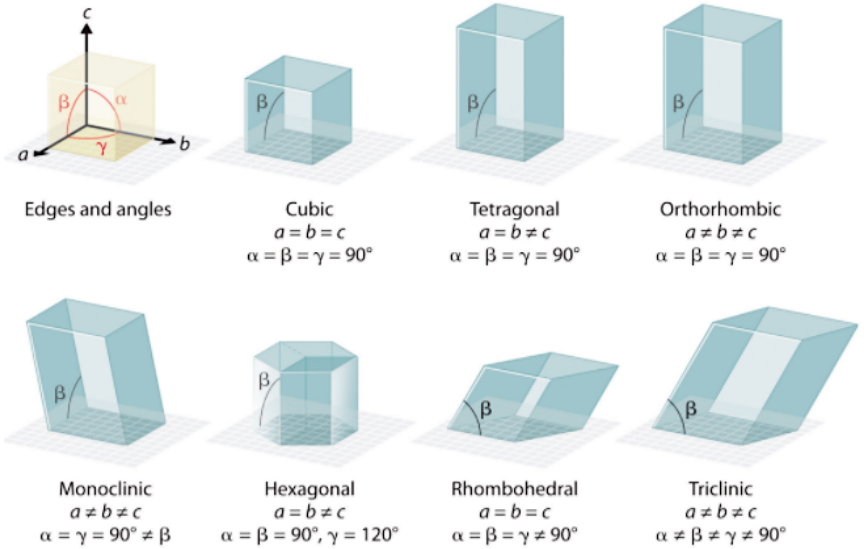

FIGURE 2.1. The seven general crystal lattices. The internal arrangement of molecules into these structures often controls the macroscopic appearance of the crystal. From Moore et al.[11]

The arrangement of the lattice has an influence on the macroscopic structure of the crystals as well. In 1669, it was observed that crystals of the same species that differ in appearance still maintain constant angles between corresponding faces, and that these angles are characteristic of the substance. For example, sodium chloride has a cubic lattice composed of alternating sodium and chloride ions; and will often form crystals with cubic symmetry. Likewise, gypsum (calcium sulfate dihydrate) often forms prismatic crystals due to its monoclinic lattice.

While internal crystal lattice and chemical composition influences the angles between faces, the crystal morphology of a given material can still vary widely. The shape of a crystal is controlled by growth of the different crystal faces, which in turn depends on the shape of the atomic unit, the form of the internal lattice, and on conditions of growth. The frequency of a crystal face is given by the Law of Bravais, which says that a higher density of lattice nodes intersecting a crystal face will result in that face occurring more often. Other conditions that are known to influence morphology of crystals include temperature, pressure, solvent, solute concentration,[12] presence of co-solutes, and available volume for growth. In addition, the speed of crystallization will influence the shape of the final crystal.

Understanding which morphology of a given crystal structure will dominate over others is not a simple task. Clearly, whichever form spontaneously emerges is thermodynamically stable under the given conditions, but the thermodynamic coupling of various effects renders precise calculation difficult. The coupled effects include heat transport, mass transport, hydrodynamic flow, electrical potential, stress and strain, etc.[9] For a crystal growing unconstrained, the stable crystal shape exhibits extremum in velocity of protruding elements. This means that small shape distortions on a crystal interface develop in directions that lead to an extremum in growth velocity or intrusion distance.[9] At equilibrium, a crystal will take the morphology that minimizes the total surface energy.[13] The surface energy (γ) is the reversible work required to create a unit of surface area at constant temperature, volume, and chemical potential, and is given as:

$$\gamma = \frac{dW}{dA} \tag{2.23}$$

Where W is work, and A is area. The energy of a surface is

$$E = \int \gamma dA \tag{2.24}$$

In a liquid droplet, this minimum equilibrium energy results in a spherical shape. However, for an anisotropic solid crystal material, the crystal faces with lowest surface energy will give preferred orientations. Therefore, surfaces with low free energy will be located closer to the center of a crystal, while surfaces with high free energy will extend away from the crystal center. This concept is given by the Wulff theorem, which says:

$$\frac{\gamma_x}{h_x} = constant \tag{2.25}$$

where h_x is the characteristic length of a face x. Despite good understanding of thermodynamic constraints on a crystallizing system, it is still difficult to predict crystal shapes because of the degree of variables that cannot be controlled or predicted in finding the surface energy, in particular the dislocation mechanisms, which are largely responsible for precipitating growth.[14] Dislocations can be considered a point defect located on a surface. On a flat surface, point defects may consistent of a vacant or excess surface site that have enhanced/reduced reactivity. Dislocations

are points at which the crystal surface structure is not flat, and therefore are regions of more energetic interactions. Examples of dislocations include step, kink, terrace, and screw.[13] The free energy change of having n possible bonds at given bonding site is:

$$\Delta G = n\Delta H - T\Delta S_m - nT\Delta S_{vib} \quad 2.26$$

where ΔH is the enthalpy of vacancy formation, $\Delta S_m$is the mixing entropy, and ΔS_{vib} is the vibrational entropy change between a bound and free unit. Thus, the energy barrier for growth will decrease with increased vacant sites under the condition that the contribution from vibrational entropy is greater than the enthalpic contribution; and crystal growth will occur faster on surfaces with more possible bonds.

2.2 Crystallization at Surfaces

Surfaces are ubiquitous in nearly all crystallization processes. They exist in chemical manufacturing (tank walls), aqueous geochemical systems, within the body, etc. In some of these scenarios, crystallization on a surface is desirable. For example, surfaces can be used to nucleate products in industrial crystallization, or can be used as a separation tool. In other cases, crystallization on a surface is detrimental, such as in any process requiring heat transfer. When salt crystals (scale) have built up heavily on heat transfer equipment, the scale acts as insulation and prevents proper functionality.[15] Scale buildup can also cause equipment failures due to blockages in water systems, and can cause aesthetic and structural damage to homes and buildings. Furthermore, surface effects can influence scale-up of crystallization and other chemical processes. A lab-scale reaction will have a higher surface area to volume ratio than a reaction occurring within an industrial sized reactor. In some cases, this can lead to difficulties in scale-up in processes involving primary nucleation.[16] Therefore, understanding and controlling the influence of interfaces in crystallization has broad importance across applications.

One reason that surfaces are so important in crystallization is that foreign solids tend to be particularly effective at enhancing nucleation.[17] Generally, the reason for this is that surfaces lower the energy barrier for nucleation. Crystal units are attracted to, and sometimes adsorb to, the surface, allowing more single units to come together and form a nucleus. Interfaces can also help with alignment of adatoms, further enhancing the rate of nucleation. From a macroscopic viewpoint, changes in crystallization kinetics at surfaces are related to the density of nucleation sites available and/or to the energy barrier. From a mechanistic viewpoint, nucleation can be enhanced by either providing a force for crystal units to come together, or by providing a force influencing the alignment of those units. However, this very general statement does not fully explain the exact influence surfaces have on kinetics or morphology of the crystal. In some cases,

it is observed that surface effects are able to nucleate crystals that otherwise do not nucleate in the bulk at the same conditions.[1] It has also been observed that different morphologies will form at different surfaces even within the same crystallizing system. This influence is not limited to solid surfaces, as many crystals will preferentially form at the air/water interface.[1,18]

Because surface interactions are so important in crystallization, surface engineering is an appropriate strategy to apply when one wishes to either enhance or reduce crystallization in a given process.[16,19,20] Functionalized surfaces can promote nucleation, control for a specific species, or selectively crystallize a desired morphology.[21] Strategies for promoting nucleation using surface engineering include: templating, maximizing surface area, controlling surface energy, creating porosity on the length scale of the critical radius of a given crystal (see equation 2.12),[16,22,23] and functionalizing a surface to promote specific chemical interactions.[24] Surfaces utilizing nano-porous confinement allow crystal nuclei to reach the critical radius faster than they are able to in the bulk and thus enhance nucleation.[24,25] Templating surfaces make use of a nano-pattern that matches the crystal lattice for nucleation, which is also known as epitaxial nucleation.[24] Finally, charged surfaces are able to attract molecules to each other via electrostatic interactions.[24] Electrostatic interactions between the surface and the molecules should not be so strong as to disrupt the weak lattice interactions between molecules that result in crystal arrangement. All of these surface engineering strategies can be applied towards promoting or inhibiting crystallization.

Surface Energy

Surface energy and interfacial phenomena are important for both ionic and macromolecular crystallization.[26,27] The strong influence of surfaces in crystallization and other reactions is rooted in energetics. In the solid state, molecules have strong attractive interactions to each other (regardless of whether the solid is crystalline or amorphous).[17] Molecules within the bulk of the solid are completely surrounded by other molecules with attractive interactions. In contrast, molecules at a solid surface will have unsaturated valences, giving rise to energetic interactions between the solid and surrounding fluid. Fluid (whether gas or liquid) molecules at a solid surface will have different (typically higher) reactivity than species of the same type within the bulk.[17]

Surface energetics are also critical for epitaxial nucleation. For a well-ordered surface composed of a single crystal, there will exist periodic "potential wells" where molecular units can bind.[17] On these surfaces, it is possible to induce epitaxial nucleation by lattice matching of the potential wells of the solid to the desired crystal structure.[28] This concept is powerful for engineering selectivity of polymorphism, and has recently been applied in a calcium carbonite system where lattice matching was used to nucleate calcite under conditions that typically favor formation of aragonite.[29] Epitaxial nucleation is difficult to achieve, as finding a perfect match between the of the solid and the precipitating crystal is challenging. An imperfectly matched lattice may initially enhance nucleation but will ultimately result in slower crystal growth due to elastic stresses.[30]

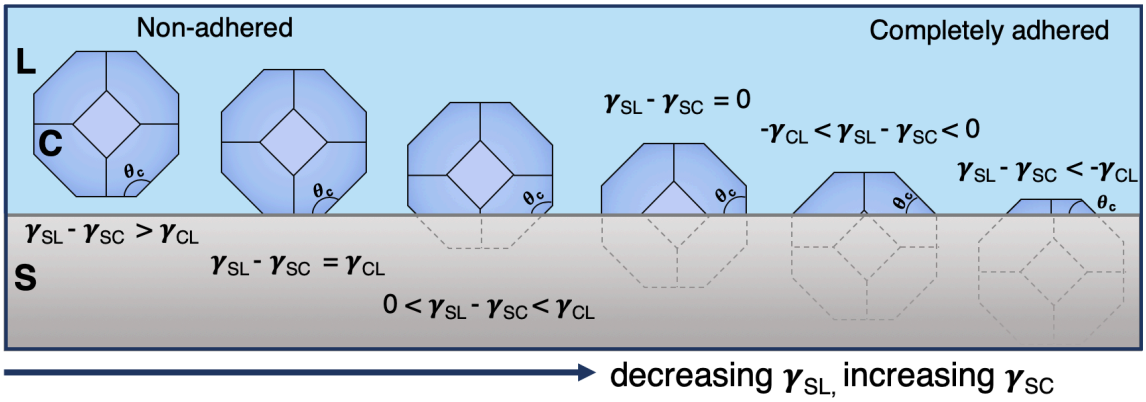

FIGURE 2.2. How surface energy between the substrate, crystal, and liquid influences crystal morphology. "Non-wetting" crystals will form in the bulk, as shown on the left. "Wetting" crystals have a preference for growing on the substrate and will form flat structures. Crystals of intermediate wetting properties will grow adhered to the substrate, but will alter their center of symmetry to adapt to the underlying substrate.

Surface energy is traditionally described in terms of the individual components of interfacial energies between the coexisting phases. For a drop of liquid (L) in the presence of a gas (V) located on a surface (S), the Young-Dupre equation describes the contact angle (θ) as a function of the surface energies between the three phases:[13]

$$\gamma_{LV} \cos\theta = \gamma_{SV} - \gamma_{SL} \qquad 2.27$$

This concept can be modified for the case of a crystal (C) growing at a surface (S) within a liquid/gas solvent (L):

$$\gamma_{CL} \cos\theta = \gamma_{SL} - \gamma_{SC} \qquad 2.28$$

This approximation can be applied towards predicting the effects of a surface on crystal morphology. For a crystallizing species in the presence of an interface, there are three possible cases. When $\gamma_{SC} - \gamma_{SL} \geq \gamma_{CL}$, the crystal particle does not "wet" the surface, and it will form in the same morphology as a free particle.[13] When $0 < \gamma_{SC} - \gamma_{SL} < \gamma_{CL}$, the equilibrium shape will be modified, as the crystallizing particle will now seek a new contact angle of a "partially-wetting" system. The Wulff center of symmetry will be modified, which then modifies the entire structure of the crystal, as demonstrated in Figure 2.2.[31] Finally, as wetting increases, $(\gamma_{SC} - \gamma_{SL}) < 0$, the equilibrium shape becomes indeterminant as the crystal seeks to fully "coat" the substrate.

The wetting properties between a crystallizing particle and an interface also influence the degree of adhesion of that crystal to the interface, with the adhesion work being:[13]

$$W_a = \gamma_{CL} + (\gamma_{SL} - \gamma_{SC}) = \gamma_{CL}(1 + \cos\theta) \qquad 2.29$$

Surface energy can be found when the adhesion work and contact angle are experimentally determined, and the adhesion work can be calculated when the surface energy and contact angle of a system are known. The adhesion work is important to understand for applications in which crystals must be cleaned from a surface or when a crystalline product must be harvested from a surface. In scale-reduction applications, the hydrophobicity of a surface is considered a key parameter for reducing scale formation.[32,33] However, the energy between a crystallizing solute and the surface must be considered in addition to the energy between the surface and the solvent. Indeed, it has been shown that smaller crystal-surface contact angles are correlated with a decrease in nucleate induction times.[16]

As previously mentioned, energy barriers for nucleation are significantly altered in the presence of surfaces. A portion of this influence is directly related to energies between the liquid, crystal, and substrate. The Gibb's free energy of formation for a crystal nucleus on a substrate is:

$$\Delta G_n = \frac{5\pi V_M^2}{3(k_B T)^2 S^2}(2\gamma_{SC} - \gamma_{LC} - \gamma_{SL})^3 \qquad 2.30$$

Where V_M is the molecular volume, k_B is the constant, T is temperature, S is supersaturation, γ_{SC} is the surface energy between the substrate and crystal, γ_{LC} is the energy between the liquid and crystal, and γ_{SL} is the energy between the substrate and liquid.

Surface Structure

Solid catalysts are (usually) most effective when they have a high specific surface area, as more valence sites on the solid are available for nucleating reactions.[17] Because of this, porous/textured surfaces such as zeolites are effective in catalyzing reactions and in promoting crystal growth.[22] In general, we can distinguish between two structural effects of importance in promoting crystallization. First is the general availability of surface area, and the second is confinement. The first set of interactions are often confused for the second type, as was demonstrated in an investigation studying surfaces with porosity between 15 and 120 nm.[20] Spherical nanopores of this size range hinder nucleation while angular pores of the same size promote it. Hexagonal pores in particular were able to sharply reduce nucleation timescales. These results suggest that nucleation enhancement at this length scale is due to the presence of angular ridges rather than due to confinement. True confinement effects will only occur on length scales similar to the size of the critical radius, about 10 nm.[16,20]

Confinement effects on the order of magnitude of the critical radius can nucleate crystals even in under-saturated conditions. In addition to this effect, nanoscale confinement can also control for polymorphism by selection of a pore size at which a desired crystal has a nucleation barrier lower than the other form (see figure 2.3).[34,35] One investigation showed that crystals grown in

nanometer scale cylindrical pores adopt preferred orientations relative to the pore direction, and that the size of the pore controlled the form of the polymorph.[36] Another study found that pore morphology, in addition to size, can influence the orientation domain structures and polymorphism.[37]

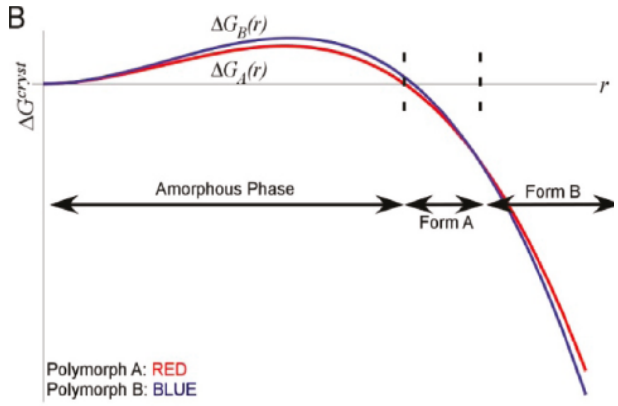

FIGURE 2.3. From Hamilton et. al[34], showing the Gibb's free energy of crystal formation for two hypothetical crystal polymorphs (A and B). Nanoscale confinement at different radii can control for the form by selecting a pore radius where the desired form has a lower energy barrier.

Nanoscale confinement can also dictate crystal growth directions. For a pore with a very small radius but longer vertical direction, a nucleating crystal growing in a radial direction may fail to reach the critical size required for stable nucleation, while a nucleus growing vertically with the alignment of the pore has far more space to grow into a stable seed. The maximum diameter of a confined pore that will result in nuclei formation is:[1]

$$d_{max} = \frac{4(\gamma_{SL}-\gamma_{SC})}{\Delta G_{SL}} \qquad 2.31$$

This maximum diameter must be greater than 2x the critical radius (equation 2.12) for stable nucleation to occur.

Conclusions

Of the many factors (temperature, pressure, solute concentration, presence of co-solutes, etc) that influence crystal morphology and kinetics, the presence and properties of interfaces may be the most important. This is because solid surface and gaseous interfaces are near-impossible to avoid and because interfaces vastly alter crystallization during both nucleation and growth.[1,24] Surface morphology,[35,5] energy, chemistry,[16] and other properties can all influence crystal kinetics and structure.

Surface energy and texture are arguably the most important interactions for controlling crystallization at surfaces. However, there are other effects worth mentioning. One of these is

electrostatics. Ionic species are obviously charged in solution, and even macromolecules such as proteins typically carry some charge. Therefore, electrostatic interactions can be fundamental in attracting crystallizing units to one another.[24] Simulations of a moderately ionic protease indicate that long-range electrostatics interactions are essential for representation of crystal formation and structure, suggesting that electrostatics (both short and long range) are key in even for protein precipitation/crystallization.[38] Surfaces with an applied charged have been previously used to induce crystallization.[21,24,39] For example, one investigation used functionalized (silanized) mica and polystyrene with exposed ionizable groups as a nucleating surface for proteins, finding that these surfaces reduce the concentration necessary to form crystals.[21]

Combinations of morphological and chemical effects can be even more effective at controlling crystallization than either factor alone. Molecular dynamics simulations of crystallization under confinement and with varying surface-liquid interaction strengths found that crystallization under severe confinement has different mechanisms of formation than in the bulk.[40] In structureless surfaces, crystallization initiates at the surface. However, for amorphous surfaces, crystallization occurs in the bulk. Increasing liquid-surface interaction strength favors crystallization for structureless surfaces, but can suppress crystallization for amorphous surfaces.[40] Electrochemical conditions are also important for crystallization induced by nanoporous confinement.[37]

The number of ways in which a surface can control the growth kinetics and morphology of a crystal structure is enormous. Surfaces influence nucleation by serving either as sites for nucleation, or by providing a force to encourage alignment. Surfaces can also alter growth by introducing anisotropic forces that can result in different morphologies than those that are observed without surface effects. While certain surface properties, such as presence/size of pores or other nano/microstructures, lattice matching, and surface energy, and provide clues as to which crystal morphology may be preferred, it is near impossible to develop many solid conclusions to this problem.

2.3 Drop Evaporation and Deposition

The method used to crystallize a given compound will depend strongly on which chemistry is being crystallized and on the environmental conditions. For example, protein crystals are often grown via "salting out," in which the concentration of a precipitant salt is added to solution. This change in the solution composition alters the solubility of the protein and induces crystallization. Another common choice is temperature manipulation, where the temperature of the solution is lowered (or increased, for the rare cases in which solubility decreases with increased temperature) to decrease solubility and induce crystallization. While salt crystals can be crystallized via changes to temperature or solution composition, their generally high solubility makes some of these methods challenging. Salt crystallization by altered solubility is often kinetically-limited, meaning that even a supersaturated solution may fail to crystallize over timescales of days. In order for salt crystallization to occur quickly, solubilities often must be pushed far beyond supersaturation.

Evaporation-induced crystallization is a method that works particularly well for salts dissolved in an aqueous media. Loss of water due to evaporation concentrates the salt and pushes it past the solubility limit. The rate of evaporation can be very fast to induce very high supersaturation levels, or it can be slow enough that the crystal and dissolved ions remain in quasi-equilibrium. Evaporation can be controlled by changing either the temperature of the water or the vapor pressure of the surrounding gas. The evaporative flux is given by:

$$J_o = \frac{D(C_{LV} - C_\infty)}{\rho_L} \tag{2.32}$$

Where J_o is the evaporative flux in units of m^2/s, D is the diffusion of solvent vapor in air, C_{LV} is the saturation concentration of solvent vapor at the solution interface, and C_∞ is the equilibrium concentration of solvent vapor in the environment, and ρ_L is the density of the liquid solvent. In this equation, both the diffusion coefficient and concentrations of vapor are functions of temperature (and pressure). Thus, the diffusive flux tends to increase exponentially with increased temperature. The rate of volume loss is proportional to the evaporative flux, and the concentration of a solute in solution decreases proportionally:

$$C(t) = \frac{C_o V_o}{V(t)} \tag{2.33}$$

Where C_o is the initial concentration in solution prior to evaporation, and V_o is the initial volume. If we begin from a saturated solution ($C_o = C_{sat}$), then $C(t)/C_o = S$ (where S is the superstation ratio), then $S = V_o/V(t)$. Thus, supersaturation and crystallization tendency increase linearly with volume reductions.

Drop Evaporation

While evaporative crystallization is often performed in a bulk container (a beaker, for example), evaporative crystallization within a drop is a particularly interesting system for exploring crystal-substrate interactions. A drop left to evaporate on a substrate can evaporate in one of two modes: constant contact radius (sometimes called CCR), or constant contact angle (CCA). For the first mode, the contact line of the drop (i.e., the circumference of the drop, which is the line where the drop contacts both the surface and the air-water interface) remains pinned and does not move. Thus, the volumetric loss manifests as a decrease in the drop contact angle. In constant contact angle evaporation, the contact angle remains the same, and the drop "glides" over the substrate with a decreasing contact radius. The second type of evaporative mode is typically associated with hydrophobic surfaces, while the first commonly occurs for more hydrophilic surfaces.

When the system of interest is an evaporating drop, the volumetric rate of evaporation can be solved for by applying a spherical or semi-spherical geometry. This problem is non-trivial, and only approximate solutions can be found. However, it is still useful to derive drop geometry as a function of the evaporative flux. A mass balance for an evaporating drop can be formulated as:

$$\begin{aligned} \frac{dm}{dt} + \nabla * (mU) &= -2\pi R\rho J(r, R, t) \\ m &= \rho V_{drop} \\ \frac{dV}{dt} + \nabla * (VU) &= -2\pi R J(r, R, t) \end{aligned} \tag{2.34}$$

Where m is the mass of the drop, U is internal hydrodynamic flow velocity, R is the radius of the drop, and r is the radius as a coordinate. Assuming an approximately cylindrical shape, $V = \pi R^2 h$, and assuming that $dh/dt > dR/dt$ (which is valid in the case of a pinned contact line, rapid evaporation, and/or slow contact line motion), this equation becomes:

$$\pi R^2 \frac{dh}{dt} + \pi R^2 \nabla * (VU) = -2\pi R J(r, R, t) \tag{2.35}$$

So, the height averaged mass balance equation with a small slope is:

$$\frac{dh}{dt} + \nabla * (hU) = -\frac{J}{R}(r, R(t), t) \tag{2.36}$$

For a very thin drop, we can ignore hydrodynamic flow[41] to find:

$$\frac{dh}{dt} = \frac{J}{R}(r, R(t), t) \tag{2.37}$$

Where evaporative flux is now given as a function of time, radial position, and contact line location:

$$J(r, R, t) = Jo * f\,(r, R, t) \tag{2.38}$$

An approximate form of $J(r, R, t)$ was derived by Deegan by analogy of an electrostatic potential, where the drop is a conductor of fixed potential with a wedge shape.[42] By this analogy:

$$J(r) \propto (R - r)^{-\lambda} \qquad 2.39$$
$$\lambda = (\pi - 2\theta)/(2\pi - 2\theta)$$

For very low contact angles, $\lambda = 0.5$, and $\lambda = 2$ as the contact angle becomes very large. Finally, we can deduce a form of the evaporation rate evaporation from this electrostatic analogy as:

$$J(r, R, t) = \frac{-J_o}{\sqrt{1-\frac{r^2}{R^2}}} \qquad 2.40$$

The form of evaporative flux given by equation 2.40 can be substituted into equation 2.35 to create a differential equation describing rate of change for a drop that can be approximated as cylindrical. When a drop is also very thin or flat (due to either a hydrophilic substrate or to pinning of the contact line during evaporation, 2.40 can be substituted into equation 2.37 to describe the rate of change of the drop height with time. Different boundary conditions should be applied for each of these equations depending on whether drop evaporation proceeds in constant contact angle or constant contact radius evaporation.

Evaporative Deposition from Drops

In this thesis I extensively use evaporation of saline drops towards understanding crystal-substrate-solvent interactions. Evaporation causes concentration and precipitation of dissolved salts, forcing crystallization to occur at the solid interface on which a drop is deposited. Clearly, observing the process of crystallization at the substrate is useful for study of heterogeneous nucleation. However, the wetting and contact line behavior of a drop during evaporation is equally (or more) revealing, and evaporative deposition from drops is accordingly a well-studied phenomena.[43] This effect has traditionally been studied for applications in ink-jet printing, where condensed, uniform deposits of ink particles create a better resolution than dispersed deposits.

In evaporative deposition (also called evaporative self-assembly, or the "coffee-ring" effect), a drop of a colloidal suspension is placed on a substrate. As evaporation proceeds, radial flow delivers colloidal particles to the contact line. Particles become trapped here, and the resulting deposit is a ring marking the boundary of the original droplet. Since 1990 (when the first investigation of the effect was published), hundreds of authors have reported methods of disrupting the "coffee-ring" effect in order to encourage particle deposition at the center instead. One notable example demonstrated that altered particle shape can disrupt ring formation in favor of a condensed deposit (where particles assemble into a cluster with a radius smaller than the boundary of the initial drop).[44] Ellipsoidal particles are prone to uniform deposition, while spherical ones move to

the contact line. Interparticle capillary attraction between ellipsoidal particles is induced by interfacial deformation, and thus packed structures of particles can resist being deposited at the contact line. Other effects caused by particles include size,[45] density,[46,47] presence of surfactants,[48] and interactions with the substrate and/or other particles.[49]

Environmental parameters, such as substrate temperature, also play a large role in controlling deposit morphology. Increasing temperature increases the likelihood of a ring emerging, while lower temperatures increase the preference for uniform or bump-like deposits.[50] Effects of relative humidity,[51] substrate wettability,[52] heat capacities of the solute and substrate, etc., have also been explored.

The preference for an evaporating colloidal system to form a rings, uniform deposits, or bumps can be reduced to the three competing interactions of evaporative flow, attractive forces between the particles and substrate, and Marangoni recirculation.[47] Evaporative flow transports particles to the contact line, favoring ring-deposits, while Marangoni re-circulation has a tendency to deliver particles towards the center of an evaporating drop. DLVO forces between particles and substrate influence whether a particle delivered to the substrate will remain where it is, or will be swept away by flow. Thus, the influence of all previously mentioned parameters (particle size, shape, chemistry, temperature, etc.) can be reduced to their effects on these three interactions, so that a phase diagram for colloidal evaporative deposits can be formed. For aqueous solutions, the Marangoni flow tends to be weak.

Particles deposited at the contact line for ring-style deposits are often remarkably ordered due to the presence of capillary interactions. Particles deposited towards the droplet edge tend to exhibit long range order; while particles deposited closer to the center exhibit less order.[53] This is likely because disorder to order transitions are kinetically limited, and particles on the exterior of the ring have sufficient time for assembly, especially true when the hydrodynamic velocity is slow. A height averaged radial velocity for evaporative flow is:[54]

$$u(r,t) = \frac{2\sqrt{2}J_o}{\pi}\frac{1}{\theta(t)R\sqrt{1-r/R}} \qquad 2.41$$

Where $\theta(t)$ is the change in contact angle with time, and constant contact radius evaporation has been assumed. While evaporation in either CCA or CCR modes are most common for pure solvent, the presence of particles complicates contact line motion. The accumulation of particles at the contact line has a tendency to pin the drop, thus increasing the chances that evaporation will proceed in constant contact radius mode. In some cases, pinning is countered by surface tension forces of the substrate and drop, and a stick-slip regime emerges. In a stick-slip drop evaporation, the drop moves between the two modes so that the contact line periodically "sticks" at a new radius, evaporates until a critical low contact angle has been reached, and then slips to a new radial position and a higher contact angle. When particles are deposited during a stick-slip motion, concentric rings of particles emerge.

The evaporation behavior of a drop is strongly correlated to energy barriers at the drop contact line. The energies between the liquid and solvent, liquid and substrate, and liquid and air all contribute to an equilibrium contact angle (θ_E) known as young's angle, previously shown in equation 2.27. However, the equilibrium contact angle is not sufficient to predict how evaporative deposits will form. To describe whether a drop will pin, recede, or move in stick-slip motion, it is also important to understand the dynamic contact angles. The advancing angle (θ_A) of a substrate is the equilibrium angle a drop will take when it "advances." Advancement can occur via sliding down a slope or due to an increasing volume. Likewise, the receding angle (θ_R) is the angle a drop forms while it recedes. The pinning force of a drop to a substrate is a function of both of these dynamic contact angles:

$$F_P = \gamma(\cos\theta_R - \cos\theta_A) \qquad 2.42$$

Where γ is the surface tension (For water, γ=73 mN/m at 25°C). The energy barrier resisting contact line motion is:[55]

$$\Delta G = \gamma\pi R^2 \left(\frac{2}{1+\cos\theta} - \cos\theta_e\right) \qquad 2.43$$

Where R is the radius of the drop, θ_e is the equilibrium (Young) contact angle, and θ is the instantaneous contact angle (which varies between θ_e and θ_R for a pinned contact line). The excess free energy increases when the triple line is pinned as the deviation of the contact angle from the equilibrium angle increases. When the excess energy exceeds the potential energy barrier for depinning, the drop will recede.

Evaporative Crystallization from Drops

While there are many parallels between evaporation of saline drops and particle-laden drops, saline drops are somewhat more complicated. For example, concentration gradients are formed at the air/water interface as the volatile phase evaporates.[56] This heightened concentration combined with the predilection of crystals to form at interfaces results in crystal formation at the drop contact line.[57] Crystallization at the contact line will pin the drop and force a ring morphology even on surfaces that would normally form a clumped deposit for particle-laden systems.[16,58] The evolution of the crystals will alter drop pinning evaporation dynamics,[59] surface adhesion,[60] and the final form/size of the deposit. Therefore, eliminating coffee-rings for crystal deposits remains a challenge despite the many approaches for eliminating coffee-rings of colloidal deposits.

Previous investigations have demonstrated that the forces controlling deposit morphology for crystals are not the same forces which control colloidal deposits from evaporating drops.[18,61,62] Crystalline deposits will form rings even on superhydrophobic surfaces,[62] are independent of the

substrate thermal conductivity,[61] and demonstrate a large dependence on the properties of the emerging crystals.[18] These results indicate that Marangoni recirculation does not contribute to crystalline patterns, and that the pathway of crystallization is important for the morphology of the final deposit. Additional evidence suggests that the internal convection of evaporating drops of saline solutions containing a high concentration of very soluble salts (NaCl, $CaCl_2$, etc.) is fundamentally altered by the presence of these salts.[63,64]

References

1. Mullin, J. W. *Crystallization, 4th Edition*. (2001).
2. De Yoreo, J. J. & Vekilov, P. G. Principles of Crystal Nucleation and Growth. *Rev. Mineral. Geochemistry* **54**, 57–93 (2003).
3. Drever, J. I. *The Geochemistry of Natural Waters. Chapter 2: Chemical Background*. (Prentice Hall, 1988).
4. Drever, J. I. *The Geochemistry of Natural Waters. Chapter 7: Kinetics*. (Prentice Hall, 1988).
5. Erdemir, D., Lee, A. Y. & Myerson, A. S. Nucleation of Crystals from Solution: Classical and Two-Step Models. *Acc. Chem. Res.* **42**, 621–629 (2009).
6. Russell, K. C. Nucleation in solids: The induction and steady state effects. *Adv. Colloid Interface Sci.* **13**, 215–318 (1980).
7. Nancollas, G. H. Kinetics of crystal growth from solution. *J. Cryst. Growth* **3**–**4**, 335–339 (1968).
8. Deen, W. M. *Analysis of Transport Phenomena*. (Oxford University Press, 2012).
9. Tiller, W. A. *The Science of Crystallization: macroscopic phenomena and defect generation*. (1991).
10. Yoder, C. H. *Ionic Compounds: Applications of Chemistry to Mineralogy*. (2006).
11. Moore, J. W. *et al.* Solids, Liquids, and Solutions. in *ChemPRIME* (LibreTexts, 2019).
12. Tran, R. T., Naseri, E., Kolasnikov, A., Bai, X. & Yang, J. A new generation of sodium chloride porogen for tissue engineering. *Biotechnol. Appl. Biochem.* **58**, 335–44 (2011).
13. Wise, H. & Oudar, J. *Material Concepts in Surface Reactivity and Catalysis*. (1990).
14. Auzoux-Bordenave, S., Brahmi, C., Badou, A., de Rafélis, M. & Huchette, S. Shell growth, microstructure and composition over the development cycle of the European abalone Haliotis tuberculata. *Mar. Biol.* **162**, 687–697 (2015).
15. Müller-Steinhagen, H., Malayeri, M. R. & Watkinson, a. P. Fouling of Heat Exchangers-New Approaches to Solve an Old Problem. *Heat Transf. Eng.* **26**, 1–4 (2005).
16. Diao, Y., Myerson, A. S., Hatton, T. A. & Trout, B. L. Surface Design for Controlled Crystallization: The Role of Surface Chemistry and Nanoscale Pores in Heterogeneous Nucleation. *Langmuir* **27**, 5324–5334 (2011).
17. Ertl, G. *Reactions at Solid Surfaces*. (2009).
18. Shahidzadeh-Bonn, N., Rafai, S., Bonn, D. & Wegdam, G. Salt Crystallization during Evaporation: Impact of Interfacial Properties. *Langmuir* **24**, 8599–8605 (2008).
19. Hamilton, B. D., Weissbuch, I., Lahav, M., Hillmyer, M. A. & Ward, M. D. Manipulating crystal orientation in nanoscale cylindrical pores by stereochemical inhibition. *J. Am. Chem. Soc.* **131**, 2588–2596 (2009).
20. Diao, Y., Harada, T., Myerson, A. S., Alan Hatton, T. & Trout, B. L. The role of nanopore shape in surface-induced crystallization. *Nat. Mater.* **10**, 867–871 (2011).
21. Tosi, G., Fermani, S., Falini, G., Gavira Gallardo, J. A. & García Ruiz, J. M. Crystallization of proteins on functionalized surfaces. *Acta Crystallogr. D. Biol. Crystallogr.* **64**, 1054–61 (2008).
22. Scherer, G. W. Crystallization in pores. *Cem. Concr. Res.* **29**, 1347–1358 (1999).
23. Jiang, Q. & Ward, M. D. Crystallization under nanoscale confinement. *Chem. Soc. Rev.* **43**, 2066–79 (2014).
24. Saridakis, E. & Chayen, N. E. Towards a 'universal' nucleant for protein crystallization. *Trends Biotechnol.* **27**, 99–106 (2009).
25. Hamilton, B. D., Weissbuch, I., Lahav, M., Hillmyer, M. A. & Ward, M. D. Manipulating Crystal Orientation in Nanoscale Cylindrical Pores by Stereochemical Inhibition. *J. Am. Chem. Soc.* **131**,

2588–2596 (2009).
26. Chevalier, N. R. & Guenoun, P. Surface Tension Drives the Orientation of Crystals at the Air−Water Interface. *J. Phys. Chem. Lett.* **7**, 2809–2813 (2016).
27. Guan, X. *et al.* Morphology control and mechanisms of CaCO3 crystallization on gas-liquid interfaces of CO2/NH3 bubbles in aqueons-glycine solutions. *Russ. J. Phys. Chem. A* **89**, 1091–1095 (2015).
28. Carter, P. W. & Ward, M. D. Topographically directed nucleation of organic crystals on molecular single-crystal substrates. *J. Am. Chem. Soc.* **115**, 11521–11535 (1993).
29. D'Souza, S. M. *et al.* Directed nucleation of calcite at a crystal-imprinted polymer surface. *Nature* **398**, 312–316 (1999).
30. Allahyarov, E., Sandomirski, K., Egelhaaf, S. U. & Löwen, H. Crystallization seeds favour crystallization only during initial growth. *Nat. Commun.* **6**, 7110 (2015).
31. Enterkin, J. A., Poeppelmeier, K. R. & Marks, L. D. Oriented Catalytic Platinum Nanoparticles on High Surface Area Strontium Titanate Nanocuboids. *Nano Lett.* **11**, 993–997 (2011).
32. Azimi, G., Cui, Y., Sabanska, A. & Varanasi, K. K. Scale-resistant surfaces: Fundamental studies of the effect of surface energy on reducing scale formation. *Appl. Surf. Sci.* **313**, 591–599 (2014).
33. Tomson, M., Kan, A., Fu, G. & Al-Thubaiti, M. A molecular theory of mineral scale inhibition. in *Corrosion* (2004).
34. Hamilton, B. D., Ha, J.-M., Hillmyer, M. A. & Ward, M. D. Manipulating Crystal Growth and Polymorphism by Confinement in Nanoscale Crystallization Chambers. *Acc. Chem. Res.* **414**, 414–423 (2012).
35. Wang, Y. W., Christenson, H. K. & Meldrum, F. C. Confinement leads to control over calcium sulfate polymorph. *Adv. Funct. Mater.* **23**, 5615–5623 (2013).
36. Ha, J.-M., Hamilton, B. D., Hillmyer, M. A. & Ward, M. D. Alignment of Organic Crystals under Nanoscale Confinement. *Cryst. Growth Des.* **12**, 4494–4504 (2012).
37. Huber, P. Soft matter in hard confinement: phase transition thermodynamics, structure, texture, diffusion and flow in nanoporous media. *J. Phys. Condens. Matter* **27**, 103102 (2015).
38. York, D. M., Darden, T. A. & Pedersen, L. G. The effect of long-range electrostatic interactions in simulations of macromolecular crystals: A comparison of the Ewald and truncated list methods. *J. Chem. Phys.* **99**, 8345 (1993).
39. Sanjoh, A., Tsukihara, T. & Gorti, S. Surface-potential controlled Si-microarray devices for heterogeneous protein crystallization screening. *J. Cryst. Growth* **232**, 618–628 (2001).
40. Sun, G., Giovambattista, N., Wang, E. & Xu, L. Effects of surface structure and solvophilicity on the crystallization of confined liquids. *Soft Matter* **9**, 11374 (2013).
41. Poulard, C., Bénichou, O. & Cazabat, A. M. Freely Receding Evaporating Droplets. *Langmuir* **19**, 8828–8824 (2003).
42. Deegan, R. D. *et al.* Capillary flow as the cause of ring stains from dried liquid drops. *Nature* **389**, 827–829 (1997).
43. Deegan, R. D. *et al.* Contact line deposits in an evaporating drop. *Phys. Rev. E* **62**, 756–765 (2000).
44. Yunker, P. J., Still, T., Lohr, M. A. & Yodh, A. G. Suppression of the coffee-ring effect by shape-dependent capillary interactions. *Nature* **476**, 308–11 (2011).
45. Wong, T.-S., Chen, T.-H., Shen, X. & Ho, C.-M. Nanochromatography Driven by the Coffee Ring Effect. *Anal. Chem.* **83**, 1871–1873 (2011).
46. Deegan, R. D. Pattern formation in drying drops. *Phys. Rev. E* **61**, 475–485 (2000).
47. Bhardwaj, R., Fang, X., Somasundaran, P. & Attinger, D. Self-Assembly of Colloidal Particles from Evaporating Droplets: Role of DLVO Interactions and Proposition of a Phase Diagram. *Langmuir* **26**, 7833–7842 (2010).
48. Anyfantakis, M., Geng, Z., Morel, M., Rudiuk, S. & Baigl, D. Modulation of the Coffee-Ring Effect in Particle/Surfactant Mixtures: the Importance of Particle–Interface Interactions. *Langmuir* **31**, 4113–4120 (2015).
49. Crivoi, A. & Duan, F. Elimination of the Coffee-Ring Effect by Promoting Particle Adsorption and

Long-Range Interaction. *Langmuir* **29**, 12067–12074 (2013).
50. Soltman, D. & Subramanian, V. Inkjet-Printed Line Morphologies and Temperature Control of the Coffee Ring Effect. *Langmuir* **24**, 2224–2231 (2008).
51. Zeid, W. B. & Brutin, D. Influence of relative humidity on spreading, pattern formation and adhesion of a drying drop of whole blood. *Colloids Surfaces A Physicochem. Eng. Asp.* **430**, 1–7 (2013).
52. Patil, N. D., Bange, P. G., Bhardwaj, R. & Sharma, A. Effects of Substrate Heating and Wettability on Evaporation Dynamics and Deposition Patterns for a Sessile Water Droplet Containing Colloidal Particles. *Langmuir* **32**, 11958–11972 (2016).
53. Malfatti, L. *et al.* Coffee stain-driven self-assembly of mesoporous rings. *Microporous Mesoporous Mater.* **163**, 356–362 (2012).
54. Popov, Y. O. Evaporative deposition patterns: Spatial dimensions of the deposit. *Phys. Rev. E* **71**, 036313 (2005).
55. Shanahan, M. E. R. & Sefiane, K. Kinetics of Triple Line Motion during Evaporation. in *Contact Angle, Wettability, and Adhesion. Vol. 6* (ed. Mittal, K. L.) 19–31 (CRC Press, 2009).
56. Li, F.-I., Thaler, S. M., Leo, P. H. & Barnard, J. a. Periodic Pattern Formation in Evaporating Drops. *J. Phys. Chem. B* **110**, 25838–25843 (2006).
57. Accardo, A. *et al.* Calcium Carbonate Mineralization: X-ray Microdiffraction Probing of the Interface of an Evaporating Drop on a Superhydrophobic Surface. *Langmuir* **27**, 8216–8222 (2011).
58. Kaya, D., Belyi, V. A. & Muthukumar, M. Pattern formation in drying droplets of polyelectrolyte and salt. *J. Chem. Phys.* **133**, 1–10 (2010).
59. Soulié, V. *et al.* The evaporation behavior of sessile droplets from aqueous saline solutions. *Phys. Chem. Chem. Phys.* **17**, 22296–22303 (2015).
60. Accardo, A. *et al.* Fast, active droplet interaction: coalescence and reactive mixing controlled by electrowetting on a superhydrophobic surface. *Lab Chip* **13**, 332–335 (2013).
61. Shahidzadeh, N., Schut, M. F. L., Desarnaud, J., Prat, M. & Bonn, D. Salt stains from evaporating droplets. *Sci. Rep.* **5**, 10335 (2015).
62. Mcbride, S. A., Dash, S. & Varanasi, K. K. Influence of superhydrophobic and lubricant impregnated surfaces on evaporative crystallization in saline drops. *Langmuir* **Submitted**, (2018).
63. Misyura, S. Y. Evaporation of a sessile water drop and a drop of aqueous salt solution. *Sci. Rep.* **7**, 14759 (2017).
64. Kang, K. H., Lim, H. C., Lee, H. W. & Lee, S. J. Evaporation-induced saline Rayleigh convection inside a colloidal droplet. *Phys. Fluids* **25**, 042001 (2013).

Chapter 3.

Surface Engineering for Scale Reduction in Desalination

Combating deterioration of pipes, reactors, and other equipment in desalination processes can significantly reduce associated costs for maintenance and replacement. Modification of water chemistry and/or addition of anti-foulants can be expensive and introduce new problems to the systems. Passive control via engineered surfaces is one way to avoid fouling without introducing additional chemistry to a water source. It is desirable to engineer scale-resistant surfaces that are are able to prevent the formation of crystalline buildup and mitigate its impact on the surface and the equipment. Such scale-resistant surfaces have a wide range of industry applications, from desalination to heat transfer and energy generation.[1,2]

In this chapter, crystallization of single salts, binary salts, and complex salt mixtures is explored on a catalogue of engineered surfaces to determine how interfacial engineering can best be applied for reducing salt-fouling (also called scale formation or mineral-fouling). While most investigations exploring scale formation look at a single, representative salt at time, multiple salts will be present in any real environmental water sample. The primary component of ocean water is sodium chloride, which is present at 32 g/L (around 10% of its saturation level). However, the ocean also contains large quantities of potassium, calcium, magnesium, sulfate, and carbonate. These ions combine to form different minerals, which will precipitate in order of least to most soluble.[3] In this chapter, I use a salt mixture of these salts to model ocean water.

Scale formation for binary salt mixtures is altered by the common-ion effect, in which salts that share an ion (for example, calcium sulfate and calcium carbonate) reduce the solubility level of the other. There is also a discrete ion effect (also termed the uncommon ion effect), in which salts without shared ions can enhance the solubility of the other (calcium sulfate and sodium chloride). A final confounding factor in multiple-salt precipitation is the chemical divide, which describes the difference in cation/anion ratios between the dissolved species and the solid form of a given salt.[4] In the experiments described here, I explore both single-salt and multiple-salt solutions to determine the effects that this confounding variables have on scale formation.

3.1 Experimental Approach

While there are multiple methods to induce crystallization in an experimental set-up, evaporation is a particularly well-suited technique for crystallization of salt minerals. Evaporation is an important process in the environmental hydrological cycle,[4] and it is straightforward to determine increases in salt concentration within a solution based on the volumetric reduction of the liquid due to evaporation. Minerals which form via evaporation of environmental waters are also called evaporites.

It is possible to calculate the progression of mineral precipitation from a water starting with the initial composition via solubility rules.[4] Calcite (calcium carbonate) will be the first to precipitate for nearly all water samples, followed closely by magnesium carbonate. This is because both calcium and carbonate ions are common in the environment, and the two ions are present in many samples at or near the calcite's saturation concentration. Magnesium is commonly found in environmental waters; though it is less common than calcium. Thus, calcite scaling is of significant concern for water treatment and transportation.[5,6]

Silicates are also a common component of mineral scale, but the relatively low saturation concentration of silicate under ambient conditions (atmospheric pressure, room temperature) mean that silicates do not tend to form significant amounts of scale in the built environment. Gypsum, the dihydrate of calcium sulfate, is typically next in the precipitation sequence, and is particularly problematic across water treatment industries (see Table 3.1).[5,7,8] This is because gypsum is common in environmental waters, soluble enough that a large amount of scale can form from a given volume of water, but insoluble enough that it precipitates readily in response to evaporation.

Other salts of interest for desalination include magnesium hydroxide (but only under high temperature and/or high pH conditions),[9] and sodium/potash salts. The last two will only form under extremely concentrated conditions. One such condition is in Zero-Liquid-Discharge (ZLD) desalination systems, in which a desalination plant seeks to extract 100% of the water contained within a sample of ocean water in order to avoid the difficulties associated with brine storage/disposal.

TABLE 3.1. Salts of interest for scaling in desalination.

Salt	Rationale	Problematic in
$CaSO_4$	Strong contributor to scaling, usual model salt for fouling	RO, distillation, membrane distillation
$CaCO_3$	Near saturation limit in ocean, usually the first precipitant to form	Water transport, desalination
$MgCO_3$	Less likely to form since $CaCO_3$ is less soluble, but can form if $CO_3^{2-} > Ca^{2+}$	Water transport, desalination
$Mg(OH)_2$	Scales in high temperature or high pH applications	Distillation
NaCl & KCl	Unlikely to form scale except in extremely concentrated brines	Zero-Liquid Discharge systems

Table 3.1 gives an overview of the primary salts of interest for desalination. These same salts are used throughout the present experiments. I begin by exploring crystallization of single salts before looking at binary mixtures. Substrate-crystal interactions were explored using evaporation induced crystallization within a bulk system, as shown in Figure 3.1. Solutions of saline water were prepared starting with deionized water and mixing the desired concentration of salts. For saturated solutions, salts were added to the DI water in a concentration that is higher than the saturation concentration. The solutions were mixed for a period of least 24 hours to ensure that solid salts had sufficient time to reach equilibrium with dissolved ions. Following equilibration, excess solid was filtered from the solution to leave a sample saturated with respect to a given ion.

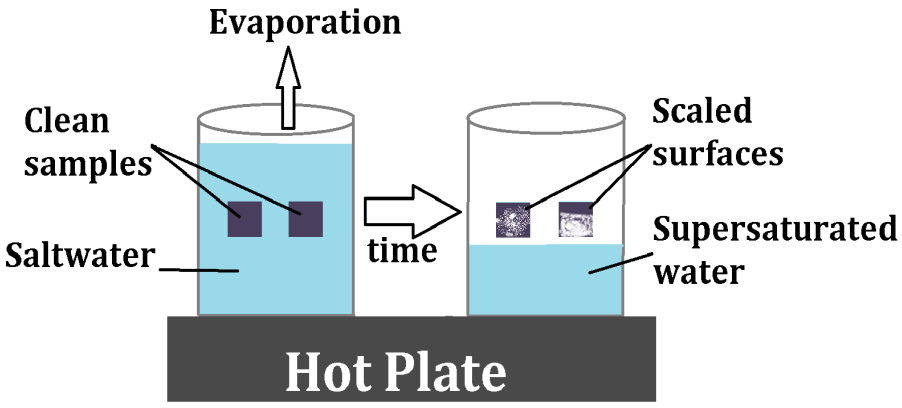

FIGURE 3.1. Bulk crystallization experiments using evaporation.

The experimental set-up shown in Figure 3.1 has been previously described in prior works.[10] First, beakers were prepared in which different surface samples were adhered to the beaker side wall. The weight and the dimensions of these samples were measured prior to adding them to the beakers. By attaching samples to the side wall of the beaker, it is possible to eliminate effects due to settling of salt crystals formed in the bulk; and instead control for salt crystals formed on the sample. After this, the solution of salt water was added to the beaker and placed on a hot plate set to 40°C. This relatively low temperature allowed for a slow evaporation of the water (~3-4 days for a 500 mL sample). As the water evaporates, salt becomes concentrated and crystallizes on the substrates.

Once crystallization was complete, samples were collected from the beaker and weighed. The original mass of the substrate was subtracted to obtain the mass of crystals formed on the sample. Optical microscope and scanning electron microscope images of the crystals formed were also collected to further characterize results. Experimental results were compared across the catalogue of salts (shown in Table 3.1) and salt mixtures for a variety of different substrates.

3.2 Influence of Surface Energy

It is well-known that surface energy of a given interface can have a large effect on the crystallization at that interface.[11–13] Thus, experiments were performed to identify the influence of changing surface energy; i.e. surface wettability, on smooth untextured substrates. This systematic investigation includes a focus on the influence of various components of surface energy, including the long-range Lifshitz-van der Waals component (γ^{LW}) and the short-range acid (γ^{+})—base (γ^{-}) electron-exchange components, on crystallization. The interfacial energy γ_{sc} between the surface and crystalline phase can be derived in terms of these components by equation 3.1.

$$\gamma_{sc} = [(\gamma_s^{LW})^{0.5} - (\gamma_c^{LW})^{0.5}]^2 + 2[(\gamma_s^{+})^{0.5} - (\gamma_c^{+})^{0.5}][(\gamma_s^{-})^{0.5} - (\gamma_c^{-})^{0.5}]. \quad 3.1$$

These components can be used to characterize surface interactions that lead to scaling. Following Good's approach, the work of adhesion between two phases A and B can be written in terms of their respective Lifshitz-van der Waals and acid-base components (equation 3.2):

$$W_{AB} = 2\left(\sqrt{\gamma_A^{LW}\gamma_B^{LW}} + \sqrt{\gamma_A^{+}\gamma_B^{-}} + \sqrt{\gamma_A^{-}\gamma_B^{+}}\right) \quad 3.2$$

Thus, surface chemistry has a profound influence on surface energy, and therefore scaling. Altering these parameters allows us to develop a catalogue of different surfaces. The test substrates given in Table 3.2 give a wide range of surface chemistries and energies. Table 3.2 shows the different chemical functionalization's applied to smooth silica substrates used in these experiments, along with the different component of surface energy.

TABLE 3.2. Surface energetic components for different chemical functionalization's of silica

Substrate	Abbreviation	γ_{LW} (mJ/m^2)	γ_{AB} (mJ/m^2)	γ_{total} (mJ/m^2)
Uncoated silicon wafer	Si	37.02	9.63	46.65
triethoxyphenylsilane	Si + TOPS	35.67	8.99	44.66
(3-aminopropyl) trimethyoxysilane	Si+ AOPS	34.29	2.82	37.11
1,2-Dichlorotetramethylsilane	Si+DTS	26.01	4.69	30.70
Octyltrichlorosilane	Si+OTS	22.89	0.04	22.93
Trichloro (1H,1H,2H,2H-perfluorooctyl) silane	Si+FS	8.69	0.03	8.72

The preparation and characterization of these functionalization's has been described previously.[11] In brief, the oxysilanes (triethoxyphenylsilane; TOPS, and (3-aminopropyl) trimethyoxysilane; AOPS) were prepared via a liquid-phase deposition. Silica samples were plasma-cleaned and then added to a mixture of 0.075% hydrochloric acid in ethanol. Silane was added and left to react for 24 hours.

Two of the other substrates (1,2-Dichlorotetramethylsilane; DTS, Octyltrichlorosilane; OTS) were prepared using a different liquid deposition method, in which plasma-cleaned substrates were added to a reaction beaker with 30 mL of toluene and 75 µL of silane. In a separate beaker, an emulsion of 20 mL toluene and 100 µL of DI water was prepared. This emulsion was poured into the reaction beaker, and substrates were sonicated for 4 minutes to facilitate the reaction. Substrates were then rinsed with acetone and isopropyl alcohol to remove excess silane. Flourosilane substrates (Trichloro (1H,1H,2H,2H-perfluorooctyl) silane; FS) were prepared via vapor deposition. Plasma-cleaned substrates were placed in a desiccator alongside a small drop of silane solution. The chamber was vacuumed, and left for a period of at least 8 hours for complete reaction.

Functionalized substrates were added to the reaction vessels shown in Figure 3.1, which were then filled with water solutions containing a single salt. The salts tested in these investigations include NaCl, KCl, and $CaSO_4$. Substrates with crystallized mass were dried with a gentle stream of air in order to remove water and any crystals that were not strongly adhered prior to measurements.

Results

The first notable result from these tests was the discovery that altered surface energies has an influence on the morphology of gypsum crystals, as shown in Figure 3.2. Samples in this figure are organized from the most hydrophilic (highest total surface energy) on the left (Si) to the most hydrophobic on the right (FS). The top panel shows a view of the entire 10 x 10 cm substrate, while the bottom shows a magnified view of the crystal morphologies.

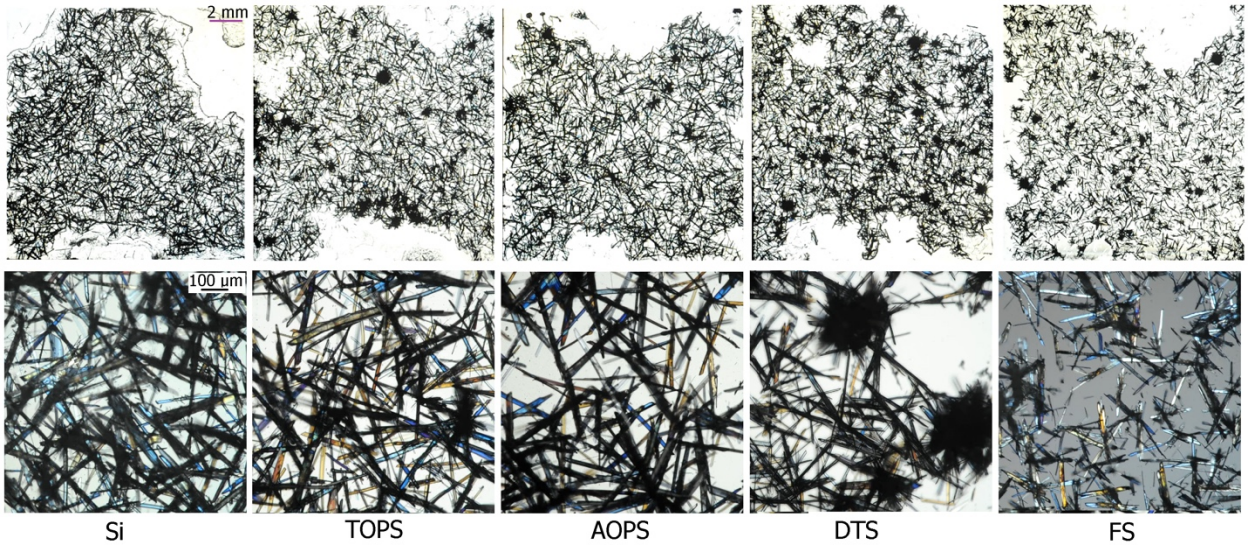

FIGURE 3.2. Different morphologies of gypsum crystals formed across substrates functionalized with polymers of differing surface energy.

Visual inspection of Figure 3.2 reveals two effects on gypsum crystal morphology induced by altered surface energies. First, the crystalline needles generally decrease in size as the substrate becomes more hydrophobic, with the smallest needles forming on the lowest surface energy substrate (FS). In contrast, the largest needles are observed on the highest surface energy substrate, unaltered silica. In general, the size of a crystal is highly dependent on the relative rates of nucleation and growth. Smaller crystals form under conditions that promote nucleation, while larger ones form when less nucleation occurs and more time is allowed for crystal growth.[14]

The second observation is the prevalence of crystal clusters across the different surfaces. These clusters appear as black circular regions in the first panel of Figure 3.2. Clusters do not appear on the silica surface. On the TOPS, AOPS, and DTS surfaces, there are a good number of larger clusters. Finally, on the hydrophobic FS surface, smaller clusters appear. The observation of crystal clusters further supports the theory that nucleation was enhanced on more hydrophobic surfaces.

Sodium chloride and potassium chloride crystals did not exhibit significant changes in morphology across different surface energies. This may be due to the different wetting properties of these species, which are significantly different from the interfacial energy of calcium sulfate.[15]

The average mass of scale formed on each substrate was normalized to the surface area of those substrates and plotted against the total surface energy, as shown in Figure 3.3. Calcium sulfate seems to have a non-linear relationship between scale formation and surface energy, which sodium chloride and potassium chloride seem to exhibit less of a relationship between fouling propensity and substrate surface energy.

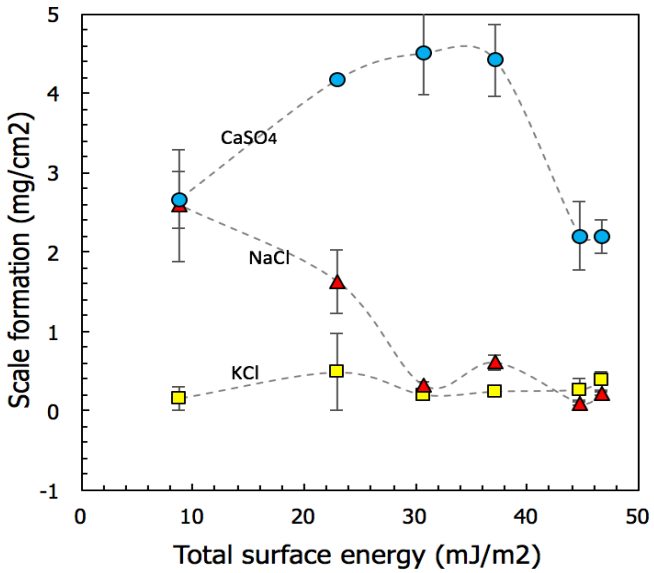

FIGURE 3.3 Mass of scale formation normalized to substrate surface area as a function of total substrate surface energy for the three salts tested.

The observations of Figure 3.3 are in line with previous results suggesting that sodium chloride has less of a propensity to form on interfaces compared to calcium sulfate.[15] Counter-intuitively, the two surfaces with the highest surface energy (i.e., the most hydrophilic ones) have the lowest mass of scale formation. This runs contrary to conventional wisdom in the field suggesting that hydrophobic surfaces are best for resisting scale formation. However, it is also observed that the most hydrophobic surface (FS) had a similarly low levels of scale accumulation.

By comparing the results of Figure 3.3 to those in Figure 3.2, it is possible to hypothesize that the mass of the scale is a function of the crystal morphology. The substrates of intermediate surface energies had the greatest amount of crystal mass formed on them, and also were most likely to form crystal clusters. Their greater crystal mass may be due, in part, to a greater density of such crystal clusters when compared to individual gypsum needles. Likewise, the crystals on the FS substrate are significantly smaller than those formed on other substrates, which likely explains the lower mass measured on the FS substrates reported in figure 3.3.

The results of Figure 3.3, while interesting, should be taken with a grain of salt. The experiments presented here were repeated in triplicate, while experimentation involving crystallizing solutions should be repeated a minimum of six times due to the inherent stochasticity involved with crystallization. In addition, the non-monotonic relationship between calcium sulfate and substrate surface energy reported by measurements of the sample weight are not visually consistent with Figure 3.2, which shows that all surfaces are fouled with gypsum scale. Thus, none of the surfaces were truly “anti-fouling” under these experimental conditions, and the results of Figure 3.3 likely have little bearing on anti-fouling performance under actual conditions.

3.3 Combined Effects of Texture and Wettability

In the previous section, substrates of different surface energies were tested to determine relationships between scale formation and substrate wettability. Now, I apply interfacial engineering to create surfaces which have both texture and wettability. The surfaces tested are (1) regular, non-functionalized silica, (2) silica functionalized with a hydrophobic polymer (OTS), (3) Nanograss, which is a nanotextured silica, (4) nanograss functionalized with OTS, and (5) Liquid impregnated surfaces.

Liguid impregnated surfaces are hard/soft composite materials in which an oil layer is impregnated within a hard texture.[16] The oil layer is held stable through capillary interactions, which are controlled by the physical size of the features of the solid material and by the surface energy. Small features (<0.1 mm) are required, and the oil layer becomes more stable with smaller length scales. Likewise, the oil layer will be more stable when oil-surface interactions are stronger. Liquid Impregnated Surfaces (LIS) have been previously shown to be effective for anti-scaling for the case of gypsum.[10]

Scale formation

Figure 3.4 shows scale formation across the different substrates. Rather than reporting total mass normalized per surface area, this figure reports the mass accumulated as a percentage of the total mass within the solution (i.e., normalized to the solubility concentration). This normalization allows for a better comparison of the anti-fouling performance across salts of vastly different solubilities.

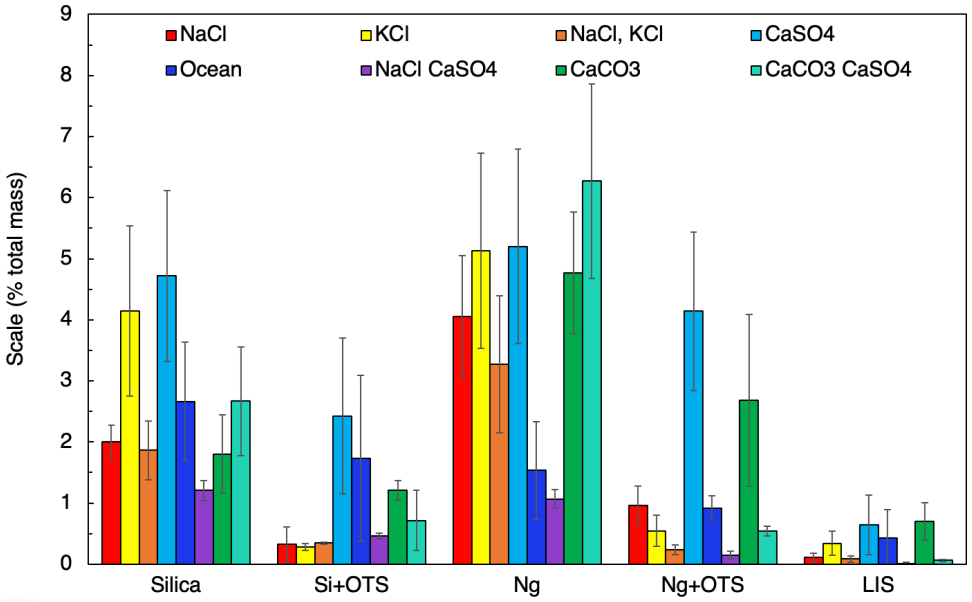

FIGURE 3.4. Scale as a percent of the total mass of salt across silica, hydrophobic silica, nanotextured silica, superhydrophobic nanotextured silica, and liquid impregnated surfaces for different salts.

Overall, the nanotextured substrate (Ng) performed worst across different salt compositions. This is in line with the known propensity for minerals to form on surfaces with defects and pores.[17] The liquid impregnated surfaces performed the best, exhibiting very little mass accumulation. Adding the hydrophobic polymer generally resulted in a decreased amount of scale formation.

The results were replotted as the scale mass normalized against scale formed on the silica substrate and separated into different categories for clarity of comparison in Figure 3.5. In the first plot, a salt composition reflecting ocean water is compared against the NaCl/KCl and NaCl/$CaSO_4$ mixtures. The relative amounts of scale found in the ocean water is similar to that of the NaCl/$CaSO_4$ scaling.

In the second plot, the mass of scale for NaCl, $CaSO_4$, and the NaCl/$CaSO_4$ are plotted. The combination of sodium chloride and calcium sulfate exhibit less scale formation across surfaces. The two salts have an uncommon ion effect, in which the presence of one decreases the solubility of the other. The solubility of calcium sulfate can be increased up to five times by the addition of sodium chloride.[18]

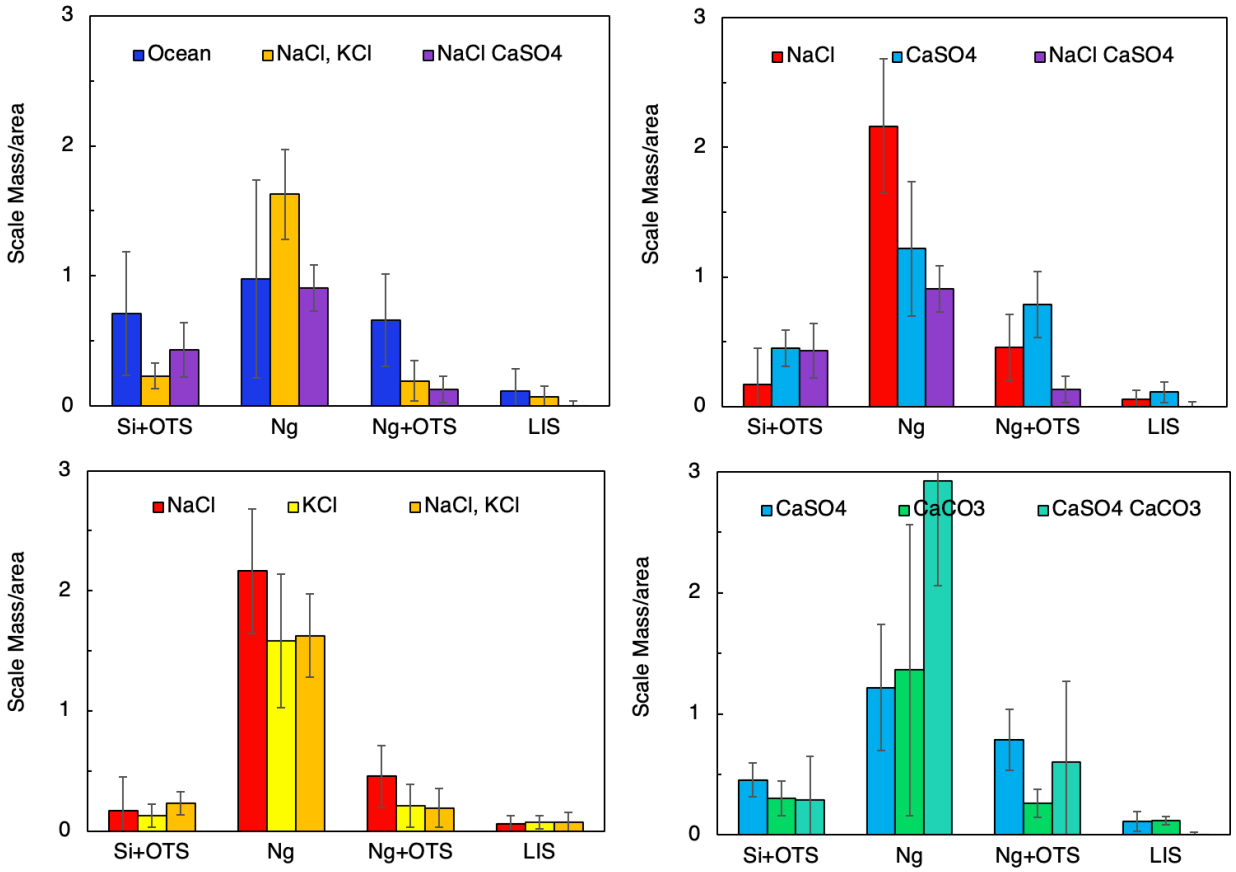

FIGURE 3.5. Scale as a percent of the total mass of salt across silica, hydrophobic silica, nanotextured silica, superhydrophobic nanotextured silica, and liquid impregnated surfaces for different salts and salt combinations.

Predictably, sodium chloride and potassium chloride exhibit similar scale formation across different substrates, as shown in the third plot of Figure 3.5. Likewise, the mixture of the two exhibits the same trend. For both of these salts, nanotexture significantly increases the scale formation, with the hydrophobic Nanograss exhibiting the greatest amount of scale formation (~1.5x the smooth control). In contrast, both hydrophobic surfaces have relatively small amounts of scale formation for all of the chloride salts and mixtures. The superhydrophobic nanograss+OTS surface still performs better than smooth, hydrophilic silica; but somewhat worse than the smooth hydrophobic silica. This is likely due to the effect of nanotexture, which promotes crystallization. Thus, even though the contact angle of this superhydrophobic substrate is far greater than that of the hydrophobic silica, the hydrophobic surface is better able to resist scale.

In the final plot of Figure 3.5, calcium sulfate, calcium carbonate, and the mixture of the two are compared. Here we see the influence of the common ion effect, in which the combined salt actually forms more scale across most of the surfaces. Error bars for both calcium carbonate and the mixture of calcium sulfate and calcium carbonate are very large due to the small solubility concentration of calcium carbonate. Because of this, it is difficult to draw conclusions from this plot.

Crystal Morphologies

Figure 3.6 shows optical images of crystallization on the different substrates for pure salts. This reveals the differences between morphology of crystals formed across the different substrates. Sodium chloride crystal morphology does not change, but we see the significant amount of mass adhered to the Nanograss surface.

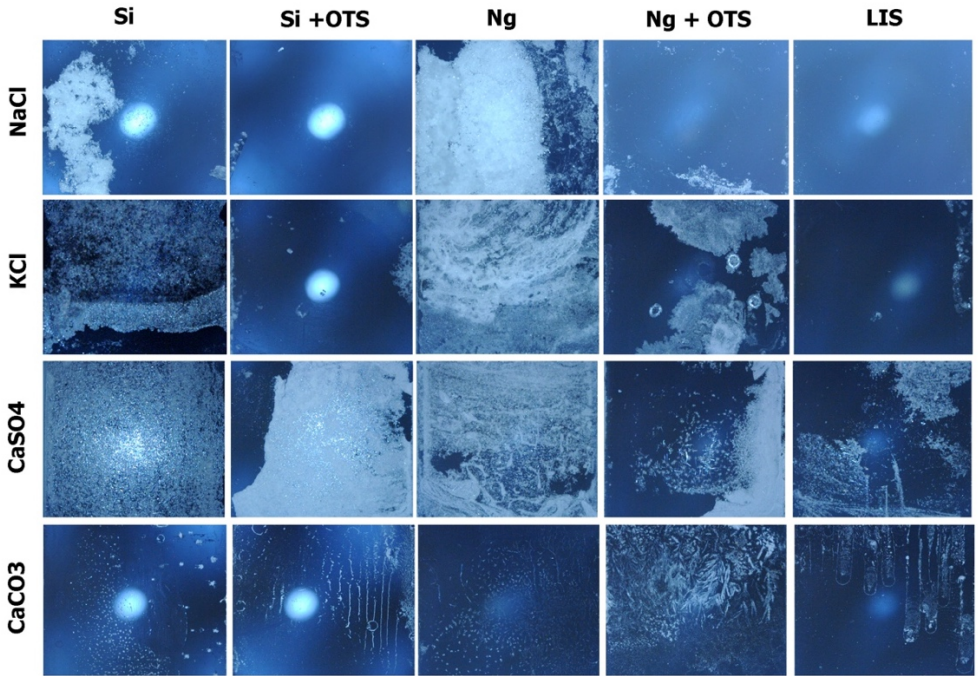

FIGURE 3.6. Scale formed for each salt across the different substrates

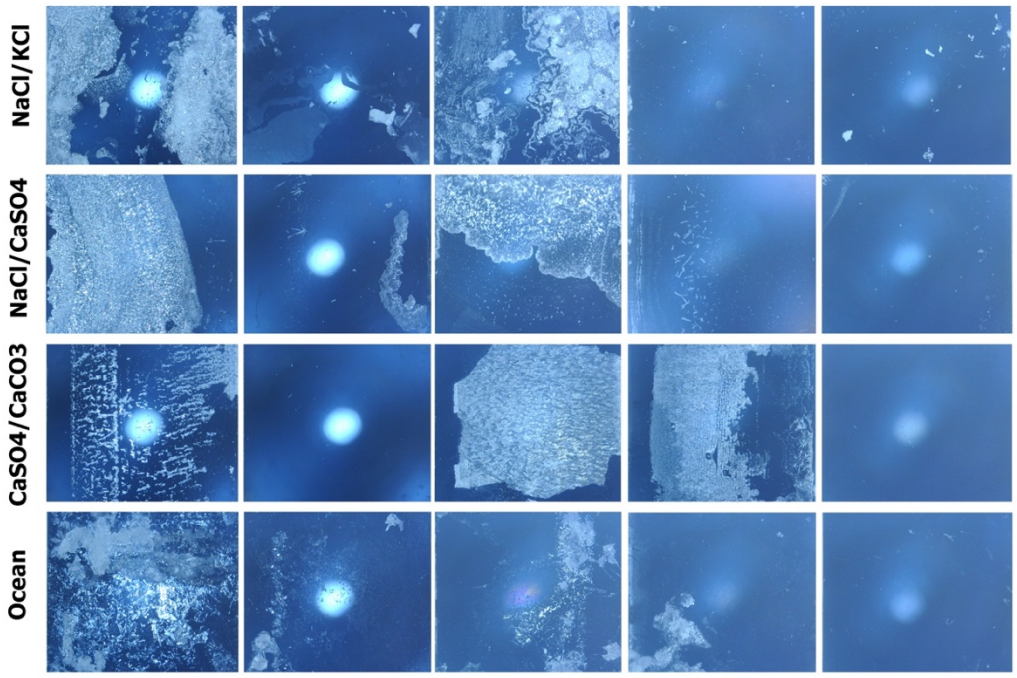

FIGURE 3.7. Scale formed for each combination of salts across the different substrates

The patterns of scale accumulation change across each surface for KCl, $CaSO_4$, and $CaCO_3$. For example, calcium sulfate crystals form a thin, even layer on the silica surfaceand thicker, non-uniform layers on the hydrophobic silica and hydrophilic nanograss. The superhydrophobic Nanograss surface exhibits a thick deposit but only on one half of the substrate. Crystal patterns also vary widely for the calcite fouling, exhibiting dot-like features on both hydrophilic surfaces and line-like features on the three hydrophobic surfaces. Figure 3.7 shows fouling across the substrates for the four salt mixtures investigated.

In addition to altering overall scale morphology, there are also differences to the microscale crystalline morphologies induced by the presence of the surfaces. Figure 3.8 shows SEM images of different potassium chloride crystals are compared across the different surfaces, showing that the morphology of the deposited crystals deviates strongly across surfaces. In the first panel, a large, three-dimensional cubic crystal has formed on hydrophilic nanograss. The ceria surface shown in the second panel is an intrinsically hydrophobic rare earth oxide ceramic material. The potassium chloride ion formed here is flat and rectangular. Close analysis of this image shows a possible dislocation site at the bottom right of the rectangular crystal. The liquid impregnated surface, which has been previously shown to reduce the number of nucleation sites available for crystallization,[10] and which also has a low surface energy, has “stop-sign” shaped crystals. These crystals may have formed in the bulk, and not at the surface.

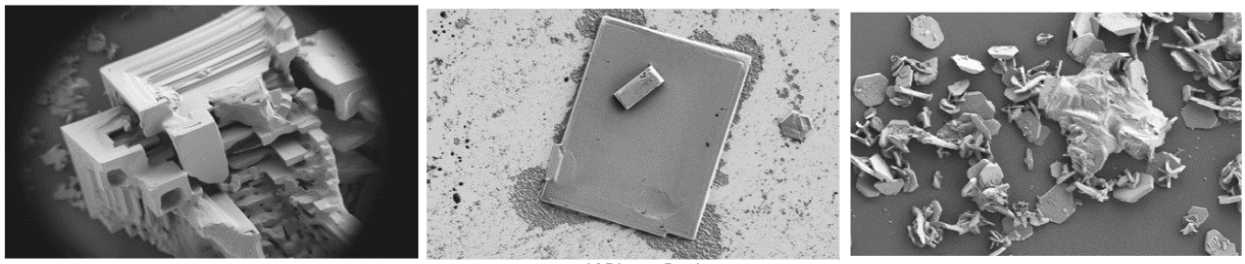

FIGURE 3.8. SEM images of potassium chloride crystals all formed in the same solution at the same concentration, but on substrates with different surface energies, textures, and chemistries.

It is tempting to say that the influence of different surfaces on crystallization is due purely to differences in substrate texture and surfaces. However, Figure 3.9 shows two morphologies of potassium chloride crystals formed on the same surface. The crystal morphology looks similar within the immediate regions of these two images; but very different across the two regions. Unless we say that these crystals are somehow inducing crystals of the same shape, we must conclude that there is some reason related to thermodynamic stability that influences why the crystals take the shape that they do. Theoretically, the salt concentration should have been constant at saturation throughout the experiment, as salt precipitates continuously while evaporation removes water, but it's possible that this system was not in equilibrium for the entire time. Understanding why certain morphologies dominate over others is important for ant-fouling applications, as the crystals in the first panel will be clearly more difficult to remove from a surface than the spherical crystals formed in the second panel.

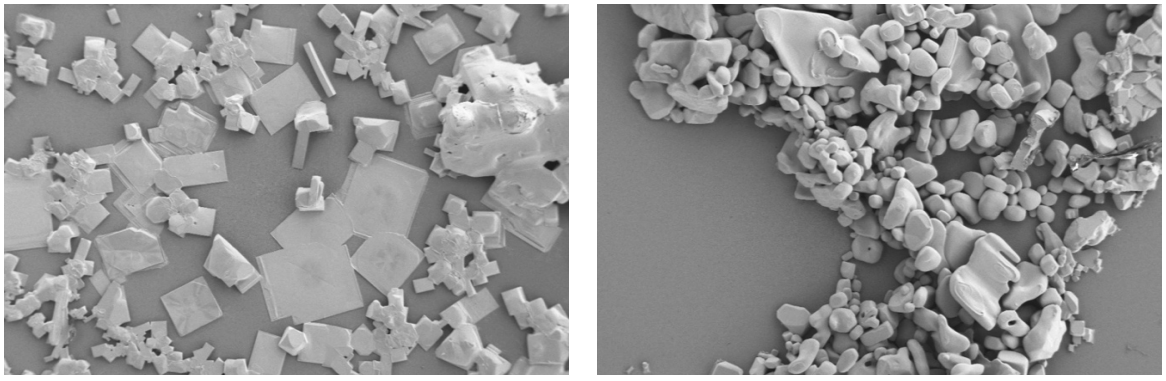

FIGURE 3.9. KCl crystals formed on the hydrophilic nanograss but on different areas.

Conclusions

The observation that calcium sulfate morphology is altered across substrates of various surface energies is in line with previous investigations, as is the observation that sodium chloride and potassium chloride did not exhibit energy-dependent morphologies. The non-monotonic relationship of calcium sulfate mass accumulation with surface energy can be explained by the differing morphologies of crystals across these surfaces.

Liquid impregnated surfaces were effective at preventing scale formation across a variety of salts and salt combinations. This result is expected, as the lubricant layer effectively prevents contact between the crystals and the underlying substrate, thereby preventing crystal adhesion and growth. Likewise, addition of the hydrophobic chemistry (OTS) generally decreases scaling across all solutions, and nanotexture increases scaling. These results are known and expected. What is more interesting is the behavior of salts in response to the superhydrophobic surface which combines nanotexture with the hydrophobic chemistry. While such surfaces are generally reported to be anti-fouling, the superhydrophobic surface actually performs worse than the smooth, hydrophobic surface for most salt solutions.

Comparing scale formation across sodium chloride, calcium sulfate, and the mixture of the two has revealed that the uncommon ion effect plays a role in fouling across all substrates. I also find that the mixture of the two is the best analogue for actual ocean water compositions. This is likely because calcium sulfate is the most problematic scale component in ocean water (where calcite will precipitate first, but in small amounts), and sodium chloride is the primary contributor to the overall salt composition.

If I were to repeat these experiments, I would begin with controls testing both the kinetics of crystallization and the mass accumulated for each salt without the presence of an engineered surface. Salt combinations (particularly NaCl and $CaSO_4$, which is an important model for simulating fouling from ocean water) would also be controlled for to determine how the mixture of the two impedes crystallization. All experiments would be replicated ten times, and the experimental system would be adjusted to prevent the air/water interface from moving past the samples during evaporation. Experimental timescales would also be extended from 3-5 days to 3 weeks to provide time for scaling to proceed in a manner that better reflects real conditions.

References

1. Awad, M. M. Fouling of heat transfer surfaces. in *Heat transfer-theoretical analysis, experimental investigations and industrial systems* (IntechOpen, 2011).
2. Pan, S.-Y., Snyder, S. W., Packman, A. I., Lin, Y. J. & Chiang, P.-C. Cooling water use in thermoelectric power generation and its associated challenges for addressing water-energy nexus. *Water-Energy Nexus* **1**, 26–41 (2018).
3. Drever, J. I. *The Geochemistry of Natural Waters. Chapter 2: Chemical Background*. (Prentice Hall, 1988).
4. Drever, J. I. Chapter 11: Evaporation and Saline Waters. in *The Geochemistry of Natural Waters* 233–260 (1988).
5. Macadam, J. & Jarvis, P. Chapter 1 - Water-Formed Scales and Deposits: Types, Characteristics, and Relevant Industries. *Miner. Scales Depos.* 3–23 (2015).
6. Wang, H., Alfredsson, V., Tropsch, J., Ettl, R. & Nylander, T. Formation of $CaCO_3$ Deposits on Hard Surfaces. Effect of Bulk Solution Conditions and Surface Properties. *ACS Appl. Mater. Interfaces* **5**, 4035–4045 (2013).
7. Ahmi, F. & Gadri, A. Kinetics and morphology of formed gypsum. *Desalination* **166**, 427–434 (2004).
8. McCool, B. C., Rahardianto, A., Faria, J. I. & Cohen, Y. Evaluation of chemically-enhanced seeded precipitation of RO concentrate for high recovery desalting of high salinity brackish water. *Desalination* **317**, 116-126 (2013).
9. Khayet, M. & Matsuura, T. Application of surface modifying macromolecules for the preparation of membranes for membrane distillation. *Desalination* **158**, 51–56 (2003).
10. Subramanyam, S. B., Azimi, G. & Varanasi, K. K. Designing Lubricant-Impregnated Textured Surfaces to Resist Scale Formation. *Adv. Mater. Interfaces* **1**, 1300068 (2014).
11. Azimi, G., Cui, Y., Sabanska, A. & Varanasi, K. K. Scale-resistant surfaces: Fundamental studies of the effect of surface energy on reducing scale formation. *Appl. Surf. Sci.* **313**, 591–599 (2014).
12. Sengupta Ghatak, A. & Ghatak, A. Precipitantless Crystallization of Protein Molecules Induced by High Surface Potential. *Cryst. Growth Des.* **16**, 5323–5329 (2016).
13. Diao, Y., Myerson, A. S., Hatton, T. A. & Trout, B. L. Surface Design for Controlled Crystallization: The Role of Surface Chemistry and Nanoscale Pores in Heterogeneous Nucleation. *Langmuir* **27**, 5324–5334 (2011).
14. De Yoreo, J. J. & Vekilov, P. G. Principles of Crystal Nucleation and Growth. *Rev. Mineral. Geochemistry* **54**, 57–93 (2003).
15. Shahidzadeh, N., Schut, M. F. L., Desarnaud, J., Prat, M. & Bonn, D. Salt stains from evaporating droplets. *Sci. Rep.* **5**, 10335 (2015).
16. Smith, J. D. *et al.* Droplet mobility on lubricant-impregnated surfaces. *Soft Matter* **9**, 1772–1780 (2013).
17. Jiang, Q. & Ward, M. D. Crystallization under nanoscale confinement. *Chem. Soc. Rev.* **43**, 2066–79 (2014).
18. Cameron, F. K. Solubility of Gypsum in Aqueous Solutions by Sodium Chloride. *J. Phys. Chem.* **5**, 556–576 (1901).

Chapter 4.

Surface Engineering for Nutrient Recovery

In the previous chapter I explore how surface engineering including substrate texture, wettability, and soft/hard composite surfaces can be applied towards preventing crystallization and fouling in water treatment and desalination. Now I seek to apply these lessons towards promoting crystallization for waste water treatment. Specifically, the goal is to enable crystallization of a nutrient crystal called struvite using interfacial engineering. Struvite naturally grows in wastewater treatment plants and is often considered a foulant. However, the mineral contains both nitrogen and phosphorous and can therefore be used as an effective fertilizer, providing economic advantage in its recovery.

Struvite precipitation from wastewater can simultaneously reduce phosphate pollution of receiving waters, create a sustainable fertilizer, and reduce corrosion of wastewater facilities. Current struvite recovery technologies have demonstrated success in achieving these goals; however, the process is energy intensive due to the air stripping required for chemical conditioning to maximize crystallization kinetics. This project seeks to develop technology that can reduce energy consumption in these reactors by nucleating struvite at sub-optimal chemical conditions on engineered seed particles. Based on the demonstrated importance of surfaces in crystallization, I explore how different surface properties including porosity influence struvite nucleation, and introduce one possible particle design that can help increase struvite recovery under non-ideal conditions.

4.1 Experiments & Controls

Objectives

The overarching goal of this work is the enhanced recovery of struvite crystals from wastewater. Struvite is an orthorhombic mineral composed of magnesium, ammonium, and phosphate ($MgNH_4PO_4 \cdot 6H_2O$) which forms according to:

$$Mg^{2+} + NH_4^+ + H_nPO_4^{3-n} + 6\ H_2O \rightarrow MgNH_4PO_4 \cdot 6H_2O + nH^+ \qquad 4.1$$

Existing struvite recovery technologies have successfully demonstrated the ability to (1) eliminate chemical costs of anti-foulants, (2) reduce phosphate concentrations in plant effluents, (3) produce struvite crystals of sufficient quality for use as fertilizer, and (4) recover between 75-92% of the remaining phosphorous following aeration. However, these technologies are still limited by the power consumption required for air stripping to modulate crystallizer pH levels. One life-cycle analysis concluded that the environmental benefits to be achieved by struvite recovery were largely offset by the additional power consumption required.[1] Sub-optimal pH, chemistry, and/or other environmental factors can all be limiting factors in struvite crystallization kinetics, necessitating the strict modulation of these parameters in struvite reactors.

Here, I use interfacial engineering techniques to vastly improve upon struvite precipitation kinetics, recovery ratios, and system resilience to chemical/environmental factors by incorporating seed particles designed with surface engineering and nanotechnology. The objective of this project was to design and test the functionality of struvite-nucleating particles that could be used to enhance the resilience of current struvite-precipitation technologies to sub-optimal chemical conditions. By doing so, struvite reactors could realize large energy and cost savings by reducing the need for chemical conditioning. These particles could be easily incorporated into existing struvite recovery reactors, as a majority of these technologies separate the ripened struvite crystals from immature ones via gravitational settling. The seed particles could then be recycled to enable sustainable recovery of struvite.

Crystallizing minerals will preferentially nucleate heterogeneously at solid interfaces, as opposed to homogeneously in bulk solution. This contributes to the troublesome tendency of scale to form on pipe and reactor interiors; however, it also presents a potential strategy for controlling crystallization and increasing resilience to chemical conditions. Surfaces and their properties (energy, morphology, chemistry, etc.) have been well-established to exert considerable influence on both precipitation kinetics and on the morphology of crystals,[2–4] allowing for the possibility of designing substrates that control precipitation and vastly outperform kinetics of homogeneous nucleation.

Controls

Prior to experimentation with engineered surfaces, it was important to determine the expected nucleation induction time for a given set of properties. The desired timescale for these experiments was short enough (less than a few hours) to enable multiple experiments; but long enough that alterations to kinetics could be measured when comparing control experiments against those containing engineered interfaces. The time required for crystallization can be modulated by changing (1) the concentration of solution by pre-concentrating, (2) temperature, (3) pH, (4) mixing rate. The kinetics of struvite formation and growth were measured using the solution pH, and the nucleation induction time was measured as the time at which pH begins to drop (see equation 4.1). Following complete precipitation, the morphology of the resulting crystals are recorded using microscopy.

Kinetics were extracted from time series data using the two-parameter Finke-Watzky crystallization model that was originally derived to describe transition-metal nanocluster formation.[5] Since then, the model has proved valuable for accurately describing other forms of kinetic data.[6] The model describes sigmoidal kinetics for the case in which nucleation and growth occur simultaneously from a supersaturated solution and where surface growth is not diffusion limited. The model is:

$$\frac{F(t)-F_o}{F_F-F_o} = \frac{k_1+k_2C_o}{k_2C_o+k_1e^{(k_1+k_2C_o)t}} \qquad 4.2$$

Where F is the signal (here, the signal is the pH level), F_F is the final strength of the signal and F_o is the initial signal. C_o is the initial concentration of soluble struvite and t is the time. In this model k_1 is the rate constant for nucleation (which is related to the nucleation induction time) and k_2 is the rate constant for growth (related to the slope of the kinetic plot). The separation of nucleation and growth into two separate parameters make this model a useful tool for determining which process is most altered by a given variable (the presence of the engineered surface/particle).

Control experiments were conducted at room temperature with a solution that is optimized for struvite precipitation. Ideal conditions for struvite precipitation are a 1:1:1 molar ratio of magnesium, ammonia, and phosphate; with a basic pH near 8.5.[7] The solubility concentration of struvite at room temperature is about 0.25 g/L (1mM). Stock solutions of 100 mM NH_4Cl, $MgCL_2$, $KHPO_4$ were prepared at a pH of 8.5.

Different molarities of struvite were prepared by first adding water (pH 8.5) to a small vial, then adding the appropriate amount of stock salt solutions. The different molarities tested are shown in Table 4.1. Table 4.1 includes data on the nucleation induction time (t_n), the total time required for growth (t_g), and the two kinetic rates (k_1 and k_2) from equation 4.2. Experiments began with 10 mM, which had an induction time of ~2 minutes. We then used 5 mM, which had an induction time ~6 minutes with a slower growth rate as compared to the 10 mM case. The solution with a

concentration of 1 mM (i.e., where the supersaturation of struvite ~1) took several hours to nucleate and had an exceptionally slow growth rate. Based on these experiments, we decided to use a concentration of 3.5 mM, which has an induction time of ~10 minutes and takes no more than an hour to reach full growth.

TABLE 4.1. Influence of concentration and supersaturation on nucleation and growth kinetics for struvite mixed at 600 RPM at room temperature.

Concentration	Supersaturation	t_n (min)	t_g (min)	k_1 (mM/ min)	k_2 (1/min)
10 mM	10	2	7.5	0.68	0.048
5 mM	5	5	20	0.16	0.045
3.5 mM	3.5	9.5	40	0.028	0.042
3.0 mM	3	18	60	0.013	0.029
1 mM	1	350	1160	0.00088	0.0036

Next, I tested the sensitivity of struvite nucleation to changes in the initial pH of the solution. Struvite nucleation increases with increased pH, which is one of the reasons why it will nucleate within aeration basins in wastewater treatment facilities. The results from this test are shown in Figure 4.1 for struvite at an initial concentration of 3.5 mM. At an initial pH of 8, the nucleation induction time is about 20 minutes, which is approximately 2x the induction time for pH 8.5 (t_n ~8 to 10 min).

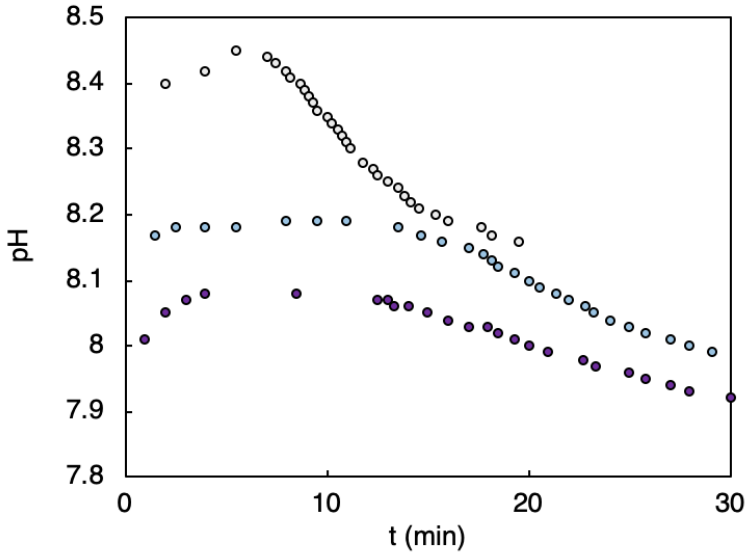

FIGURE 4.1. Influence of initial pH on kinetics.

Struvite growth is a diffusion limited process,[8] and therefore mixing has a significant influence on growth kinetics.[7] Thus, experiments were conducted under both quiescent and flowing conditions to gauge how important mixing is on the kinetics; as shown in Figure 4.2. Because the model presented in equation 4.2 requires non-diffusion limited growth, it will only be valid for mixed conditions.

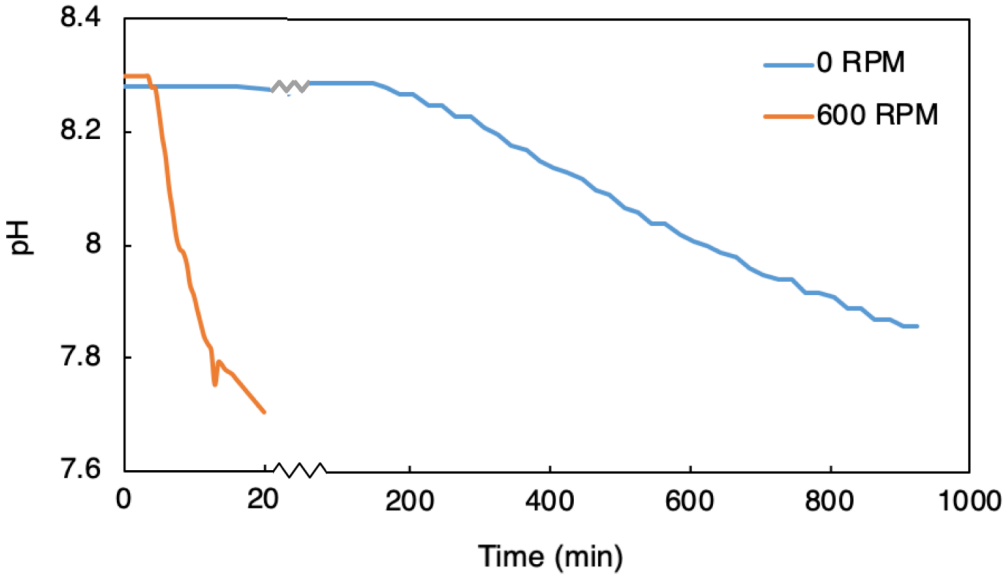

FIGURE 4.2. Mixed vs. unmixed struvite crystallization kinetics at 5 mM.

The kinetics of struvite growth with and without mixing are shown in Figure 4.2 for a 5 mM solution. Under mixed conditions, crystals nucleate after about 4 minutes, and growth levels off after 20 minutes. In contrast, the quiescent 5 mM system took 165 minutes (~3 hours) for nucleation and around 1000 minutes for the growth curve to begin leveling off.

4.2 Confinement

Porosity and confinement both contribute to enhanced nucleation kinetics because pores are able to stabilize a crystal phase and prevent dissolution in moderately saturated conditions. True confinement effects occur on the length scale of the critical radius of nucleation, while pores of larger sizes enhance crystallization by providing surface area and edges for nucleation.[9] In the first set of experiments, shown in Figure 4.3, struvite was crystallized in the presence of nanoporous zeolite particles. The nucleation induction time for the control solution was ~15-18 minutes and decreased to ~10-12 minutes in the presence of particles as shown in Figure 4.3a.

Quiescent experiments were also conducted in the absence and presence of nanoporous zeolite, shown in Figure 4.3 b and c respectively. With particles, the nucleation induction time was about 16 hours, and the solution had completely crystallized after 48. For the control case with no particles present, no crystals were observed after 4 days, and small nucleates were only observed on 5th day. This suggests that particles are more effective at enhancing nucleation rates under quiescent conditions (~5x increase in nucleation induction time, as compared to ~1.5x increase under 600 RPM mixed conditions).

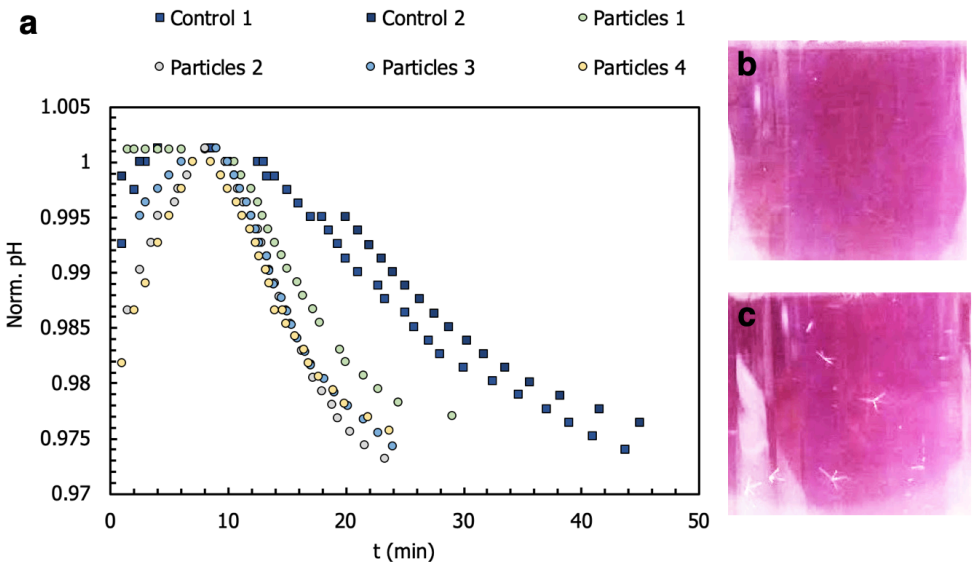

FIGURE 4.3. (a) Kinetics of crystallization for a 3.5 mM solution mixed at 600 RPM with and without particles. (b) quiescent 3.5 mM solution without particles after 48 hours, (c) quiescent 3.5 mM solution with particles.

To further explore the effect of pore size on struvite crystallization, crystals were grown in the presence of Anodisc isopore membranes of pore sizes 0.02 and 0.1 μm at a concentration of 3.0 mM, 600 RPM, and an initial pH of 8.0. The results from this experiment are shown in Figure 4.4, which confirms that the smallest pore size (0.02 μm) achieved the fastest kinetics with a nucleation induction time of 18 minutes, compared to 28 minutes for the 0.1 μm membrane and 34 minutes for the control solution containing no membrane. This change in kinetics is reflected by an increase in the nucleation constant k_1 from equation 4.2 as the pore size is decreased (see Table 4.2). The presence of the porous membrane materials also has affected the rate of crystal growth (k_2), though there is little observed effect between the two different pore sizes.

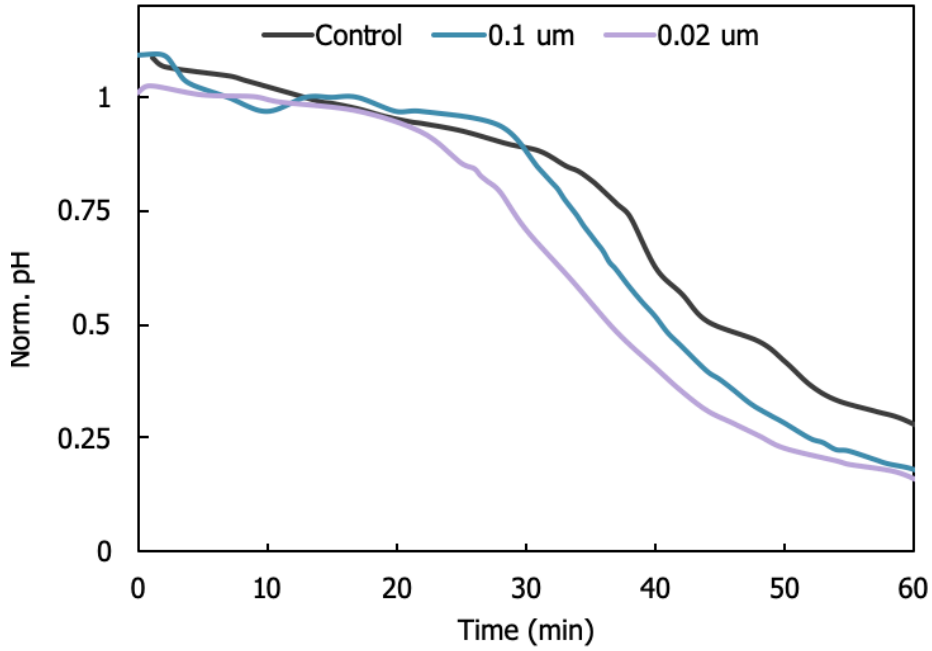

FIGURE 4.4. Struvite kinetics for different pore sizes.

TABLE 4.2. Influence of pore size on nucleation and growth kinetics for struvite mixed at 600 RPM at room temperature.

Pore size	t_n (min)	k_1 (mM/ min)	k_2 (1/min)
Control	34	0.015	0.065
0.1 μm	28	0.0165	0.08
0.02 μm	18	0.018	0.07

Although Figure 4.4 and Table 4.2 demonstrate that there is some effect of the nano/micro-scale porosity on the crystal growth process, these results are not as dramatic as the changes in kinetics induced by the zeolite particles. The zeolite particles' porosity is on the length scale of 1 nm or less and have a greater influence on nucleation kinetics than the membrane materials.

4.3 Engineered Particles

Next, I explore the possibility of translating the results found in the first set of experiments to create multiscale particles with ideal properties for precipitating struvite. The previous set of experiments found that nanoscale porosity of zeolite particles can greatly enhance the precipitation rate for struvite. The goal of this work is to enable collection of struvite from wastewater treatment facilities using nano-engineered particles. For collection and removal of particles, the ideal length scale ranges from microns to millimeters to prevent entrainment of particles by the fluid flow. The zeolite particles used in the previous section have this required multi-scale structure.

In addition to simply increasing the kinetics of struvite formation, this project also seeks to improve nucleation and growth under un-favorable conditions. While crystallization will not occur under under-saturated conditions, it may be possible to decrease the solubility of struvite in the local area surround the particles by the slow release of sodium hydroxide to increase the pH of the vicinity near the particle. These particles can be designed by employing strategies used in drug delivery for targeted, slow dissolution. Here I use alginate hydrogels as a model system for slow diffusion.

Porous zeolite microparticles can be "impregnated" in one half with a hydrogel, as shown in Figure 4.5. This hydrogel does not encompass the entire particle, as some solid/porous parts should remain in contact with the liquid in order to provide a surface for crystals to nucleate on. The hydrogel is swollen with a strongly basic solution so that sodium hydroxide will begin diffusing out of the hydrogel into solution and increase the pH when moved into a water source. Struvite crystals should then nucleate on the porous side of the particle due to the local increase in pH, as shown in Figure 4.5. The fabrication strategy for creating these particles is shown in Figure 4.6.

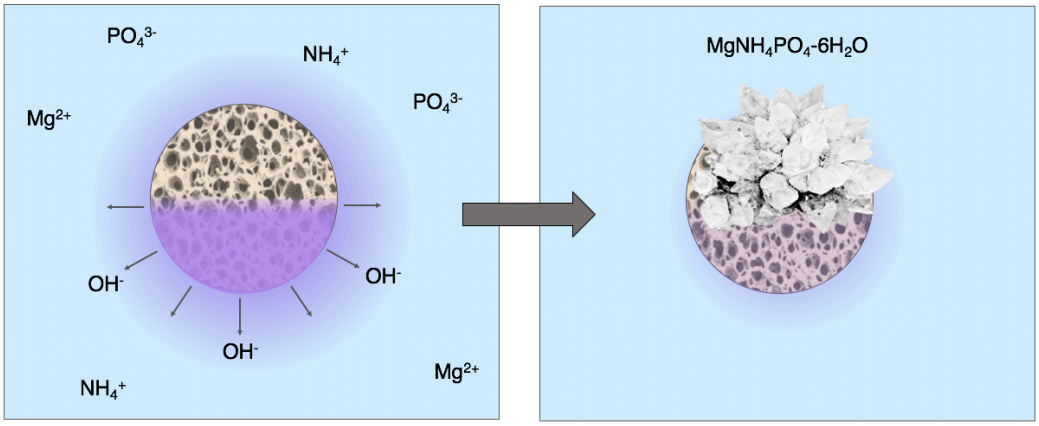

FIGURE 4.5. Mechanism of action for local solubility altering particles.

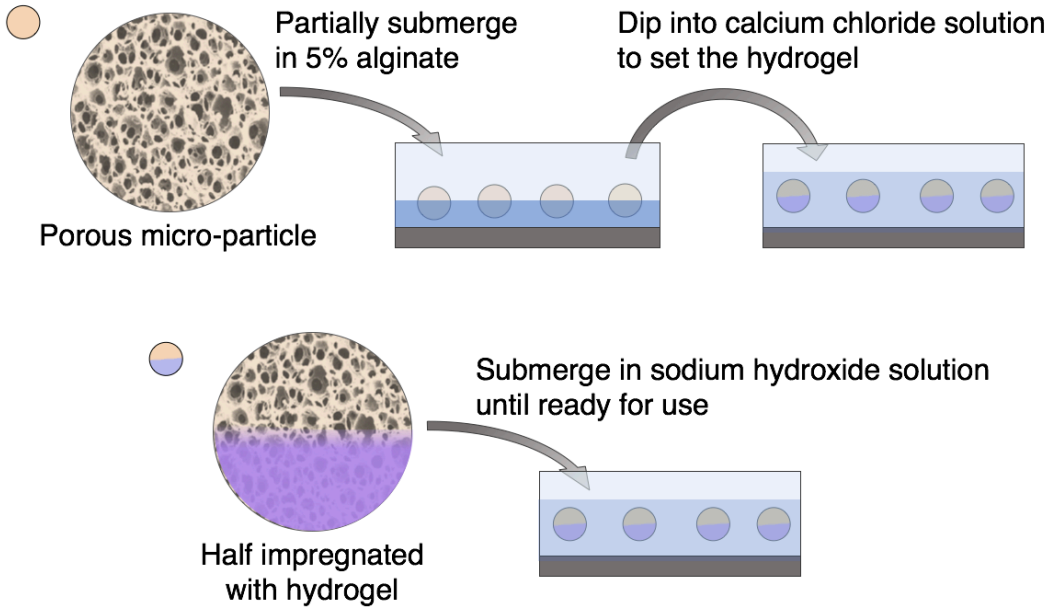

FIGURE 4.6.(a) Fabrication of solubility-altering Janus particles. (b) Microscope image of resulting particles

A proof-of-concept experiment tested whether the Janus particles described in Figures 4.5 and 4.6 could further improve the performance of the zeolite particles for nucleation and growth of struvite from solution. The results of this experiment are shown in Figure 4.7. As shown previously in Figure 4.3, the zeolite particles decrease the nucleation induction time and increase the growth rate as compared to a control solution with no additional particles added. Next, zeolite particles were imbued with a hydrogel on one part of the face and left to soak in sodium hydroxide to form the Janus particles. Interestingly, the sodium hydroxide imbued particle exhibited the same nucleation induction time (approximately 10 minutes) as the native zeolite particles but enabled a faster growth rate of the struvite. This faster rate of growth is reflected by the steeper drop in pH levels shown in Figure 4.7.

Altering the local pH surrounding the Janus particles should influence both the rate of growth and the nucleation rate; however, the preliminary results of Figure 4.7 only show a change to the growth rate. This is in contrast with the results presented in Figure 4.1, where slight increases to the solution pH drastically change both the nucleation induction time and the rate of growth. The counter-intuitive results of Figure 4.7 might be explained by a slow rate of diffusion of the sodium hydroxide solution out of the hydrogel and into the bulk solution. In the case of a slow diffusion rate, the pH of the local area surrounding the particle would change slowly enough that there is little effect on nucleation. However, there is a clear effect on the growth rate, suggesting that the change in pH has been significant enough following nucleation to alter growth. It is likely that the diffusion rate of the material can be tuned to optimize the kinetics.

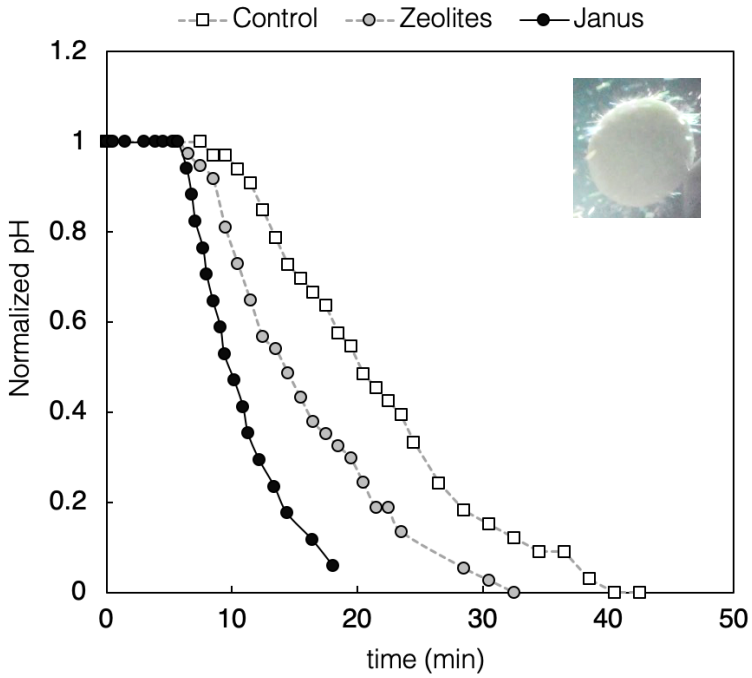

FIGURE 4.7. Kinetics of growth for control without particles, zeolite particles, and Janus hydrogel particles swollen with sodium hydroxide.

Conclusions

The results presented in this chapter demonstrate that interfacial engineering can be a powerful tool for enhanced recovery of struvite from waste water. This result is not surprising, as interfacial engineering has been previously applied towards enhancing crystallization of proteins,[10] controlling the polymorph of inorganic crystals,[2] and generally controlling crystal nucleation.[11] Despite the importance of interfacial processes in crystallization, this work has been the first to explore struvite crystallization on engineered materials. As expected, exposure of a struvite solution to porous materials increased both the nucleation and growth rates of struvite crystallization. This effect was most significant for the material with the smallest pore size, which was the zeolite particles. In addition, a proof-of-concept experiment demonstrated that Janus particles composed of a zeolite texture imbued with a hydrogel for slow-release of sodium hydroxide can enhance struvite growth kinetics.

A quite a bit of work remains to be done in this area. First, there are a huge number of parameters contributing to the nucleation and growth of struvite crystals. Some of these properties pertain to the solution (pH, chemical composition, concentration, mixing rate, temperature, etc.), and some pertain to the engineered material (length scale of micro/nano features, shape of features, length scale of overall particle, surface energy, surface chemistry, etc.). A more systematic investigation of how the different combinations of all of these properties would be highly informative for design

of materials that could function across real-world conditions encountered in wastewater treatment facilities. Computational studies could supplement experiments in order to reduce the parameter space and down-select which properties of engineered seeds would enable the best performance under the largest range of conditions.

One parameter of particular importance is the combined effects of engineered particles and of mixing. The preliminary results described in Figure 4.3b and in the accompanying text suggest that the presence of zeolite particles had an even more dramatic effect on struvite crystallization kinetics in the absence of flow than they did under mixed conditions. This introduces the possibility of using surface engineering for mineral recovery outside of a traditional well-mixed crystallization reactor. For example, particles could be directly added to existing operations in wastewater treatment facilities (the aeration basin, in particular) and recovered during a subsequent filtration step. Such an operation could eliminate the requirement for retrofitting from existing wastewater treatment facilities. Other possibilities include adding engineered baffle surfaces in agricultural run-off channels to promote nucleation and growth of struvite on the materials.

Further work could also be done in the area of designing Janus particles with slow-release chemistries for alteration of local solubility for enhanced precipitation. The key to the success of such a technology is a balance between the diffusion rate of the active chemistry and the reaction rate of precipitation. If the active solubility-altering chemistry diffuses too quickly, the chemistry will become diluted by the bulk phase and no changes in solubility will occur. The diffusion rate can be tuned by adapting strategies developed for the field of drug-delivery,[12,13] where diffusion rates must be precisely controlled for therapeutic effects. One such strategy is the use of gels with precise electrostatic, chemical, and physical properties to control the rate of release of the active chemistry. The length scale of the pores can also be tuned for ideal diffusion rates of the active chemistry while also maximizing the nucleation rate of the porous face.

Additional work in the area of applying interfacial engineering towards mineral recovery from waste should also explore the potential cost and energy savings to be gained from the implementation of such a technology. Part of this practical analysis would include comparing the performance of engineered seed particles to homogeneous struvite seeds; which are currently the industry standard for seeding struvite crystallizers. It is therefore important to determine whether nano-engineered materials can actually out-perform seed crystals, and whether or not the benefits gained would outweigh the costs of manufacturing.

References

1. Nemethy, A. Analyzing the process of struvite recovery with life cycle assessment: a case study. (Swedish University of Agricultural Sciences, 2016).
2. Page, A. J. & Sear, R. P. Crystallization Controlled by the Geometry of a Surface. *J. Am. Chem. Soc.* **131**, 17550–17551 (2009).
3. Diao, Y., Myerson, A. S., Hatton, T. A. & Trout, B. L. Surface Design for Controlled Crystallization: The Role of Surface Chemistry and Nanoscale Pores in Heterogeneous Nucleation. *Langmuir* **27**, 5324–5334 (2011).
4. Mullin, J. W. *Crystallization, 4th Edition*. (2001).
5. Thanh, N. T. K., Maclean, N. & Mahiddine, S. Mechanisms of Nucleation and Growth of Nanoparticles in Solution. *Chem. Rev.* **114**, 7610–7630 (2014).
6. Bentea, L., Watzky, M. A. & Finke, R. G. Sigmoidal Nucleation and Growth Curves Across Nature Fit by the Finke–Watzky Model of Slow Continuous Nucleation and Autocatalytic Growth: Explicit Formulas for the Lag and Growth Times Plus Other Key Insights. *J. Phys. Chem. C* **121**, 5302–5312 (2017).
7. Le Corre, K. S., Valsami-Jones, E., Hobbs, P. & Parsons, S. A. Phosphorus Recovery from Wastewater by Struvite Crystallization: A Review. *Critical Reviews in Environmental Science and Technology* (2009). doi:10.1080/10643380701640573
8. Ye, X. *et al.* A comprehensive understanding of saturation index and upflow velocity in a pilot-scale fluidized bed reactor for struvite recovery from swine wastewater. *Powder Technol.* **295**, 16–26 (2016).
9. Diao, Y., Harada, T., Myerson, A. S., Alan Hatton, T. & Trout, B. L. The role of nanopore shape in surface-induced crystallization. *Nat. Mater.* **10**, 867–871 (2011).
10. Saridakis, E. & Chayen, N. E. Towards a 'universal' nucleant for protein crystallization. *Trends Biotechnol.* **27**, 99–106 (2009).
11. Wang, H., Alfredsson, V., Tropsch, J., Ettl, R. & Nylander, T. Formation of CaCO 3 Deposits on Hard Surfaces: Effect of Bulk Solution Conditions and Surface Properties. *ACS Appl. Mater. Interfaces* **5**, 4035–4045 (2013).
12. Betancourt, T. & Brannon-Peppas, L. Micro- and nanofabrication methods in nanotechnological medical and pharmaceutical devices. *Int. J. Nanomedicine* **1**, 483–95 (2006).
13. Barbé, C. *et al.* Silica Particles: A Novel Drug-Delivery System. *Adv. Mater.* **16**, 1959–1966 (2004).

Chapter 5.

Substrate Wettability and Crystal Chemistry for Evaporative Crystallization from Drops

The coffee-ring effect refers to the phenomena in which a drop of a colloidal suspension evaporates on a substrate and deposits an ordered ring-structure due to the radially outward evaporative flow. Evaporative deposits are widely studied due to their numerous applications in low effort self-assembly, such as ink-jet printing, microscale separations, and sensing/diagnostics. However, this phenomenon has been less quantified for a crystallizing solution. When a drop of salt solution is evaporated, the salt becomes supersaturated and crystals begin to emerge at the substrate-drop contact line. The emerging crystals alter the local wettability of the substrate and fundamentally alter the dynamics of evaporation, which in turn alters the resultant deposit. Therefore, exploring deposition of crystals from evaporating drops is a useful tool for studying interactions between a substrate and a crystallizing solute. In addition, these experiments yield information on crystal adhesion, which can directly inform design of substrates for anti-fouling.

Chapter 3 explored how substrate wettability and crystal chemistry influences crystal growth and adhesion to surfaces. Here, the same parameters are explored in the context of a system of crystallization from an evaporating drop. I test the hypothesis that competition between contact line mobility and crystallization nucleation barriers ultimately control deposit morphology using an experimental matrix of various substrate chemistries, evaporation rates, and saline solutions. Because study regarding the evaporative crystallization from drops has thus far been limited, the results from the present chapter will be essential for subsequent chapters exploring crystalline coffee-rings on unique substrates.

5.1 Hypothesis & Experiments

Motivation

Scientific and technological interest in evaporative self-assembly and pattern formation has proliferated rapidly since the seminal analysis of ring-stains performed by Deegan et al. in 1997.[1] Since then, evaporation of volatile solvent drops containing nonvolatile solutes has been used to engineer complex patterns ranging from rings, concentric rings,[2,3] spirals,[4] colloidal crystals,[5,6] hexagonal networks,[7] three-dimensional shapes,[8,9] and more.[10] This facile method of producing ordered structures is attractive as an alternative to traditional fabrication of electronics[11] and sensors,[12] and can be applied for micro-scale separations[13] and ink-jet printing.[14]

Of the 4,300+ investigations citing Deegan's original "coffee-ring" paper, approximately 3,400 cover deposition patterns formed by colloidal particles. These investigations have explored the influence of particle shape,[15] size,[13] density,[10,16] presence of surfactants,[17] and interactions with the substrate and/or other particles.[18] External parameters including temperature,[19] relative humidity,[20] substrate wettability,[21] heat capacities of the solute and substrate, etc., have also been explored. The depositions are typically categorized as rings, uniform deposits, or bumps. The emergence of one deposit morphology over another is due to the competing interactions of evaporative flow, attractive forces between the particles and substrate, and Marangoni recirculation.[16]

Despite the abundance of work exploring evaporative self-assembly of colloids from drops, less is known regarding crystallizing solutes. Study of crystalline evaporative deposits is motivated by the same self-assembly applications as is the study of colloidal deposits; and warrants additional motivation in the form of understanding and controlling device disfunction related to crystal fouling.[22–25] Crystal fouling (also called scaling) becomes even more problematic in micro-devices, where miniscule amounts of precipitate can dramatically reduce device functionality.[26,27] Thus, understanding and controlling crystallization at interfaces is critical towards continued development and implementation of microfluidic systems.

Previous investigations have demonstrated that the forces controlling deposit morphology for crystals are distinct from those that control colloidal deposits from evaporating drops.[9,24,28] Crystalline deposits will form rings even on superhydrophobic surfaces,[9] are independent of the substrate thermal conductivity,[28] and demonstrate a large dependence on the properties of the emerging crystals.[24] Additional evidence suggests that the internal convection of evaporating drops of saline solutions containing a high concentration of very soluble salts (NaCl, $CaCl_2$, etc.) is fundamentally altered by the presence of these salts.[22,29] High salt concentrations can also influence the drop contact angle and evaporation rate, which in turn will influence the deposit pattern.[30,31]

Hypothesis

Here, I explore the interplay between crystallization and surface interactions in the "coffee-ring" deposition of a crystallizing solution and seek to understand the physics controlling formation of crystalline deposits. Specifically, I test the hypothesis that competition between contact line mobility and crystallization nucleation barriers control deposit morphologies (Figure 5.1). Salts which crystallize readily on a given substrate are predicted to form ring-deposits (Figure 5.1a,b), while salts with a higher heterogeneous nucleation barrier on a given substrate will form bump-like deposits (Figure 5.1c,d), This effect can be quantified via the area localization (A_{loc}, the ratio between the substrate area in contact with the initial drop (A_O) and the area of the final deposit (A_E)), and by the supersaturation at the moment of crystallization, which is directly related to the nucleation barrier.

To test this hypothesis and explore how crystalline coffee-rings are different from colloidal ones, three sparingly soluble salts were compared to a typical colloidal solution containing latex particles to investigate differences across salts as well as the differences between saline and colloidal drops. These solutions were evaporated on five different substrates at three different temperatures to form a complete picture of how crystalline and colloidal coffee-rings differ.

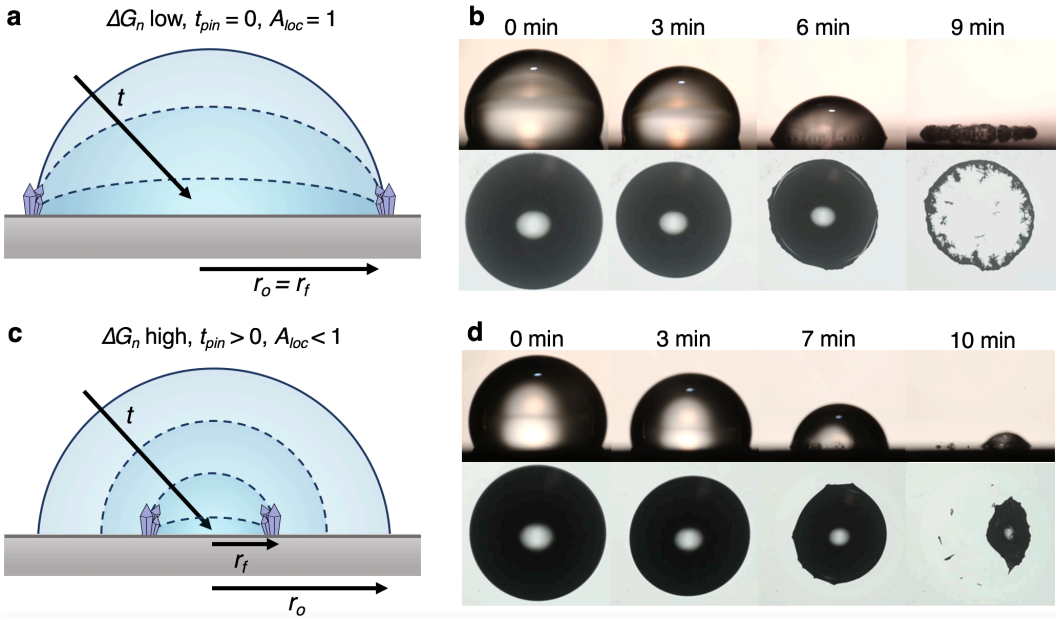

FIGURE 5.1. (a,b) Crystals with lower nucleation barriers will pin a contact line to form rings, (c,d) crystals with high nucleation barriers will form lumped deposits. Experiment shown in (b) is evaporation of a 5 µL drop of saturated calcium sulfate solution at 40°C on OTS, and (d) shows evaporation of a 5 µL drop of saturated silver sulfate solution at 40°C on OTS. Scale is the same for all images shown in (b,d), and is 2.8 mm across.

Substrates

Silicon wafers (or glass slides) were functionalized with the silane groups listed in Table 5.1 to create a range of wetting properties, and their preparation has been described previously.[32] For the oxysilanes (triethoxyphenylsilane; TOPS, and (3-aminopropyl) trimethyoxysilane; AMS), plasma-cleaned silicon substrates were added to a mixture of 0.075% hydrochloric acid in ethanol. Silane was added to 0.2% (volume) concentration, and beakers were capped and left to react for at least 24 hours. Two other silanized substrates (1,2-Dichlorotetramethylsilane; DTS, Octyltrichlorosilane; OTS) were prepared using a different liquid deposition method, in which plasma-cleaned substrates are added to a reaction beaker with 30 mL of toluene and 75 µL of silane. In a separate beaker, an emulsion of 20 mL toluene and 100 µL of DI water was prepared. This emulsion was poured into the reaction beaker, and substrates were sonicated for 4 minutes to facilitate the reaction. Substrates were then rinsed with acetone and isopropyl alcohol to remove excess silane. Flourosilane substrates (Trichloro (1H,1H,2H,2H-perfluorooctyl) silane; FS) were prepared via vapor deposition. Plasma-cleaned substrates were placed in a desiccator alongside a small drop of silane solution. The chamber was vacuumed, and left for a period of at least 8 hours for complete reaction. Samples were stored in air-tight containers and used within one month of preparation.

TABLE 5.1. Properties of different substrates used in this study, including the non-polar (γ_{LW}), and polar (γ_{AB}) components of surface energy. Advancing (θ_A), receding (θ_R), and equilibrium (θ_E) contact angles listed here are for DI water, along with the contact angle hysteresis between the advancing and receding angle ($\Delta\theta_{AR}$), and the hysteresis between the equilibrium and receding angle ($\Delta\theta_{ER}$)

Full name	**Abbr.**	**γ_{LW} (mJ/m^2)**	**γ_{AB} (mJ/m^2)**	**γ_{total} (mJ/m^2)**	**θ_A**	**θ_E**	**θ_R**	**$\Delta\theta_{AR}$**	**$\Delta\theta_{ER}$**
triethoxyphenylsilane	TOPS	35.7	9.0	44.7	40º	34º	12º	28º	22º
(3-aminopropyl) trimethyoxysilane	AMS	34.3	2.8	37.1	57º	54º	31º	26º	23º
1,2-Dichlorotetramethylsilane	DTS	26.0	4.7	30.7	82º	68º	62º	20º	6º
Octyltrichlorosilane	OTS	22.9	0.04	22.9	112º	106º	98º	14º	8º
Trichloro (1H,1H,2H,2H-perfluorooctyl) silane	FS	8.7	0.03	8.7	124º	110º	100º	24º	10º

A goniometer was used to characterize substrate contact angles. Three different probe liquids (Water, ethylene glycol, and diiodomethane) were used to extract the different components of surface energy listed in Table 5.1. For XPS spectra of substrates prepared, see Azimi et. al 2014.[32] Dynamic (θ_A, θ_R) and equilibrium (θ_E) contact angles were measured for each surface using DI water. As previously noted, the low saturation concentration of the salts used here are not predicted

to have a significant influence on wetting properties measured for DI water, and experimental results confirm that no significant deviations are observed. The contact angle hysteresis is typically defined as the difference between the advancing and receding angles. However, the hysteresis between the equilibrium (also referred to as the Young angle) and receding angles is also included in table 5.1, and will be more relevant for characterizing the present experiments where the initial state of the drop is the equilibrium angle.

Salts

Evaporative deposits for three different saline solutions were compared to deposits from a typical colloidal solution in these experiments. Calcium sulfate, silver sulfate, and calcium iodate were purchased as solids from Sigma-Aldrich. Some of the properties of these salts are shown in Table 5.2. Salts were added to DI water at a concentration in excess of their solubility limits, allowed to mix and dissolve for a period of at least 18 hours at ambient temperature before excess solid was filtered out to leave a particle-free, saturated salt solution. The relatively low saturation concentration of these sparingly soluble salts did not cause significant changes to the evaporation rate or the drop contact angle. These particular salt solutions were chosen specifically for their solubility properties (Table 5.2) which are on the same order of magnitude across the three solutions and fall into the upper range of the sparingly soluble category. By comparing three salts with similar saturation concentrations, concentration effects are reduced as much as feasible.

TABLE 5.2. Crystal solubilities in water, and surface energy (when available)

Crystal	**C_{sat} at 20°C**	**C_{sat} at 40°C**	**C_{sat} at 60°C**	**C_{sat} at 80°C**	**$\gamma_{crystal}$**	**$\rho_{crystal}$**	**Crystal Structure**	**ΔH_f^o**
Calcium Sulfate	2.4 g/L	2.6 g/L	2.5 g/L	2.3 g/L	0.35 to 0.4 J/m^2	2.96 g/cm^3	Dihydrate: orthorhombic	-1433 kJ/mol
Calcium Iodate	2.4 g/L	4.8 g/L	6.1 gL	6.7 g/L		4.52 g/cm^3	Anhydrous: monoclinic monohydrate: monoclinic	
Silver Sulfate	7.8 g/L	9.6 g/L	11 g/L	13.3 g/L		5.45 g/cm^3	Dihydrate: Orthorhombic	-716 kJ/mol

Salt solutions were compared to a typical colloidal solution. Latex particles of 1 μm diameter were added to DI water at a concentration of 0.1% V/V to create the colloidal solution. The coffee-ring behavior of colloidal solutions is highly dependent on particle size, shape, chemistry (in particular, how that chemistry affects particle-particle and/or substrate/particle attraction), and concentration.

5.2 Evaporative Deposits

Experiments were conducted by heating functionalized substrates to a controlled temperature (20, 40, 60, or 80°C) and depositing 5 μL drops of the saline or particle-laden solution. Evaporation was recorded using a Zeiss microscope equipped with a Nikon D300 camera from the top, and side-views to capture contact angle dynamics were recorded using a Nikon D800 equipped with a Navitar lens. Resultant videos were processed to extract the following parameters: Time until crystallization (t_c), total evaporation time (t_E), contact area between the drop and substrate at first deposition (A_o), the initial contact angle (θ_o), the contact angle and contact area at the first appearance of crystals (θ_c, A_c), the contact angle as a function of time, and the final area covered by the resultant deposit after complete evaporation (A_E). For non-circular final deposits, the "diameter" of the resultant deposit was taken as the average between the longest dimension and the shortest.

In the classic case of an evaporating colloidal drop, evaporation proceeds in one of two modes: constant contact angle (cca) or constant contact radius (ccr).[33] Constant contact angle means that the drop contact area decreases with time as the contact line slides over the substrate, leaving a condensed deposit. In constant contact radius evaporation, the drop contact line remains pinned to the substrate, and the contact angle decreases with time. This picture is somewhat complicated when the colloidal drop is replaced by a saline drop, as both the wetting properties and supersaturation change with time. Rather than accumulating particles at the triple contact line due to outward radial flow, the supersaturation of salt increases at the contact line where ions are unable to follow water into the vapor phase. This leads to crystallization in the vicinity of the contact line, which may then influence pinning. Pinning of the contact line will be enhanced when crystals adhere to the substrate, and will fundamentally alter the receding contact angle due to the altered wettability caused by crystal formation.

Figure 5.2 shows the change in contact angle with time during evaporation of drops at 60ºC on the different substrates. The top left panel shows the control case using a particle-laden colloidal drop. For the two most hydrophobic surfaces (OTS and FS), the drop evaporates with a relatively constant contact angle, suggesting a highly condensed deposit will form (see Figure 5.3c, last two columns). This trend also follows for two of the salt solutions, calcium iodate and silver sulfate. However, for calcium sulfate, we see that the contact angle of the drop on the OTS surface begins dropping about halfway through the experiment; suggesting that the drop has become pinned and is now evaporating in constant contact radius mode. The two most hydrophilic substrates (TOPS and AMS) show relatively little difference across the different solutions, in that they all occur in constant contact radius and thus leave ring-deposits (Figure 5.3c, first two columns).

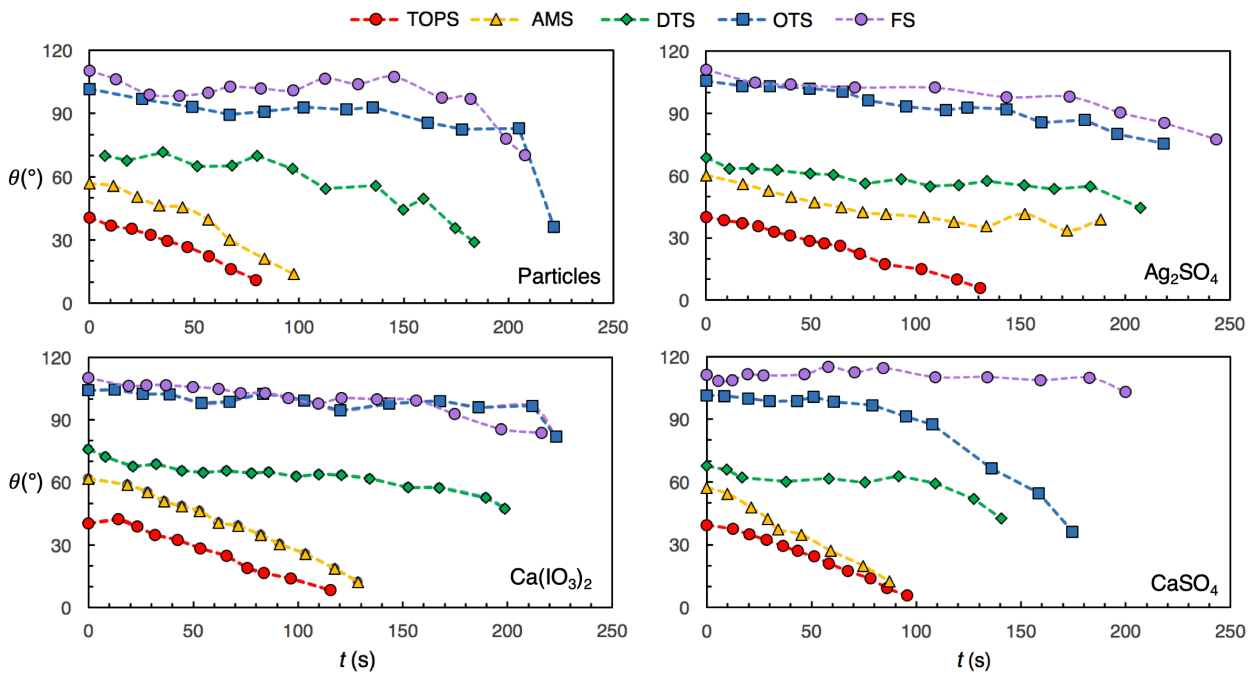

FIGURE 5.2. Drop evaporation with time for the different solutions at 60°C. Contact angle measurements were terminated at the point at which the contact line became too distorted by particle/crystal accumulation to extract an angle.

The results of figure 5.2 hint at some differences between the evaporative modes for saline and colloidal drops. The outcomes of these differences are shown in figure 5.3, which show representative patterns from experiments at 20°C (figure 5.3a), 40°C (figure 5.3b), 60°C (figure 5.3c), and 80°C (figure 5.3d). As expected, the hydrophilic substrates (TOPS and AMS, $\theta_E = 34°$ and 54°, respectively) form ring patterns across temperatures and solutions. At very high evaporation rates (80°C), particles leave behind ring-shaped deposits even on the most hydrophobic surfaces. This is an expected and previously observed result, and can be attributed to internal evaporative flow exceeding Marangoni recirculation which acts to move particles towards the drop center.[16,21,34] In contrast, the deposits left by calcium iodate on the hydrophobic surfaces are ring-like at 20°C, and become more condensed with increasing temperature.

Another notable result of figure 5.3 is the lack of influence of temperature on calcium sulfate and silver sulfate. Changing temperatures does not seem to significantly alter deposits formed for either solution. However, the two do not exhibit the same behavior. We see that drops tend to pin at the onset of crystallization for calcium sulfate; while for silver sulfate, the contact line continues to move even once crystals have begun to form. The result is that calcium sulfate deposits tend to be ring-shaped across temperatures and substrates; while silver sulfate deposits tend to be clumped gathering of individual crystals.

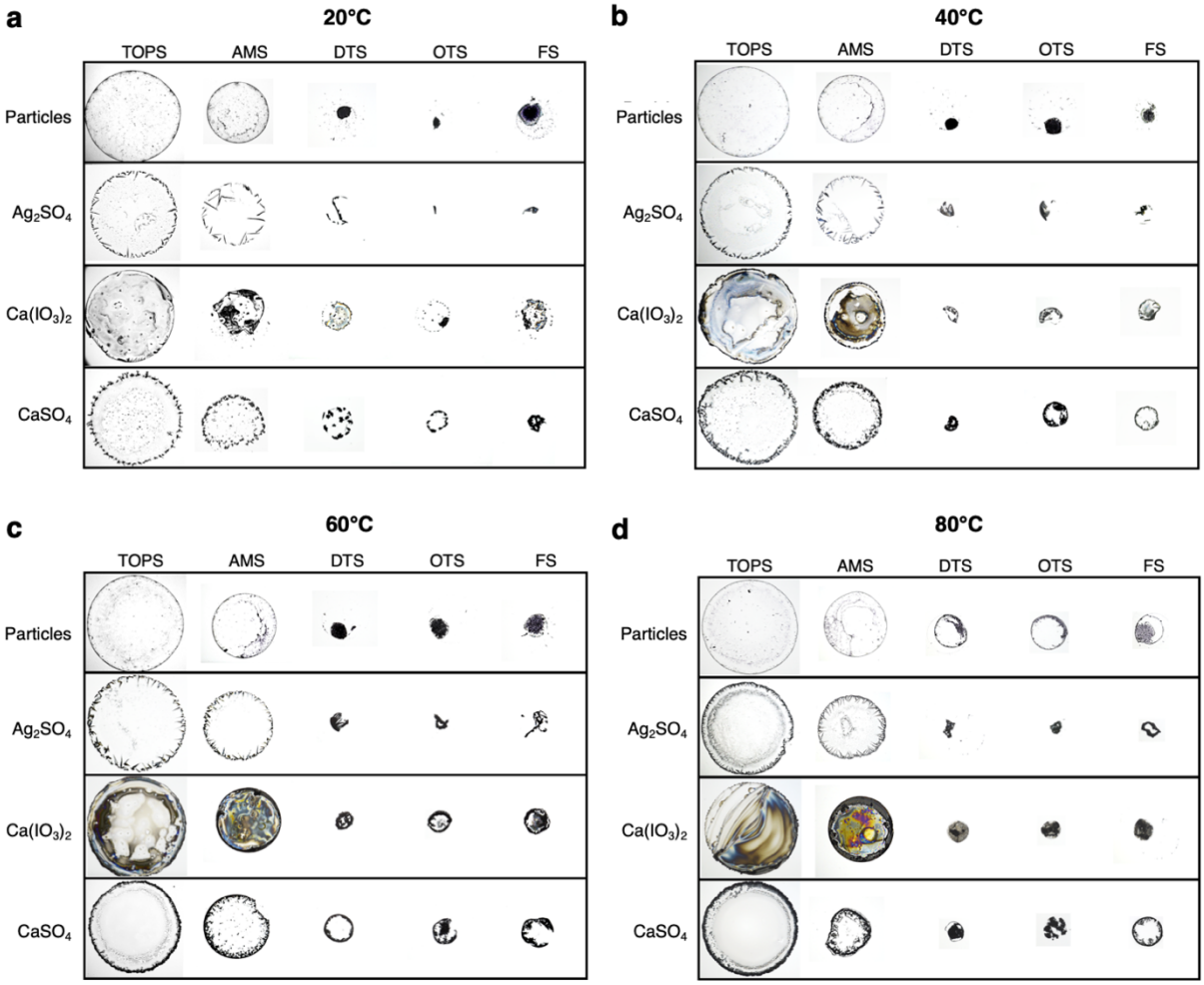

FIGURE 5.3. Representative patterns from experiments for (top) particles, (second row) silver sulfate, (third row) calcium iodate, (fourth row) calcium sulfate. (a) 20°C, (b) 40°C, (c) 60°C, (d) 80°C. Length scale is the same for all images, and the diameter of the TOPS deposits is ~4mm.

An expected result shown in figure 5.3 is the relationship between evaporation rate and crystal growth. At low temperatures, fewer crystals nucleate, and those crystals grow larger. At higher temperatures, more crystals nucleate and these crystals do not grow to large sizes. This trend is particularly apparent amongst silver sulfate deposits (the selected image shown for silver sulfate on OTS at 20°C is a single crystal). The size of individual silver sulfate crystals increases with increasing contact angle, as shown in Figure 5.4. This observation can be rationalized by lowered evaporation times with increasing contact angles, as crystals grown at slower rates tend towards larger grain size.

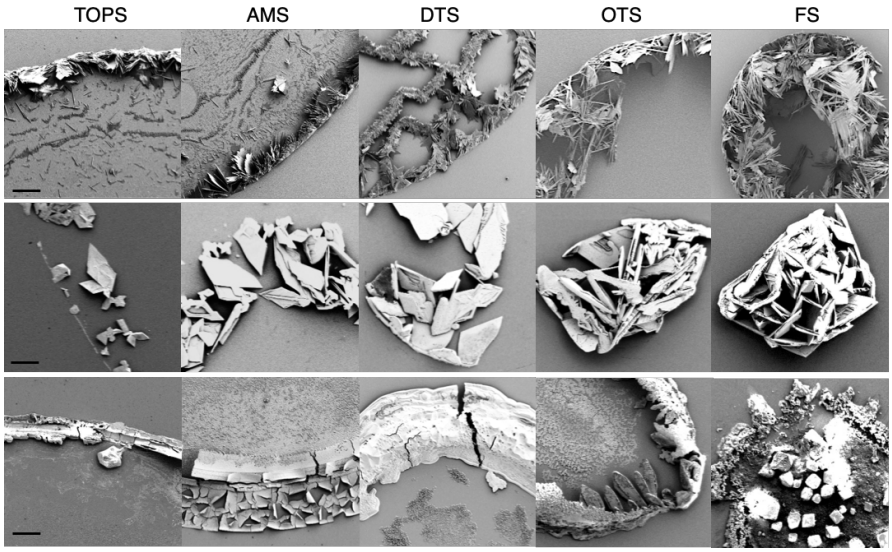

FIGURE 5.4. Influence of surface energy on deposit morphology formed at 60°C for (top) calcium sulfate, (middle) silver sulfate, and (bottom) calcium iodate.

In addition to the effect of temperature, there also appears to be some effect of substrate chemistry on the crystal morphologies shown in Figure 5.4. This effect is particularly potent for the calcium iodate crystals, in which structures formed at lower wettability's do not grow distinct facets. The kinetics of crystallization for calcium iodate are significantly slower than for the other two crystals; meaning that without sufficient time for crystal formation the calcium iodate instead precipitates in a random and condensed fashion.

A quantitative method of describing the deposit morphology is the area localization; which is the ratio of the initial contact area between the drop and the substrate to the final area of the resultant deposit. This dimensionless ratio is a more useful metric than the area because it gives an indication of contact line motion during evaporation. For a drop that remains pinned and evaporates in a constant contact radius mode, this ratio will be 1, as the initial area of the drop and final area of the deposit will be the same. The resulting deposit for such a drop will be a ring. For a drop evaporating in constant contact angle mode with constant recession of the contact line, the resultant deposit will be highly condensed compared to the initial area, and we might expect this ratio to be closer to 0.2-0.4. The area localization will be somewhere in between for a drop that falls into neither of the two categories. This ratio has been plotted as a function of the substrate surface energy (see Table 5.1, higher surface energy = more hydrophilic) in Figure 5.5a across temperatures for each of the four solutions.

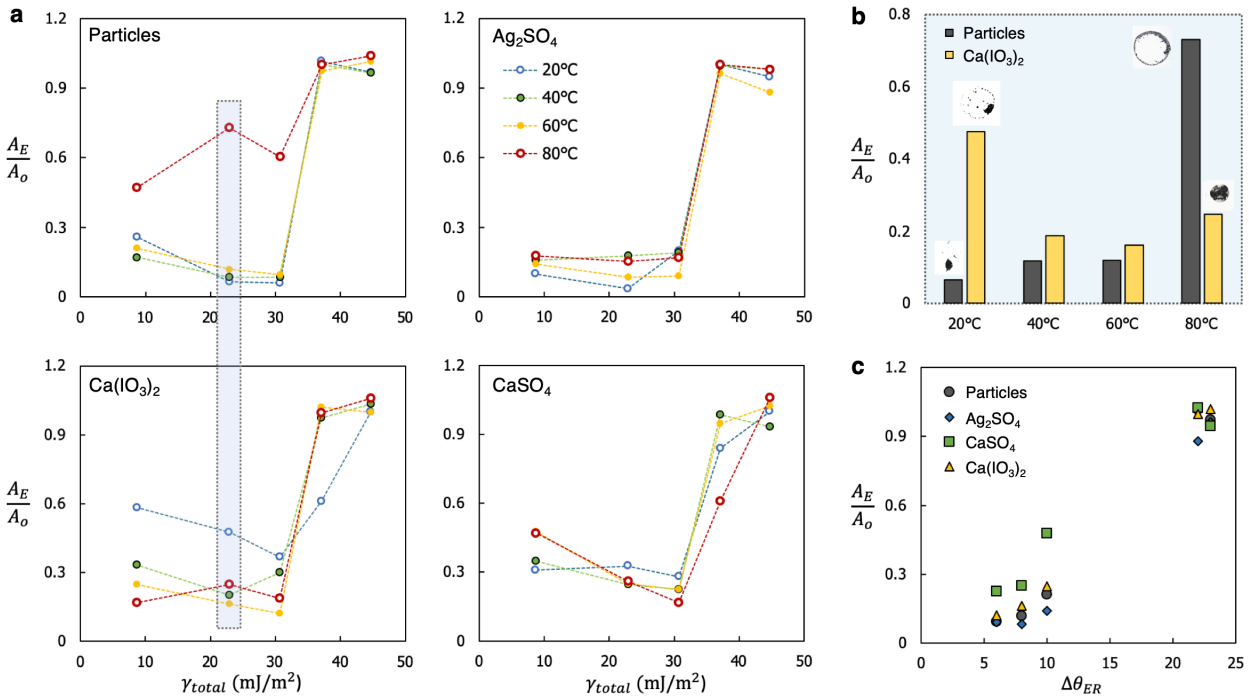

FIGURE 5.5. (a) Area localization (ratio of final contact area of deposit to contact area of initial drop) as a function of substrate surface area (where the more wettable substrates have a higher energy) across temperatures. (b) bar graph for OTS data outlined in blue in part "a," comparing temperature dependence of the particles and calcium iodate deposits. (c) Area localization as a function of the contact angle hysteresis (between the equilibrium angle and receding angle) at 60°C.

Comparing the area localization data of Figure 5.5a across calcium iodate and particles confirms the observation from Figure 5.3 that the two solutions reverse trends with temperature. This trend reversal is highlighted in Figure 5.5b, which displays data for the OTS surface (i.e., the points highlighted in blue on Figure 5.5a). The calcium iodate deposits are largest at the lowest temperature, and form a ring-shape. At the highest temperature of 80°C, the calcium iodate deposit is clumped. This result is in line with predictions from a previous molecular dynamics investigation, which found that sodium chloride is more likely to form rings under slow evaporation conditions.[31] In contrast, the particle deposit is largest (and ring-shaped) at 80°C, and clumped at 20°C.

In general, deposits on lower surface energy (more hydrophobic) substrates have a lower area localization. However, the area localization on the most hydrophobic surfaces (FS, γ_{total} = 8.7 mJ/m^2) is often higher than it is for the OTS or DTS surfaces (γ_{total} = 22.9 and 30.7 mJ/m^2, respectively). This effect is particularly pronounced for the calcium sulfate deposits (bottom right of Figure 5.5a). Unlike the absolute deposit area that can be observed in Figure 5.3, the area localization is a function of the contact line dynamics. This means, for example, that a hydrophilic substrate with low contact angle hysteresis can form a deposit with a relatively large physical size but small area localization; and that a deposit on a hydrophobic substrate with high contact angle

hysteresis can have a small size but large area localization. Thus, area localization has a strong dependence on the contact angle hysteresis between the equilibrium angle and receding angle (Table 5.1, last column), as shown in Figure 5.5c.

For calcium sulfate deposits, the minimum area localization occurs on the DTS surface (γ_{total} = 30.7mJ/m^2), which also has the lowest contact angle hysteresis ($\Delta\theta_{ER}$ = 6°). Similarly, while FS exhibits the largest overall contact angle, the calcium sulfate deposits on the FS surface have the largest area localization of the three hydrophobic surfaces. This is likely due to the slightly higher contact angle hysteresis ($\Delta\theta_{ER}$ = 10°). While this trend is most apparent in Figure 5.5a for the calcium sulfate deposits, it also holds well across solutions, as shown in Figure 5.5c for the deposits formed at 60°C. The observation that the area localization of the calcium sulfate deposits is more sensitive to contact angle hysteresis than other solutions (particularly silver sulfate), suggests that burgeoning calcium sulfate crystals pin the receding interface more readily than silver sulfate crystals; which is indeed observed (see Figure 5.2, where calcium sulfate deposits are more likely to form rings than silver sulfate).

5.3 Crystallization vs. Contact Line Motion

The previous section demonstrated that crystallizing solutes do not behave the same as a colloidal solution (silver sulfate and calcium sulfate do not demonstrate a significant temperature dependence), and that calcium iodate in particular demonstrates the reverse trend of the colloidal solution (where the colloidal solution is more likely to form rings at high evaporation rates, and calcium iodate forms condensed deposits at high evaporation rates). Now the relationship between crystal nucleation and substrate contact line dynamics is explored in order to explain this relationship.

Figure 5.5c showed that the area localization could be correlated to the substrate contact angle hysteresis, which hints at the importance of contact line pinning. However, crystallization also plays a role, as the area localization differs across salt solutions. Calcium sulfate, the salt most likely to form ring deposits, exhibits the largest area localization for a given contact angle hysteresis; while silver sulfate and calcium iodate exhibit lower area localization and are more likely to form condensed deposits. To explore the role of crystallization in contact line pinning and therefore area localization, the ratio between the crystallization time (t_c) and the total evaporation time (t_E) is plotted against the area localization (Figure 5.6a). This timescale ratio gives an indication of how readily the crystals form, where a lower ratio indicates that crystals emerge relatively early in the process, and a higher ratio indicates that crystals begin to emerge later.

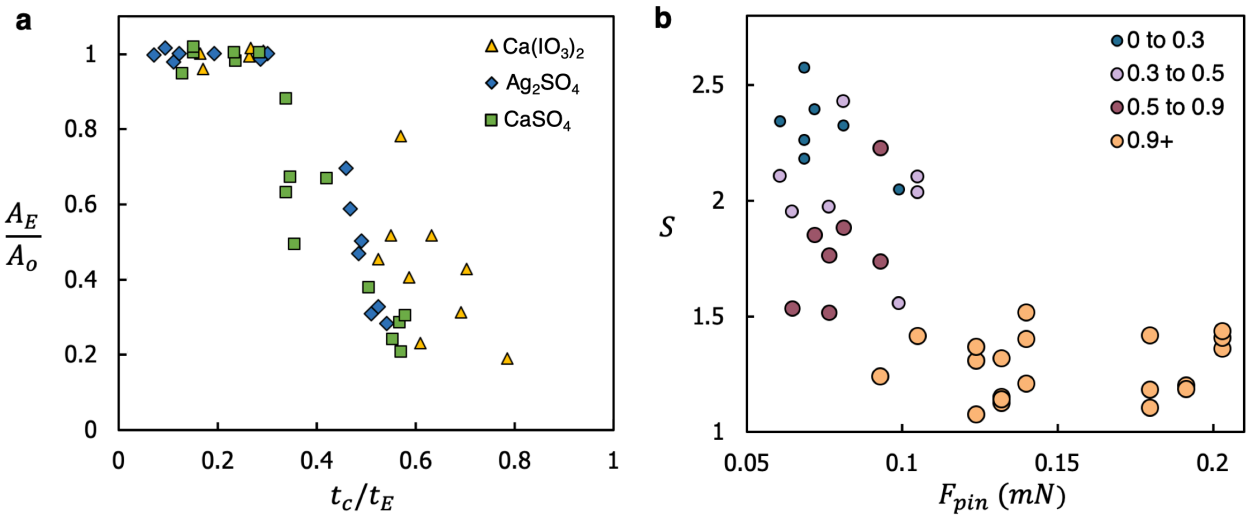

FIGURE 5.6. Data across five substrates and three temperatures (40°C, 60°C, 80°C) collapse onto a single trend based on the supersaturation at crystal nucleation. (a) squares = calcium sulfate, diamonds = silver sulfate, triangles = calcium iodate. (b) phase diagram of the pinning force against the supersaturation, where $F_{pin} = 2\pi R\,\gamma(T)(\cos\theta_R - \cos\theta_A)$, S_c is from experimental data, estimated as $S_c = V_o/V_c$, and data was classified according to the area localization. Data comes from experiments conducted at 40°C, 60°C, and 80°C.

Comparing the results of Figure 5.6a across the three solutions shows that, for a given area localization, the calcium sulfate and silver sulfate crystals generally emerge earlier in the evaporation process than calcium iodate crystals. This trend might be explained by the changing solubilities with temperature. The three salts used in this study were chosen for having solubilities within the same order of magnitude to reduce concentration-induced variations. However, they do not all exhibit the same change in solubility with temperature (see Table 5.2). Calcium sulfate exhibits very little change in solubility with temperature, while the solubility of silver sulfate increases by 1.7x between 20° and 80°C. Calcium iodate has a 3x increase in solubility between the same temperatures. This difference in solubility with temperature allows us to understand the trend observed in Figure 5.5b; where calcium iodate formed the most localized deposits at the highest temperature. Although increased temperature increases the evaporation rate and therefore increases the rate at which ions accumulate at the contact line; the relative supersaturation for calcium iodate also decreases. In contrast, calcium sulfate does not become more soluble with temperature, and therefore the supersaturation is only a function of the evaporated volume of the drop. This result confirms that supersaturation is an essential variable in crystalline coffee-ring formation.

To explain the importance of supersaturation and its relationship to crystal nucleation induction, we consider the thermodynamics of the process. The Gibb's free energy of formation for a crystal on a substrate is:[35]

$$\Delta g_n = \frac{5\pi V_M^2}{3(k_B T)^2 S^2}(2\gamma_{SC} - \gamma_{LC} - \gamma_{SL})^3 \quad 5.1$$

Where V_M is the molecular volume, k_B is the Boltzmann constant, T is temperature, S is supersaturation, γ_{SC} is the surface energy between the substrate and crystal, γ_{LC} is the energy between the liquid and crystal, and γ_{SL} is the energy between the substrate and liquid. Thus, the energetics between the three phases (substrate, crystal, and liquid) all contribute to the nucleation barrier. Isolating values for these parameters is challenging, and thus it is difficult to say whether or not interactions between the substrate and crystal (captured by γ_{SC}) significantly influence the results. However, it is straightforward to obtain values for the supersaturation at the onset of crystallization. The average supersaturation, *S*, inside a drop can be related to the volume of the drop with time:

$$S = \frac{C(t)}{C_{sat}} = \frac{V_o}{V(t)} \quad 5.2$$

Where, as previously noted, the value of C_{sat} is a function of temperature. We are particularly interested in the drop supersaturation at the moment at which crystals first begin to form (and become visible under the microscope), t_c. Under conditions where the nucleation barrier is exceedingly small, crystals may begin to nucleate soon after the solution becomes supersaturated. In contrast, when the nucleation barrier is high, the solution can become highly supersaturated before crystals begin to emerge. The supersaturation of calcium sulfate can reach values of 6 or higher on surfaces with no heterogeneous nucleation sites before crystals start to form.[9]

With supersaturation as a metric to quantify crystallization propensity (where a low value of S_c indicates a high propensity of crystallization, and a high value indicates a high nucleation barrier and low propensity), we now define a metric to quantify contact line dynamics. An appropriate choice is the pinning force, which is a function of both the equilibrium (θ_E) and receding (θ_R) angles of the surface:[36]

$$F_P = 2\pi r_o \gamma(\cos\theta_R - \cos\theta_E) \quad 5.3$$

Where γ is the surface tension of water, 72 mJ/m^2 at 20°C (66 mJ/m^2 at 60°C), and r_o is the radius of the initial contact line. This equation gives the force required for depinning of the contact line, so that when the contact angle hysteresis is zero, there is no resistance to contact line motion. Plotting the pinning force of equation 5.3 (where contact angles are taken as values shown in Table 5.1, and surface tension is taken as a function of temperature) against the supersaturation at crystallization (S_c) yields the diagram shown in Figure 5.6b. In this diagram, the area localization of the deposits has been separated into four categories: highly condensed (A_E/A_C = 0 to 0.3)

condensed (A_E/A_C = 0.3 to 0.5), some reduction (A_E/A_C = 0.5 to 0.9), and non-reduced (A_E/A_C > 0.9). Higher pinning forces and high crystallization propensity result in non-reduced (and ring-shaped) deposits, while the highly reduced deposits occur at the lowest pinning forces and the lowest propensities for crystallization.

The results of Figure 5.6b show that, in general, a crystal deposit will be ring-shaped and non-localized when crystallization occurs before the volume reduces enough to overcome the substrate pinning force. However, it is not always true that crystallization pins the interface and stops mobility. In some cases, crystallization occurs at the contact line, and yet, the line continues to recede (this is particularly true for the silver sulfate experiments, in which crystals form but do not always pin the contact line). Instead, these silver sulfate crystals move with the contact line to form condensed deposits. It is here where I believe (but will not quantify here), that the substrate-crystal energy, γ_{SC}, from Equation 5.1 contributes to the deposit morphology. Crystals that preferentially interact with the substrate will grow on that substrate, and therefore pin the contact line. Crystals without strong interactions with the substrate will still form at the contact line due to concentration polarization, but will not be adhered to the substrate (i.e., they will exist in the bulk). Such crystals may move with the contact line as it recedes.

Crystalline patterns differ from colloidal patterns deposited from an evaporating drop under the same conditions, and have demonstrated that the area localization is correlated with the supersaturation (and therefore nucleation barrier) at which crystals begin to form. I now briefly consider the hypothesis that saline-induced convection, which has been previously shown to strongly alter the interior flow of the drop,[22,37,38] influences these results. Recent work has demonstrated that salt-induced Marangoni flow can significantly increase (double or more) the rate of deposition of colloidal particles at the contact line during coffee-ring evaporation.[38] The effect of solutal convection is more difficult to quantify here, as the effect of saline flow cannot be decoupled from deposition of crystals at the contact line. However, it can be inferred from this result that Marangoni flow likely elevates supersaturation at the contact line beyond the concentration that would exist from evaporative flow alone. A higher supersaturation leads to faster nucleation, a higher likelihood of contact line pinning due to crystallization, and more mass accumulated at the contact line. Thus, the influence of Marangoni convection in crystalline coffee ring formation is likely the opposite of the influence of Marangoni convection in colloidal deposits. For colloidal solutions, re-circulation leads to more deposition of particles at the interior of the drop, and increases the likelihood of a lumped deposit; while Marangoni flow in saline solutions transports more salt to the contact line, and thus increases the likelihood of a ring-deposit.

Conclusions

The contact line dynamics and evaporative crystallization from a drop both depend on the same parameters; namely the evaporation rate and surface energy of the substrate. We have explored the relationship between the two and demonstrated that the supersaturation at the onset of crystallization (which is directly related to the crystallization nucleation barrier) can explain the different deposit morphologies across the various solutions/substrates. Previous work exploring this relationship has suggested that crystalline deposits are independent of evaporation rate and depend only on wettability properties of the crystals and substrates.[28] I revise this conclusion to state that crystalline deposits are dependent on the nucleation barrier, which is largely dependent on the wettability properties but is also dependent on the evaporation rate due to the supersaturation term. This conclusion can be applied towards developing design rules for controlling the morphology of crystalline evaporative deposits, or towards understanding/controlling mechanisms of crystal fouling associated with wetting/evaporation cycles.

In addition to exploring the fundamental relationship between wetting, evaporation, and crystallization, these experiments have also elucidated important differences between colloidal and crystalline evaporative deposition. Supersaturation is an essential parameter for prediction of crystalline deposit morphology, and altered solubility with temperature can cause crystalline deposits to have a temperature relationship inverse to the one for colloidal deposits. Another difference is the role of Marangoni circulation, which promotes localized deposits in colloidal deposition patterns. In contrast, no evidence was observed to suggest that convective flows redistribute crystals towards the drop interior; and, based on previous results,[28] if Marangoni flow plays any role in crystalline evaporative deposits, it instead may act to promote ring formation. These differences between solutal and colloidal evaporative deposition demonstrate that the two related processes are nevertheless controlled by different physics, and highlight the need for further study of the many complex factors that contribute to crystalline evaporative assembly.

References

1. Deegan, R. D. *et al.* Capillary flow as the cause of ring stains from dried liquid drops. *Nature* **389,** 827–829 (1997).
2. Xu, J. *et al.* Self-Assembly of Gradient Concentric Rings via Solvent Evaporation from a Capillary Bridge. *Phys. Rev. Lett.* **96,** 66104 (2006).
3. Mu, J., Lin, P. & Xia, Q. Concentric rings of polystyrene and titanium dioxide nanoparticles patterned by alternating current signal guided coffee ring effect. *Cit. Appl. Phys. Lett* **104,** (2014).
4. McBride, S., Khan, S., Dash, S. & Varanasi, K. K. Crystallization of Spirals from Drops. *Langmuir* **Just Accepted,** (2019).
5. Paria, S., Ghosh Chaudhuri, R. & Jason, N. N. Self-assembly of colloidal sulfur particles on a glass surface from evaporating sessile drops: influence of different salts. *New J. Chem.* **38,** 5943–5951 (2014).
6. Prevo, B. G. & Velev, O. D. Controlled, Rapid Deposition of Structured Coatings from Micro- and Nanoparticle Suspensions. *Langmuir* **20,** 2099–2107 (2004).
7. Gonuguntla, M. & Sharma, A. Polymer Patterns in Evaporating Droplets on Dissolving Substrates. *Langmuir* **20,** 3456–3463 (2004).
8. Shin, B., Moon, M.-W. & Kim, H.-Y. Rings, Igloos, and Pebbles of Salt Formed by Drying Saline Drops. *Langmuir* **30,** 12837–12842 (2014).
9. McBride, S. A., Dash, S. & Varanasi, K. K. Evaporative Crystallization in Drops on Superhydrophobic and Liquid-Impregnated Surfaces. *Langmuir* **34,** 12350–12358 (2018).
10. Deegan, R. D. Pattern formation in drying drops. *Phys. Rev. E* **61,** 475–485 (2000).
11. Vakarelski, I. U., Chan, D. Y. C., Nonoguchi, T., Shinto, H. & Higashitani, K. Assembly of Gold Nanoparticles into Microwire Networks Induced by Drying Liquid Bridges. *Phys. Rev. Lett.* **102,** 58303 (2009).
12. Wilson, S. A. *et al.* New materials for micro-scale sensors and actuators: An engineering review. *Mater. Sci. Eng. R Reports* **56,** 1–129 (2007).
13. Wong, T.-S., Chen, T.-H., Shen, X. & Ho, C.-M. Nanochromatography Driven by the Coffee Ring Effect. *Anal. Chem.* **83,** 1871–1873 (2011).
14. He, P. & Derby, B. Controlling Coffee Ring Formation during Drying of Inkjet Printed 2D Inks. *Adv. Mater. Interfaces* **4,** 1–6 (2017).
15. Yunker, P. J., Still, T., Lohr, M. A. & Yodh, A. G. Suppression of the coffee-ring effect by shape-dependent capillary interactions. *Nature* **476,** 308–11 (2011).
16. Bhardwaj, R., Fang, X., Somasundaran, P. & Attinger, D. Self-Assembly of Colloidal Particles from Evaporating Droplets: Role of DLVO Interactions and Proposition of a Phase Diagram. *Langmuir* **26,** 7833–7842 (2010).
17. Anyfantakis, M., Geng, Z., Morel, M., Rudiuk, S. & Baigl, D. Modulation of the Coffee-Ring Effect in Particle/Surfactant Mixtures: the Importance of Particle–Interface Interactions. *Langmuir* **31,** 4113–4120 (2015).
18. Crivoi, A. & Duan, F. Elimination of the Coffee-Ring Effect by Promoting Particle Adsorption and Long-Range Interaction. *Langmuir* **29,** 12067–12074 (2013).
19. Soltman, D. & Subramanian, V. Inkjet-Printed Line Morphologies and Temperature Control of the Coffee Ring Effect. *Langmuir* **24,** 2224–2231 (2008).
20. Zeid, W. B. & Brutin, D. Influence of relative humidity on spreading, pattern formation and adhesion of a drying drop of whole blood. *Colloids Surfaces A Physicochem. Eng. Asp.* **430,** 1–7 (2013).
21. Patil, N. D., Bange, P. G., Bhardwaj, R. & Sharma, A. Effects of Substrate Heating and Wettability on Evaporation Dynamics and Deposition Patterns for a Sessile Water Droplet Containing Colloidal Particles. *Langmuir* **32,** 11958–11972 (2016).

22. Misyura, S. Y. Evaporation of a sessile water drop and a drop of aqueous salt solution. *Sci. Rep.* **7,** 14759 (2017).
23. Desarnaud, J., Bonn, D. & Shahidzadeh, N. The Pressure induced by salt crystallization in confinement. *Sci. Rep.* **6,** 30856 (2016).
24. Shahidzadeh-Bonn, N., Rafai, S., Bonn, D. & Wegdam, G. Salt Crystallization during Evaporation: Impact of Interfacial Properties. *Langmuir* **24,** 8599–8605 (2008).
25. Müller-Steinhagen, H., Malayeri, M. R. & Watkinson, a. P. Fouling of Heat Exchangers-New Approaches to Solve an Old Problem. *Heat Transf. Eng.* **26,** 1–4 (2005).
26. Schoenitz, M., Grundemann, L., Augustin, W. & Scholl, S. Fouling in microstructured devices: a review. *Chem. Commun.* **51,** 8213–8228 (2015).
27. Mayer, M. *et al.* Crystallization Fouling in Experimental Micro Heat Exchangers—Optical and Thermal Investigations. *Exp. Heat Transf.* **26,** 487–502 (2013).
28. Shahidzadeh, N., Schut, M. F. L., Desarnaud, J., Prat, M. & Bonn, D. Salt stains from evaporating droplets. *Sci. Rep.* **5,** 10335 (2015).
29. Kang, K. H., Lim, H. C., Lee, H. W. & Lee, S. J. Evaporation-induced saline Rayleigh convection inside a colloidal droplet. *Phys. Fluids* **25,** 42001 (2013).
30. Zhong, X., Ren, J. & Duan, F. Wettability Effect on Evaporation Dynamics and Crystalline Patterns of Sessile Saline Droplets. *J. Phys. Chem. B* **121,** 7924–7933 (2017).
31. Zhang, J., Borg, M. K., Sefiane, K. & Reese, J. M. Wetting and evaporation of salt-water nanodroplets: A molecular dynamics investigation. *Phys. Rev. E - Stat. Nonlinear, Soft Matter Phys.* **92,** 1–11 (2015).
32. Azimi, G., Cui, Y., Sabanska, A. & Varanasi, K. K. Scale-resistant surfaces: Fundamental studies of the effect of surface energy on reducing scale formation. *Appl. Surf. Sci.* **313,** 591–599 (2014).
33. Baldwin, K. A. & Fairhurst, D. J. Classifying dynamic contact line modes in drying drops. *Soft Matter* **11,** 1628–1633 (2015).
34. Hua Hu & Larson, R. G. Marangoni Effect Reverses Coffee-Ring Depositions. *J. Phys. Chem. B Lett.* **110,** 7090–7094 (2006).
35. Mullin, J. W. *Crystallization, 4th Edition*. (2001).
36. Gennes, P.-G. de., Brochard-Wyart, F. & Quéré, D. *Capillarity and wetting phenomena : drops, bubbles, pearls, waves*. (Springer, 2004).
37. Kang, K. H., Lim, H. C., Lee, H. W. & Lee, S. J. Evaporation-induced saline Rayleigh convection inside a colloidal droplet. *Phys. Fluids* **25,** 42001 (2013).
38. Marin, A. *et al.* Solutal Marangoni flow as the cause of ring stains from drying salty colloidal drops. *Phys. Rev. Fluids* **4,** 41601 (2019).

Chapter 6.

Drop Crystallization on Superhydrophobic & Liquid Impregnated Surfaces

Evaporative deposition of crystals from drops is pervasive and, in some cases, contributes to material degradation. Rain drops, spray from fast vehicles on wet roads, and ocean-generated aerosols are all examples in which particles/solutes may be deposited on surfaces. Costs associated with seaspray deposition run in the billions of dollars,[1,2] and primarily result from gypsum ($CaSO_4$-$2H_2O$) formation on concrete and metallic structures.[3,4] Corrosion of structures occurs via surface mineral-fouling, cracking (in which crystals engrained in a crevice grow and apply pressure), and delamination.[3,5,6] This damage can be inhibited using hydrophobic coatings,[3,4] though coatings face challenges regarding their temporal stability, environmental impacts,[7] and performance.[7,8]

In the previous chapter, I demonstrated that crystallization from saline drops is somewhat more complicated than deposition from evaporating colloidal solutions. This is due to variable solubility, concentration gradients at the air/water interface,[9] and the predilection of crystals to form at interfaces.[10] We have seen that crystallization at the contact line can pin a drop and force a ring morphology even on surfaces that would normally form a clumped deposit for a particle-laden system.[11,12] The evolution of the crystals alters drop pinning evaporation dynamics,[13] surface adhesion,[14] and the final form/size of the deposit. Therefore, eliminating coffee-rings (and therefore reducing fouling potential) for crystal deposits remains a challenge despite the many approaches for eliminating coffee-rings of colloidal deposits.

In this chapter, I explore crystallization from saline drops for two classes of anti-fouling substrate: superhydrophobic and liquid impregnated. Ring patterns persist for gypsum deposits even on hydrophobic surfaces,[15] which then modify contact angle hysteresis and the final form of evaporative deposits.[16] Superhydrophobic surfaces reduce contact-line pinning and should force formation of condensed deposits, as has been observed for colloids.[17] However, crystal formation will likely alter this behavior. Liquid impregnated surfaces (LIS), in which a thin layer of oil or other lubricant fills a micro- or nano-texture of a superhydrophobic surface, can create a protective barrier between a solid substrate and mineral foulants, and should therefore also inhibit ring formation.[18] I test this theory by comparing superhydrophobic and liquid impregnated surfaces with systematically varied micro-textures.

6.1 Experiments & Controls

Drop Evaporation

Experiments were conducted by placing the test substrate on top of a plate heater maintained at 60°C with a thin layer of thermal paste. Droplets of 5 µL saturated calcium sulfate solution were deposited on the substrate, and evaporation was recorded from both the top and side of the drops. Saturated calcium sulfate solution was prepared by adding calcium sulfate dihydrate in excess to DI water, mixing over a period of several days, and filtering out undissolved solid.

Evaporation occurs at the liquid/vapor interface when the vapor phase is undersaturated with respect to the evaporating species. The process of evaporation also changes the vapor concentration of the surrounding air. In the present experiments, evaporation of a 5 µL drop will not strongly influence the vapor concentration (humidity) of the ambient environment. At the immediate surface of the drop, the vapor concentration is therefore approximately equal to the saturated concentration (c_s), while far from the drop the vapor concentration returns to that of the ambient air (c_a = RH*c_s where RH is the relative humidity). Evaporation is driven by diffusion of vapor from the drop interface to the surrounding environment due to this concentration gradient:[19]

$$\frac{\partial c}{\partial t} = D(c_s - c_a) \tag{6.1}$$

Where D is diffusion (~2.8 x 10^{-5} m^2/s for water in air at 25°C). Assuming evaporation is limited by diffusion from the air/water interface to the ambient environment, the evaporation time for a drop will be:

$$t_E = \frac{R^2 \rho_L}{J} \approx \frac{R^2 \rho_L}{D(c_s - c_a)} \tag{6.2}$$

Where J is mass flux, ρ_L is liquid density, and R is the radius of the drop. For the experiments presented here, the evaporation time at 60°C on the superhydrophobic surfaces ranges from 2.5 to 4 minutes for the calcium sulfate solution and between 4.5 to 6 minutes for DI water. The relative humidity within our lab was tracked, and had a range between 22% to 45% while experiments were being conducted.

Using $c_s = 0.13\ \mathrm{kg/m^3}$ (for water in air at 60°C) at the drop surface, and an ambient concentration of $c_a = RH\ (c_s)$, with c_S for water in air at 20°C being $0.00171\ \mathrm{kg/m^3}$, the estimate for the evaporation time ranges from 270.76 seconds at 20% humidity to 271.66 seconds at 45% humidity (4.51 to 4.53 minutes). Therefore, the evaporation timescale was significantly influenced by both the substrate and by the presence/absence of calcium sulfate in the water, but was not significantly influenced by variable humidity levels within the lab. This is because the elevated temperature at the substrate was the primary driver for evaporation, so that the influence of environmental variation was tempered.

Heat Transfer & Convection

Because of the imposed temperature gradient across the drop, convection will occur. However, this convection is primarily driven by thermo-capillary flows rather than thermo-gravitational flows because the drops are below the capillary length.[20] The dynamic Bond number (Bd) compares the capillarity (given by the Bond number) to natural convection (given by the Rayleigh number):

$$Bd = \frac{Ra}{Ma} = \frac{\beta g \rho R^2}{-\frac{d\sigma}{dT}} \tag{6.3}$$

Where β is thermal expansivity, g is gravity, ρ is density, R is the radius of the drop, and $\frac{d\sigma}{dT}$ is the gradient of surface tension with temperature. For water, β is 2.07 x 10^{-4} 1/°C at 20°C and 5.22 x 10^{-4} 1/°C at 60°C, and $\frac{d\sigma}{dT}$ is -1.65 x 10^{-4} N/m°C for water between these two temperatures. Taking β at it's 60°C value, the dynamic Bond number is 0.0307; which confirms that capillary convection will be greater than convection due to gravity. The convection in these experiments occured on a timescale much smaller (~0.1s) than that of evaporation.

To model the evaporative flux and role of relative humidity, it is estimated that the water drop is heated to the temperature of the substrate, 60°C. For this to hold true, the timescale of the drop heating must be an order of magnitude or more smaller than the timescale of evaporation. Neglecting convection, the timescale of conduction is:

$$t_c = \frac{R^2}{\alpha} \tag{6.4}$$

Where α is the thermal diffusivity of water and has a value of 1.44 x 10^{-7} m^2/s at 20°C. For the 1 mm radius drops, this timescale is ~7 seconds, which is suitably smaller than the evaporation timescale of 150+ seconds experimentally observed. Because superhydrophobic surfaces have lower solid fractions than non-textured surfaces, it may be expected that this timescale will change for superhydrophobic materials. However, transient drop temperatures on heated superhydrophobic surfaces have previously been measured, and are ~5-10 seconds regardless of surface solid fraction.[21] This same study showed that equilibrium temperature of the drop on a superhydrophobic surface heated to 80°C is a function of the solid fraction, with the drop temperature reaching 95% of the absolute temperature of the substrate for a surface with solid fraction of 0.05, while a drop on a smooth surface reached 97% of the absolute temperature of the substrate after the initial transient period. Therefore, the drops in the present experiments should reach their equilibrium temperatures of ~60°C after a transient period of less than 10 seconds.

Data Collection

Each experiment was repeated 3-6 times per substrate. High resolution images of deposits were collected via SEM (scanning electron microscope, Zeiss Supra5). Experimental movies were analyzed to find: (1) the contact angle (θ) as a function of time, (2) the initial contact area of the drop (A_o), (3) the evaporation time (t_E), and (4) the final two-dimensional area of the crystal deposit (A_c).

Because pinning is essential for formation of ring-shaped deposits,[22] the area localization of deposits is a good predictor for deposit morphology. The area localization is defined as the ratio between the area covered by the final crystal deposit and the initial contact area of the drop (A_c/A_o). An area localization of ~1 suggests pinning of the contact line and therefore ring or uniform deposits, while smaller values suggest condensed deposits. Because formation of rings suggests pinning, rings deposits may be more strongly adhered to the surface; while clumped deposits form from a lack of pinning and therefore should be easier to remove.

Hydrophilic Control

Evaporation of sessile drops can proceed in either constant contact radius mode or in constant contact angle mode; with the former occurring for drops that have pinned to the surface. As we have seen in the previous chapter, evaporation on hydrophilic ($\theta = 24°$) silicon occurs in constant contact radius mode and results in the formation of ring-shaped deposits (Figure 6.1A). Crystallization initiates near the three-phase contact line approximately 10 seconds after drop deposition on the heated surface. The solution is then observed to wick into the precipitating crystals, further increasing the total footprint (A_c/A_o =1.09±0.30) of the crystalline deposit. SEM

images (Figure 6.1B) reveal needle-shaped crystals (a common structure for gypsum) oriented in the direction of the radial evaporative flow. These needles become thicker at the outer rim, likely due to the dramatic increase in flow velocity towards the end of evaporation.[23] These two-dimensional needles provide a counter example for comparing the performance of the superhydrophobic and liquid impregnated surfaces.

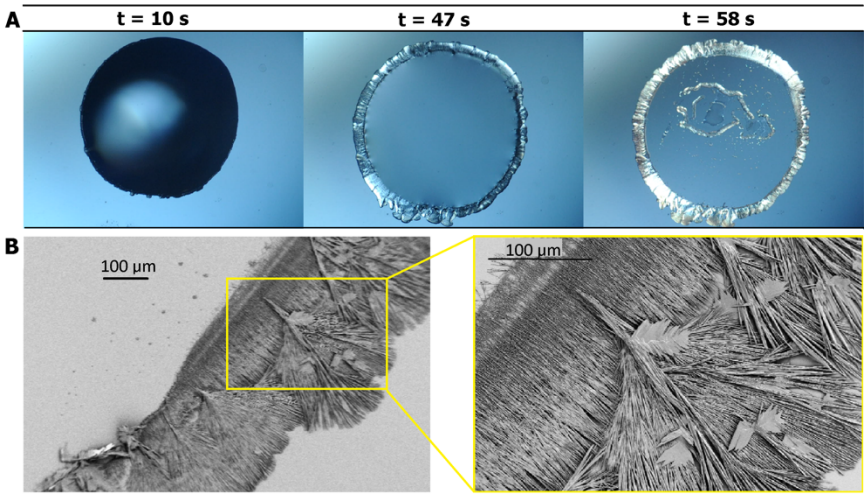

FIGURE 6.1. Evaporative crystallization on a hydrophilic silicon surface. (A) Progression of drop evaporation and crystal deposition. (B) SEM images from one deposit, showing dendritic needle-shaped gypsum crystals in-plane with the substrate.

Substrate Preparation

Photolithography using chrome masks (Advance Reproductions Corporations) was used to create arrays of square (10 µm wide) microposts with seven edge-to-edge post spacings: **5, 10, 25, 30, 40, 50, and 75 µm**. The posts were etched to a height of 10 µm by reactive ion etch (Surface Technology Systems Inductively Coupled Reactive Ion Etch) at a pressure of 20 mTorr, rate of 500 nm/min, temperature of 40°C, and coil power of 1200 W.[24,25] Photoresist was removed using Piranha solution, and the samples were further cleaned with acetone, IPA, and DI water.

Substrates were rendered hydrophobic by coating them with OTS (octadecyltrichlorosilane, from Sigma-Alrich) using liquid deposition by placing surfaces in 50 mL of toluene, and adding 70 µL of OTS and 100 µL of DI water under sonication for 3 minutes. Any excess silane was removed through two minutes of sonication in an acetone bath, followed by additional rinses with acetone, IPA, and DI water. Silicone oil with a viscosity of 100 cSt was added to the surfaces using a dipcoater (KSV Nima) to create the lubricant impregnated surfaces (LIS) without an excess film.[26]

6.2 Superhydrophobic Surfaces

Superhydrophobic surfaces combine micro-texture with a hydrophobic chemistry to create contact angles greater than ~140°. Seven different superhydrophobic microposts surfaces were prepared for these experiments. Each substrate had square micro-posts with a base of area 10x10 μm. The only difference was the edge-to-edge distances between the microposts, which effectively varied the substrate solid fraction, contact angles, and wetting behaviors. The seven tested substrates had post spacings of **5, 10, 25, 30, 40, 50, and 75 μm**. When air is trapped in this microtexture beneath a drop, the superhydrophobic contact angle is described by the Cassie model:[27,28]

$$\cos\theta^C = \phi_S(1 + \cos\theta) - 1 \qquad 6.5$$

Where θ^C is the superhydrophobic Cassie angle, ϕ_S is the fraction of solid contacting the drop, and θ is the Young's contact angle for a flat (untextured) surface of the same chemistry. The Wenzel model describes the contact angle of a textured superhydrophobic surface for the case where the drop fully contacts the surface (i.e., there is no trapped air):[28,29]

$$\cos\theta^W = r\cos\theta \qquad 6.6$$

Where *r* is the roughness, defined as the ratio of the actual to the apparent surface area and θ^W is the Wenzel angle. For very large values of *r*, this formula predicts complete drop ejection (θ^W=180°). The theoretical Cassie and Wenzel angles for the substrates used here are given in Table 6.1, along with the actual measured advancing, receding, and equilibrium, contact angles.

TABLE 6.1. Theoretical contact angles from the cassie (θ^C) and wenzel (θ^W) equations plus experimental data for initial static contact angle (θ_0), the advancing angle (θ_A), the receding angle (θ_R), and the contact angle hysteresis ($\Delta\theta$). Data for initial static angle were obtained from experiments using calcium sulfate solution, while contact angle hysteresis measurements were performed using DI water. The saturation concentration of gypsum is not large enough to modify the contact angle of water.

Surface	θ^C	θ^W	θ_0	θ_A	θ_R	$\Delta\theta$
b5	139.5°	180°	142.6°± 1.2°	145°	115°	30°
b10	149.9°	157.2°	147.2°± 0.8°	158°	143°	18°
b25	162.9°	132.0°	155.3°± 3.7°	159°	142°	17°
b30	165.1°	129.1°	156.4°± 3.1°	162°	146°	16°
b40	168.1°	125.9°	157.4°± 0.8°	165°	152°	13°
b50	170.1°	124.1°	161.7°± 1.7°	167°	157°	10°
b75	173°	122.2°	122.8°± 0.6°	119°	91°	28°

On a superhydrophobic surface with minimal contact angle hysteresis, evaporation of a suspended drop in the Cassie state will generally occur in constant contact angle mode where the contact line continuously recedes.[30] Here, it is observed that evaporation of calcium sulfate solution results in crystallization at the triple-phase contact line, which pins the contact line and changes the evaporative mode to constant contact radius mode. This is shown in Figure 6.2A(i), which shows the progression of an evaporating drop of calcium sulfate solution on a superhydrophobic surface of 5 μm edge-to-edge spacing between posts (b5). The drop pins due to formation of crystals, so that the final size of the deposit is similar to the contact area of the droplet (A_c/A_o=0.93), and a ring-deposit forms. However, this pinning is not observed for all the micropost surfaces. Figure 6.2A(ii) shows evaporation on the b25 surface, in which the contact line recedes before pinning occurs and more condensed deposits (A_c/A_o=0.68) result.

In total, four regimes are observed for evaporative crystallization on superhydrophobic micro-post surfaces. First, there is the Cassie pinning regime where ring deposits form, as seen in the case of the b5 surface (Figure 6.2A). As post spacing increases (b10, b25 and b30), evaporation begins in a constant contact angle mode with the drop sliding over the posts to form condensed deposits (A_c/A_o=0.69 for b10, 0.68 for b25, and 0.74 for b30). In the third regime, drops are initially suspended in the Cassie state but transition to the Wenzel state (Figure 6.2A(iii)). This transition causes a double ring deposit (seen most clearly on the b50 SEM image of Figure 6.2A) and a large area localization (A_c/A_o =1.5 for b40, 2.72 for b50). The fourth and final regime is observed in the case of the b75 surface, in which drops evaporate in constant contact radius mode in the Wenzel state to form a simple ring deposit.

The disparate deposit regimes across the different post surfaces can be rationalized by differences in contact angle and contact angle hysteresis. A surface with a large contact angle hysteresis will evaporate in constant contact radius mode until the contact angle reduces to the receding angle. A drop on a low hysteresis surface (with a receding angle similar to the advancing angle) will begin receding shortly after onset of evaporation. Hence, we predict that saline droplets evaporating on a surface with a higher hysteresis will become pinned by emerging crystals before receding begins. In contrast, drops on low hysteresis surfaces will recede before crystals can form and pin the contact line. Here, the b5 surface has the largest solid fraction and highest contact angle hysteresis of the Cassie surfaces (see Table 6.1), resulting in crystals pinning the contact line into the ring shape before the drop begins to recede from evaporation. The b10, b25, and b30 surfaces have lower hysteresis and recede significantly prior to crystallization, resulting in the clumped deposits observed in the constant contact angle regime.

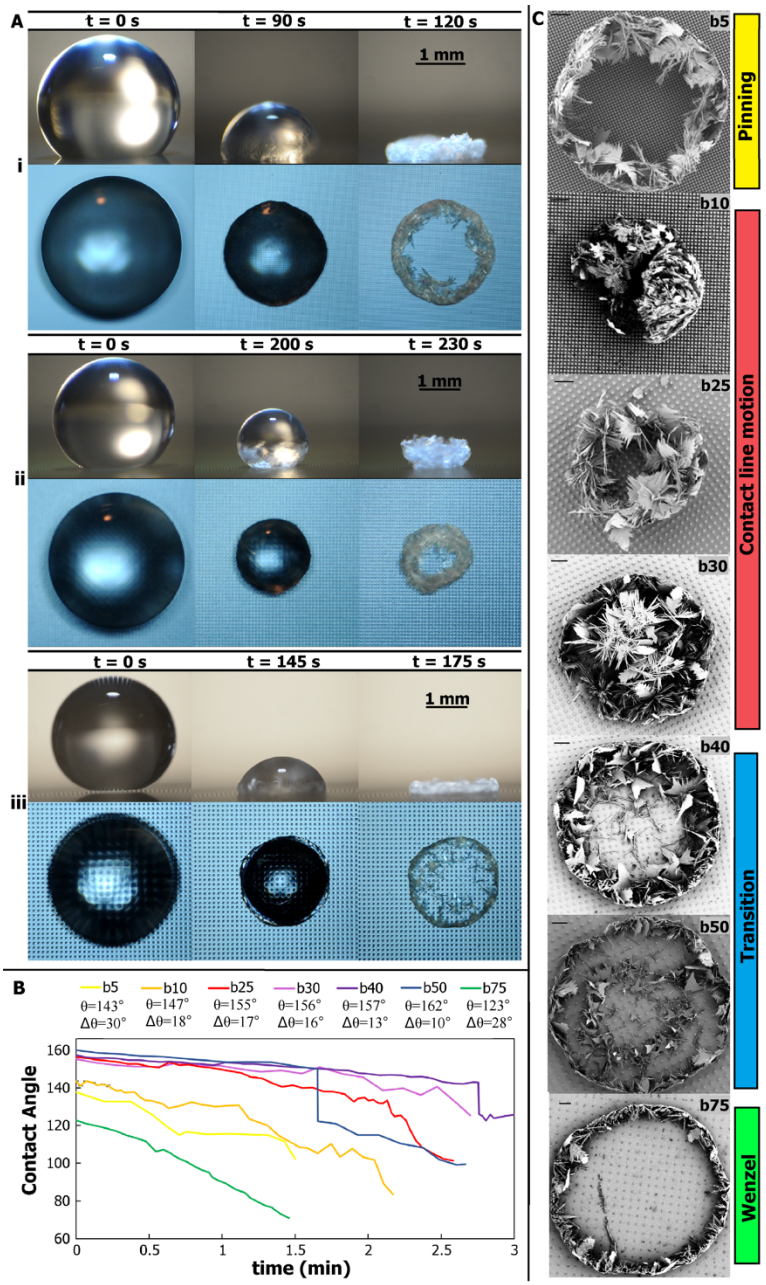

FIGURE 6.2. A) Representative examples of evaporative crystallization on superhydrophobic micropost surfaces with edge-to-edge post spacing of (i) 5, (ii) 25, and (iii) 50 µm. The images show the top and side views of drops at three different times instants: (left) experiment initiation, (middle) shortly after crystals at triple phase contact line have pinned the drop, and (right) end of evaporation. B) Contact angle as a function of time throughout evaporation (until crystal deposits obscure measurements) C) SEM images of crystalline deposits. Scale bars represent 100 µm.

As crystallization impacts the contact angle hysteresis, it also changes the evaporation dynamics and total evaporation time as a result. Figure 6.2B shows contact angle as a function of time, with measurements terminated at the point at which the crystal deposit became prominent enough that no contact angle could be accurately determined. Moving from b5 (yellow line) to b40 (pink line), we see an increase in initial contact angle with a corresponding increase in the evaporation time. This trend is due to high contact angle surfaces having a lowered rate of heat transfer from the heated surface to the drops.[31,32] However, the trend is disrupted by the Cassie to Wenzel transition. The transition on the b50 surface occurs much earlier than it does on the b40 surface because of reduced stability of the Cassie state on the b50 surface. The drop on the b50 surface evaporates

faster than the one on the b40 surface because it spends more time in the Wenzel state, which has a higher rate of heat transfer than the Cassie state.[32]

The dynamics of drop evaporation and formation of salt crystals are interdependent. For example, we see that evaporation time decreases due to the presence of the calcium sulfate in water. This result may seem at odds with the known decrease in saturation vapor pressure of evaporating saline water; but the saturation concentration of calcium sulfate in water is low enough such that neither the saturation vapor pressure nor the colligative properties of water are strongly altered by it's presence. The change in evaporation time here is instead caused by contact line pinning due to crystallization, forcing the drop into constant radius mode and thereby increasing surface area and evaporation rate.

The overall deposit shape is readily explainable by the contact angle, hysteresis, and presence/absence of the transition. However, the morphologies of crystals are also varied between the deposits, as seen in the SEM images of Figure 6.2C. Faster evaporation concentrates salt rapidly and increases supersaturation, which causes faster nucleation and smaller crystals. In contrast, crystals grown from slower processes at lower supersaturation levels will be larger and exhibit fewer defects.[33] This is qualitatively observed in Figure 6.2C, where deposits with slower evaporation times tend to have large, leaf-like crystals and fewer overall crystals; while deposits formed by faster evaporation tend to have a larger number of overall crystals, many of which are thin needles.

Cassie-Wenzel Transition

The transition from the Cassie to Wenzel state observed for drops on the b40 and b50 surfaces is expected, as the Cassie state is meta-stable for these surfaces.[34] To further probe the dynamics of this transition and the influence of crystallization, control experiments using DI water were conducted (Figure 6.3). For the DI water drops, evaporation of the 5 μL volume drops proceeds for 5.6 minutes on the b40 surface and for 6 minutes on the b50 surface prior to transition. This is contrasted by the evaporation of the 5 μL drops of saturated calcium sulfate solution, which transition to the Wenzel state after 2.7 minutes on the b40 and 1.6 minutes on the b50 surface. While one may expect this is due to a difference in surface tension caused by the presence of solute, the low solubility concentration of calcium sulfate does not result in significant deviations from the surface tension of DI water.[15,35] Instead, the enhancement in transition time is due to formation of crystals (which are hydrophilic) within the texture leading to drop impalement, as opposed to the typical Laplace pressure-driven transitions for DI water. This phenomenon is confirmed by the existence of the interior ring of the "double ring" structure of the b50 surface (see Figure 6.3), which provide clear evidence that crystals form on the texture at the Cassie contact line prior to impalement. The water will preferentially wet the hydrophilic crystals at the air/water interface, causing a decrease in Cassie angle and a consequent transition to the Wenzel state.

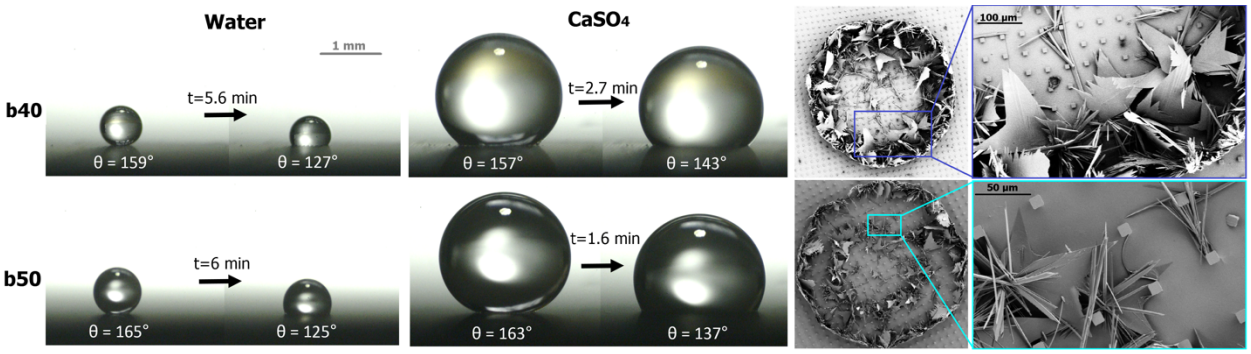

FIGURE 6.3. Comparing the b40 and b50 Cassie to Wenzel transitions for water to those for calcium sulfate solution. SEM images show crystal growth on posts.

To further confirm that the Cassie-Wenzel transition is driven by precipitation rather than by evaporation, additional experiments on the b50 surface were performed across a temperature range from 20 to 80°C. The ratio of the transition time (i.e., time at which the drop transitions from the Cassie to Wenzel state) to the total evaporation time remains relatively constant at all temperatures. This is true for both the water control, which had a ratio near 0.95 for all temperatures, and for the drops of calcium sulfate solution, which had a ratio between 0.66 and 0.77. However, the area localization of the resulting deposits from the calcium sulfate solution showed a temperature dependence despite observing transition at all temperatures. At room temperature, the deposit exhibits a ring-like morphology. Increasing the temperature increases the area localization, and the deposit formed at 50°C shows the double-ring structure observed at 60°C. Further increasing the temperature results in a condensed deposit, with needle-like crystals obscuring the interior of the deposit. For drops evaporating on heated hydrophobic substrates, contact angles increase by about 10% between ambient temperature and 75°C,[20] explaining the reduction of physical size and increase of area localization with increasing temperature.

TABLE 6.2. Ratio of the drop transition times to the total evaporation time, and the area localization for five microliter drops evaporating on the superhydrophobic b50 surface at different temperatures.

Temperature	**$t_{transition}/t_{evaporation}$**		**Area Localization**
	Water	**$CaSO_4$**	
20°C			1.53
40°C	0.96	0.77	1.26
50°C	0.97	0.72	2.28
60°C	0.93	0.66	2.15
70°C	0.95	0.72	2.14
80°C	0.97	0.66	2.84

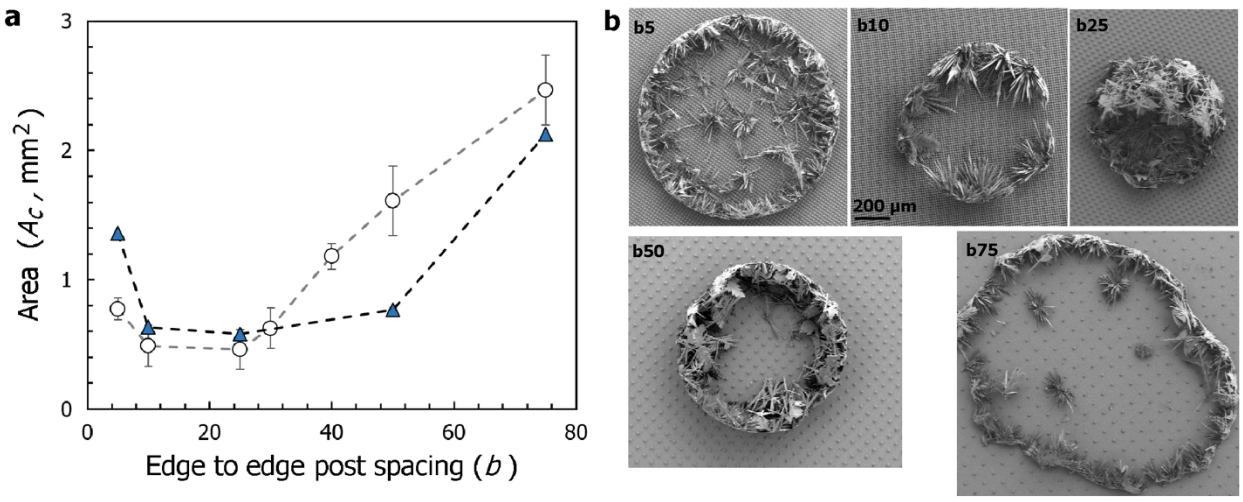

FIGURE 6.4. Room temperature vs. 60°C C for superhydrophobic surfaces (a) area of crystal deposit as a function of edge to edge post spacing, where filled triangles were conducted at ambient temperature, and empty circles are results from 60°C (b) SEM images of deposits formed at room temperature for b5, b10, b25, b40, and b75 surfaces. Scale is the same for all 5 images.

As a further test, room temperature experiments were conducted to confirm that the rapid evaporation and associated heat transfers played little role in the final deposit morphology. The results of these experiments are shown in Figure 6.4, which confirms that the four regimes reported in Figure 6.2 remain relevant across temperatures. The morphological differences between the deposits formed at room temperature and elevated temperature are predictable when comparing the SEM images formed at 60°C (Figure 6.2c) and those formed at 20°C (Figure 6.4b). Individual crystal sizes are generally larger at lower temperatures, as crystals that take longer to form tend to be better developed. The wetting regimes are not significantly changed between room temperature and elevated temperature. The drop on the b5 surface still evaporates in a pinned Cassie state and forms a ring-like deposits, the drops on the b10 and b25 surfaces evaporate in a gliding Cassie state and form more localized deposits, and the b75 drop begins and ends in a pinned Wenzel state. The primary difference is for the "transition regime" of b50 drops, in which room temperature drops do not demonstrate the double-ring morphology observed for the deposits formed at elevated temperatures, as shown in Figure 6.5.

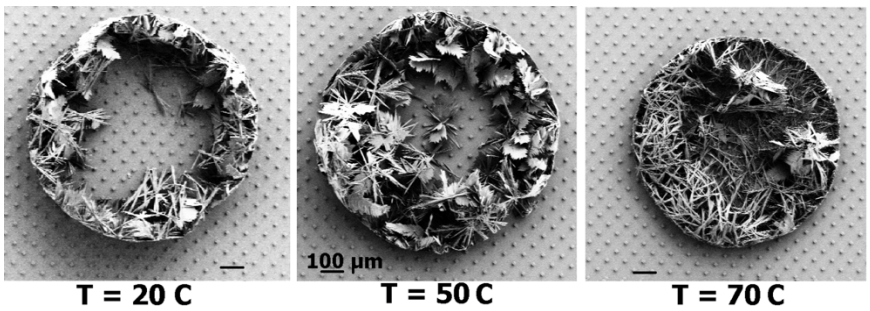

FIGURE 6.5. Deposits left on the b50 surface with different temperatures. Scale bars indicate 100 µm on all surfaces.

6.3 Lubricant Impregnated Surfaces

Despite the promise of superhydrophobic post surfaces in preventing formation of ring deposits, crystallization at the surface still causes contact line pinning. Therefore, additional experiments tested the performance of Liquid Impregnated Surfaces (LIS) with the same micropost morphology as the superhydrophobic surfaces to reduce contact line pinning (Figure 6.6). LIS are textured substrates impregnated with a liquid.[36–39] These surfaces can eliminate crystallization on the textures by reducing pinning of the drop to the surface. A system composed of a drop on top of a LIS can exist in 12 possible thermodynamic states dictated by the droplet, impregnating lubricant, and texture.[36] For stability, the lubricant-substrate contact angle must be less than the critical angle:

$$\theta_C = \cos^{-1}(1-\varphi)/(r-\varphi) \tag{6.7}$$

where φ is the solid fraction and r is the substrate roughness.[26] The state of the lubricant impregnated within the textures is dictated by the spreading coefficient:

$$S_{LS(W)} = \gamma_{SW} - \gamma_{LS} - \gamma_{LW} \tag{6.8}$$

where γ is interfacial energy between the phases of the lubricant (L) on the substrate (S) in the presence of the droplet (W). When $S_{LS(W)} > 0$, the lubricant completely spreads on the texture and creates a barrier between the drop and the surface. When $S_{LS(W)} < 0$, the tops of the texture remain emerged and dictate the pinning of the droplet.[36] Based on previous results that have shown crystal formation atop the textures on a non-spreading LIS ($S_{LS(W)} < 0$), here we focus on spreading LIS ($S_{LS(W)} > 0$).[18] In addition, a thin layer of the oil cloaks the droplet as the spreading coefficient of oil on the water droplet in the presence of air is positive ($S_{LW(A)} > 0$).

Figure 6.6A shows the progression of drop evaporation on liquid impregnated b5, b25, and b50 surfaces, respectively. Unlike the superhydrophobic surfaces, disparate regimes are not observed. Instead, drop evaporation occurs in near-constant contact angle mode throughout the entire period of evaporation on all surfaces with varying textures (Figure 6.6B). The drops on LIS continue to shrink in size even after the first signs of crystallization are observed, in contrast to the drops on superhydrophobic substrates that were pinned by emerging crystals. Evidence of this lack of pinning is clear from the b25 LIS progression (Figure 6.6A(ii)), where the drop has migrated towards the top of the field of view even while crystals begin to form. Lack of contact line pinning results in a complete absence of the ring-shaped structures observed on the hydrophilic and superhydrophobic surfaces.

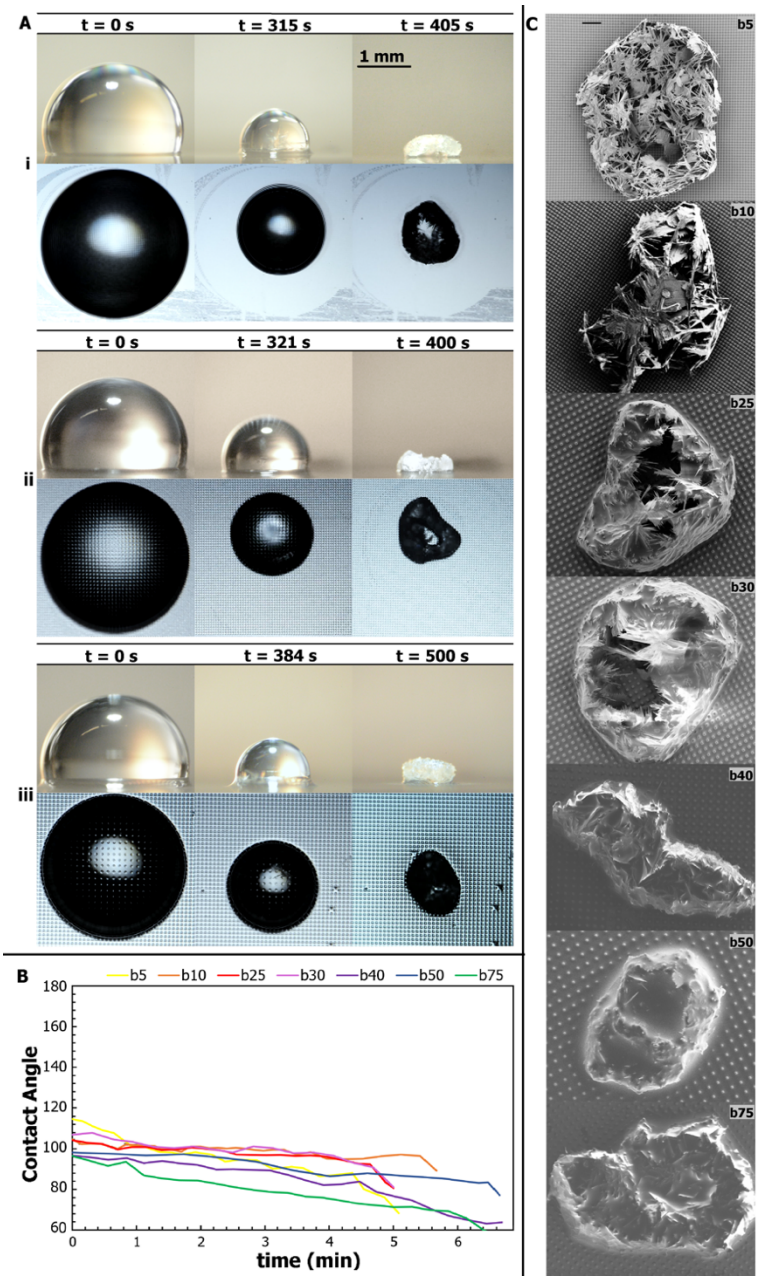

FIGURE 6.6. A) Progression of evaporative crystallization on liquid impregnated surfaces of (i) b5, (ii) b25, and (iii) b50. Top and side view images are shown for three time instants: (left) experiment onset (middle) shortly after crystals become apparent (right) end of evaporation. (B) Contact angle as a function of time for LIS surfaces, with measurements terminated after crystal deposits become too prominent for accurate measurement. (C) SEM images showing crystal deposits on the different LIS surfaces. Scale bar represents 100 μm and is the same for all images.

The lack of contact line pinning on LIS result in highly condensed deposits, which are composed of relatively large crystals (Figure 6.6C). It is observed that oil can wick into the crystal deposit; consistent with a previous investigation where oil from LIS wicked into frost deposits.[40] In the SEM images of Figure 6.6C, this creates an appearance of "smoothness", as the sharp crystal formations are covered by oil wicked into the scale deposit. The degree of oil migration into the crystals is dictated by the relative balance between capillary wicking of the crystal deposit and the underlying texture. Denser textures (b5, b10) retain oil more readily when compared to sparser textures. In addition to the lack of dependence of deposit morphology across textures, LIS also reduces variations in evaporation progression (Figure 6.6B).

6.4 Comparing Anti-fouling Strategies

The differences between evaporative deposition of crystals on the superhydrophobic surfaces and LIS are reflected in the overall deposit size (Figure 6.7A) and the area localization (Figure 6.7B) as a function of the substrate solid fraction. For the superhydrophobic surfaces, the deposit area has a clear trend with the texture dependent on the wetting state, while the deposit area is independent of texture on LIS. The deposits on the superhydrophobic surfaces in the "Cassie-gliding" regime have similar contact area to the deposits on LIS; however, the area localization is significantly lower on the liquid impregnated surfaces due to constant contact angle evaporation (A_c/A_o = 0.68 for superhydrophobic, 0.2 for LIS, Figure 6B).

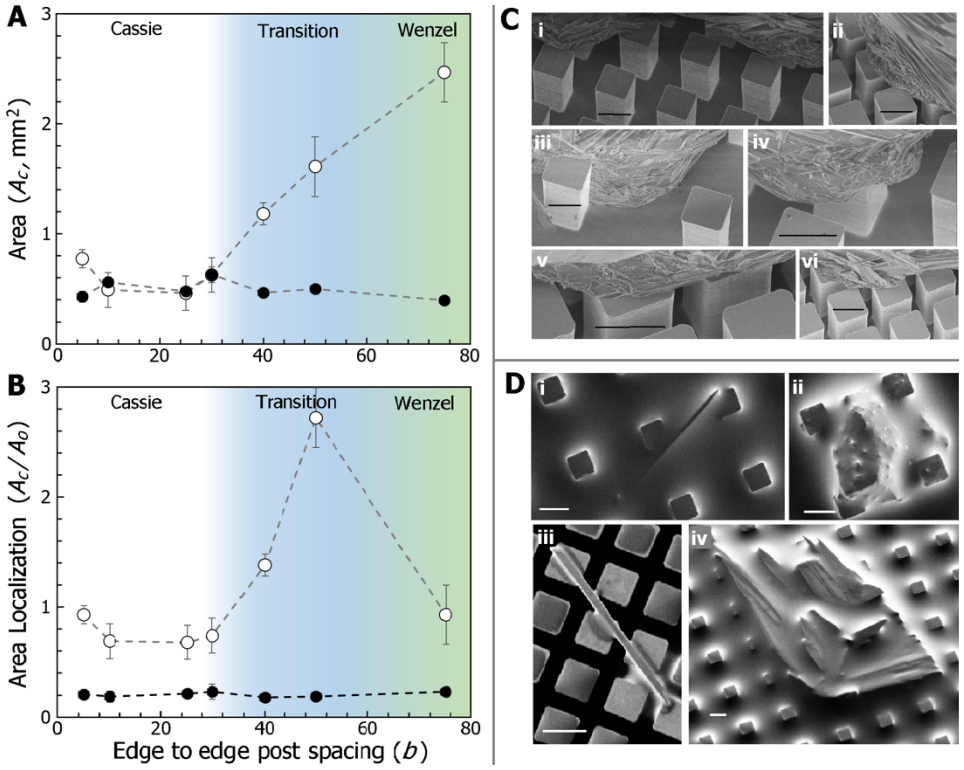

FIGURE 6.7. Comparison of evaporation behavior on the (○) superhydrophobic and (●) liquid impregnated surfaces as functions of substrate pitch. (A) The total area of deposits. (B) Area Localization, the ratio of the area of the final crystal deposit to the initial footprint of the drop. (C) Points of pinning on Cassie superhydrophobic post surfaces with many small crystals. (i) crystals formed on b10 posts (ii) crystals covering b5 posts (iii) crystals have engulfed a b50 post (iv) pinning crystals that have engulfed the top of a b10 post (v) close up of crystals on b5 posts. Scale bars represent 10 μm. (D) Crystals left over after removing deposits from LIS surfaces. (i) needle-like crystal that has fallen into the oil between posts on a b25 surface. (ii) chunk of crystal stuck between posts on b25. (iii) needle crystal deposited on top of b5 LIS posts (iii) large leaf-like crystal deposited on top of b25 posts. Scale bars represent 10 μm.

Figure 6.7C shows a variety of examples of pinning points across different superhydrophobic post surfaces. These pinning points comprise of many small crystals, suggesting a large amount of crystal nucleation in these areas. Crystal nucleation occurs readily in the presence of surfaces containing imperfections that can serve as nucleation sites or that can lower the energy barrier for nucleation.[41] Hydrophobic coatings increase the energy barrier for nucleation at the surface, yet it is clear that crystals are still able to find nucleation sites on the posts. This is contrasted by the deposits left behind on the LIS surfaces (Figure 6.7D), where only large crystals that are not pinned to the posts are observed. Because of the lubricating layer, these large crystals were highly mobile and easily removed by rinsing with saturated calcium sulfate solution.

Conclusions

I investigated the role of contact line pinning on deposit morphology from evaporating saline drops using superhydrophobic and liquid impregnated micropost surfaces with varying solid fraction, and show that the formation of ring-shaped crystalline deposits on superhydrophobic surfaces can be disrupted by tuning the solid fraction to ensure evaporation occurs in the "cassie-gliding" regime. This ideal regime contains surfaces with solid fractions that minimize contact angle hysteresis while also remaining stable to Cassie-Wenzel transitions. Unlike superhydrophobic surfaces, experiments on spreading liquid impregnated surfaces were invariable to the solid fraction due to the presence of an oil layer preventing both nucleation and pinning of crystals at the surface. Hence, LIS can serve as an efficient anti-fouling surface to prevent seaspray deposition and resulting corrosion. These results also introduce new strategies for controlling crystalline deposits and for disrupting the coffee-ring effect, which has proven to be more difficult for crystals than for colloids. The delayed onset of crystallization on LIS may also allow for new approaches of growing large, well-defined crystals as well as for concentrating dilute solutions of valuable materials such as difficult-to-synthesize pharmaceuticals.

References

1. Sastri, V. S. in *Challenges in Corrosion* 95–126 (John Wiley & Sons, Inc, 2015). doi:10.1002/9781119069638.ch2
2. Amani, M. & Hjeij, D. A Comprehensive Review of Corrosion and its Inhibition in the Oil and Gas Industry. in *Society of Petroleum Engineers* 1–14 (2015).
3. Doehne, E. in *Natural Stone, Weathering Phenomena, Conservation Strategies and Case Studies.* (ed. Siegard, S; Weiss, T.; Vollbrecht, A.) 51–64 (2001).
4. Scherer, G. W., Flatt, R. & Wheeler, G. Materials Science Research for the Conservation of Sculpture and Monuments. *MRS Bull.* **26,** 44–50 (2001).
5. Scherer, G. W. Crystallization in pores. *Cem. Concr. Res.* **29,** 1347–1358 (1999).
6. Desarnaud, J., Bonn, D. & Shahidzadeh, N. The Pressure induced by salt crystallization in confinement. *Sci. Rep.* **6,** 30856 (2016).
7. Doehne, E. & Price, C. A. *Stone Conservation: An Overview of Current Research*. (Getty Publications, 2010).
8. Shahidzadeh-Bonn, N., Rafai, S., Bonn, D. & Wegdam, G. Salt Crystallization during Evaporation: Impact of Interfacial Properties. *Langmuir* **24,** 8599–8605 (2008).
9. Li, F.-I., Thaler, S. M., Leo, P. H. & Barnard, J. a. Periodic Pattern Formation in Evaporating Drops. *J. Phys. Chem. B* **110,** 25838–25843 (2006).
10. Accardo, A. *et al.* Calcium Carbonate Mineralization: X-ray Microdiffraction Probing of the Interface of an Evaporating Drop on a Superhydrophobic Surface. *Langmuir* **27,** 8216–8222 (2011).
11. Diao, Y., Myerson, A. S., Hatton, T. A. & Trout, B. L. Surface Design for Controlled Crystallization: The Role of Surface Chemistry and Nanoscale Pores in Heterogeneous Nucleation. *Langmuir* **27,** 5324–5334 (2011).
12. Kaya, D., Belyi, V. A. & Muthukumar, M. Pattern formation in drying droplets of polyelectrolyte and salt. *J. Chem. Phys.* **133,** 1–10 (2010).
13. Soulié, V. *et al.* The evaporation behavior of sessile droplets from aqueous saline solutions. *Phys. Chem. Chem. Phys.* **17,** 22296–22303 (2015).
14. Accardo, A. *et al.* Fast, active droplet interaction: coalescence and reactive mixing controlled by electrowetting on a superhydrophobic surface. *Lab Chip* **13,** 332–335 (2013).
15. Shahidzadeh, N., Schut, M. F. L., Desarnaud, J., Prat, M. & Bonn, D. Salt stains from evaporating droplets. *Sci. Rep.* **5,** 10335 (2015).
16. Eral, H. B., 't Mannetje, D. J. C. M. & Oh, J. M. Contact angle hysteresis: a review of fundamentals and applications. *Colloid Polym. Sci.* **291,** 247–260 (2013).
17. Zhang, J., Borg, M. K., Sefiane, K. & Reese, J. M. Wetting and evaporation of salt-water nanodroplets: A molecular dynamics investigation. *Phys. Rev. E - Stat. Nonlinear, Soft Matter Phys.* **92,** 1–11 (2015).
18. Subramanyam, S. B., Azimi, G. & Varanasi, K. K. Designing Lubricant-Impregnated Textured Surfaces to Resist Scale Formation. *Adv. Mater. Interfaces* **1,** 1300068 (2014).
19. Sobac, B. & Brutin, D. Chapter 8. Pure Diffusion. *Droplet Wetting and Evaporation* 101–114 (2015). doi:10.1016/B978-0-12-800722-8.00008-4
20. Carle, F. & Brutin, D. Chapter 9. Convection. *Droplet Wetting and Evaporation* 115–128 (2015). doi:10.1016/B978-0-12-800722-8.00009-6
21. Hays, R. C. Thermal Transport to Sessile Water Droplets on Heated Superhydrophobic Surfaces of Varying Cavity Fraction. (Brigham Young University, 2013).
22. Hua Hu & Larson, R. G. Marangoni Effect Reverses Coffee-Ring Depositions. *J. Phys. Chem. B Lett.* **110,** 7090–7094 (2006).

23. Marín, Á. G., Gelderblom, H., Lohse, D. & Snoeijer, J. H. Order-to-Disorder Transition in Ring-Shaped Colloidal Stains. *Phys. Rev. Lett.* **107,** 85502 (2011).
24. Subramanyam, S. B., Rykaczewski, K. & Varanasi, K. K. Ice adhesion on lubricant-impregnated textured surfaces. *Langmuir* **29,** 13414–13418 (2013).
25. Dorrer, C. & Rühe, J. Wetting of Silicon Nanograss: From Superhydrophilic to Superhydrophobic Surfaces. *Adv. Mater.* **20,** 159–163 (2008).
26. Seiwert, J., Clanet, C. & Quere, D. Coating of a textured solid. *J. Fluid Mech.* **669,** 55–63 (2011).
27. Cassie, A. B. D. & Baxter, S. Wettability of porous surfaces. *Trans. Faraday Soc.* **40,** 546 (1944).
28. Lafuma, A. & Quéré, D. Superhydrophobic states. *Nat. Mater.* **2,** 457–460 (2003).
29. Wenzel, R. N. RESISTANCE OF SOLID SURFACES TO WETTING BY WATER. *Ind. Eng. Chem.* **28,** 988–994 (1936).
30. Dicuangco, M., Dash, S., Weibel, J. A. & Garimella, S. V. Effect of superhydrophobic surface morphology on evaporative deposition patterns. *Appl. Phys. Lett.* **104,** 18–23 (2014).
31. Chen, X. *et al.* Evaporation of Droplets on Superhydrophobic Surfaces: Surface Roughness and Small Droplet Size Effects. *Phys. Rev. Lett.* **109,** 116101(1-6) (2012).
32. Dash, S. & Garimella, S. V. Droplet Evaporation on Heated Hydrophobic and Superhydrophobic Surfaces Droplet evaporation on heated hydrophobic and superhydrophobic surfaces. *Phys. Rev. E* **8910,** (2014).
33. Mullin, J. W. *Crystallization, 4th Edition*. (2001).
34. Patankar, N. A. On the Modeling of Hydrophobic Contact Angles on Rough Surfaces. *Langmuir* **19,** 1249–1253 (2003).
35. Ferron, G. A. & Soderholm, S. C. Estimation of the times for evaporation of pure water droplets and for stabilization of salt solution particles. *J. Aerosol Sci.* **21,** 415–429 (1990).
36. Smith, J. D. *et al.* Droplet mobility on lubricant-impregnated surfaces. *Soft Matter* **9,** 1772–1780 (2013).
37. Quéré, D. Non-sticking drops. *Reports Prog. Phys.* **68,** 2495–2532 (2005).
38. Wong, T.-S. *et al.* Bioinspired self-repairing slippery surfaces with pressure-stable omniphobicity. *Nature* **477,** 443–7 (2011).
39. Schellenberger, F. *et al.* Direct observation of drops on slippery lubricant-infused surfaces. *Soft Matter* **11,** 7617–7626 (2015).
40. Rykaczewski, K., Anand, S., Subramanyam, S. B. & Varanasi, K. K. Mechanism of frost formation on lubricant-impregnated surfaces. *Langmuir* **29,** 5230–5238 (2013).
41. Russell, K. C. Nucleation in solids: The induction and steady state effects. *Adv. Colloid Interface Sci.* **13,** 215–318 (1980).

Chapter 7.

Spirals from Evaporating Drops

The previous two chapters demonstrated that evaporative crystallization of calcium sulfate will form three-dimensional structures on hydrophobic surfaces, and flat, two-dimensional patterns on hydrophilic substrates.[1] Here, I explore what happens when a drop of calcium sulfate is evaporated on a substrate that exhibits both hydrophobic and hydrophilic nature. Such substrates have an extreme contact angle hysteresis (θ_A ~80-110°, θ_R ~5-40°, $\Delta\theta$ >45° ; where θ_A is the substrate advancing angle, θ_R is the substrate receding angle, and $\Delta\theta$ is the contact angle hysteresis: $\Delta\theta = \theta_A - \theta_R$).

The large contact angle hysteresis of these substrates enables a dual behavior with both two-dimensional and three-dimensional crystalline structures arising. First, a three-dimensional crystalline ring at the drop contact line emerges due to the initially hydrophobic contact angle. This outer ring is similar to those observed in the Cassie-pinning regime of the superhydrophobic experiments from chapter 6. However, this outer ring encourages pinning, so that evaporation proceeds in constant contact radius mode. At the final stages of evaporation, a thin film pinned by the large outer ring ruptures from the center of the drop. Crystallization from this thin film follows contact line motion, leaving a two-dimensional pattern at the deposit center. Further investigation into the remarkable ability of thin, crystallizing films to generate patterns which record contact line motion is the subject of the following chapter, chapter 8.

7.1 Evaporative Deposition on Extreme Hysteresis

Contact angle hysteresis is the difference between a substrate's advancing and receding angles; also called the dynamic contact angles. The behavior of an evaporating drop is characterized by the dynamic contact angles; and particularly by the receding contact angle (i.e., the angle at which drop contact line begins to move inward).[2,3]

As in previous chapters, these experiments were performed by evaporating 5 μL water drops containing calcium sulfate salt dissolved to its solubility concentration on heated (Between 45°C and 95°C) rare earth oxide substrates with high contact angle hysteresis ($\Delta\theta > 45°$). Preparation and characterization methods for extreme hysteresis surfaces have been reported in previous investigations.[4] In short, surfaces were prepared by sputtering ceria or erbia rare earth oxide chemistries onto silicon wafers to depths ranging between 300-400 nm. Because sputtered coatings often result in non-equilibrium films and are heavily dependent on the process parameters, these surfaces were relaxed under vacuum for periods of months to years to reach optimal surface stiochiometry.[5] The sputter depth gives rise to the different substrate colors observed throughout the figures, and contributes to altered contact angles.

The origin of the large contact angle hysteresis of these rare earth oxide surfaces is not fully understood, but likely originates from a combination of chemical inhomogeneity and nanoscale roughness which contributes to both large advancing angles and to low receding contact angles. Surface advancing, equilibrium, and receding contact angles were recorded prior to experiments using a goniometer and 5 μl drops of DI water.

Because of the low receding contact angle, drops remain pinned to the substrate throughout evaporation and maintain a constant contact radius. As evaporation proceeds, gypsum crystals form in a three-dimensional ring at the contact line; an expected and previously observed result (Figure 7.1).[1,6] However, as the drop gets close to complete evaporation the geometry deviates strongly from a spherical cap,[7] and a thin film pinned by the exterior crystal ring develops. This film ruptures at the center of the drop and propagates radially outward towards the ring of crystals in a mode that falls into neither of the classic modes of drop evaporation (constant contact angle, and constant contact radius).[8] The ruptured film is pinned by salt crystals that form at the newly formed contact line near the drop center, leaving behind a record of the contact line movement. This results in individual gypsum needles that align into a spiral, as shown in Figure 7.1.

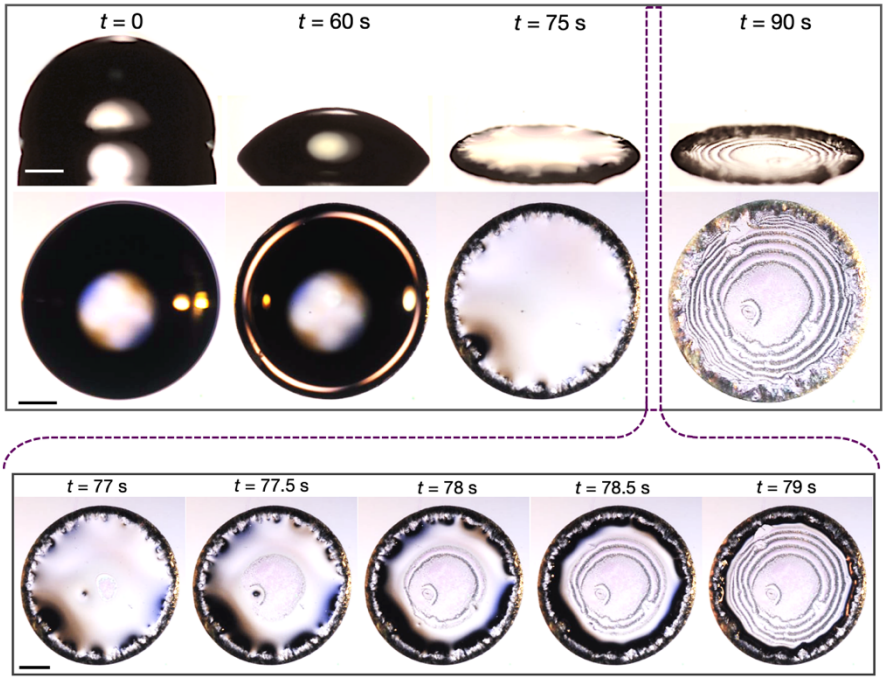

FIGURE 7.1. Evaporation of a drop on a high advancing, low receding contact angle substrate ($\theta_A = 98°$, $\theta_R = 18°$, $T = 70°C$). First row shows a side view, second shows a top-down view of drop evaporation. Final row shows top-down view of the thin film rupture and contact line motion that leads to pattern formation on the drop interior. Scale bar is 0.5 mm.

Nanoparticles

In contrast to the crystalline case, spiral patterning does not occur for a drop containing latex nanoparticles under the same experimental conditions, suggesting that this patterning is unique to crystallizing solutes.[9–11] Experiments using a 0.1% latex nanosphere suspension in water were conducted on a substrate with $\theta_A = 98°$, $\theta_R = 18°$ at 70ºC (Figure 7.2). The evaporation proceeds similarly to the experiments using dissolved calcium sulfate solution. A thin ring of particles deposit at the outer contact ring, which then pins the contact line. The drop evaporates into a thin film which eventually ruptures. The rupturing film entrains the particles, dragging them with the fluid instead of depositing on the substrate. Unlike the crystallizing solution, this film ruptures somewhat randomly and does not retract towards the outer ring. This is because the particles do not form the three-dimensional outer ring. Thus, the spiral and concentric ring patterns are unique to the crystallizing solution in this system.

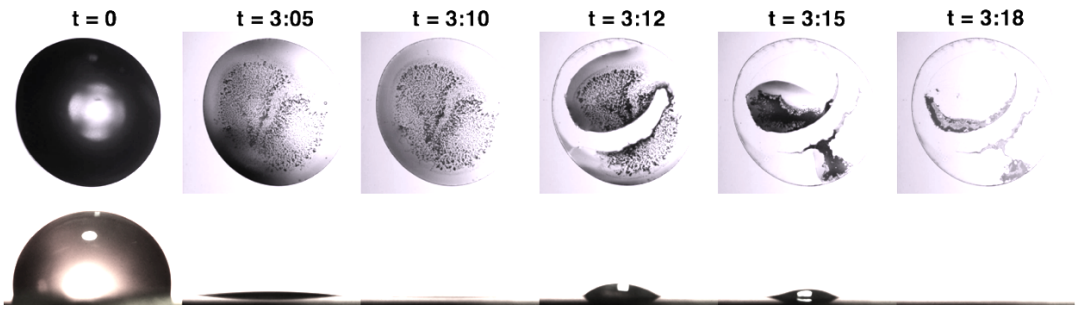

FIGURE 7.2. Time series showing evaporation of a drop containing 0.1% latex nanospheres. Width of each image is 3mm.

Modeling

There are a number of time scales occurring throughout the patterning process shown in Figure 7.1 The first is the overall time between deposition of the 5 μL drop and complete evaporation (t_1). The second is the "rupture" time, t_2, defined here as the time between the rupture of the interface and complete desiccation. A third timescale, t_3, is the time between drop rupture and the first instance of contact line pinning. This timescale shows a strong dependence on the surface and less dependence on the substrate temperature due to its inertial origins. The fourth experimental timescale shown here is the pinning timescale, t_4 defined as the time starting at the point a given section of the contact line pins and ending when that same segment of the contact line depins from the formed crystalline needles. A depiction of these timescales are shown in Figure 7.3.

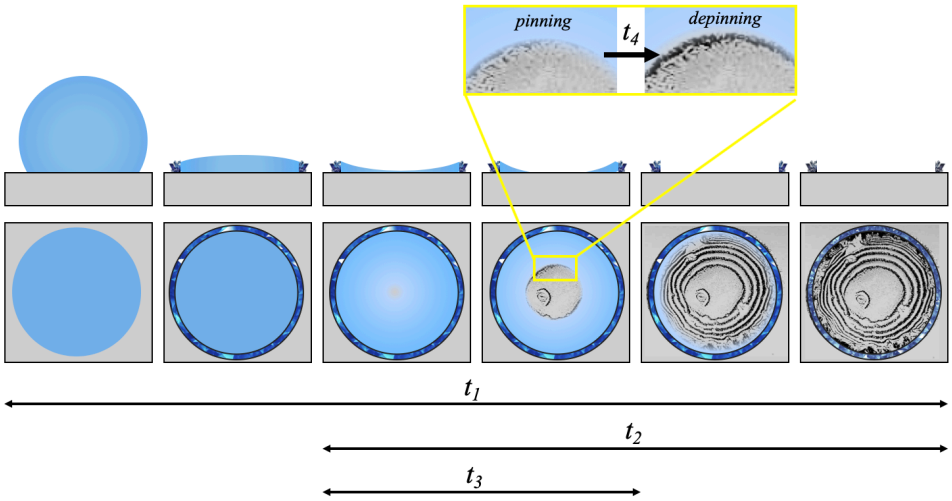

FIGURE 7.3. Defining experimental timescales, where t_1 is the global evaporation time from start to finish, t_2 is the time between rupture and complete evaporation, t_3 is the time between rupture and pinning of the newly formed contact line, and t_4 is the timescale at which a given segment of a pattern remains pinned.

The observation of spirals from drops is unusual. However, this phenomenon is not entirely unique to the high hysteresis surfaces used in the present study. Previous investigations have observed equi-distant spiral deposition of fullerene crystals on hydrophilic substrates when used in conjunction with a glass bead placed at the center of the drop.[12–14] In these studies, the moving interface retracted from the outside of the drop inwards towards the glass bead, leaving behind Archimedean spirals (in which the spirals become more tightly wound as the interface approaches the glass bead. Different spiral windings are found as a function of concentration[12,14] and temperature.[13] Comparing details of that investigation to the present reveals that both involve crystallization at a contact line moving towards a three-dimensional structure; suggesting that the unusual geometry of our system with the three-dimensional outer crystalline ring allows for formation of the two-dimensional crystalline patterns on the interior.

The unusual geometry of the system during the final stages of evaporations leads to contact line motion that leaves a record in the form of crystals, as shown in the bottom row of Figure 7.1. To quantify this effect, a model of the system geometry during the final phases of evaporation (i.e., during timescale t_2) is developed. This model is shown in Figure 7.4a (side-view) and Figure 7.4b (top-down). Figure 7.4c shows SEM images of crystalline needles from the interior of the drop, providing a relevant length scale for patterning.

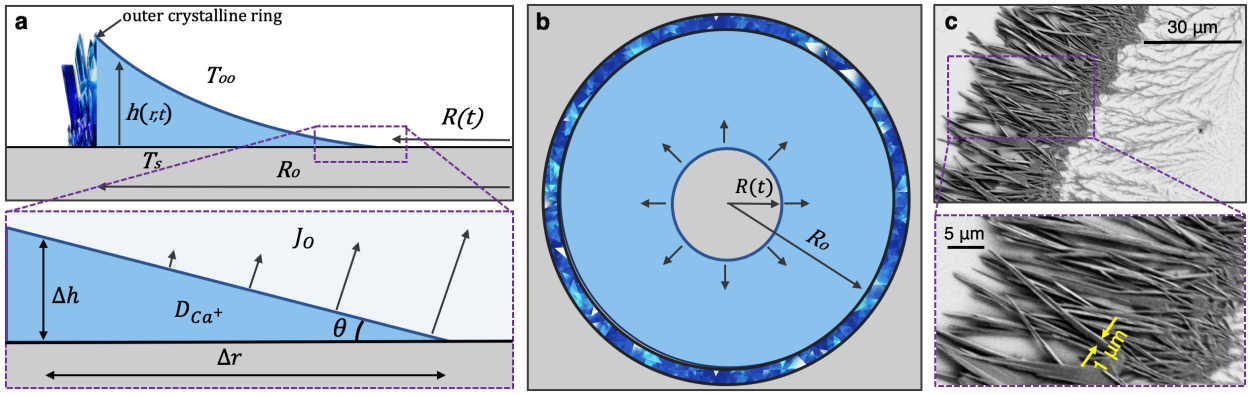

FIGURE 7.4. (a) Schematic of the geometry of the drop during the thin-film evaporation phase, where *R(t)* is the position of the moving contact line, R_o is the radius between the center of the drop and the outer crystal ring, *h(r,t)* is the height profile of the liquid, and J_o is the evaporative flux. At the moving contact line $R(t)$, the evaporative flux is at a maximum and the height profile can be approximated as a triangular wedge. (b) Schematic showing drop geometry from a top view. (c) SEM showing size of the crystalline needles, where the width of the needles serves as an estimate for the film thickness in the region of the moving contact line.

The time required for complete evaporation after initial rupture is different from the timescales usually associated with drop evaporation. It also deviates from timescales associated with inertially-driven rupture (t_3).[15] The evaporation timescale between rupture and complete dessication (t_2 in Figure 7.3) for the present experiments can be modelled starting with a mass balance across the liquid vapor interface:

$$\frac{dV}{dt} = \int_{R(t)}^{R_o} \frac{\partial h}{\partial t} 2\pi r \, dr = -2\pi\big(R_o - R(t)\big)J_o \tag{7.1}$$

$$J_o = \frac{D(C_{LV} - C_\infty)}{\rho_L}$$

Where J_o is the evaporative flux, D is the diffusion of water vapor in air, C_{LV} is the saturation concentration of water vapor at the heated air/water interface, and C_∞ is the equilibrium concentration of water vapor in the bulk.

The height profile of the drop (shown in the top panel of Figure 7.4a) during rupture is subject to three boundary conditions: (1) The height is equal to the height of the crystal ring at the outer radius ($h(r = R_o) = h_c$), (2) the height is zero at the receding contact line ($h(r = R(t)) = 0$), and (3) the curvature of the profile at the contact line is given by $dh/dr(r = R(t)) = \tan\theta_R$. A quadratic self-similar profile is assumed for the depth based on previous experimental[8] and theoretical[15] investigations as well as observations of the present system. Solving a quadratic equation for the given boundary conditions, an estimate for the depth profile is:

$$h(r) = \left[\frac{h_c - \big(R_o - R(t)\big)\tan\theta_R}{\big(R_o - R(t)\big)^2}\right]\big(r - R(t)\big)^2 + \tan\theta_R\big(r - R(t)\big) \tag{7.2}$$

Neglecting all terms containing the factor $\tan\theta_R$ due to the very low receding angle then allows for simplification of the height profile as:

$$h(r) = \frac{h_c\big(r - R(t)\big)^2}{\big(R_{max} - R(t)\big)^2} \tag{7.3}$$

Plugging equation 7.3 into the mass balance of equation 7.1 and solving gives a differential equation of the form:

$$\left[\frac{1}{12}(-R_o^4 + R(t)^4) + \frac{1}{6}(-R_o R(t)^3 + R_o^3 R(t))\right]\frac{dR}{dt} = \big(R_o - R(t)\big)^4 \frac{j_o}{2h_c} \tag{7.4}$$

Which can be simplified and rearranged as:

$$\left[\frac{R_o + R(t)}{R_o - R(t)}\right]\frac{dR}{dt} = -\frac{6J_o}{h_c} \tag{7.5}$$

This differential equation is then solved to find an expression for the retracting inner radius as a function of time:

$$R(t) = R_o\left(1 + 2W\left(\frac{-1}{2R_o}\exp\left(\frac{-3j_o}{h_c R_o}t - \frac{1}{2}\right)\right)\right) \quad 7.6$$

Where W is the product log function, sometimes called the Lambert W-function. This somewhat complicated expression for the retracting front with time allows for the extraction of a simple timescale describing thin-film rupture and evaporation (i.e., timescale t_2)

$$t_{model} = \frac{1}{3\pi}\frac{h_c R_{max}}{j_o} \quad 7.7$$

Plotting this evaporation timescale against experimental data yields Figure 7.5. The model of equation 7.7 successfully predicts the timescale for most of the data, but breaks down at the lowest temperature of 45 ºC; likely due to a decreased dependence of the phenomena on heat transfer.

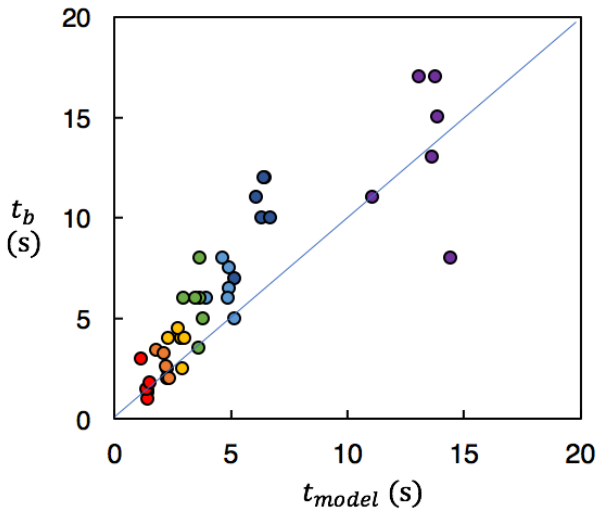

FIGURE 7.5 Experimental timescale of drop rupture plotted against predicted values from equation 7.7. Colored circles correspond to different temperatures (red = 85 ºC, orange = 75 ºC, yellow = 70 ºC, green = 65 ºC, light blue = 60 ºC, dark blue = 55 ºC, purple = 45 ºC). Line indicates a 1:1 ratio of experimental data to predicted values.

Spirals vs. Concentric Rings

An experimental matrix containing six substrates and eight substrate temperatures was used to study the patterning phenomenon in further detail (Figure 7.6). The substrates used were all sputter-coated with rare earth oxide chemistries and exhibit a high contact angle hysteresis. However, the exact values of the dynamic contact angles and hysteresis are varied, as indicated on the leftmost side of Figure 7.6. From these experiments, it is possible to make a few observations on the role of evaporation and of contact angle hysteresis. At low temperatures (below ~60ºC), evaporation is slow, and salt crystallizes at the contact line, forming a ring shape with a radius identical to that of the initially deposited drop. Increasing substrate temperature past 85ºC causes evaporation to occur rapidly, resulting in disordered, amorphous crystalline deposits that fill the center of the ring. Patterning of spirals or concentric rings only occurs at intermediate temperatures when some amount of the salt precipitates in the center to form regular patterns that mirror the movement of the contact line. In general, the substrates with lower receding contact angles (θ_R) tend to result in tighter winding of the spirals or rings. Spirals also seem to be more likely to form on these substrates.

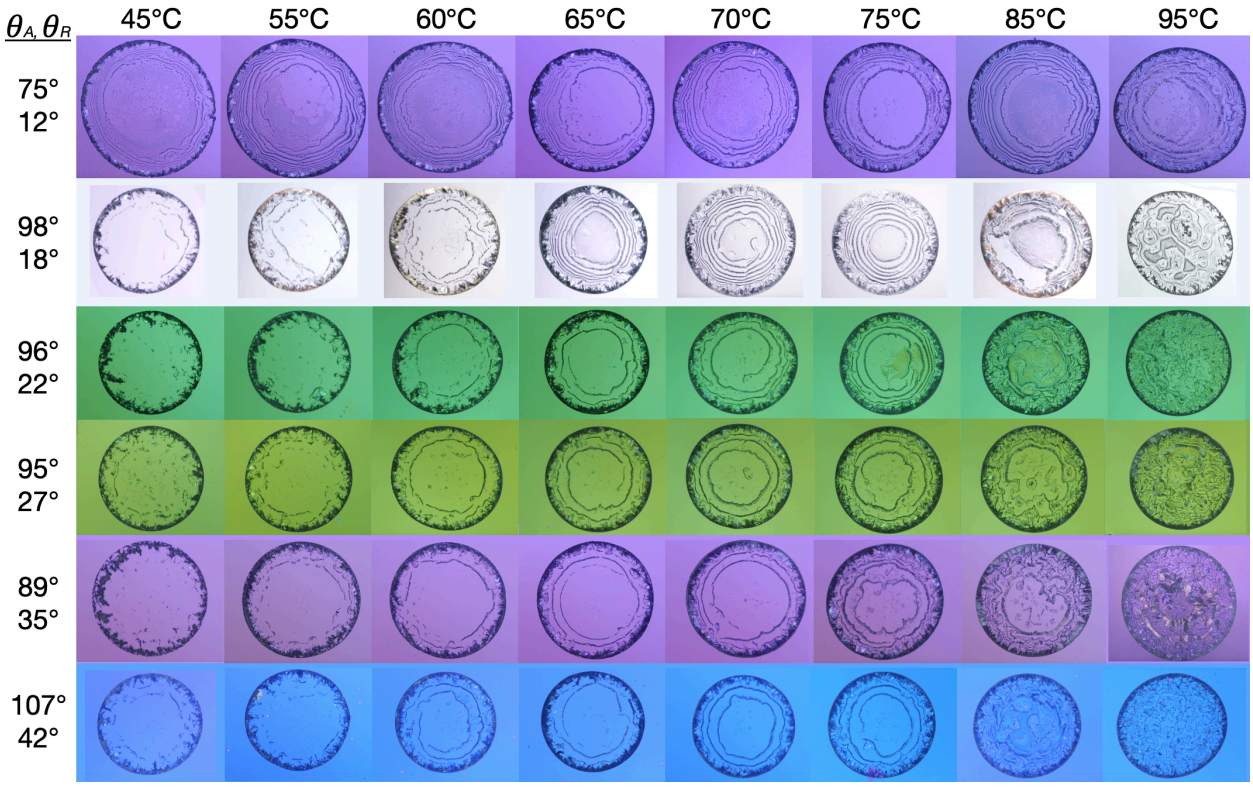

FIGURE 7.6. A selection of patterns formed on different substrates and temperatures. Different substrate colors are due to thickness and chemistry of the sputtered surface coating. Length scale is the same for all images, and is 2.8mm wide.

Both spiral and concentric ring patterns emerge from these experiments depending on the uniformity of the pinning of the contact line. Concentric rings form when the contact line pins and depins uniformly, and spirals emerge when the contact line pins non-uniformly in the azimuthal direction (i.e., when one side pins faster than the others), as shown in Figure 7.7. The formation of concentric rings has been well-quantified for colloidal deposits, and is due to "stick-slip" phenomena where an energy barrier periodically prevents contact line movement.[16–18] The volume loss for an evaporating drop with a pinned contact line manifests as a steady decrease in contact angle. When this contact angle reaches the receding angle for the substrate (this angle will be significantly lowered from that of pure water due to crystallization at the contact line), the drop will "slip" in a sudden decrease in contact radius, and then continue to evaporate in constant contact radius mode at the new radius. Spiral patterns form from a similar behavior, except that the pinning/depinning is not global across the contact line. Instead, one portion of the contact line is constantly depinning while another portion pins at a different location so that the radius increases smoothly with time.

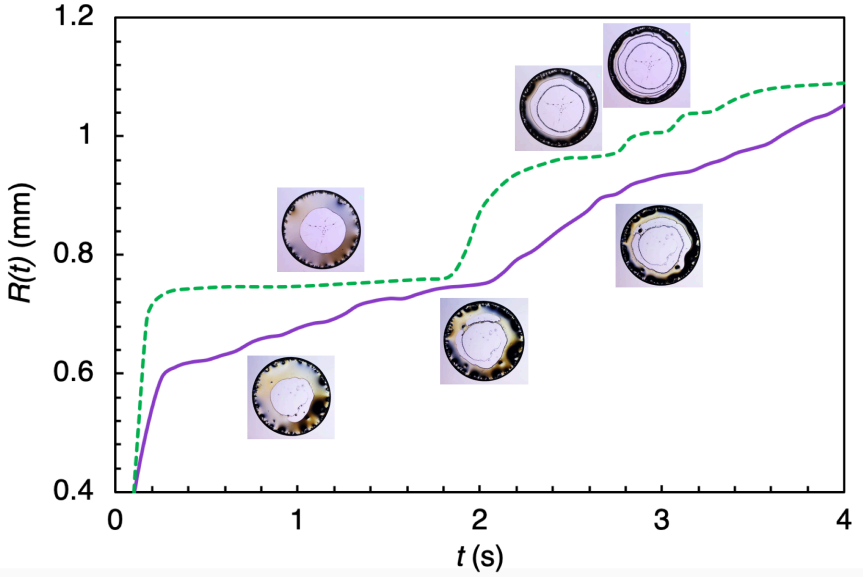

FIGURE 7.7. The position of the moving contact line with time after rupture (where $R(t) = 0$ indicates the drop center) for a concentric ring (green dashed line) and for a spiral (purple continuous line). The concentric ring demonstrates a terraced dependence where the contact line sticks at the position of the ring over a period of time, while the spiral contact line demonstrates a smoother dependence.

To quantify the observation that spirals are more likely to emerge at lower contact angles, the number of pattern-forming samples resulting in spirals was tabulated. Table 7.1 gives the percent of pattern-forming (i.e., forming either concentric rings or spirals) samples that resulted in spiral patterns, confirming that spirals are more likely to form on substrates with lower receding contact angles. Lowered substrate receding angles may be more likely to give rise to spiral shapes due to

faster pinning and an associated increased likelihood of the contact line pinning in a non-uniform manner. Data for Table 7.1 comes from experiments shown in Figure 7.6 and from additional experiments not presented.

TABLE 7.1. Percent of pattern-forming samples that form spirals

Surface	**Color**	$\boldsymbol{\theta_R}$	**#Samples**	**%Spiral**
Ceria12	Purple	12°	9	77%
Ceria18	light purple	18°	20	55%
Ceria22	Green	22°	11	64%
Erbia27	Green	27°	13	38%
Ceria35	Purple/Pink	35°	14	43%
Ceria42	Blue	42°	15	23%

7.2 Fermat's Spiral

When spirals do emerge in these experiments, the emergent patterns are well-described by Fermat's spiral equation. Fermat's spiral is a subclass of Archimedean spirals with a dependence of radius *r* on the square root of the polar angle $\emptyset$:

$$r = a\sqrt{\emptyset} \tag{7.8}$$

where a is a proportionality constant).[19] Fermat's spiral has the special property of having zero curvature at the origin and a decreasing distance between subsequent arcs.

Spirals have long captivated the human imagination and are a recurrent theme in art ranging from prehistoric to modern. Indeed, spirals are one of the most common geometric motifs of the ancient world and appear as art and petroglyphs in Neolithic Great Britain,[20] America,[21] and east Asia.[22] Nature too, is apparently obsessed with spirals as they appear in hundreds of naturally occurring phenomena:[23] the arrangement of flower seeds and petals, galaxies, seashells, pinecones, the alpha-helix of DNA, hurricanes, the cochlea of the inner ear, and more.[23] Determining an exact reason, or a unifying underlying mechanism, for why spirals appear so often throughout nature has eluded scientists for decades.[23,24]

We do know, however, that the prevalence of spirals in biology is almost certainly due to the principle of parsimony – which states that nature develops in the simplest and most efficient path. Sunflower seeds arrange in a spiral for close and efficient packing, and seashells twist into logarithmic spirals because they allow for a constant shape with a constant areal increase to make room for the growing mollusk.[24] This principle can (and should) also be applied to engineering.

For example, a recent investigation found that arrangement of solar energy heliostats into Fermat's spiral drastically outperformed traditional staggered arrangements.[25] Another found that winding of mesh into dual Fermat's spirals creates a hydraulic fluid filter with improved filter performance.[26] Other uses of spirals in engineering include heat exchangers, gauges, spiral mold coolers, spiral cutterheads, actuators,[27] intrauterine devices, and many more examples in which "compact length" is desired.[19] Thus, the spiral patterns created here via drop evaporation may serve as useful templates for future micro-devices.

The spiral patterns created by drop evaporation are incomplete, in the sense that they do not begin at the origin (i.e., the center of the drop). Instead, the drop ruptures, and the contact line rapidly recedes towards the exterior crystal ring for a period of time before crystallization is able to pin the contact line and commence formation of the spiral shape. For this reason, Fermat's equation must be adjusted so that the spiral begins at some interior radius by designating a radial dimension where the spiral begins, $\emptyset_{min}$:

$$r(\emptyset) = a\sqrt{\emptyset + \emptyset_{min}} \tag{7.9}$$

The radial dimension $\emptyset$ can be converted from radians into the number of spiral arcs, *n*:

$$\emptyset = 2\pi n \tag{7.10}$$

And Fermat's equation can be rewritten as:

$$r(n) = a\sqrt{2\pi(n_{min} + n)} \tag{7.11}$$

Where n_{min} is the number of "invisible" spiral arcs, i.e, the portion of the shape that would have formed on the interior of the drop if the spiral started at the origin. The maximum radius of the spiral shapes is constrained by the inner radius of the crystalline coffee-ring, so that r_{max} is a constant (which, for a constant volume, is dictated by the initial contact angle):

$$r_{max} = a\sqrt{2\pi(n_{min}+n_{obs})} = a\sqrt{2\pi n_{tot}} \tag{7.12}$$

Where n_{obs} is the number of spirals observed, and n_{tot} is the total number of spirals for a complete shape. Figure 7.8 shows a selection of other spiral patterns and the fit of Fermat's equation.

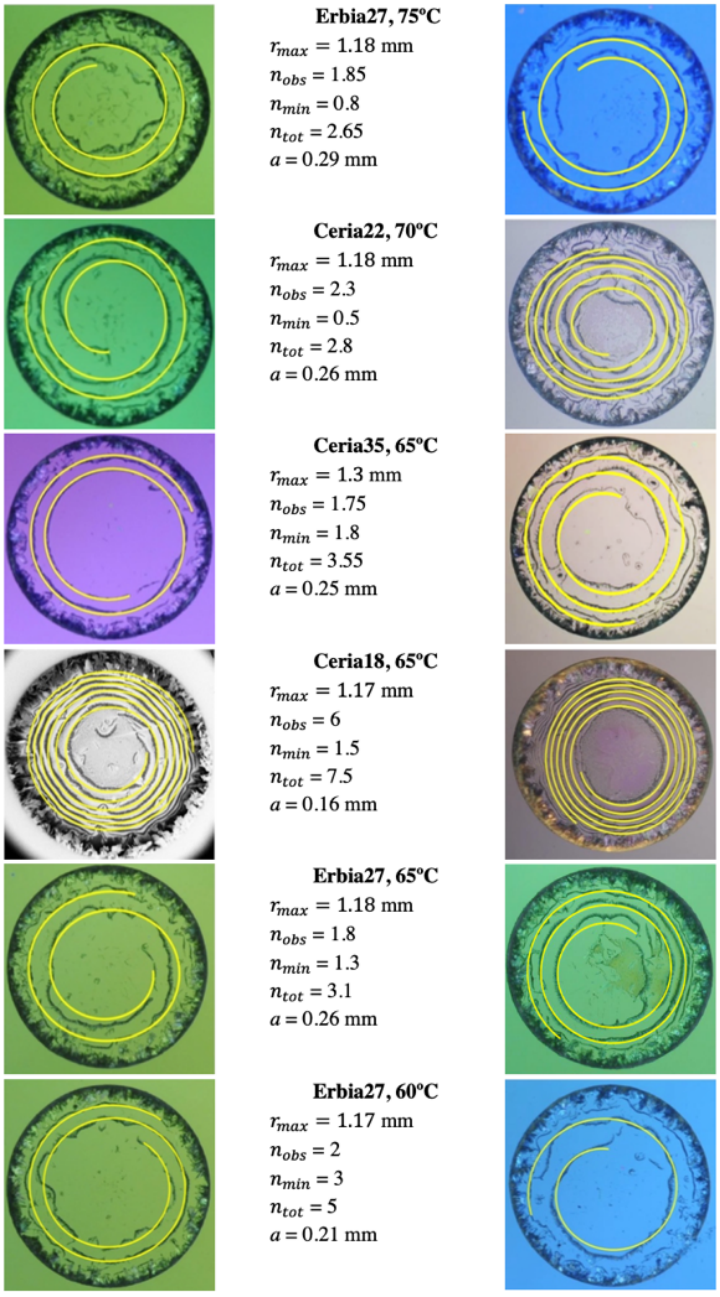

FIGURE 7.8. Optical microscope images with overlaid Fermat's spiral to measure parameter "a".

Finally, to understand why Fermat's spiral in particular emerges from the contact line motion in these experiments, the time-dependence of the radial position of the contact line must be incorporated. Equation 7.12 can be altered to include this time dependence:

$$R(t) = a\sqrt{2\pi n(t)} \tag{7.13}$$

This time dependence of the radial position is tracked and plotted in Figure 7.9a, where n(t) is approximately equivalent to the radial position of the "pinning" locations.

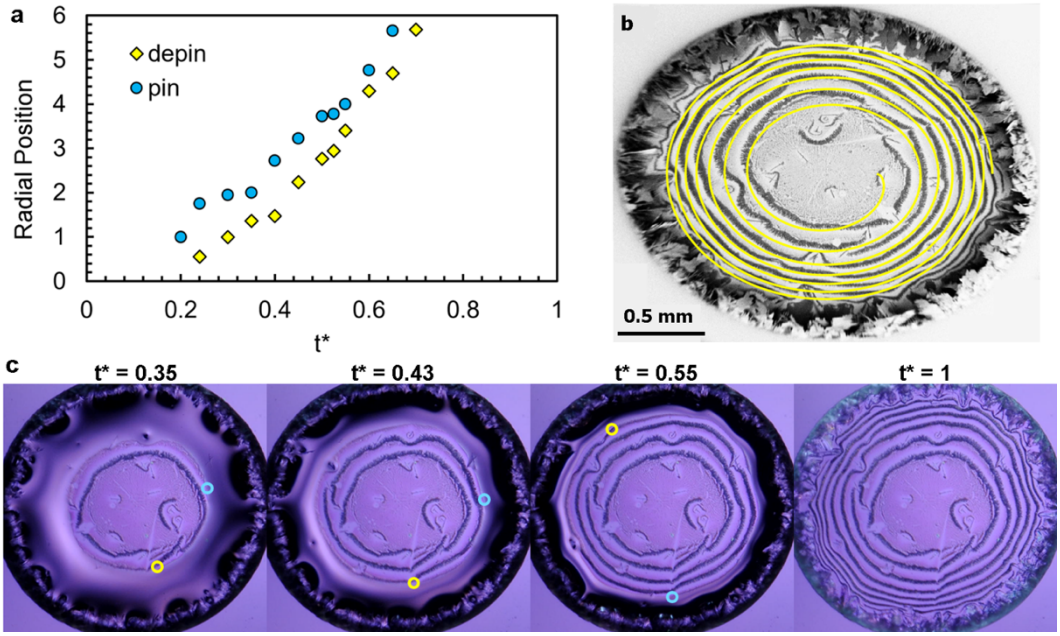

FIGURE 7.9. (a) The radial position, n, as a function of normalized time ($t^*=t/t_2$, where t_2 is the burst time defined in Figure S1) (b) Fermat's equation overlaid on SEM image for the example tracked in part a. (c) Time series demonstrating the movement of the pinning and depinning points for the given sample.

From Figure 7.9a, we see that n(t) is approximately linear with time ($n(t) \sim C * t/t_2$, where C is a constant describing the slope) and the time dependence can be written as:

$$R(t) = a\sqrt{\frac{2\pi C t}{t_2}} \qquad 7.14$$

A normalized version of this equation is plotted in Figure 7.10, along with a normalized version of the time-dependent radial position predicted from equation 7.6 for the purposes of comparing the shapes of the two curves. The square-root dependence predicted by Fermat's equation (equation 7,14) and the shape of the Lambert W-function predicted from a mass balance have good agreement. While not a perfect match, it is possible to understand how the physical model of Equation 7.6 can give rise to a shape that is relatively well-matched with the Fermat spiral equation.

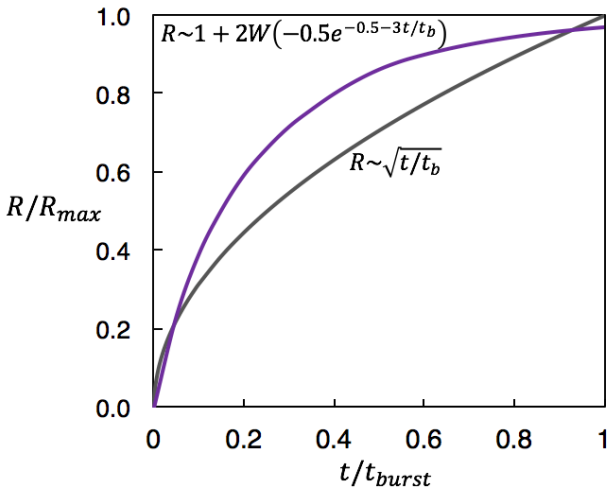

FIGURE 7.10. Plot of normalized equations 7.6 and 7.14, showing the general shape of the radial position of the contact line with time predicted by the physical model (equation 7.6) and from the Fermat spiral equation (equation 7.14).

The previous analysis explains how Fermat's spiral arises from contact line dynamics, but fails to provide a prediction for the proportionality constant "*a*" as a function of experimental parameters. The proportionality parameter describes the relative distance between concentric arcs of the spiral. Inspection of Figure 7.6 demonstrates that lowered substrate receding angles decrease the distance between subsequent arcs, which corresponds to a lowered value of a. It is therefore expected that this parameter will be heavily dependent on the relative rates of pinning and depinning of the moving contact line. When the pinning rate is slow, the interface can significantly recede before re-pinning, and the value of a will be high. If the pinning rate is fast compared to the depinning rate, the contact line will not recede significantly before another row of crystals begins to form, and a will be low.

The dependence of the spiral shape on the stick-slip motion of the contact line can be quantified following a mass-balance argument,[18] where the distance between concentric rings is estimated in the limit where the volume lost to evaporation is negligible during the short timescale of a stick-slip event. We consider a triangle-shaped wedge of fluid (see inset of Figure 7.4a) with a pre-slip contact angle of θ_{depin} and base dimension equal to $(R_o - R(t))$. After slip, the base dimension of the wedge will have changed by a small amount which will be approximately equal to a; but with a new contact angle equal to θ_{pin}. If mass loss during this motion is assumed to be negligible, then:

$$\frac{1}{2}(R_o - R(t))^2 \tan\theta_{depin} \sim \frac{1}{2}(R_o - R(t) - a)^2 \tan\theta_{pin} \qquad 7.15$$

Applying the low angle approximation and substituting $(R_o - R(t)) \sim R_o/2$:

$$a \approx \frac{R_o}{2}\left[1 - \left(\frac{\theta_{depin}}{\theta_{pin}}\right)^{1/2}\right] \qquad 7.16$$

Where R_o is the radius of the deposit, θ_{depin} is the contact angle immediately prior to depinning from the array of crystalline needles, and θ_{pin} is the contact angle just after re-pinning. For a drop evaporating in a standard mode (where the contact line motion moves inwards), θ_{depin} would be equivalent to the receding contact angle θ_R, and θ_{pin} could be estimated as the equilibrium contact angle. Here, the contact line motion of the evaporating thin film deviates strongly from this case. Crystals formed at the pinned contact line are highly wetting, meaning that the depinning contact angle becomes a function of the crystal morphology rather than of the surface itself. Thus, θ_{depin} will be constant across substrates, and have a value smaller than that of the actual receding contact angles. Likewise, θ_{pin} is not equal to the equilibrium contact angle, but is rather much smaller; and is likely even smaller than the substrate's contact angle. However, unlike θ_{depin}, there is a clear dependence of θ_{pin} on the substrate wetting properties. Thus, we approximate θ_{pin} as the receding contact angle for the purposes of plotting equation 7.16 against experimental data (Figure 7.11, with $\theta_{depin} = 10°$, R_o=1.2 mm).

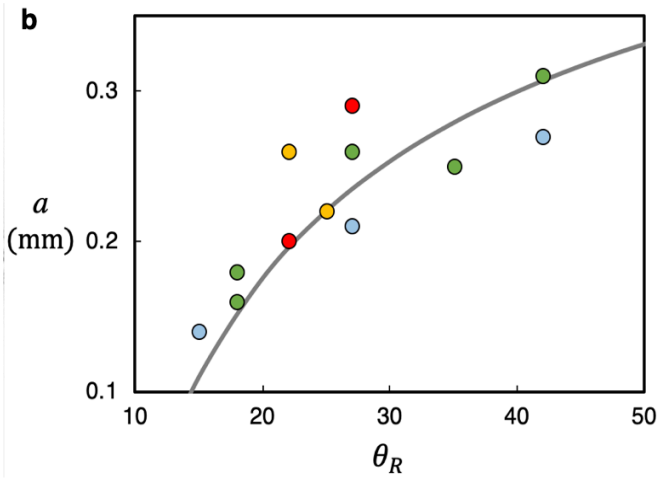

FIGURE 7.11. Proportionality constant a as a function of receding contact angle, where circle markers indicate experimental values (red = 75ºC, orange = 70ºC, green = 65ºC, blue =60ºC), and the grey line is the model presented in equation 2, with $\theta_{depin} = 10°$, R_o=1.2 mm, and $\theta_{pin} = \theta_R$. Scale bar indicates 0.5 mm.

The experimental data presented in Figure 7.11 include spirals formed at 60ºC (blue), 65ºC (green), 70ºC (orange), and 75ºC (red). The geometric parameter a generally increases with increasing temperature. A temperature correction could easily be incorporated into this model by altering the assumption that mass lost during a stick-slip event is negligible, and adding a loss term on the right-hand side of equation 7.15. This term would increase the value of a, consistent with the result that a increases with increasing temperatures/evaporation rates. Previous work showing formation of fullerene spirals in conjunction with a glass bead on a hydrophilic surface demonstrated a strong temperature dependence of the winding, in which the distance between pattern arcs increased with temperature.[13] In the present work, the temperature dependence is much less dramatic; which might be attributed to the negligible change of calcium sulfate's solubility with temperature.

7.3 Patterning Mechanisms

So far, it has been demonstrated that contact line dynamics control both the pattern type (spiral or concentric ring) and the pattern geometry (the distance between subsequent spiral arcs or concentric rings). However, additional dynamics are required to understand the regimes in which patterns form. Regular patterns which mirror the contact line motion on the drop interior only form on substrates heated to temperatures between ~60-75ºC. Slower evaporation on cooler substrates form few, or no, crystals on the drop interior, while faster evaporation on hotter substrates forms a more chaotic distribution of crystals. Thus, evaporative dynamics are considered to understand this behavior, starting with the rate of change for the local height of a thin film for a completely wetting, evaporating drop:[28]

$$\frac{dh(r,t)}{dt} = -\frac{J_o}{R(t)\sqrt{\frac{r^2}{R(t)^2}-1}} \tag{7.17}$$

where J_o is the diffusion driven evaporative flux in m^2/s ($J_o = D_{vap}(C_T - C_{oo})/\rho$, where D_{vap} is the diffusion coefficient of water vapor in air, C_T is the concentration of water vapor at the interface at the substrate temperature T, C_{oo} is the concentration of water vapor in the ambient environment, and ρ is the density of water). In this equation, r is the radial position starting from the drop interior and moving towards the outer crystal ring so that evaporation flux has a minimum at $r = R_o$ and a singularity at the moving contact line where evaporative flux is largest (see Figure 7.4 for geometry).[29]

To estimate the timescale of evaporation in the region of the mobile contact line and avoid the singularity at $r = R(t)$, I use $r = R(t) + \Delta r$, where Δr is some small length scale (see Figure 7.4c). Substituting this relation into equation 7.17, dropping the term $\Delta r^2/R(t)^2$ due to its insignificant size, and rearranging as a scaling argument where $R(t) = R_{pin}$ (where $R_{pin}$is the radius at which patterning begins), we find:

$$\frac{\Delta h}{t_E} \sim \frac{j_o}{\sqrt{\Delta r R_{pin}}} \tag{7.18}$$

Where t_E is the timescale of evaporation at the moving contact line:

$$t_E = \frac{\Delta h\sqrt{\Delta r R_{pin}}}{j_o} \tag{7.19}$$

To understand the physics of pattern formation, the evaporative timescale must be compared to a timescale describing the process of crystallization at the mobile contact line. Previously, it was observed that rings form at low evaporation rates (Figure 7.6), while spiral or concentric ring

patterns form at higher rates, and amorphous crystals form at the highest evaporation rates. If salt ions are able to move away from the contact line faster than the mobile contact line can "catch" them, crystallization will occur at the already existing outer crystalline ring, resulting in a single ring. If the movement of the salt ions is slow, they will be forced to precipitate as crystals as the contact line moves past them. When the motion of the contact line is too fast, the precipitation occurs randomly, giving rise to the amorphous deposits observed at the very highest temperatures. Calcium ions are smaller and more mobile than sulfate ions, and therefore, we use the diffusivity of calcium ions to capture the timescale of ion motion:

$$t_D = \frac{\Delta r^2}{D_{Ca^{2+}}} \tag{7.20}$$

Where $D_{Ca^{2+}}$ is the diffusion coefficient of calcium ions in water. Finally, the ratio between the evaporative timescale of equation 7.19 and the diffusive scale of equation 7.20 should allow for dimensionless prediction of pattern formation. This ratio is:

$$\frac{t_D}{t_E} = \frac{J_o}{D_{Ca^{2+}}} \frac{\Delta r}{\Delta h} \sqrt{\frac{\Delta r}{R_{pin}}} \tag{7.21}$$

This ratio can be solved for by assuming that Δr is approximately equal to the width of the crystalline rings as shown in Figure 7.4c (30 μm), and estimating that $\Delta h = \Delta r \tan \theta_{depin} \approx 5$ μm, for $\theta_{depin} = 10°$. The evaporative flux J_o and diffusion $D_{Ca^{2+}}$ are both functions of temperature and R_{pin} is taken from experimental data. The hypothesis that this ratio can be used to classify the emergence of patterns is tested by solving equation 7.21 for each of the examples shown in Figure 7.6. The results of this analysis are shown in Figure 7.12, where blue circles indicate a single, empty ring; purple triangles indicate interior patterning (either concentric ring or spiral); and yellow squares indicate random crystalline deposits at the drop interior. Although both the diffusion rate and evaporation rate increase with temperature; the evaporative flux increases faster, leading to good separation between the different categories.

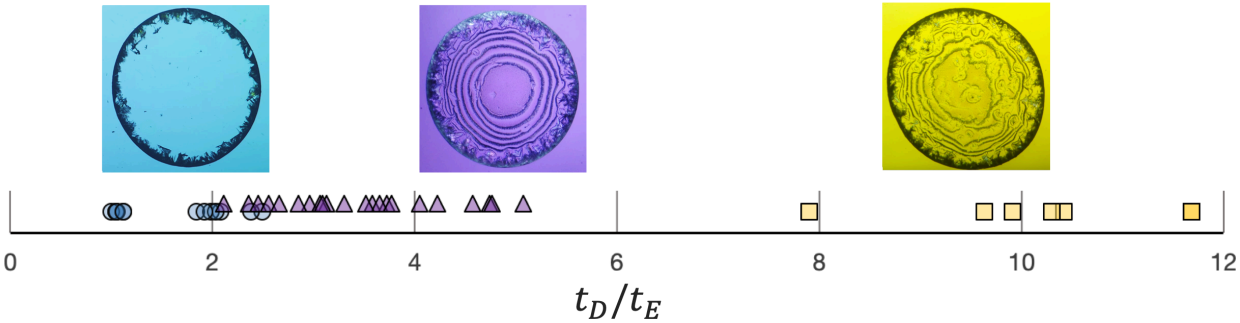

FIGURE 7.12. Line plot of equation 7, where rings (blue circles) form at low values, patterns (purple triangles) form in the intermediate region, and random deposition (yellow squares) occurs at higher values. Selected images show examples of the patterns represented.

Other Salts

Based on the results of Figure 7.12 and Equation 7.21, the two parameters important for patterning are (1) the system geometry, and (2) the ratio of evaporation to diffusion. In particular, the ratio between the relative height and radial dimension of the evaporating drop profile will affect whether or not this contact line patterning phenomena will occur. These dimensions are partially controlled by the height of the outer crystalline ring which grows during the first stages of evaporation. Without this three-dimensional feature, the interior patterns would fail to form. However, patterning via this process is not unique to calcium sulfate. Any solutal solution that forms a three-dimensional exterior ring during the early stages of evaporation when evaporated on high hysteresis surfaces has the potential to form patterns, so long as both the drop geometry and evaporation to diffusion ratios are within the correct regime as predicted by equation 7.21. This result also provides an explanation for why the latex beads do not exhibit the same contact line behavior, as the beads also do not form a three-dimensional outer ring.

To further probe the hypothesis developed previously (i.e., that the ratio of equation 7.21 controls pattern formation), experiments were conducted with different salts, as shown in Figure 7.13. All of these 5 μL samples were deposited on the same substrate (θ_A=98°, θ_R=30°) heated to 70°C, and calcium sulfate was included as a control for direct comparison (7.13c).

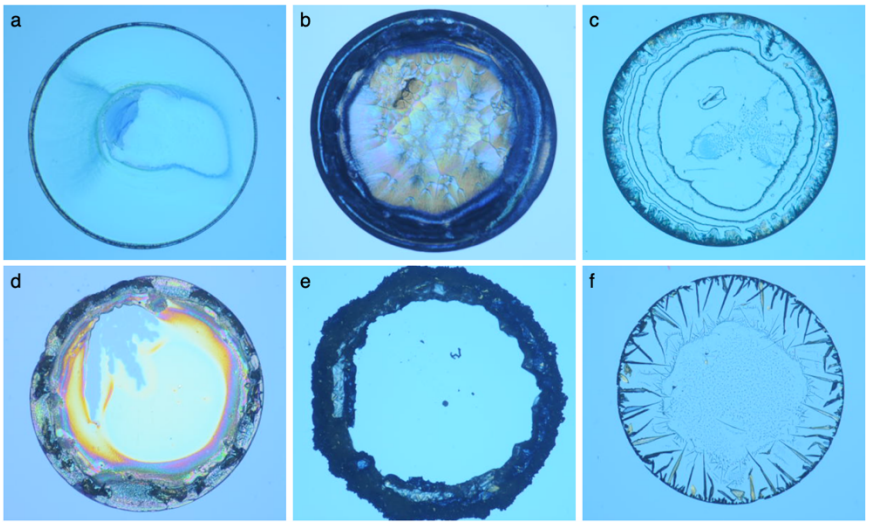

FIGURE 7.13. Deposits left on the substrates by different salt solutions on a substrate (θ_A=98°, θ_R=30°) heated to 70°C. (a) calcium carbonate, (b) sodium carbonate, (c) calcium sulfate, (d) calcium iodate, (e) sodium chloride (at 10% of saturation concentration), and (f) silver sulfate.

The ratio between the relative height and radial dimension of the evaporating drop profile strongly controls the ratio between the evaporative and crystallization timescales. The other salts shown in Figure 7.13 fail to form patterns primarily due to geometrical reasons. Calcium carbonate (7.13a) has a solubility ~100x smaller than that of calcium sulfate (0.015 vs. 2.1 g/L), and there is

insufficient mass to allow for formation of an outer ring. Thus, the geometry of the evaporating wedge is altered. Sodium carbonate (7.13b) and calcium iodate (7.13d) have sufficient solubilities (2.4 g/L and 200 g/L at 20°C, respectively); however, the kinetics of crystal growth are slower; meaning that the resulting precipitate at the outer edge does not form the well-shaped crystalline "bowl" modeling the shape of the drop that calcium sulfate does. Thus, the width to height ratio is large in the evaporating wedge, and the resulting interior deposit is most similar to the random regime that occurs at large values of equation 7.21. In contrast, the sodium chloride solution (at a concentration of 36 g/L, ~10% saturation concentration and fast crystallization kinetics) creates an outer ring that is too large, skewing the width to height ratio in the other direction and placing the final deposit in the "ring" regime of equation 7.21. Of the salts tested, silver sulfate (7.13f) is the closest to creating a geometry similar to that of the calcium sulfate and forms a three-dimensional ring of well-formed crystals. Thus, the drop ruptures at the interior and forms an interior ring composed of aligned crystalline needles when the contact line re-pins. However, the morphology of these crystals are different from the calcium sulfate, and the ring structures are less defined.

To confirm the prediction of equation 7.21 and demonstrate that the correct geometrical ratios will give rise to patterning for salts other than calcium sulfate, experiments with sodium chloride were repeated at other concentrations. By altering the concentration, the height of outer crystal ring is altered while maintaining a constant radius (which is set by the contact angle of the substrate). Therefore, a concentration which creates a three-dimensional outer crystalline ring at the correct width to height ratio is sought. The results of these experiments are shown in Figure 7.14, where concentric ring patterns successfully emerge around 5% of the saturation concentration. At lower concentrations, the deposits fall into random regime due to insufficient outer height; while higher concentrations fall into the "ring" regime.

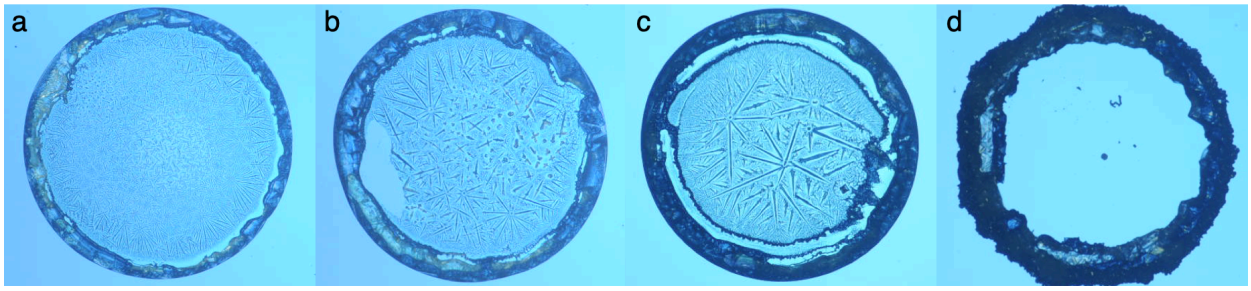

FIGURE 7.14. Deposits from different concentrations of sodium chloride on a substrate (θ_A=98°, θ_R=30°) heated to 70°C. (a) 1% of saturation (3.6 g/L), (b) 2% of saturation concentration, (c) 5% of saturation concentration, (d) 10% of saturation concentration.

While calcium sulfate is not unique in the ability to form patterns on these surfaces, it is unique in that both its solubility concentration and its crystallization kinetics are ideally suited for creating the three-dimensional geometry that gives rise to this patterning phenomena. It also has the added benefit of maintaining a relatively constant solubility concentration across temperatures. This property is rare, as most salts have a large increase in solubility with temperature.

If it is desirable to create patterns of a chemistry that does not have the unique properties of calcium sulfate, one strategy could be to use an O-ring placed on a hydrophilic substrate. A drop containing the desired solute would be placed in middle of the O-ring and allowed to evaporate. The forced geometry created by the O-ring would allow for the rupture of the drop at the interior that then allows for contact line motion patterning. Experimentalists would need to tune the height and radius of the O-ring, the evaporation rate, the solute concentration (which influences crystallization rate, crystal morphology, and -to some extent- diffusion), and the substrate wettability to fabricate the desired pattern.

Conclusions

Evaporating drops of calcium sulfate on substrates with extreme contact angle hysteresis always leads to the formation of a three-dimensional outer crystalline ring at the drop contact radius. However, relatively flat crystalline patterns may also arise on the interior of this ring depending on ratio between the evaporation rate and the diffusion rate. Fast evaporation leads to formation of amorphous, chaotic crystal deposits on the interior, while slower evaporation leads to no crystallization at the interior contact line. At intermediate rates, crystalline patterns in the form of concentric rings or spirals emerge. A simple mass balance argument can be used to calculate the geometry of spiral patterns, where lower substrate receding contact angles result in tighter winding of the patterns.

Spiral shapes are pervasive throughout nature and biology, and are also desirable in any application in which "compact length" is desired.[19] Two-dimensional Fermat spirals such as those formed here have a range of applications including: creation of substrates with alternating hydrophobic/hydrophilic regions, templates for spiral microfluidic channels,[30,31] ring resonators for optics (where the low curvature of the Fermat spiral at the center allows for minimal losses),[32] spiral cantilevers for micro-scale sensors[27] and cochlear implants,[33] spiral antennas,[34,35] and spiral electrodes for harvesting mechanical energy.[36] Aside from being fast and low cost, this method for designing spiral templates from evaporating drops is scalable and easy to implement; and therefore has potential to alter how micro- and milli-metric scale spiral devices are produced.

References

1. McBride, S. A., Dash, S. & Varanasi, K. K. Evaporative Crystallization in Drops on Superhydrophobic and Liquid-Impregnated Surfaces. *Langmuir* **34,** (2018).
2. Good, R. J. in *Contact Angle, Wettability, and Adhesion.* (ed. Mittal, K. L.) 3–36 (1993).
3. Gao, N. *et al.* How drops start sliding over solid surfaces. *Nat. Phys.* **14,** 191–196 (2017).
4. Azimi, G., Dhiman, R., Kwon, H.-M., Paxson, A. T. & Varanasi, K. K. Hydrophobicity of rare-earth oxide ceramics. *Nat. Mater.* **12,** 315–20 (2013).
5. Chin, C. C. *et al.* On the off stoichiometry of cerium oxide thin films deposited by RF sputtering. *Phys. C Supercond. its Appl.* **260,** 86–92 (1996).
6. Shahidzadeh, N., Schut, M. F. L., Desarnaud, J., Prat, M. & Bonn, D. Salt stains from evaporating droplets. *Sci. Rep.* **5,** 10335 (2015).
7. McHale, G., Erbil, H. Y., Newton, M. I. & Natterer, S. Analysis of shape distortions in sessile drops. *Langmuir* **17,** 6995–6998 (2001).
8. Baldwin, K. A. & Fairhurst, D. J. Classifying dynamic contact line modes in drying drops. *Soft Matter* **11,** 1628–1633 (2015).
9. Bhardwaj, R., Fang, X., Somasundaran, P. & Attinger, D. Self-Assembly of Colloidal Particles from Evaporating Droplets: Role of DLVO Interactions and Proposition of a Phase Diagram. *Langmuir* **26,** 7833–7842 (2010).
10. Deegan, R. D. Pattern formation in drying drops. *Phys. Rev. E* **61,** 475–485 (2000).
11. Li, W., Lan, D. & Wang, Y. Dewetting-mediated pattern formation inside the coffee ring. *Phys. Rev. E* **95,** (2017).
12. Mae, K. *et al.* Self-Organized Micro-Spiral of Single-Walled Carbon Nanotubes. *Sci. Rep.* **7,** 5267 (2017).
13. Chen, Y.-J., Suzuki, K. & Yoshikawa, K. Self-organized target and spiral patterns through the 'coffee ring' effect. *J. Chem. Phys.* **143,** 84702 (2015).
14. Chen, Y.-J., Suzuki, K., Mahara, H., Yoshikawa, K. & Yamaguchi, T. Self-organized Archimedean spiral pattern: Regular bundling of fullerene through solvent evaporation. *Appl. Phys. Lett.* **102,** 41911 (2013).
15. Keller, J. B. Breaking of liquid films and threads. *Phys. Fluids* **26,** 3451–1128 (1983).
16. Shanahan, M. E. R. Simple Theory of Stick-Slip and Wetting Hysteresis. *Langmuir* **11,** 1041–1043 (1995).
17. Shanahan, M. E. R. & Sefiane, K. in *Contact Angle, Wettability, and Adhesion. Vol. 6* (ed. Mittal, K. L.) 19–31 (CRC Press, 2009).
18. Wu, M., Man, X. & Doi, M. Multi-ring Deposition Pattern of Drying Droplets. *Langmuir* (2018).
19. Pickover, C. A. Mathematics and Beauty: A Sampling of Spirals and 'Strange' Spirals in Science, Nature, and Art. *Leonardo* **21,** 173–181 (1988).
20. Morris, R. W. B. The Prehistoric Rock Art of Great Britain: A Survey of All Sites Bearing Motifs more Complex than Simple Cup-marks. *Proc. Prehist. Soc.* **55,** 45–88 (1989).
21. Schaafsma, P. *Indian rock art of the Southwest*. (UNM Press, 1986).
22. Zhushchikhovskaya, I. & Danilova, O. Spiral patterns on the Neolithic pottery of East Asia and the Far East. *Doc. Praehist.* **35,** 215 (2008).
23. Ball, P. *Shapes: nature's patterns: a tapestry in three parts*. (OUP Oxford, 2009).
24. Thompson, D. W. *On Growth and Form: A New Edition*. (Dover Publications, 1942).
25. Noone, C. J., Torrilhon, M. & Mitsos, A. Heliostat field optimization: A new computationally efficient model and biomimetic layout. *Sol. Energy* **86,** 792–803 (2012).
26. Reuter, M. Filter for cleaning hydraulic fluid. U.S. Patent (2009).

27. Wilson, S. A. *et al.* New materials for micro-scale sensors and actuators: An engineering review. *Mater. Sci. Eng. R Reports* **56,** 1–129 (2007).
28. Cachile, M., Bénichou, O. & Cazabat, A. M. Evaporating Droplets of Completely Wetting Liquids. *Langmuir* **18,** 7985–7990 (2012).
29. Hu, H. & Larson, R. G. Evaporation of a Sessile Droplet on a Substrate. *J. Phys. Chem. B* **106,** (2002).
30. Nie, Y., Hao, N. & Zhang, J. X. J. Ultrafast Synthesis of Multifunctional Submicrometer Hollow Silica Spheres in Microfluidic Spiral Channels. *Sci. Rep.* **7,** 12616 (2017).
31. Warkiani, M. E., Tay, A. K. P., Guan, G. & Han, J. Membrane-less microfiltration using inertial microfluidics. *Sci. Rep.* **5,** 11018 (2015).
32. Xu, D.-X. *et al.* Archimedean spiral cavity ring resonators in silicon as ultra-compact optical comb filters. *Opt. Express* **18,** 1937 (2010).
33. Udvardi, P. *et al.* Spiral-Shaped Piezoelectric MEMS Cantilever Array for Fully Implantable Hearing Systems. *Micromachines* **8,** 311 (2017).
34. Mao, L. *et al.* Far-field radially polarized focal spot from plasmonic spiral structure combined with central aperture antenna. *Sci. Rep.* **6,** 23751 (2016).
35. Wen, H., Yang, J., Zhang, W. & Zhang, J. Optical resonant Archimedean spiral antennas. *J. Nanophotonics* **5,** 53523 (2011).
36. Chen, L. *et al.* Novel Spiral-Like Electrode Structure Design for Realization of Two Modes of Energy Harvesting. *ACS Appl. Mater. Interfaces* **7,** 16450–16457 (2015).

Chapter 8.

Crystal Patterning from Dewetting From Instabilities

So far, I have shown how evaporative self-assembly can be used to pattern spirals in Chapter 7, three-dimensional bowls and clusters in Chapter 6, and rings or clusters in Chapter 5. Evaporative assembly is a useful patterning technique due to its simplicity and extreme low-cost;[1] however, the method suffers from limited controllability and from the restricted number of patterns that can arise. In this chapter, I expand on the patterning work from previous chapters and show how thin-film instabilities can be used to generate a number of extraordinarily ordered crystalline nano- and micro-structures. These patterns form by evaporating drops of calcium sulfate solution on extremely hydrophilic surfaces heated to temperatures ranging from ambient to boiling.

The patterns that arise from crystalline patterning on hydrophilic substrates are reminiscent of those formed via reaction-diffusion mechanisms and include hexagonal arrays, lines, branches, and sawtooth structures.[2] Despite this similarity, the patterning mechanisms seem to be driven by two distinct fluid instabilities combined with crystallization at the dewetting front. The triangular structures are of particular interest, as they routinely form on wetting substrates, but their presence has not been satisfactorily explained. I propose that patterning is a combination of Maraongoni and thin-film spinodal-like instabilities.

The extremely simple technique presented here can be applied to create water-soluble masks for a variety of applications requiring patterned textures or patterned chemistries. I demonstrate two such applications, including how the crystal patterns can be used as a mask for creating three-dimensional silica textures using reactive ion etch.

8.1 Observations

Gypsum Patterns

The crystalline patterning observed in these experiments is accomplished from a single drop without the use of specific geometries, masks, or special substrates (Figure 8.1). To form these patterns, a single 5 μL drop of saturated calcium sulfate dissolved in water is deposited on heated, oxidized silica substrates. The drop spreads into an equilibrium shape (side view shown in the first panel of Figure 8.1a, top view in Figure 8.1b) with a pinned contact line, so that the contact area between drop and surface remains constant and both the height and contact angle of the drop decrease temporally. During this pinned (constant contact area) evaporation, crystals emerge at the contact line due to concentration polarization caused by the evaporative flow.[3]

As the drop evaporates, the volume reduces until the remaining fluid becomes a thin film pinned by an outer ring of crystals. Continued evaporation eventually results in the liquid depinning from the outer ring, and the contact line retracts towards the drop center (second panel of Figure 8.1b). As the contact line recedes, crystals are deposited at the moving dewetting front until complete evaporation (third panel of Figure 8.1b). These micro-scale crystals left form a number of organized patterns including sawtooth patterns, branches, and hexagonal arrays, as shown in Figure 8.1c.

Just two experimental parameters, the substrate temperature and substrate contact angle, allow for general classification of patterns, as shown in Figure 8.1d. This phase diagram shows that five distinct regimes emerge. Higher contact angles ($\theta > 20°$) and lower temperatures (<60°C) result in the formation of a single crystalline coffee ring with no interior patterning (open circles of Figure 8.1d), while low contact angles ($\theta < 5°$) at high temperatures (> 60°C) lead to the formation of concentric crystalline rings with no microscale patterning of interest.

At intermediate regimes, three general classes of patterns emerge: sawtooth structures composed of dendritic crystals (Figure 8.1c(i), yellow triangles of Figure 8.1d), line/branched structures composed of aligned clusters of crystals (Figure 8.1c(ii), green squares of Figure 8.1d), and periodic arrays composed of larger crystal clusters ((Figure 8.1c(iii), blue dots of Figure 8.1d). This trend of patterning is highly consistent so long as temperatures and contact angles are in range shown in phase diagram. The phenomena is particularly robust for saturated calcium sulfate, whose solubility exhibits only a small temperature variations. Patterns for phase diagram were selected halfway between the outer crystal ring and the drop center, as indicated in Figure 8.1b (see SI for pattern images used to generate the phase diagram).

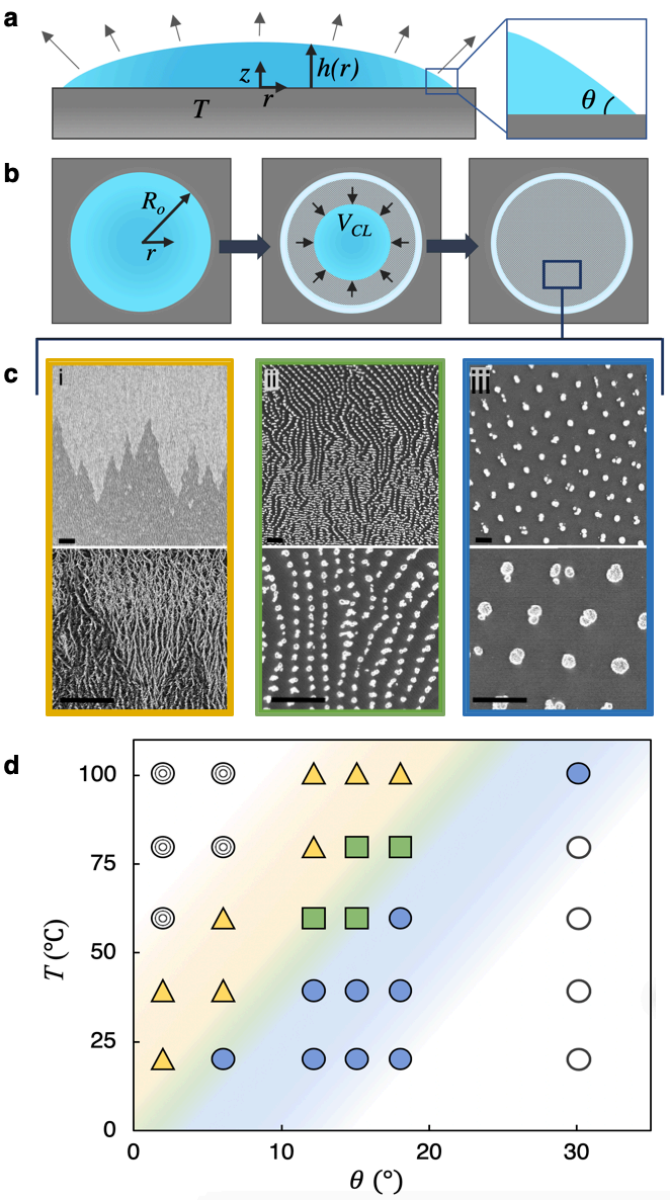

FIGURE 8.1. Experiments and observations. (a) Schematic showing drop geometry from the side and defining the contact angle. (b) Schematic of temporal evolution of evaporation: A ring of crystals develops at the initial drop contact line, evaporation causes the contact line to retract with velocity $V_{CL}(r)$, and an interior crystalline pattern is left behind following complete evaporation. (c) SEM images of patterns left on the interior following evaporation: (i) dendrites with sawtooth pattern, (ii) aligned branches, (iii) hexagonal lattice of spherical calcium sulfate clusters. Scale bars are 20 μm. (d) Classification of patterns according to substrate temperature and substrate contact angle, where open circles (bottom right) indicate formation of an empty ring with no patterns, blue circles indicate a lattice pattern (c,iii), green squares indicate aligned dotted lines (c, ii), yellow triangles indicate the dendritic branches that form sawtooth patterns (c, i), and targets indicate formation of multiple concentric rings with no pattern (top left).

The mechanisms resulting in the non-patterning limits of the phase diagram (concentric rings at high temperatures and low contact angles; and single rings with no interior patterns at lower temperatures and higher contact angles) have been previously established. Single rings with no interior deposits are commonly found in evaporative deposition experiments and are colloquially referred to as coffee-ring patterns.[3] These emerge as radial flow during evaporation transports solutes or particles outward towards the contact line where they accumulate into a ring. Pinning of the contact line is self-propagating due to a feedback loop in which the ring grows thicker while it remains pinned, and thicker rings are more likely to remain pinned.

For the single-ring deposits here, evaporation is slow so that this outer ring is able to develop. When the pinned drop eventually depins from the outer ring, there is very little solute left to crystallize at the drop center. In contrast, on the samples of lower contact angles and higher temperatures, the drop depins relatively earlier in the evaporation process while much solute remains. It periodically re-pins and re-wets as a consequence of the higher temperatures and hydrophilicity (which both act to promote re-wetting),[4] leaving behind concentric rings.

The patterning regimes within the phase diagram of Figure 8.1d are caused by the combination of crystallization and fluid instabilities which propagate during contact line dewetting. The resulting crystalline patterns form a record of contact line motion caused by these instabilities at nano- and micro- metric scales (similarly to the crystalline spirals of Chapter 7). Within the patterning regime, evaporation occurs slow enough that an outer ring forms, pinning the drop and enabling thinning of the pinned film; but fast enough that sufficient solute remains to precipitate during dewetting.

Dendritic sawtooth structures aligned within concentric rings of the drop repeatedly emerge on the most heavily oxidized (aka, hydrophilic) substrates (Figure 8.1c(i)). Dendritic patterns are common in desiccation of complex fluids,[5–8] and can be attributed to a diffusion-limited growth mechanism.[9,10] Less obvious is the reason for the periodic sawtooth structures imposed on the dendrites, which SEM and AFM analysis reveal to be layers of different heights, as show in in Figure 8.2.

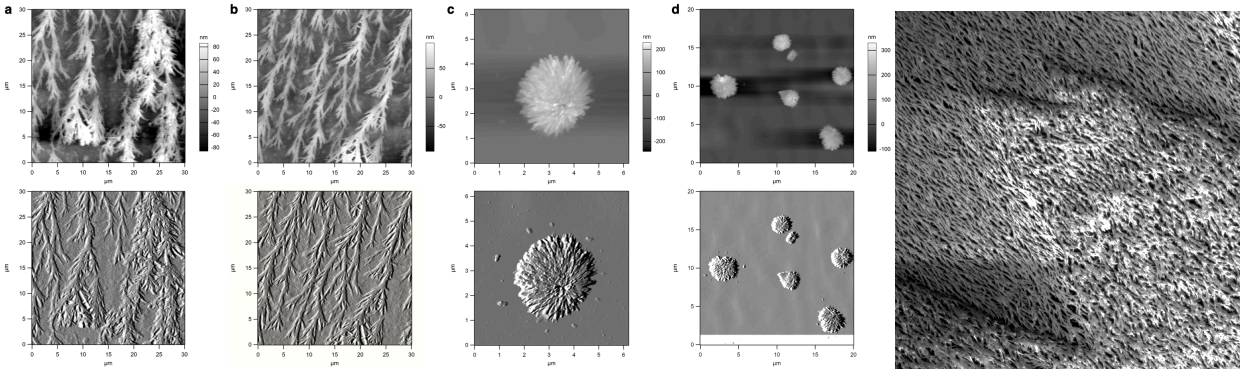

FIGURE 8.2. (a-d) shows AFM images, where the top row gives topographic image, and the second row shows amplitude image. (a) and (b) show different regions of dendrite triangles, where the thicker phase corresponds to the darker phases observed from SEM images. The thin, light regions are ~40nm thick, while the thicker regions are ~80 nm thick. (c) shows a magnified image of a single crystal cluster left from an array, and (d) shows a group of 5 clusters. Clusters are approximately 200 nm tall, 3 μm in diameter, and (for the array in (d)) are about 10 μm between cluster centers. (e) Tilted SEM image shows that the “darker” triangular phase is thicker than the “lighter” one.

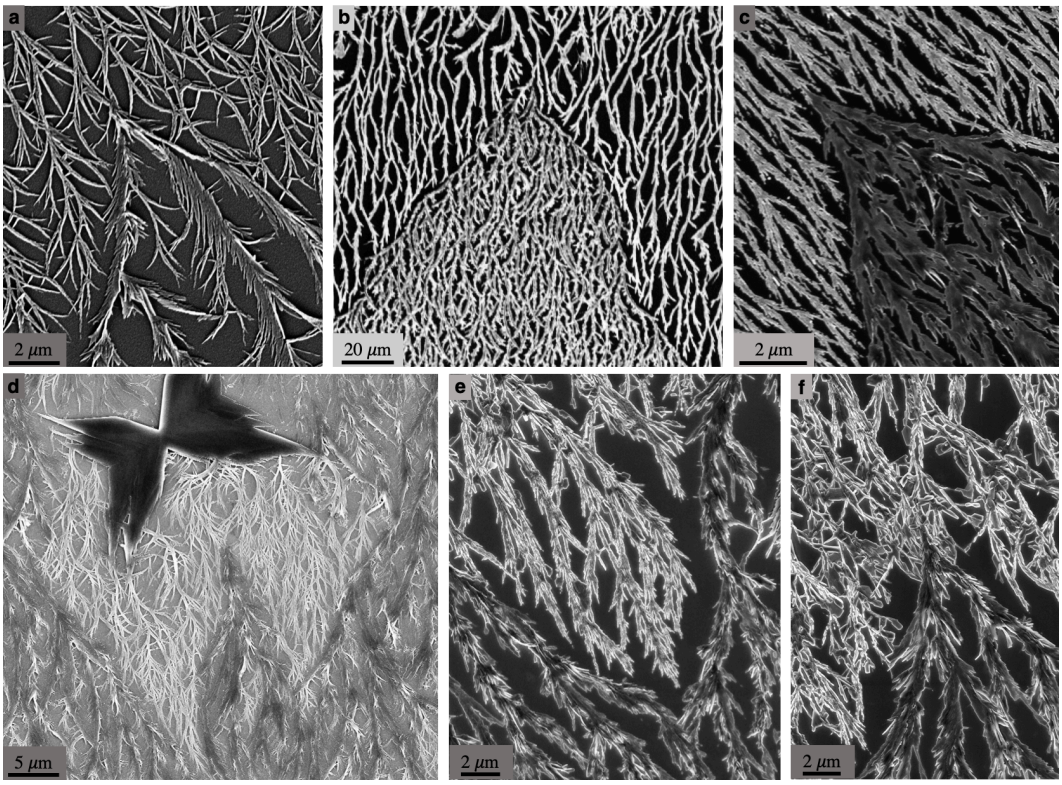

FIGURE 8.3. Close up of triangle pinning points. (a) – (c) show nucleation of second phase triangle, where (a) and (b) were imaged using the SE2 detector, and (c) was imaged with the InLens. (d) shows a region where the lighter, thinner phase has nucleated from a bulk crystal that settled on the surface (InLens detector). Parts (e) and (f) show close up images of the same sample, with (e) showing the tip of the lighter, thinner phase, and (f) showing the tip of the darker, thicker phase. The thick phase nucleates from the thinner phase, grows in the vertical dimension until it meets another "thick" phase branch.

The thicker triangle phase (which appears darker in the SEM image of Figure 8.1ci) always points towards the outer ring, and thus grows in the same radial direction as the moving contact line. This is shown by a collage of pinning points in Figure 8.3, where the thicker (darker) triangles point outwards towards the outer ring, and then thinner (lighter) triangles point towards the drop interior. A similar effect has been previously observed in 1990 by Deegan, who observed sawtooth patterns forming from mono- and bi-layers of 0.1 μm nanoparticles deposited at room temperature on hydrophilic mica.[11] Thus, although this patterning phenomena is particularly robust in the present system of dissolved calcium sulfate in water, -assuming that the mechanisms across the two systems are identical- the phenomena must be driven by interfacial physics rather than by some particular effect of the gypsum crystallization.

The most hydrophobic samples within the patterning regimes give rise to a periodic array structure composed of clusters of crystals (Figure 8.1c(iii)). Similar patterns have been observed previously in dewetting phenemona, and are the result of a fingering instability.[12–14] Such a fingering instability can have a number of origins including Marangoni flows,[12,14,15] Rayleigh-Plateau break-

up of a fluid ridge or thread,[16] or forced wetting/dewetting of a visco-elastic fluid.[17,18] To my knowledge, the present experiments are the first observation of such a fingering phenomenon in a purely aqueous (i.e., no surfactant or other solvent) solution at elevated temperatures. High speed videos of pure water controls do not exhibit fingering at the contact line, suggesting that this instability is related to crystallization.

Between the triangular and array regimes lies an intermediate regime, in which individual crystal clusters still appear, but align into branched structures rather than into arrays (Figure 8.1c(ii)). Clusters formed within this regime tend to be smaller than those formed in the array regime, with an associated decrease in spacing between "lines" of crystals. These branched patterns exhibit features of both the triangular and the array regimes.

Other Chemistries

Patterning experiments were repeated on substrates with different base chemistry (Figure 8.4) and using salts other than calcium sulfate (Figure 8.5) to show that chemistry does not control patterning. Silica substrates were sputter coated with different chemistries (erbia, titania, and silica. The sputter-coated silica film will have different equilibrium structural and chemical properties from the plain silica substrate) and then plasma-cleaned. The plasma cleaning resulted in a highly wetting contact angle across all substrates and triangular patterns are observed across the substrates regardless of the chemistry.

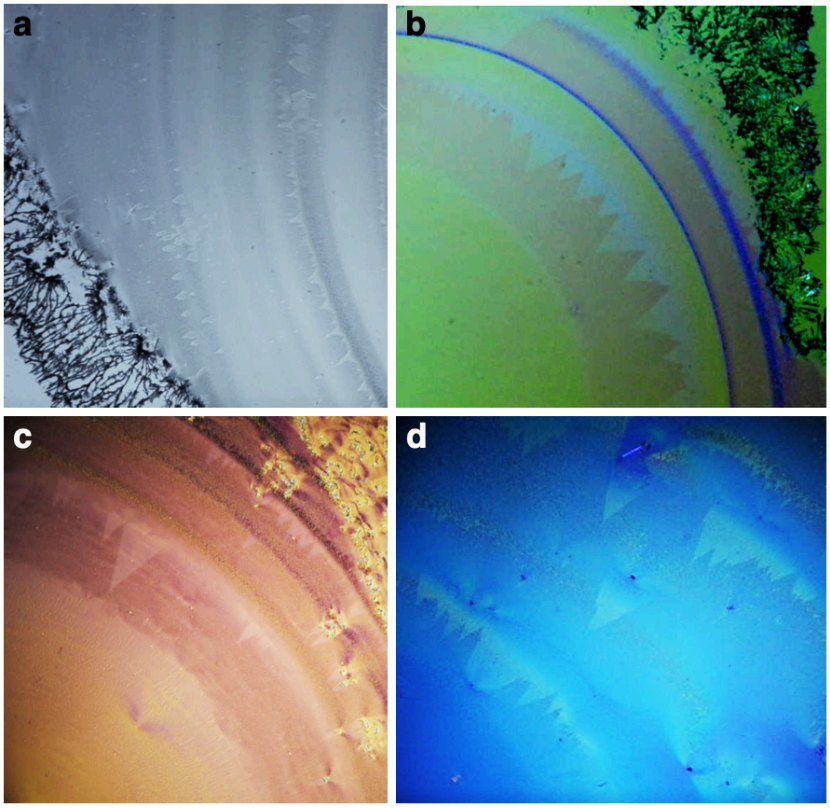

FIGURE 8.4. Triangles on other substrates. (a) plain silica wafer, (b), sputter-coated erbia (c) Sputter-coated titanium dioxide, (d) sputter- coated silicate. The universality of the patterning suggests that patterns can be formed on any substrate so long as the contact angle and temperature are within the regimes shown in Figure 8.1d.

While chemistry is not responsible for formation of the triangular structures, it appears that the pre-disposition of different salts to form different structures does influence the appearance of the triangular patterns. Figure 8.5 shows triangular-like structures formed from other salt chemistries under typical experimental conditions (θ =5°, T= 60°C). While other salts form triangular structures, the ability of calcium sulfate to precipitate quickly into dendrites contributes to the consistency and repeatability of sawtooth patterning. Unlike colloidal particles, crystals are constrained by their desired crystalline morphology, which often reflects the internal lattice structure of the crystals.

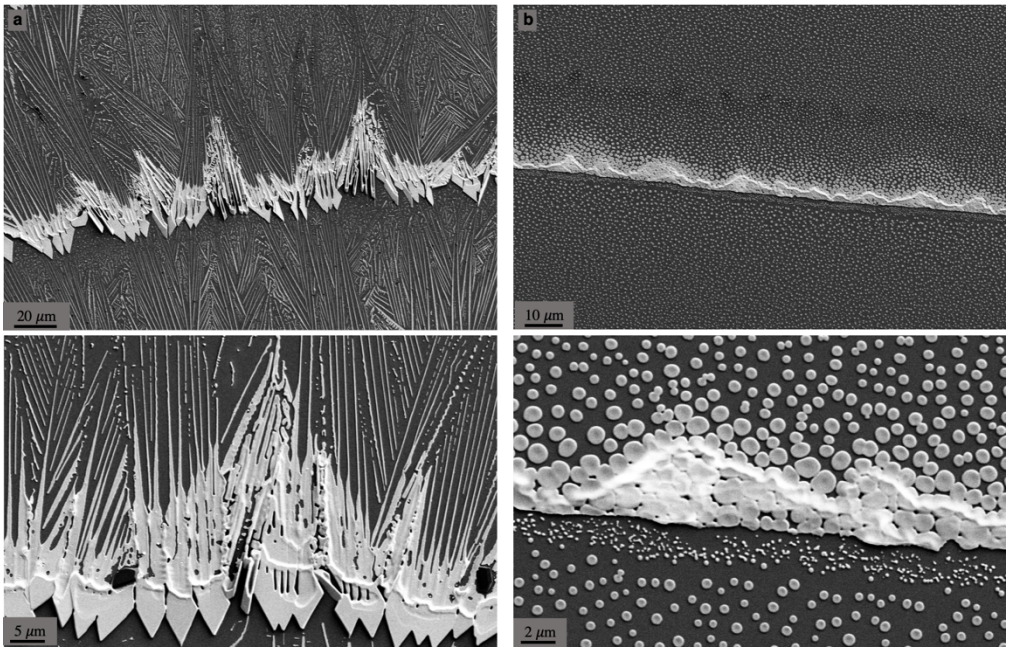

FIGURE 8.5**.** Triangle patterns formed from other salt chemistries. (a) silver sulfate, and (b) calcium iodate.

Next, the inorganic surfactant Sodium Dodecyl Sulfate (SDS) was added to a solution of calcium sulfate. Addition of the surfactant changed the crystal structure and created an unusual branching of triangular structures, as shown in Figure 8.6. Rather than nucleating periodically in rows (as shown in Figures 8.4 and observed throughout all prior sawtooth patterns), there is a continuous nucleation cascade in which a new triangle nucleates off the tip of another to create Sierpinksi-like triangle structure. As expected, samples containing surfactant did not form the periodic arrays associated with the Marangoni instability, as the surfactant counter-acts the effect of the salts (sometimes called “anti-surfactant” effects). A decreased surface tension seems to promote nucleation of thick regions from the tips of other thick regions to create the Sierpinksi-like structure.

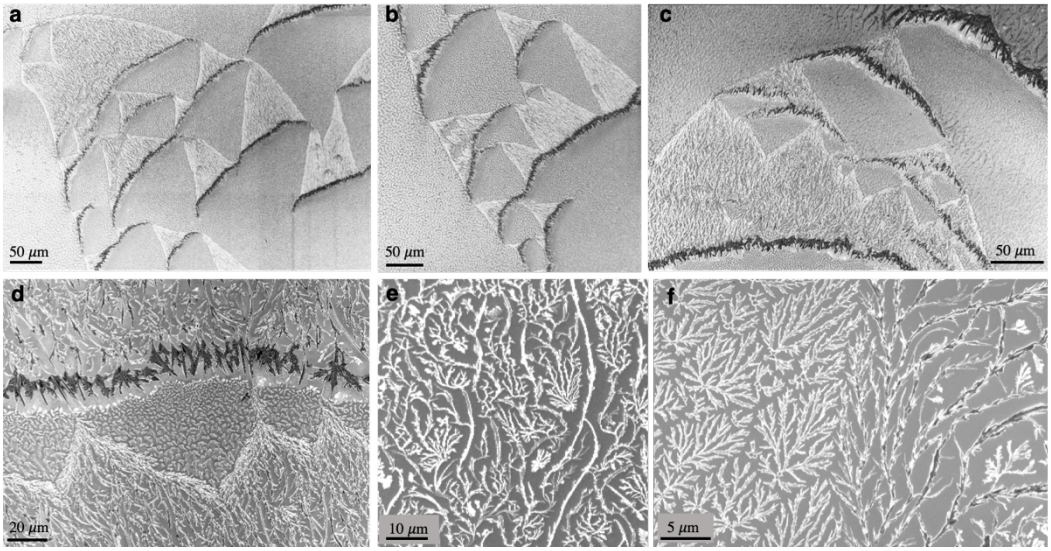

FIGURE 8.6. Influence of surfactant. (a-c) show a branched network of triangles reminiscent of Sierpinski triangles. (d) close up of region of triangles, (e) altered morphology of calcium sulfate dendrites due to surfactant, (f) close up of boundary between two phases of crystal, where the left is a lighter sawtooth phase, and the right is a darker sawtooth phase.

Triangles from Other Studies

While this is the first (to my knowledge) study to systematically explore the emergence of triangular patterns, a thorough literature search reveals that sawtooth patterns have emerged during other studies. The first comes from a seminal work by Deegan,[11] in which pattern formation from colloidal particles was systematically explored as a function of the particle size and volume concentration. He found that a sawtooth structure emerges from a solution of 0.1%V/V of 0.1 um nanoparticles evaporated on a freshly cleaved mica substrate (as shown in Figure 8.7a) in which the "darker" phase is a monolayer of particles, and the "lighter" phase is a double layer of particles. As explained in the main text, we believe that this patterning emerges via the same mechanism of a spinodal-like rupture.

Figure 8.7b comes from the previous work reported in Chapter 7 on the formation of spiral patterns on substrates of extreme contact angle hysteresis.[19] There, the drop ruptured at the center, and fluid propagated towards the outer crystalline ring. In some cases, dendritic sawtooth structures were observed at the center of this pattern, where the fluid height was exceptionally thin, and the contact line motion was fast. Like other patterns, a "thin" region of dendritic structure emerged first, with a "thicker" region emerging in a sawtooth structure. Because the fluid motion moved outwards rather than inwards, the thicker phase points inward for these examples.

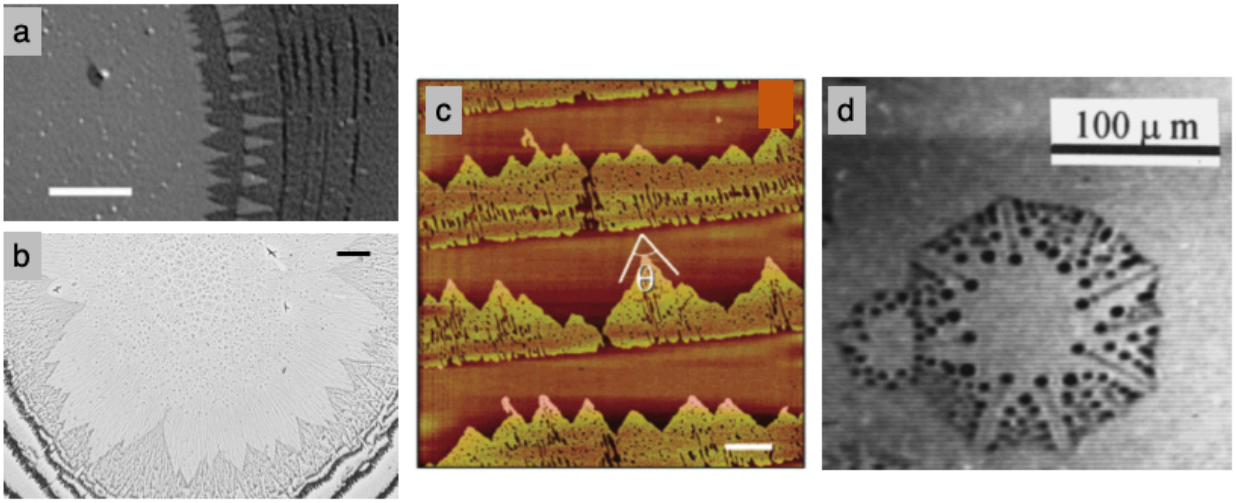

FIGURE 8.7. Sawtooth patterns from other studies. (a) Sawtooth structures composed of mono- and double-layers of 0.1 μm particles from Deegan.[11] Scale bar is 250 μm. (b) Calcium sulfate sawtooth structures formed on a drop in which the interface ruptured at the center, and propagated outward.[19] Scale bar is 100 μm. (c) DPPC Langmuir-Blodgett film deposited onto curved mica.[20] Scale bar is 5 μm. (d) Water drops deposited during rupture of a thin film at room temperature, which have features similar to the branching regime in the present work.[21,22]

The third example (Figure 8.7c) comes from Yuan & Fisher (2007).[20] who observed the emergence of sawtooth structures during Langmuir-Blodgett transfer of a polymer (dipalmitoylphosphatidylcholine, DPPC) from water onto curved mica surfaces. Here, the "darker phase" is a monolayer of the polymer, and the lighter phase is the liquid condensed phase of the polymer. The authors attribute the emergence of this pattern to a Marangoni instability, in which advection dominates in the sub-phase near the boundary layer. Because the radius of curvature in their work was larger than both diffusive and capillary length scales, they argue that the flow of the layer is therefore a long range, hydrodynamic effect.

The final example shown in Figure 8.7d comes from Samid-Merzel *et al.* and Elbaum & Lipson, who show that a rupturing thin film of water creates a pattern of drops aligned into angular shapes from a dewetting point.[21,22] The initial water film was deposited onto a freshly cleaved mica substrate and allowed to evaporate. In their work, evaporation occurs uniformly until the film was a few tens of nanometers thick, at which point the dewetting instability occurs. Wherever the dewetting points nucleate, the water accumulates in a rim and leaves behind the pattern of broken water droplets. In their work, the substrate was completely wetting, and evaporation occurred gradually. This is in contrast to the present work, where the thinness of the film is induced by contact-line pinning caused by the coffee ring effect, and where evaporation is rapid. The combination of these two differences enables the contact line patterning observed here.

Global Drop Behavior

Characterization of the global contact line motion is of interesting for understanding pattern classification and behavior. For a drop evaporating on a completely wetting surface, mass conservation is:

$$\frac{\partial h}{\partial t} + \frac{\gamma}{3\mu}\nabla[h^3 \nabla C] = -\frac{j_o}{R\sqrt{1-\frac{r^2}{R^2}}} \tag{8.1}$$

Where h is the height profile of the drop, R is the outer radius of the drop, γ is surface tension, μ is viscosity, C is curvature of the interface, j_o is the evaporative flux [m^2/s], and r is the radial coordinate. From the analysis of Cachile *et al.,* by neglecting curvature and assuming a constant contact angle (θ),[23] the receding radius due to evaporation of a completely wetting fluid is:

$$R(t) = \sqrt{\frac{16 j_o}{3\theta}(t_{evap} - t)} \tag{8.2}$$

The square root dependence of the position of the contact line with time is well-matched to experimental data as shown in Figure 8.8, which tracks contact line motion with time for an extremely wetting substrate (θ=3°) and a moderately hydrophilic substrate (θ=12°).

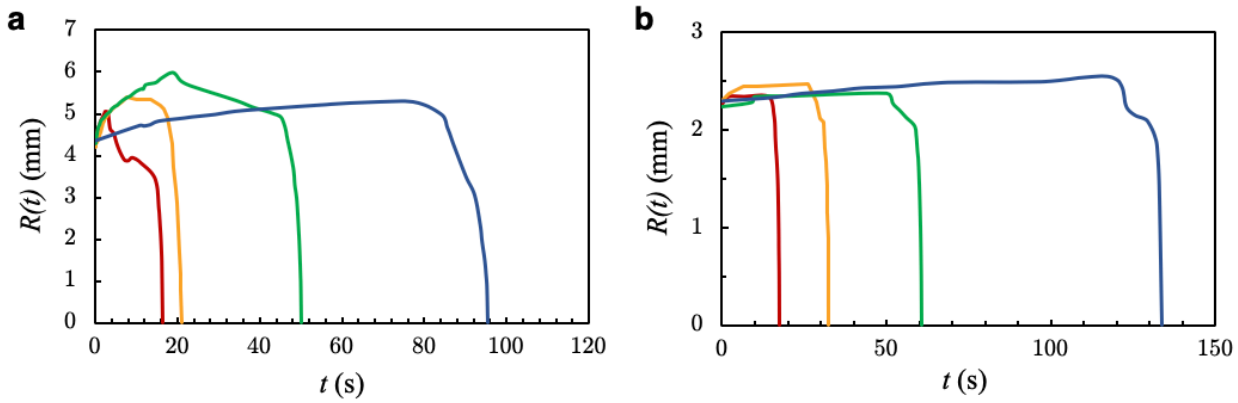

FIGURE 8.8. Radius with time for calcium sulfate solution. (a) for contact angle of 3°, (b) for contact angle 12°. Blue line indicates 40°C, green is 60°C, orange is 8°0C, red is 100°C.

The velocity of the receding interface can be found by taking the time derivative of equation 8.2:

$$V(t) = \sqrt{\frac{4D\Delta C}{3\rho\theta\Delta t}} \tag{8.3}$$

Where $j_o = D\Delta C/\rho$ has been substituted in equation 8.3 (D being diffusivity of water vapor in air, ΔC being the difference in water vapor concentration at the drop interface and in the surrounding air, and ρ being the density of liquid water). From Figure 8.7, we see that the drops on the more hydrophobic samples (contact angle 12°) remain pinned for a longer duration. This highlights the role that the crystalline coffee-ring plays in keeping the drop pinned.

It is also of interest to explore how the spreading of the drop initially placed on the substrate is influenced by the presence of salt. Spreading does not proceed according to Tanner's law ($a(t) \sim t^{1/10}$), as shown in Figure 8.9. It occurs much faster due thermocapillary motion on the hot substrate. Formation of crystals at the contact line decreases the rate of spreading observed for pure water.

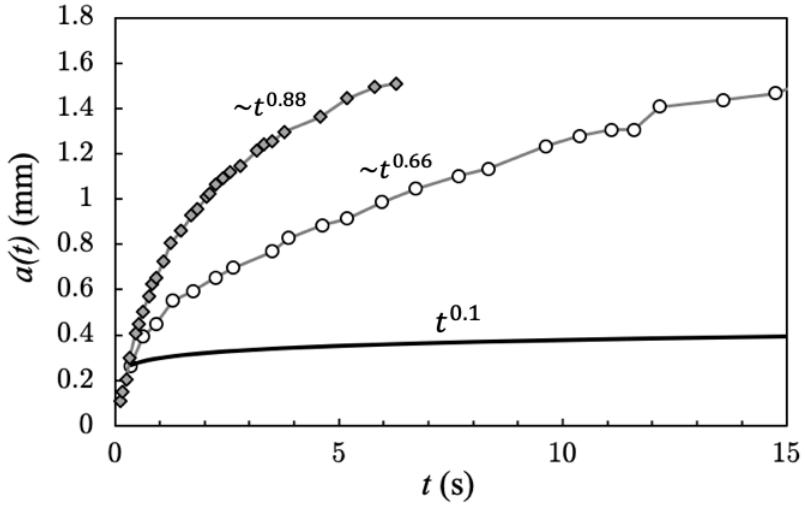

FIGURE 8.9. Snapshot of increase in radius directly after drop deposition with time, on the substrate with contact angle 3° and temperature 60°C. The grey diamonds show the spreading of a drop of pure water, and white circles indicate experimental data for a crystallizing drop. The black line is a model for Tanner's law.

A fingering instability during drop spreading leads to formation of triangles at the initial "coffee-ring" outer diameter, as shown in Figure 8.10. This creates a slower and larger analogy to the mechanism of triangle formation during drop retraction. Small "fingers" form, creating areas of local curvature. As the drop spreads radially, these fingers grow in both azimuthal directions ahead of the main front, leading to formation of triangle shapes.

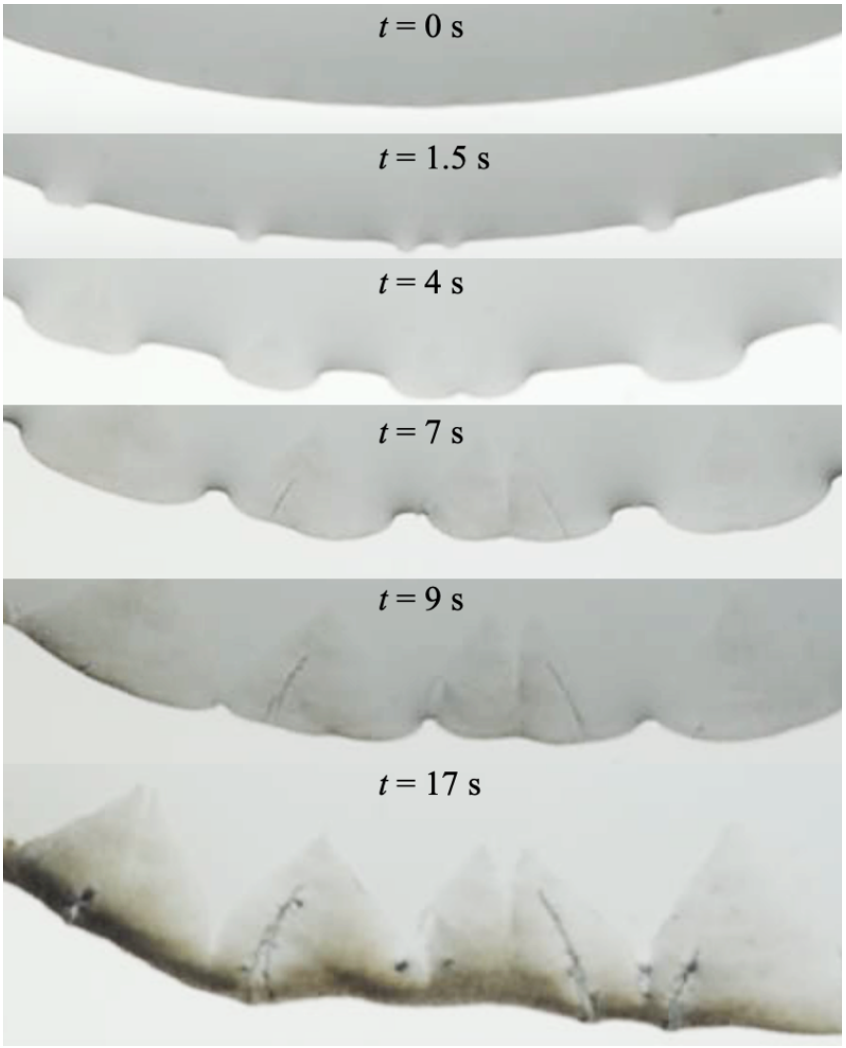

FIGURE 8.10. Fingering instability during drop spreading can lead to triangular formations at the crystalline coffee-ring.

High Speed Analysis

To help extricate the patterning mechanism (or mechanisms), high speed videos were taken to observe the dynamics of pattern formation at the retracting fluid front (Figure 8.11). Careful observation reveals that the thicker, darker phase of the sawtooth patterns retracts faster and has an associated increase in fluid height (Figure 8.11a). This observation indicates that sawtooth patterns are not formed due to air entrainment, such as occurs for sawtooth dewetting fronts that arise during forced dewetting above a critical speed.[18] Instead, regions where the thicker dendrites form have a corresponding thicker fluid film which dewets faster than the thinner region. Eventually, the faster-growing thicker crystalline phases meet, and the thinner phase triangles are terminated.

Branched patterns form from miniscule (<1μm in diameter) drops deposited from the moving contact line, and high-speed videos (Figure 8.11b) suggest that they are not the result of a Rayleigh-like break-up of a fluid filament left on the surface (the mechanism observed in patterning from visco-elastic dewetting fronts). Instead, individual drops are deposited in a row, with the previous drop having dried into a crystal before the next has been deposited from the contact line. Likewise, the periodic arrays (Figure 8.11c) form via deposition of larger (though still small, ~1-5 μm) drops regularly spaced across the moving contact line. Like the branched case, these smaller drops evaporate quickly, so that a crystalline deposit is left in the place of the deposited droplet before the next droplet has disconnected from the contact line.

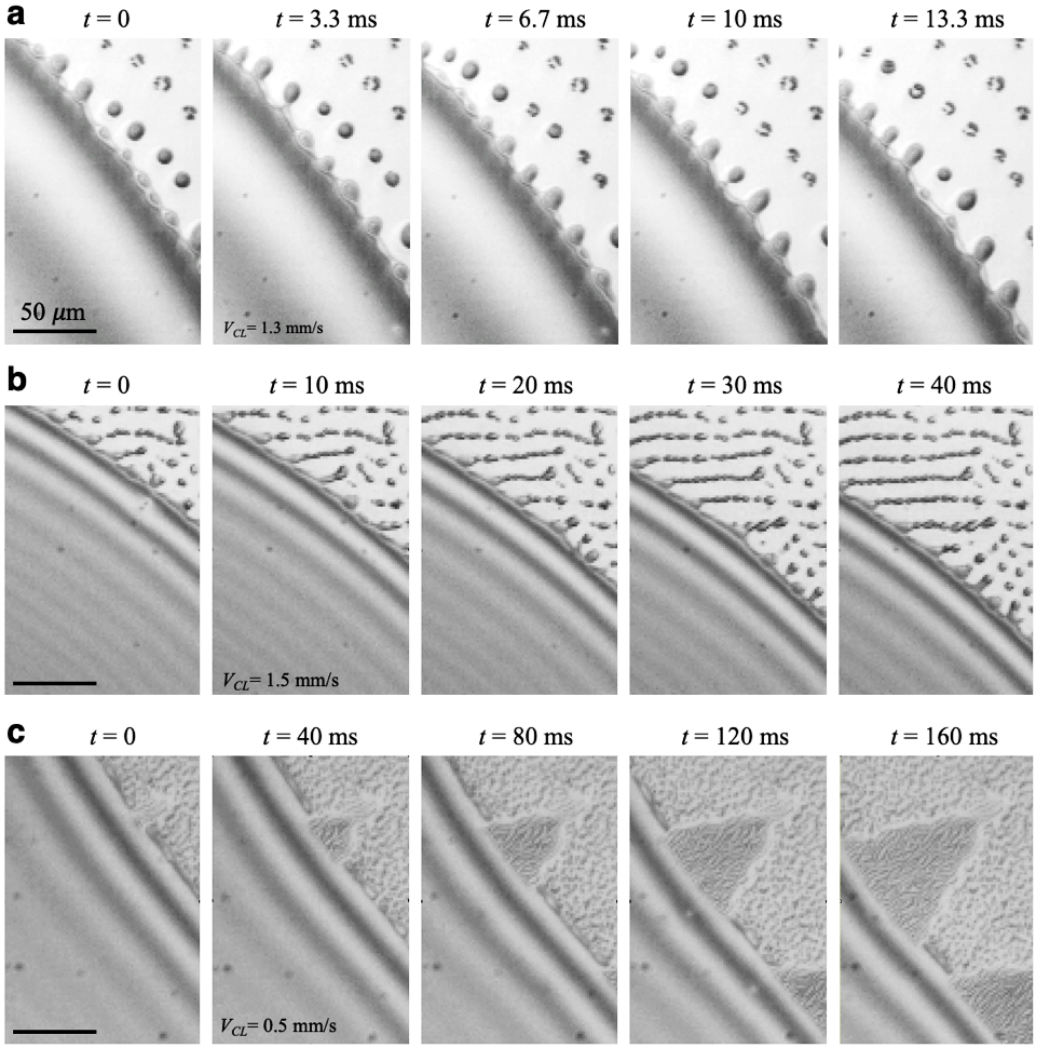

FIGURE 8.11. High speed video frames showing patterning (a) growth of a thicker triangle phase from the mobile contact line. (b) deposition of aligned branches composed of small crystal clusters. (c) deposition of periodic arrays of crystal clusters.

8.2 Mechanisms & Modelling

Marangoni & Spinodal Instabilities

Evidence from high-speed videos and previous experiments allows us to begin to isolate the patterning mechanisms. The array and branched patterns formed here are highly reminiscent of those formed via a previously reported Marangoni instability.[12] In that work, a Marangoni instability formed from differential evaporation rates of water and ethanol resulted in deposition of droplets containing nanoparticles into periodic hexagonal arrays. Here, there are two contributions to a possible Marangoni instability. The first is evaporative cooling. Previous works have seen festoon-like instabilities indicating surface tension gradients in the vicinity of the contact line, suggesting that evaporation could maintain this instability due to heat transfer.[24] The majority of evaporation occurs at the contact line, and thus, a temperature gradient between the mobile contact line and bulk film can form.[25] Second is the influence of the calcium sulfate salt. In thin film Marangoni instabilities, protruding segments of the contact line have a reduced pressure which leads to flow from the thin regions to thicker ones. Salt ions accumulate at the contact line and increase the surface tension. The wavelength of a Marangoni instability is:

$$\lambda_M = 2\pi h/\alpha \tag{8.4}$$

Where h is the height of the thin film and α is a dimensionless parameter describing the magnitude of the Marangoni flow.

A schematic showing the patterning mechanism for a Marangoni instability is shown in Figure 8.12a. The experimental data does exhibit a linear trend with the height of the fluid film, as shown in Figure 8.12b; lending credence to the hypothesis that Marangoni instabilities of the type described by Equation 8.4 dictate the azimuthal wavelength between droplets. Extracting the height of the fluid film at the contact line in the instantaneous moment of patterning is complicated, and this height was approximated as the height of the resultant crystalline features.

Experimental data for radial distance between droplets is also a function of height, as shown in Figure 8.12c. Although both the radial and azimuthal distances increase linearly with height, the slopes of the two differ and there is no clear relationship between these two distances for a given data point. By inspecting the mechanism described in Figure 8.12a, it is possible to write the form of a generic model for the radial dimension β by multiplying a Marangoni timescale by the contact line velocity. Because the Marangoni timescale will be λ/V_{Ma} where V_{Ma} is the characteristic velocity of azimuthal patterning, this model takes the form of:

$$\beta = \lambda V_{CL}/V_{Ma} \tag{8.5}$$

The Marangoni velocity, V_{Ma}, will be a function of both temperature and contact angle.

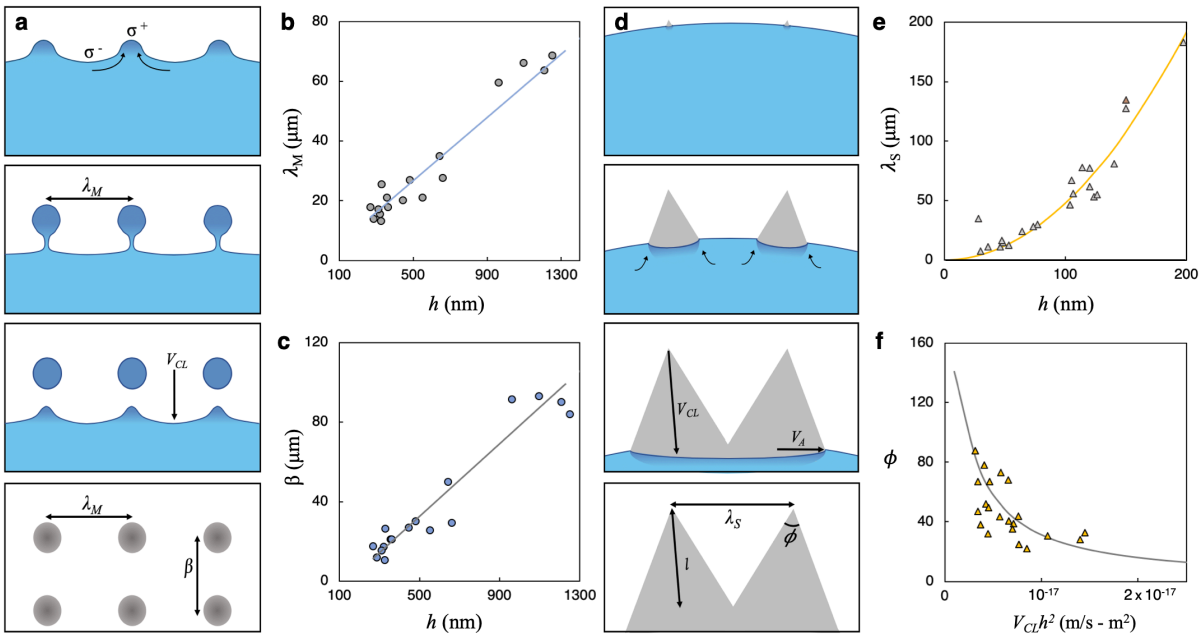

FIGURE 8.12. Patterning Mechanisms. (a) Cartoon showing formation of arrays due to a Marangoni instability. (b) Array wavelength as a function of thin film height (c) distance between consecutive drops as a function of contact line velocity, (d) cartoon showing growth of sawtooth structures, where the curvature of the contact line is exaggerated. (4) wavelength between sawtooth peaks as a function of thin film height, (f) peak angle of sawtooth structures as a function of the height and contact line velocity.

While Marangoni flows seem to control the formation of micro-scale arrays, they do not dictate the formation of the multi-layer sawtooth structures. The formation of these patterns can be understood in the context of a hole opening up in the thin film in a manner than is analogous to spinodal decomposition. Spinodal decomposition is a process in which a thin film (usually of a polymer on a substrate) becomes unstable due to destabilizing effects of polar interactions due to the disjoining pressure, and fluid begins to flow from thinner regions to thicker.[26–28] After a ripening period, the thin regions of the film begin to rupture, and the holes created meet each other to leave behind rings or connected hexagonal branches.

Here, rather than rupturing uniformly across the substrate, “holes” rupture periodically only in the vicinity of the moving contact line; as this is the only region in which the film is thin enough to become subject to such instabilities. The fluid at the contact line increases in depth in the area where these holes nucleate due to the faster retraction. This rupture then becomes the nucleation tip for the thicker triangular structure (first panel of Figure 8.12d). For an immobile contact line, spinodal rupturing creates a circular pattern of dendrites.[29] For a moving contact line, the rupturing “hole” moves slightly faster than the mobile contact line, causing the region of thicker fluid to move both radially and azimuthally (second panel of figure 8.12d). Thus, the thicker crystalline phase grows faster than the thinner phase allowing for creation of the sawtooth structures of periodic thickness. This effect is hydrodynamically driven rather than a consequence of any specific properties of calcium sulfate; and can therefore occur for films of nanoparticles[11] or other solutes as shown in Figure 8.5.[20]

The wavelength of instability for the purely viscous regime of spinodal dewetting has a quadratic dependence with thin film height when Van der Waals forces dominate:[30]

$$\lambda_S = \sqrt{\frac{2\gamma\pi}{A}}h^2 = \frac{h^2}{a} \quad 8.6$$

Where a is a molecular dimension found from surface tension (γ) and Van der Waals forces (A). The use of this equation describing a purely viscous regime is validated by an estimate of the Reynolds number ($Re = hV/\nu$) as $2*10^{-4}$, where the height of the thin film h is the characteristic dimension, V_{CL} is the relevant velocity, and the kinematic viscosity of water was taken at 60°C ($5*10^{-7}$ m^2/s). The molecular dimension a is calculated as 0.2 nm using using A=1.6 $*10^{-20}$ J for a water/silica system, allowing us to plot equation 8.6 (solid yellow line) against experimental data (grey triangles) as shown in Figure 8.12e. The single red triangle in Figure 8.12e at h=150 nm represents the triangular structures reported by Deegan[11]; where the thin film height was estimated at 150 nm because his triangular pattern was a phase boundary between a monolayer of 100 nm particles and a double layer of particles at a height of 200 nm.[11]

The base angle of the triangular features decreases with increasing speed of the receding contact line. This is in line with the observations from sawtooth pattern formation in adverse reaction fronts, in which increased flow speed increased the sharpness of sawtooth angles.[31] Thus, the triangle angle ϕ (see bottom panel of figure 8.12d) here should be a function of the velocity of the contact line and the velocity of the azimuthal instability velocity, V_A:

$$\phi = 2\tan^{-1} V_A/2V_{CL} \quad 8.7$$

The timescale for spinodal rupture in a purely viscous regime is:[30]

$$\tau_S = \frac{\mu\lambda_S^3}{\gamma h^2} \quad 8.8$$

Where λ_s is given by equation 8.6, h is the height of the thin film, γ is the surface tension of water, and μ is the viscosity of water. Assuming that the azimuthal velocity of the instability is equal to the wavelength given in equation 8.6 divided by the timescale of equation 8.8, the velocity becomes:

$$V_A = \frac{\lambda_S}{\tau_S} = \frac{\gamma h^2}{\mu\lambda_S^2} = \frac{\gamma a^2}{\mu h^2} \quad 8.9$$

Substituting this relation into equation 8.7, the angle of the triangular features becomes:

$$\phi = 2\tan^{-1} V_A/2V_{CL} = 2\tan^{-1}\frac{\gamma a^2}{2\mu V_{CL}h^2} = 2\tan^{-1}\frac{A(T)}{V_{CL}h^2} \quad 8.10$$

Where *A(T)* is a function combining all of the temperature dependent terms ($A(T) = \gamma a^2/2\mu$). Equation 8.10 is plotted in figure 8.12f using values for *A(T)* at 60°C as the grey line. Experimental data (yellow triangles) exhibits some deviation from the model; but are within the same order of magnitude.

The final category of patterning, branching, lies in a regime between the array and triangular regimes. These patterns seem to have features of both the arrays (individual dots with characteristic spacings) and of the triangles (branches align into specific angles, and occasionally have phase transitions where the phase boundary is semi-triangular, see Figure 8.1c(ii)). It is therefore reasonable to assume that both the mechanism responsible for arrays (hypothesized to be Marangoni), and that for the triangles (hypothesized to be a spinodal-like instability) contribute to the branching regime.

Figure 8.13 shows a transition from a chaotic patterning into the branched region. The phase boundary between the two is triangular. The larger height of the moving contact line exaggerates the difference in the contact line motion between the two regions as compared to the triangular regime, where differences are difficult to see. We are able to better see how a nucleating "dry region" in the thin films expands into a triangular phase boundary as the contact line retracts; and shows how the branching regime is able to have characteristics from both the triangular regime caused by a spinodal-like instability and the Marangoni regime in which drops are deposited from the film.

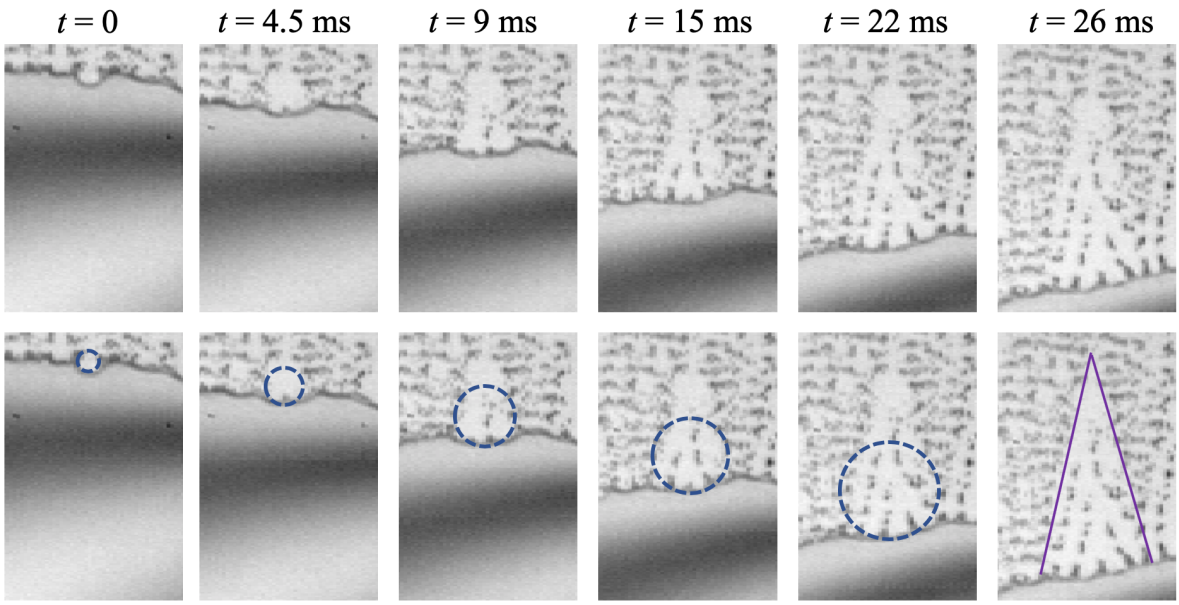

FIGURE 8.13. Triangular phase boundary formation in the branching regime.

Alternative Mechanisms

I have argued that a Marangoni instability is responsible for patterning of arrays, while a hydrodynamic spinodal-like effect leads to triangular patterns. Experimental data is well-matched to the predictions based on these mechanisms. However, as with many patterning phenomena, there are multiple mechanisms that could lead to similar patterns. I therefore briefly discuss some of those mechanisms and the reasons for which they were rejected.

Reaction-Diffusion Patterning. Periodic precipitation (aka, Liesegang) patterns formed via reaction-diffusion can be strikingly similar to the patterns observed here (see reference).[2] Liesegang precipitation occurs when one reactive ion is embedded within a tightly packed matrix such as a gel or sedimentary rock, and a reactive counter ion slowly permeates into this matrix with no advective mixing.[32] As the two species of reactive ions come into contact, they precipitate as periodic patterns rather than uniformly throughout the matrix.[33] The mechanism behind this phenomenon is debated, but is typically attributed to some variation of a supersaturation-nucleation-depletion cycle, first proposed by Ostwald.[34] In a cylindrical geometry, these reaction-diffusion precipitation patterns typically leave concentric rings; but one investigation in which sulfide (S^{2-}) ions were introduced at the center of a gel imbedded with cadmium ions (Cd^{+2}) and allowed to diffuse for 48 hours observed formation of sawtooth patterns and hexagonal lattices of the resulting cadmium sulfide crystals.[2]

Because of the similarities between reaction-diffusion patterns and those formed here, I considered the hypothesis that crystal patterns form at the substrate via some form of a reaction-diffusion mechanism prior to dewetting. In this case, the dewetting interfaces would retract around existing crystals and the interface movement/deformations would be attributed to these existing obstacles. However, I reject this hypothesis in favor of the hypothesis that crystal patterning occurs only in the immediate vicinity of the retracting interface due to the following observations: (1) high speed videos reveal that the droplets are sometimes dragged with the moving interface and can be displaced up to 30 nm from their original position, (2) videos taken from below on a glass substrate show crystal formation at the interface while little is observed in the bulk, and (3) previous studies which have concluded that crystallization leaves a record of hydrodynamic behavior.[6]

Rayleigh – Plateau Instability. The Rayleigh-Plateau (RP) instability describes the growth of perturbations on a column of fluid until the column eventually breaks into discrete drops, and is controlled by surface tension, density, and viscosity of the fluid. While typically used to describe break-up of a fluid jet, the same mechanics can describe a fluid rim created during dewetting/retraction of a thin film.[35] The dewetting rim grows as the film ruptures, and can become unstable, leading to pinch off of discrete droplets. Typically, such an instability leads to a polygonal network of drops.[36] However, in our case, evaporation is also occurring. The timescale of the RP type instability observed for viscous films is much larger (~2 minutes to form 1 row of drops) than the timescale we see here (~0.1 s to form 1 row of drops). For the Rayleigh-Plateau breakup of a liquid film, the wavelength of instability is:

$$\lambda = \frac{4h\pi}{\theta} \quad 8.11$$

And the timescale of the same instability is:

$$\tau = \frac{64\mu h}{\gamma\theta^4} \quad 8.12$$

Given that the height-dependence of this instability is similar to that of the Marangoni one discussed previously, it is reasonable to wonder whether these drops are due to the Rayleigh-Plateau instability of a liquid rim rather than due to Marangoni flows. For a typical experiment on a substrate of contact angle 10, height of 100 nm, and 60°C, I estimate a wavelength of 7.2 μm and timescale of 50 micro-seconds; which is indeed on the correct order of magnitudes for these patterns. However, based on careful observation of the highspeed videos, the drops do not appear to be formed from break-up of an unstable rim of fluid. It is likely that there is some cross-over between the Marangoni and RP instabilities in these studies, and that the RP dominates when the thin-film break up is fast compared to evaporation. However, when evaporation is the dominant process in driving contact line motion, Marangoni effects should dominate.

Other Thin Film Effects. For nanometric-thin films such as those in the present investigations, a disjoining pressure comprised of Van der Waals forces, electrostatic interactions, and other surface forces dictates drop spreading and film dynamics.[37,38] . When films are thinned to about 100 nm, intermolecular forces have a huge influence on the dynamics.[21] For an ultra-low energy solid substrate such as our oxidized silica, these forces become destabilizing and amplify perturbations. When films thin even more to ~10nm, short-range electrostatic repulsive forces form from the overlapping double layers at the substrate surface and the air-water interface; creating a stabilizing force countering rupture.[37] Thicker portions recede more slowly, and thus the instability grows.[24] Previous investigations have observed hexagonal arrangements of nanoparticles deposited from dewetting of thin films.[27,39]

In the previous explanation shown in Figure 8.12, I only consider the influence of the Van der Waals forces on thin film instabilities. However, it is worth briefly considering other contributors to the short range interfacial forces. The four forces to consider: hydration, electrostatic, van der Waals, and elasticity. The first, hydration forces, refers to the network of hydrogen bonds between the surface and the water which alters the structure of water molecules in the vicinity of the substrate. This structural force decays exponentially with the length scale of the water molecule, and disappears within 1-2 nm. Elastic forces arise from structural interactions as well. Water near a hydrophilic substrate will attempt to organize itself into a lattice that matches its crystallization structure (i.e., the lattice of ice). However, it is rare that the underlying substrate and distribution of hydroxyl radicals will match this lattice. Thus, there is an epitaxial mismatch between the water and substrate causing the water lattice to deform, and generating an elastic strain. Like hydration force, this is a structural force and decays within a few length scales of the water molecules.

Electrostatic forces are more long-range for dilute ionic solutions and are important for a water solution containing ions. The length scale of this force is typically given as the Debye double layer length:

$$\lambda_D = \sqrt{\frac{\epsilon k_B T}{e^2 I}} \tag{8.13}$$

For 2:2 electrolytes such as calcium sulfate, this becomes:

$$\lambda_D = \frac{0.152}{\sqrt{C_{CaSO4}}} \tag{8.14}$$

Where C_{CaSO4} is the molar concentration of calcium sulfate, which is the saturation concentration of 0.015 M (2.1 g/L, MW 136.14 g/mol), giving the Debye double layer length as 1.24 nm. The potential energy density for a water film of thickness h is:

$$w_{el}(h) = 64 k_B T \rho \gamma^2 \lambda_D \exp -h/\lambda_D \tag{8.15}$$

Where k_B is the Boltzmann constant, *T* is the temperature in Kelvin, ρ is the bulk concentration of salt, γ^2 is a factor related to the surface potential (~0.5 for oxidized silica in the presence of water containing calcium sulfate). Van der Waals forces tend to be weaker than hydration or electrostatic forces, but become important on length scales between 10 and 50 nm. The energy density is:

$$w_{VDW}(h) = -\frac{A}{12\pi h^2} \tag{8.16}$$

For water on silica in the presence of air, A ranges between -1 and -2 $*10^{-20}$ J, where the negative value indicates an increase in energy for thinner films. The value used previously to match experimental data was $-1.6*10^{-20}$ J.

The total energy density of the system is the sum of the different components:

$$w = w_{el} + w_{VDW} + w_{structural} \tag{8.17}$$

Typically, electrostatic and structural components are neglected in studies of thin film dynamics because of the small length scales on which they matter. When only electrostatic and VDW forces are considered, the DLVO theory arises. Whether or not structural and electrostatic forces matter for the present work could be debated, as the film thickness in the vicinity of the contact line is estimated to be ~30-100 nm for triangular patterns, and ~150-250 nm for the arrays. Neglecting structural forces, the disjoining pressure of the solution is:

$$P(h) = -\frac{dw}{dh} = \left(64 k_B T \rho \gamma^2 \exp -\frac{h}{\lambda_D}\right) - \frac{A}{6\pi h^3} \tag{8.18}$$

Where the disjoining pressure gives the difference in pressure that accounts for thin-film interactions. For this formulation of disjoining pressure, stability analysis yields a critical wavelength of instability as:

$$\lambda = \sqrt{\frac{4\gamma\pi^2}{\frac{A}{2\pi h^4}+\frac{32k_BT\rho}{\lambda_D}\exp-\frac{h}{\lambda_D}}} \qquad 8.19$$

Thus, Equation 8.6 could be altered to take both VDW and electrostatic forces into account. Application of this equation yields worse predictions for experimental data than does version shown in equation 8.6.

Convection Cells. Internal convection is an important mechanism for many evaporation-induced patterning effects. Global recirculation in an evaporating drop of colloidal solution can lead to re-distribution of nanoparticles from the drop contact line towards the drop interior (thus disrupting the coffee ring effect). A recent study has attributed the formation of dendritic patterns from a quickly evaporating drop containing reactive zinc oxide nanoparticles to Benard-Marangoni convection (caused by balance between surface tension gradients, and temperature-induced density differences causing gravitational convection). In Benard-Marangoni (BM) convection, hexagonal convective cells arise due to a temperature gradient between a heated substrate and cooler air-fluid interface. Unlike pure Benard convection, BM flows also have a contribution from the variability in surface tension due to temperature differences at the free surface. Another study has predicted that a Rayleigh-Taylor instability (for a thin film on the underside of a cooled substrate) can create branched and/or periodic hexagonal arrays from the rupture of a thin film stabilized by evaporation.[40]

Ejection of Microdrops. A final alternative hypothesis of interest arises from the observation of self-organization of microdroplets into hexagonal arrays levitated over heated substrates or heated water films (where substrate temperature is varied between 80-90°C).[41] In these levitation experiments, microdrops are ejected from a macroscopic drop contact line due to the large evaporative flux at contact lines, and settle into a levitated position above the dry region of the substrate until they evaporate. The mechanisms of both levitation and the patterning into hexagonal arrays are debated, but may be attributed to evaporative Stefan flows.[41] Given the similarity in experimental conditions and patterns formed between the present study and those investigating patterned levitating drops, it is conceivable that similar mechanisms contribute to both; though our observation of hexagonal patterning at room temperature for contact angles between 2-4º suggests that the mechanism here is more reliant on the hydrodynamic instability than on powerful evaporative fluxes. Furthermore, high speed videos demonstrate that microdrops grow from a contact line instability, rather than being ejected; and that these drops pin to the substrate rather than levitating.

8.3 Masking Applications

Patterns such as the ones described here have several applications in sensors, diagnostics, optics, and more. The patterning effect could therefore be used for a number of applications relying on physical or chemical masking to create micro- or nano-scale patterns.

One application of relevance for fluid mechanics is creating substrates with controlled three-dimensional micro-structures for creating superhydrophobic surfaces with calculable properties.[42] Micro-pillar textures are routinely etched into silicon wafers using a procedure following these generic steps: (1) coating and baking of a photoresist, (2) patterning the photoresist using a mask aligner, (3) developing the photoresist, (4) reactive ion etch (which etches silica in regions where photoresist was removed by the masking/development), and (5) removing the photoresist. Steps 1,3 and 5 involve use of expensive and toxic chemicals.

By using the technique for patterned deposition reported here, it is possible to skip steps 1-3 for developing micro-pillar textures completely. A patterned substrate was placed directly in a reactive ion etch and etched to a depth of ~10 μm, as shown in Figure 8.14a. The presence of the gypsum crystals effectively prevented etching of those regions to create a micro-pillar structure. The crystals were then removed by soaking in a bath of saline water for about 10 minutes followed by rinsing with DI water. Calcium sulfate and sodium chloride exhibit an effect called the uncommon ion effect, in which the presence of one salt increases the solubility of the other.[43] Thus, I am able to fabricate a silica surface with microscale three-dimensional patterns without the use of any solvent chemicals. This procedure is also significantly faster than the normal procedure for etching silica patterns.

Another potential application is the creation of patterned metallic surfaces; which are notoriously difficult to etch in controlled ways. A patterned substrate was sputter coated with a 20 nm layer of gold, as shown in Figure 8.14b. Defects in the sputter coating caused by the crystal mask allow for water intrusion and dissolution of the crystals after soaking in a saline bath for a period of 6 hours. The resulting sample is patterned gold/silica. Because this method is invariable to substrate chemistry (see Figure 8.4), it is possible to deposit crystalline patterns on a variety of substrates, including metallic ones. Thus, this masking/sputter coating procedure can be applied to generate any number of patterned chemical combinations.

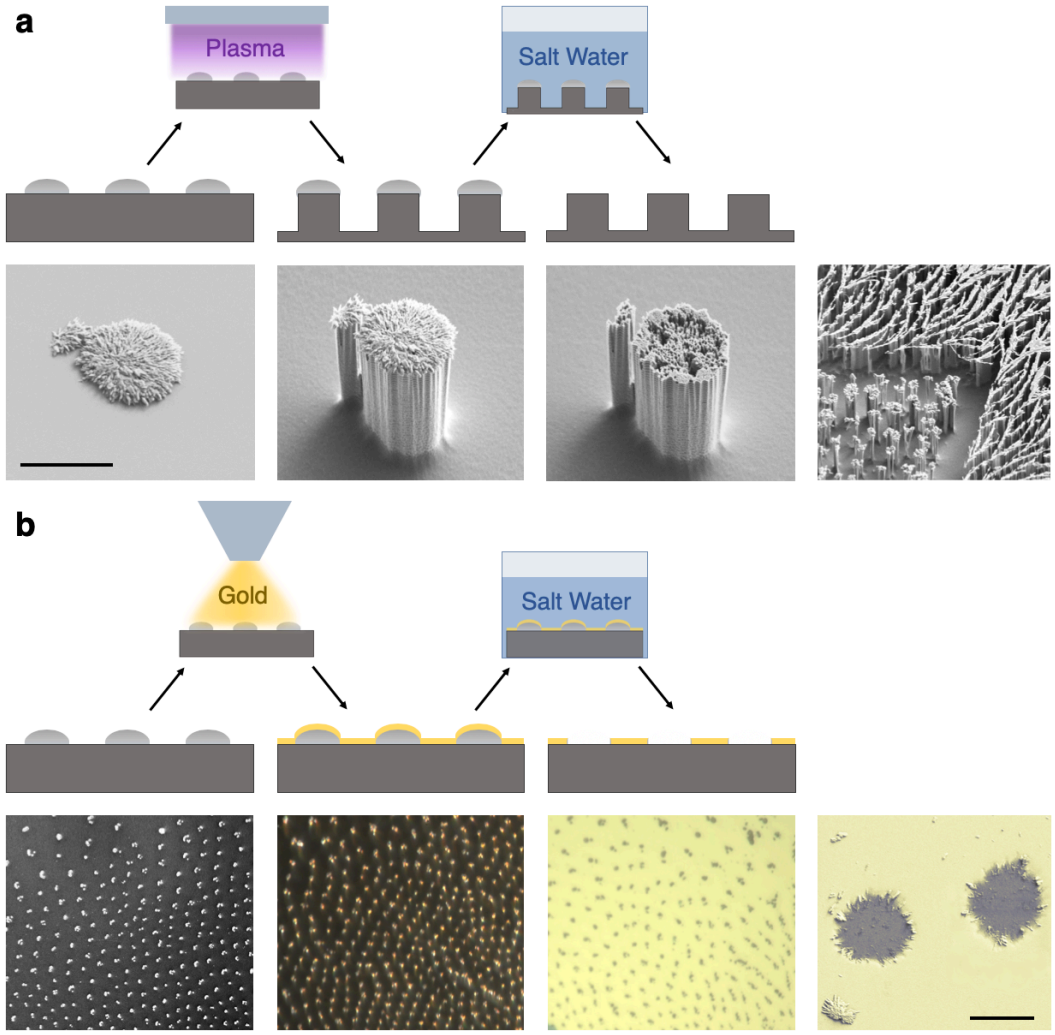

FIGURE 8.14. Demonstration of masking applications. (a) Creation of three-dimensional microstructures by placing patterned substrates directly in reactive ion etch, followed by removal of gypsum crystals using saline water. Scale bar is 5 μm. (b) Patterned gold/silica regions. A patterned sample was sputter-coated with gold to a depth of 20 nm. Crystals were then removed using saline water to create a substrate of patterned gold/silica region.

A final application of note for these instability-generated masks is creating a sample of patterned hydrophobicity, which have applications for anti-fouling, microfluidics control, and more. The silica substrate can be functionalized with a hydrophobic polymer by either a vapor phase or solvent-phase deposition. Once crystals are dissolved, the resulting substrate has patterned regions of hydrophilic and hydrophobic features. Triangular hydrophilic/hydrophobic patterns can be used for directional transport of drops and fog collection.[44]

Conclusions

I have shown how a cooperative effect between crystallization and fluid instabilities can generate a number of patterns which reflect contact line motion during dewetting. These patterns include sawtooth structures, periodic arrays, and a third branching regime which exhibits characteristics of the two prior regimes. These regimes are controlled by the wettability of the substrate and evaporation rate of the water.

Triangular patterns have been previously observed by other studies but never explored in depth. Such patterns are phase boundaries between a relatively thin and thick region, and form across a number of different substrates and from several different solutes including polymers and nanoparticles. The observation of triangular features from drying films across so many systems provides strong evidence that the formation is controlled by interfacial physics and instabilities rather than by some effect of the solute/crystals. However, I do find that patterning is particularly robust for calcium sulfate crystals. This is due to a combination of calcium sulfate's solubility and crystallization properties.

Evidence from experimental data and observations has allowed me to refine a hypothesis explaining pattern formation. There seem to be two thin-film instabilities contributing to the geometrical properties of resulting patterns: Marangoni and Spinodal. The Marangoni instability occurs in the regimes with higher thin film thicknesses (lower temperatures, higher contact angles). It arises from a combination of temperature and chemical induced changes to surface tension, and causes micro-droplets to pinch off from the unstable dewetting front.

The second mechanism, spinodal dewetting, can explain the formation of triangular shapes on the most hydrophilic substrates. Spinodal dewetting usually occurs in thin polymeric films, and describes the nucleation of dry zones which occurs under a critical film thickness. Dry zones retract and accumulate liquid around a ridge. Here, dry zones are only able to nucleate in the immediate vicinity of the contact line, as this is the only area where liquid is thin enough to be subject to thin film instabilities. Because the contact line is moving, retraction of the rim moves in the same direction as the contact line, but at a slightly faster rate. This results in an expanding region of a relatively thicker fluid height which leaves behind a sawtooth pattern. Both the Marangoni and spinodal-like mechansisms are sufficient to explain formation of the two patterning regimes, and models from these instabilities are well-matched to experimental data.

The crystalline patterns can be used as a mask for a huge variety of applications. The tested applications include (1) as a mask for reactive ion etch to create three-dimensional silica microposts, (2) as a mask for sputter coating areas of different chemistries, (3) as a mask for deposition of a hydrophobic polymer to create a substrate with patterned hydrophobicity. There are many more possible applications too numerous to explore here.

References

1. Epstein, I. R. & Xu, B. Reaction–diffusion processes at the nano- and microscales. *Nat. Nanotechnol.* **11**, 312–319 (2016).
2. Dayeh, M., Ammar, M. & Al-Ghoul, M. Transition from rings to spots in a precipitation reaction–diffusion system. *RSC Adv.* **4**, 60034 (2014).
3. Deegan, R. D. *et al.* Capillary flow as the cause of ring stains from dried liquid drops. *Nature* **389**, 827–829 (1997).
4. Zahedi, H. & Foroutan, M. Molecular dynamics simulation of a water nano-droplet on graphene oxide surface at high temperature: Evaporation or spreading? *Appl. Surf. Sci.* **455**, 789–794 (2018).
5. Tarasevich, Y. & Pravoslavnova, D. Segregation in desiccated sessile drops of biological fluids. *Eur. Phys. J. E* **22**, 311–314 (2007).
6. Rogowski, R. Z. & Darhuber, A. A. Crystal Growth near Moving Contact Lines on Homogeneous and Chemically Patterned Surfaces. *Langmuir* **26**, 11485–11493 (2010).
7. Wu, H. & Briscoe, W. H. Morphogenesis of polycrystalline dendritic patterns from evaporation of a reactive nanofluid sessile drop. *Phys. Rev. Mater.* **2**, 045601 (2018).
8. Harrington, G. F., Campbell, J. M. & Christenson, H. K. Crystal Patterns Created by Rupture of a Thin Film. *Cryst. Growth Des.* **13**, 5062–5067 (2013).
9. Rigos, A. A. & Deutch, J. M. Concentration Effects on the Mullins-Sekerka Instability. *J. Appl. Phys.* **86**, 264 (1987).
10. Ben-Jacob, E. & Garik, P. The formation of patterns in non-equilibrium growth. *Nature* **343**, 523–530 (1990).
11. Deegan, R. D. Pattern formation in drying drops. *Phys. Rev. E* **61**, 475–485 (2000).
12. Cai, Y. & Zhang Newby, B. Marangoni Flow-Induced Self-Assembly of Hexagonal and Stripelike Nanoparticle Patterns. *J. Am. Chem. Soc.* **130**, 6076–6077 (2008).
13. Thiele, U. Patterned deposition at moving contact lines. *Adv. Colloid Interface Sci.* **206**, 399–413 (2014).
14. Fanton, X. & Cazabat, A. M. Spreading and Instabilities Induced by a Solutal Marangoni Effect. *Langmuir* **14**, 2554–2561 (1998).
15. Cazabat, A. M., Heslot, F., Troian, S. M. & Carles, P. Fingering instability of thin spreading films driven by temperature gradients. *Nature* **346**, 824–826 (1990).
16. Bäumchen, O. *et al.* Influence of Slip on the Rayleigh-Plateau Rim Instability in Dewetting Viscous Films. *Phys. Rev. Lett.* **113**, 014501 (2014).
17. Deblais, A., Harich, R., Colin, A. & Kellay, H. Taming contact line instability for pattern formation. *Nat. Commun. 2016 7* **7**, 12458 (2016).
18. Blake, T. D. & Ruschak, K. J. A maximum speed of wetting. *Nature* **282**, 489–491 (1979).
19. McBride, S., Khan, S., Dash, S. & Varanasi, K. K. Crystallization of Spirals from Drops. *Langmuir* **Just Accep**, (2019).
20. Yuan, J. & Fischer, T. M. Modulated Pattern Formation of Phospholipid Monolayers on Curved Surfaces. *Langmuir* **23**, 3603–3605 (2007).
21. Samid-Merzel, N., Lipson, S. G. & Tannhauser, D. S. Pattern formation in drying water films. *Phys. Rev. E* **57**, 2906–2913 (1998).
22. Elbaum, M. & Lipson, S. G. How Does a Thin Wetted Film Dry Up? *Phys. Rev. Lett.* **77**, (1994).
23. Cachile, M., Bénichou, O. & Cazabat, A. M. Evaporating Droplets of Completely Wetting Liquids. *Langmuir* **18**, 7985–7990 (2012).
24. Poulard, C., Bénichou, O. & Cazabat, A. M. Freely Receding Evaporating Droplets. *Langmuir* **19**, 8828–8824 (2003).
25. Yiantsios, S. G. & Higgins, B. G. Marangoni flows during drying of colloidal films. *Cit. Phys.*

Fluids **18**, (2006).
26. Higgins, A. M. & Jones, R. A. L. Anisotropic spinodal dewetting as a route to self-assembly of patterned surfaces. *Nature* **404**, 476–478 (2000).
27. Thiele, U., Mertig, M. & Pompe, W. Dewetting of an Evaporating Thin Liquid Film: Heterogeneous Nucleation and Surface Instability. **30**, (1998).
28. Stannard, A., Martin, C. P., Pauliac-Vaujour, E., Moriarty, P. & Thiele, U. Dual-Scale Pattern Formation in Nanoparticle Assemblies. *J. Phys. Chem. C* **112**, 15195–15203 (2008).
29. Vancea, I. *et al.* Front instabilities in evaporatively dewetting nanofluids. *Phys. Rev. E* **78**, 041601 (2008).
30. Gennes, P.-G. de., Brochard-Wyart, F. & Quéré, D. *Capillarity and wetting phenomena : drops, bubbles, pearls, waves*. (Springer, 2004).
31. Atis, S., Saha, S., Auradou, H., Salin, D. & Talon, L. Autocatalytic Reaction Fronts Inside a Porous Medium of Glass Spheres. *Phys. Rev. Lett.* **110**, 148301 (2013).
32. Cartwright, J. H. E., García-Ruiz, J. M. & Villacampa, A. I. Pattern formation in crystal growth: Liesegang rings. *Comput. Phys. Commun.* **121**, 411–413 (1999).
33. Liesegang, R. Ueber einige eigenschaften von gallerten. *Naturwissenschaftliche Wochenschrift* **10**, 353–362 (1896).
34. Ostwald, W. Zur Theorie der Liesegang-Ringe. *Kolloid-Zeitschrift* **40**, 144–148 (1926).
35. Peschka, D. *et al.* Signatures of slip in dewetting polymer films. *Proc. Natl. Acad. Sci. U. S. A.* **116**, 9275–9284 (2019).
36. Alizadeh Pahlavan, A., Cueto-Felgueroso, L., Hosoi, A. E., McKinley, G. H. & Juanes, R. Thin films in partial wetting: stability, dewetting and coarsening. *J. Fluid Mech.* **845**, 642–681 (2018).
37. Craster, R. V. & Matar, O. K. Dynamics and stability of thin liquid films. *Rev. Mod. Phys.* **81**, 1131–1198 (2009).
38. Craster, R. V, Matar, O. K. & Sefiane, K. Pinning, Retraction, and Terracing of Evaporating Droplets Containing Nanoparticles. *Langmuir* **25**, 3601–3609 (2009).
39. Herminghaus, S. *et al.* Spinodal dewetting in liquid crystal and liquid metal films. *Science* **282**, 916–9 (1998).
40. Bestehorn, M. & Merkt, D. Regular Surface Patterns on Rayleigh-Taylor Unstable Evaporating Films Heated from Below. *Phys. Rev. Lett.* **97**, 127802 (2006).
41. Zaitsev, D. V, Kirichenko, D. P., Ajaev, V. S. & Kabov, O. A. Levitation and Self-Organization of Liquid Microdroplets over Dry Heated Substrates. *Phys. Rev. Lett.* **119**, 094503 (2017).
42. Patankar, N. A. On the Modeling of Hydrophobic Contact Angles on Rough Surfaces. *Langmuir* **19**, 1249–1253 (2003).
43. Cameron, F. K. Solubility of Gypsum in Aqueous Solutions by Sodium Chloride. *J. Phys. Chem.* **5**, 556–576 (1901).
44. Song, Y. *et al.* Temperature-tunable wettability on a bioinspired structured graphene surface for fog collection and unidirectional transport. *Nanoscale* **10**, 3813–3822 (2018).

Chapter 9.

Crystal Critters: Ejection of Salt from Nanostructure Surfaces

The motivation stated at the beginning of this thesis was to use the drop evaporation as a tool to explore mineral-fouling. Mineral fouling occurs when crystal growth causes damage to a solid material, and is a pervasive problem in water treatment, desalination, thermoelectric power production, and other industrial processes. Thus far, I have explored problems related to bulk mineral fouling in Chapter 3 and have investigated crystal patterning as a function of wetting properties throughout Chapters 5,6,7 and 8. In the present chapter, these two concepts merge into a final study on drop evaporation with direct implications for mineral fouling prevention.

In this chapter, I present a curious phenomenon in which crystal globes grown from an evaporating drop on a heated superhydrophobic surface proceed to self-eject from that surface via growth of crystalline legs. We call these structures "crystal critters" due to a resemblance to living creatures. Crystal critters have exceedingly minimal contact with the substrate and are easily removed. This unusual effect is robust to contamination of other salts and even to surfactants, and we demonstrate that it is caused by the specific texture of superhydrophobic surface which prevents salt intrusion and spreading. We also develop a simple model predicting the growth rate of critter legs as a function of the evaporation rate and confirm predictions against experimental data. This peculiar effect has potential application in cooling towers using water spray heat exchange, where pure water is typically required to impede mineral fouling. By implementing substrates that induce self-ejection of crystals, it may be possible to use salt brines rather than ultra-pure water, and thus preserve fresh water resources while also reducing water treatment costs.

9.1 Crystal Critters

Motivation

Many of the uses for water are intimately familiar to us. Drinking water, wash water, water for agriculture, and even water used for recreation have an omnipresent and essential impact on our lives. However, water's impact and importance extend far beyond these everyday uses. In many developed countries, thermoelectric power production is one of the largest sources of water consumption,[1] where it is used to cool reactors and transport heat. In 2015, 41% of all surface water withdrawals in the U.S. went towards cooling in thermoelectric power plants.[2] Thermoelectric power accounts for 90% of all electricity generated within the US and encompasses many forms of power production, including nuclear, coal, natural gas, and oil.

In its role as a coolant, water is either sprayed on, flown through, or otherwise placed in contact with hot equipment (pipes, tanks, reactors, etc.). Many cooling processes use evaporation as a vital part of heat exchange due to the large heat transfer associated with phase change. However, when water is evaporated, contaminants within the water (including minerals) will be deposited at the point of evaporation. Over time, accumulation of these impurities reduce heat transfer performance, block pipes, and generally cause material corrosion and deterioration.[3] Mineral fouling, in particular, is a leading cause of equipment degradation and failure in heat exchange processes.[4] To prevent mineral fouling, significant effort and monetary investment goes towards pre-treatment of coolant water using technologies such as ion exchange and reverse osmosis.[2]

Due to the ever increasing importance of water-conservation,[5] more and more water for thermoelectric cooling is being sourced from saline surface waters or from desalination waste brines rather than from freshwater sources;[6] despite the associated increases in pre-treatment costs. Surface engineering for control of salt-substrate interactions is one alternative method to excessive water treatment that can effectively address mineral-fouling in heat exchange.

One method of examining interactions between a liquid, surface, and crystallizing solute is via drop evaporation. Traditionally, drop evaporation experiments are motivated by applications in self-assembly and detection.[7,8] Previous investigations have demonstrated that this technique can be used as a method of exploring crystal adhesion and interfacial properties,[9] and can inform on how damage to surfaces caused by crystallization occurs.[10] Interfacial properties[11] and nucleation barriers associated with different crystal chemistries control deposit morphologies (see Chapter 5).

Evaporating a drop of a volatile liquid containing a non-volatile solute will induce crystallization of said solute due to rising concentrations eventually exceeding the solubility limit. For solutes of low solubility, the patterns left by evaporative crystallization are similar to "coffee-ring" patterns formed by evaporation of a particle-laden drop.[7,9] However, when the dissolved mass is excessive, three-dimensional crystal structures may arise. In particular, when a drop containing saturated

sodium chloride is evaporated on a hydrophobic surface, “salt globes” form due to the propensity of crystals to nucleate at the air/water interface.[12] These globes leave a record of the shape of the evaporating drop at the point at which the solubility limit is exceeded.

Observation

In these experiments, a 5 μL drop of water containing sodium chloride dissolved to its solubility limit is placed on a superhydrophobic surface heated to a temperature T (Figure 9.1a). We use a specific superhydrophobic texture that we call “Nanograss” (also sometimes called black silicon).[13] Nanograss is a low solid-fraction surface composed of a distribution of holes and pointed grass-like features, as shown in Figure 9.1b. Drops begin to evaporate shortly after placement on the hot surface and salt crystals begin to grow. Because the initial solution is concentrated with respect to salt, volumetric losses due to evaporation (V_{evap}) have a corresponding increase in crystal mass: $M_{crystal} = C_{sat}V_{evap}$. The immediate growth of crystals is shown in the first column of Figure 1c, where salt crystals have grown only a few seconds after drop deposition on a Nanograss substrate heated to 90°C. The first stage of evaporation proceeds as expected, with salt crystals accumulating at the air water interface to form “globes” as previously observed.[12]

The unusual critter phenomenon occurs during the second stage of evaporation. Once the salt globe has formed, there comes a time when the remaining water de-wets from the substrate due to preferential wetting of the newly-formed mass of hydrophilic sodium chloride crystals. We dub this moment the lift-off time (t_{lift}), which is shown in the second column of Figure 9.1c. In this instant, water is no longer in contact with the substrate. Instead, there are a handful (3 in this example) of contact points between the crystal globe and the substrate. Evaporation slows significantly following de-wetting due to reduced contact between the water and the hot substrate, and evaporative flow concentrated at these contact points induces a flow towards the substrate. As a result of this flow, crystalline “legs” develop from the contact points and continue to grow in length until the evaporation of water is complete. We call this second phase of evaporation the growth phase (t_{grow}, so that total evaporation time $t_{evap} = t_{lift} + t_{grow}$), which is shown in the last two columns of Figure 9.1c.

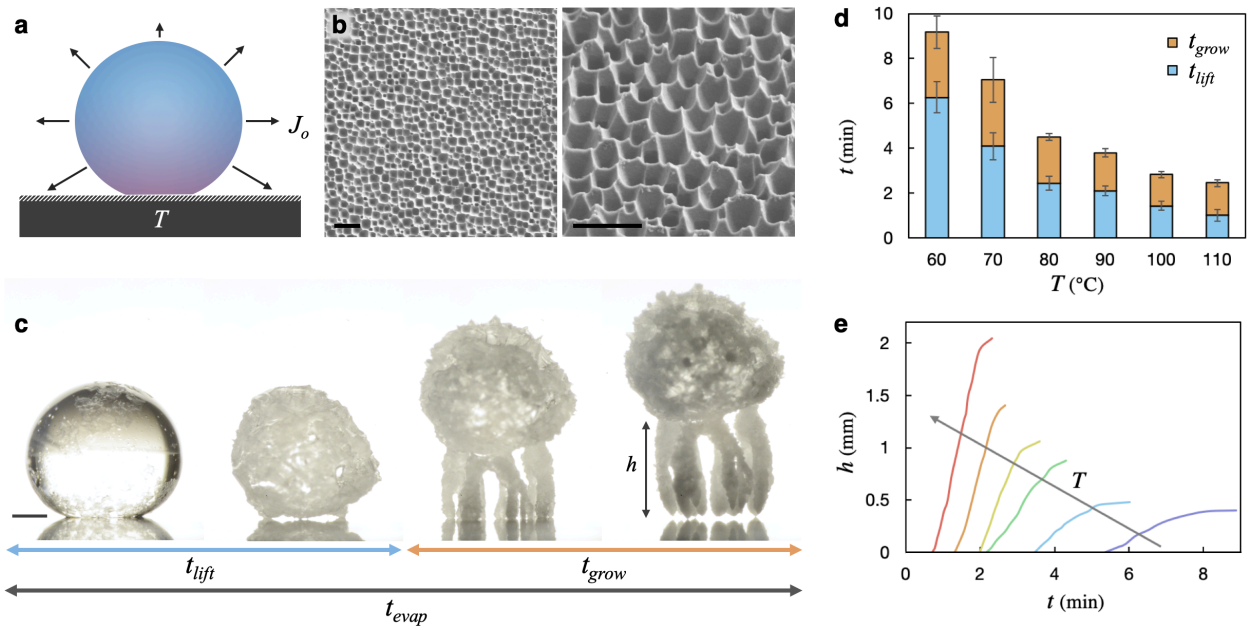

FIGURE 9.1. Growth of crystal critters. (a) Cartoon of experiment, where a drop of water containing dissolved salt is evaporated on a hot, superhydrophobic substrate. (b) SEM images showing nanotexture of superhydrophobic surface. Scale bar for both images is 3 μm. (c) growth of crystal critters with time, where substrate temperature is 90°C. Scale bar is 0.5 mm. (d) Time for evaporation as a function of temperature. Entire bar represents the total evaporation time, the blue segment is the first stage of evaporation prior to leg growth, and the orange segment is the second stage of evaporation during which legs grow. (e) Growth of legs with time as a function of temperature, where the lowest temperature (purple line) is 60°C and hottest (red line) is 110°C.

The three contact points between the crystal globe and substrate in the example shown in Figure 9.1c branch into multiple legs during the growth phase and taper off towards the end of evaporation. This tapering effect is due to there being less water (and therefore less dissolved salt) near the end of the process. The resulting structure is a crystal globe balanced on legs which are barely adhered to the substrate. The final structure shown in the last column of figure 1c shows a good deal of space between the substrate and crystal legs and has only two locations where tubes are still connected to the surface. Crystal critters are easily removed from the substrate and will occasionally roll away on their own volition during or after evaporation.

The crystal critter effect is a strong function of temperature, as shown in Figures 9.1(d,e). Below substrate temperatures of ~50°C, legs fail to form and no lift off occurs. As temperatures are increased, the growth becomes more dramatic and evaporation times are reduced. The overall evaporation time is significantly longer than it would be for a drop evaporating on a heated, superhydrophobic surface without crystallization.[14] The ratio between the time spent in the first stage of evaporation to the time spent in the growth stage decreases with increased temperature (Figure 9.1d). Thus, critters formed on hotter substrates tend to lift-off earlier in the evaporation phase, as shown in Figure 1e. The growth rate (the slope in Figure 9.1e) also significantly increases with substrate temperature, leading to larger final leg heights on the hotter substrates.

Critter Legs

It is now desirable to understand the nature of the legs and why they form in certain locations on the substrate. A drop of water placed on superhydrophobic Nanograss is imaged from above using a microscope focused at the surface, as shown in Figure 9.2(a,b). The drop is mostly suspended on this low-solid fraction superhydrophobic surface. However, there are periodic dimples showing areas where fluid impinges into the texture. It is in these areas with maximum solid-liquid interaction that legs will grow. It is clear from videos of crystal critter growth that there is a flow towards the substrate through the legs, and visual evidence (Figure 9.2c,e) confirms that legs are hollow, crystalline tubes. Figure 9.2e, in particular, shows an SEM image of a rare example in which a portion of a critter leg has remained adhered to the substrate long enough for imaging. The close-up image shown in Figure 9.2d reveals that the tips of the legs are visually similar to miniature sodium chloride (halite) stalactites found in some parts of the world (such as in the Sodom salt cave in Israel).

Figure 9.2f shows an SEM (Scanning Electron Microscope) image of an area where a critter had previously grown. This image was captured using an in-lens detector (which generates high contrast between disparate chemistries) and reveals a number of salt stains ranging in diameter from 20 to 200 μm (median size ~30 to 50 μm). A closer inspection of two of these stains are shown in Figures 2g and 2h, and we see from the inset of Figure 9.2h that the stains are composed of small amounts of residue within the nano-pores of the nanograss texture. In Figure 9.2h, a small amount of macroscopic crystals from the original tube have been left in addition to the impinged salt stain. In most cases only the salt stain remains, and any macroscopic crystals are removed with the critter.

The leg growth observed here mirrors the coffee-ring effect observed for evaporating drops; but on a much smaller scale. In the coffee-ring effect, a drop of water evaporating on a substrate leaves behind a ring stain due to radial evaporative flow transporting solutes/particles towards a pinned contact line.[7] Here, fluid/solid contact is confined to specific points. Evaporation occurs at these points due to substrate heating, and evaporating vapor flows radially outward. This flow transports salt to the contact line where it is forced to precipitate, creating a circular deposit (such as the one left behind in Figure 9.2h). The crystalline deposit grows outward; however, it also is simultaneously pushed upwards as new crystals form in the space below between the substrate and surface. Thus, as a given crystalline ring grows horizontally, it also moves upward, and the resulting leg structure is that of a cone. The continuation of this effect results in growth of a crystalline tube with a tapered conical tip. Water moves down this tube towards substrate due to the temperature gradient until growth terminates due to complete vaporization of the water.

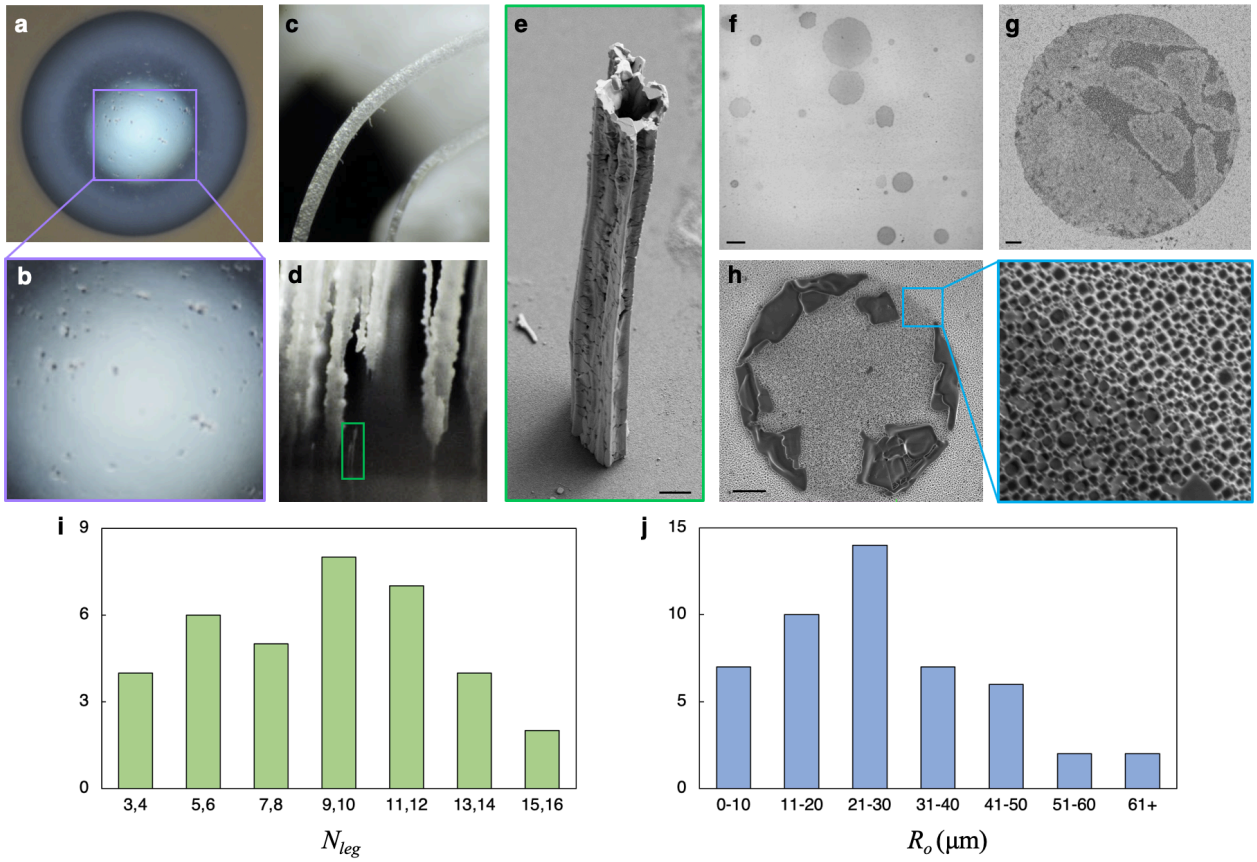

FIGURE 9.2. Crystalline legs are tubes grown from regions where fluid impinges in nanotexture. (a,b) Top view of a drop immediately after placement on a surface revealing areas where liquid has impinged within the texture. (c) Optical image of crystalline tubes where liquid is observed to be flowing through. (d) Optical image of tubes near surface, where a very thin tube still connected to the surface is outlined in green. (e) SEM image of the bottom of a tube. Scale bar is 20 μm. (f) SEM image of a region where salt stains reveal where critter legs previously grew. Scale bar is 100 μm. (g) SEM image showing details of a large salt stain. Diameter of this stain is about 70 μm, scale bar is 5 μm. (h) SEM image showing detail of a salt stain where the outer perimeter has also been left behind. Outer diameter is 30 μm, inner diameter is about 25 μm, and scale bar is 5 μm.

Statistics on the occurrence of different numbers of legs (Figure 9.2i) and of the size of the legs (Figure 9.2j) were compiled. The number of legs is seemingly random, which is in line with the hypothesis that legs form at the positions where a given drop impinges into the nanotexture of the substrate. A given crystal critter will form several legs if it forms at a location where there are several points of impingement, and fewer legs will form if there are fewer impinging points. The statistics the leg diameter (i.e., the diameter of the microscale impinging points) are less random, with a majority of legs being between 10 and 40 μm in diameter; and a median diameter of 30 μm. Neither of these two metrics display a temperature dependence.

9.2 Other Substrates

The salt stains left within the nanoscale texture of the Nanograss hint at the importance of the texture in the critter phenomenon. Indeed, a previous investigation exploring evaporation of sodium chloride on heated, superhydrophobic surfaces reported formation of salt globes alone with no lift-off associated with critter growth.[12] So then, why do crystal critters form specifically on this surface texture? To probe this question, experiments were repeated on other common superhydrophobic textures heated to a temperature of 70°C, as shown in Figure 9.3.

Untextured hydrophobic silicon (Figure 9.3a) served as a control, with the expected result of no leg growth. On this untextured surface, salt crystals grow and pin the contact line between the drop, the air, and the substrate. The presence of these crystals changes the wettability of the drop; and we see the contact angle dramatically decrease with further evaporation. As the drop moves to wet the newly formed crystals at the contact line, it spreads over the surface, creating new crystals along the way. After complete evaporation, we are left with a thick, flat crystalline ring on the hydrophobic surface.

As previously established, the superhydrophobic Nanograss substrate (Figure 9.3b) successfully forms critters. Next, a superhydrophobic micropost surface was tested (Figure 9.3c). Periodically spaced micro-posts are a commonly used superhydrophobic texture, and 10 μm square microposts with 5 μm inter-post spacings were used here. While this surface had a contact angle similar to that of the Nanograss, the resulting crystal structure grew horizontally into a ring rather than into a globe and exhibited no vertical growth. The initially deposited drop starts in the Cassie state (i.e., suspended on top of the pillars). However, as evaporation proceeds, the drop slides into the Wenzel state (impinged between the pillars), as shown in the intermediate timestep in Figure 9.3c. Previous work (see Chapter 7) has shown that crystallization on top of superhydrophobic pillars during evaporation can drastically alter the transition between the Cassie and Wenzel states.[15] As salt crystals form, they enter the channels between the pillars and induce the transition to the Wenzel state, and the resulting crystalline deposit grows horizontally rather than vertically. Horizontal spreading and a transition to the impinged Wenzel state is also observed on a superhydrophobic micro-hole substrate (Figure 9.3d) and on a micropost surface with a second, hierarchal Nanograss texture (Figure 9.3e).

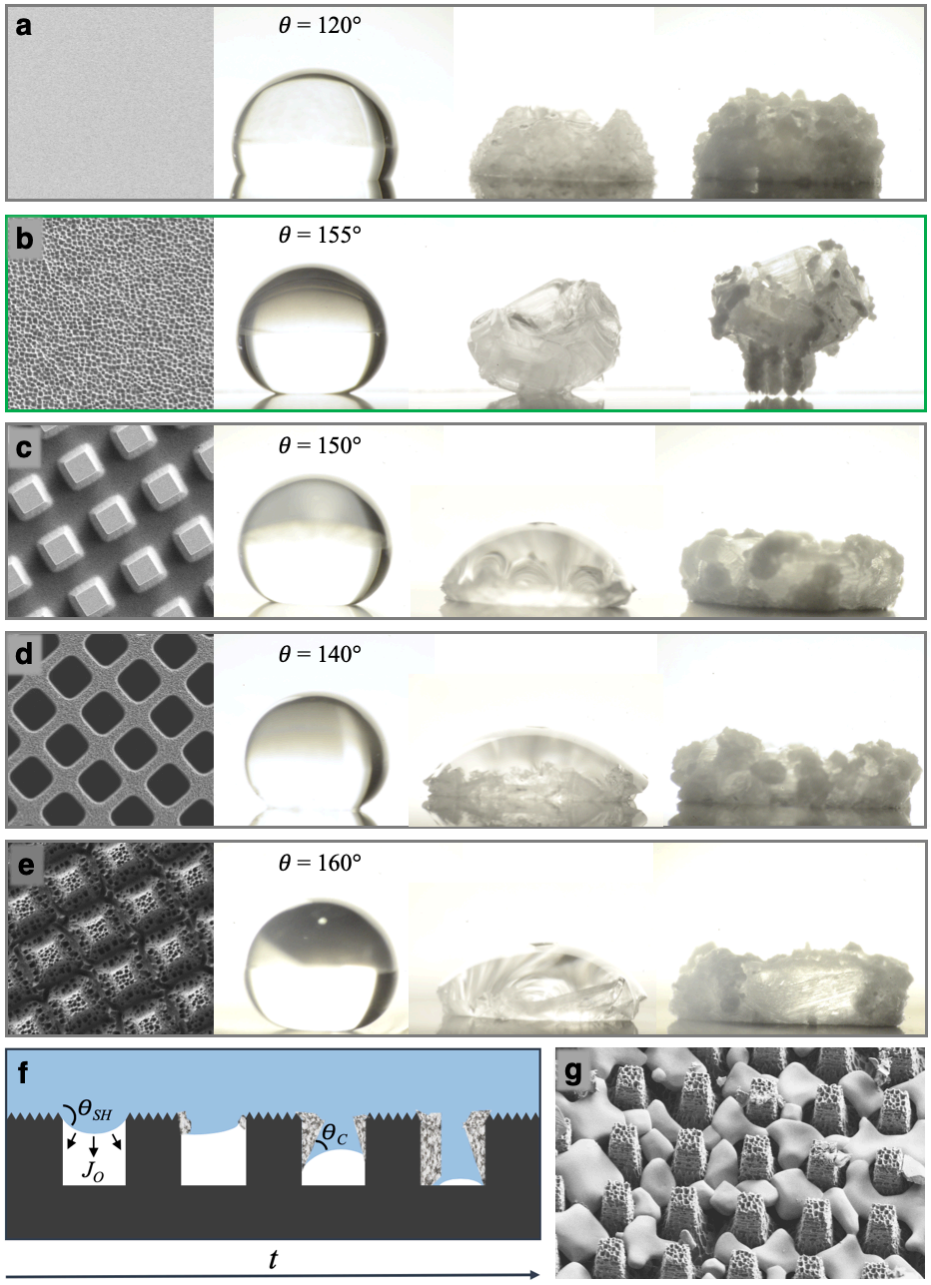

FIGURE 9.3. Critters only grow on Nanograss texture. From left to right, images show SEM of substrate texture, initial drop contact angle, intermediate step where crystals have begun to form, and final crystalline deposit formed during evaporation on substrates heated to 70°C for (a) hydrophobic flat silicon, (b) superhydrophobic Nanograss (i.e., the same texture used in Figures 1 and 2), (c) superhydrophobic micro-posts, (d) superhydrophobic micro-holes, and (e) superhydrophobic micro-posts further textured with Nanograss. SEM images for (1-e) are 50 μm wide. (f) Cartoon examining how crystal intrusion into micro-textures leads to a Cassie-Wenzel Transition (e) SEM image of salt deposit inside the micro-texture of the superhydrophobic micro-posts +Nanograss substrate.

For all the micro-textured superhydrophobic surfaces tested in Figure 9.3, the drop begins in the Cassie state and slowly transitions to the Wenzel state due to crystallization within the texture (see cartoon of Figure 9.3f). In contrast, on the Nanograss surface, there is no Wenzel state for the drop to fall into. In a sense, the initially deposited drop is simultaneously in the Cassie and Wenzel state: parts of the drop are suspended, and parts are impinged into the texture as shown in Figure 2a,b. While a small amount of precipitated salt fills the valleys to create the stains shown in Figure 2f-g, it does not spread in the vertical direction. I confirm that macroscopic crystals form within the micro-scale texture of a hierarchal micro-post and Nanograss surface but not within the nanoscale texture, as shown in the SEM image of Figure 9.3g. A similar effect was observed for ice nucleation on nanoscale surfaces, in which ice crystals formed in the confined nano-scale texture are unable to grow.[16] Thus, the role of the Nanograss texture is to prevent crystal intrusion, which then prevents pinning and spreading of the contact line.

9.3 Other Chemistries

Contamination

The key to the critter phenomena lies within the first stage of evaporation prior to dewettting and leg growth. If the contact line becomes pinned by crystallization during this stage, no critter growth will occur. In contrast, if the contact line remains mobile so that remaining water is able to de-wet from the surface, leg growth will occur.

To test this theory, "contaminant" chemistries were added to the saturated sodium chloride solution to explore their effects on pinning. An inorganic surfactant, sodium dodecyl sulfate (SDS) was added to a solution of saturated sodium chloride to test whether changes to surface tension would alter the effect. Interestingly, critter growth still occurs, though the anatomy of the resulting structure is altered by presence of surfactant as shown in Figure 9.4a. Rather than having several small contact points, the crystal structure maintains an entire ring of contact with the substrate. Rather than forming discrete legs, this ring grows to form a mushroom-like crystalline structure. This result matches intuition, as reduced surface tension results in a less dramatic "dewetting" event so that there are more contact points between the substrate and crystal structure prior to leg growth. Because the surfactant does not influence pinning of the contact line, it therefore does not disrupt the critter effect.

Calcium carbonate is a common component of ocean water that is particularly problematic for mineral fouling. In the ocean and many other environmental waters, calcium carbonate is dissolved at its solubility limit (C_{sat} =0.013 g/L) so that it is quick to precipitate following evaporation. In ocean water, sodium chloride is present at 10% of its solubility limit (C_{sat} = 360 g/L and C_{ocean} = 35 g/L) while calcium carbonate is fully saturated. This combination of sodium chloride and calcium carbonate was tested at their ocean water concentrations (Figure 9.4b) with the result that

calcium carbonate precipitates at the contact line prior to formation of the crystal globe. This causes contact line pinning which disrupts critter growth. In contrast, a solution of 10% sodium chloride without calcium carbonate successfully forms critters. Next, the concentration of sodium chloride is increased to 50% of its saturation concentration and again combined with saturated calcium carbonate (Figure 9.4c). It is observed that calcite precipitation pins the contact line once again. Critter growth is effectively disrupted by pinning, and a bowl-shaped deposit forms.

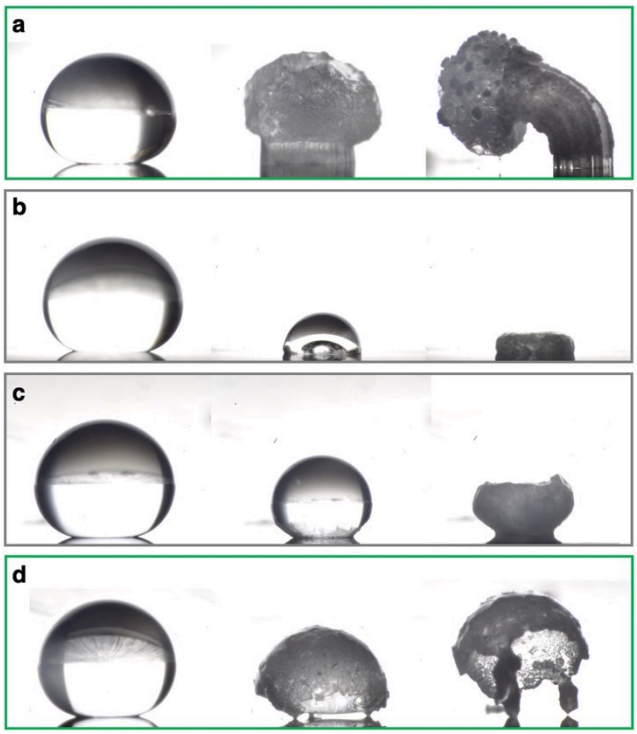

FIGURE 9.4. Changes to critter effect induced by other chemistries. (a) Saturated sodium chloride with 0.01% SDS (sodium dodecyl sulfate) grows critters, but alters the morphology of growth. (b) Sodium chloride at 10% saturation concentration with saturated calcium carbonate forms a ring deposit. (c) Sodium chloride at 50% saturation concentration with saturated calcium carbonate forms a bowl-deposit. (d) Sodium chloride at saturation concentration with saturated calcium carbonate successfully forms a critter.

The results of Figure 9.4(b,c) confirm that crystallization/pinning at the contact line during the initial phases of evaporation disrupt the critter effect. However, contamination by other salts/minerals will be pervasive for any salt water source used for spray-cooling heat exchange. Thus, it is important to overcome limitations associated with pinning of the contact line by other salts. The final solution tested (Figure 9.4d) is saturated sodium chloride with saturated calcium carbonate. Here, sodium chloride crystals begin forming before the calcium carbonate precipitates. Newly formed sodium chloride likely presents a more favorable site for heterogeneous nucleation of calcium carbonate than does the hydrophobic Nanograss, and we do not observe calcite formation at the contact line. Instead, the evaporation proceeds similarly to pure sodium chloride solutions, and a crystal critter develops. Thus, the disruption of the critter effect by other minerals can be circumvented by having a sufficiently high concentration of sodium chloride. One source water that fits this requirement is the rejected brine from reverse osmosis (or other forms of desalination) plants.

Other Salts

A final question on the critter effect is whether it can work for other salts beyond sodium chloride. These salts need to fit within a somewhat narrow range of criteria. First, the salt must crystallize readily and begin to precipitate soon after the supersaturation concentration has been exceeded. Salts with kinetically limited crystallization may fail to form the initial salt globe during the first phase of evaporation. The salt must also be highly soluble so that there is enough mass for forming the three-dimensional crystal structures that make up the crystal critters. However, the salt cannot be too soluble, as the crystallizing mass cannot be so great that the legs cannot lift it. In addition, highly soluble salts have a tendency to effervesce, which creates a cycle of evaporation and condensation that prevents total evaporation (and therefore crystallization) under the experimental conditions used here. Sodium chloride has a unique advantage over other salts for forming crystal critters in this regard. The solubility concentration of sodium chloride exhibits only small increases with increasing temperature (360 g/L at 20°C, 380 at 90°C). Thus, salt crystals begin to precipitate shortly after drop deposition on the heated surface despite the increased temperature. For salts with a more dramatic solubility-temperature relationship, the increased temperature and associated change in supersaturation concentration delays crystallization and therefore delays the possibility of leg formation.

I explore the relationship between temperature dependent solubility and critter formation by testing salts with temperature dependencies, as shown in Figure 9.5. Of the salts tested, potassium chloride is the most similar to sodium chloride (C_{sat}= 280 g/L at 20°C, 530 g/L at 90°C). Potassium chloride successfully forms critter structures, albeit with shorter legs than the sodium chloride structures. Ammonia chloride (C_{sat}= 410 g/L at 20°C, 700 g/L at 90°C) also forms critter-like legs, which are significantly shorter than those formed for sodium or potassium chloride. Copper sulfate, known for its' vibrant blue crystals, has the most dramatic change in solubility with temperature of the salts tested, with a saturation concentration of 200 g/L at 20°C and 670 g/L at 90°C. Formation of copper sulfate crystals is also more kinetically limited than the other salts. Thus, while the copper sulfate deposit did de-pin from the surface (as shown by the space between the crystal and the substrate in Figure 5), it did not form critter-like legs.

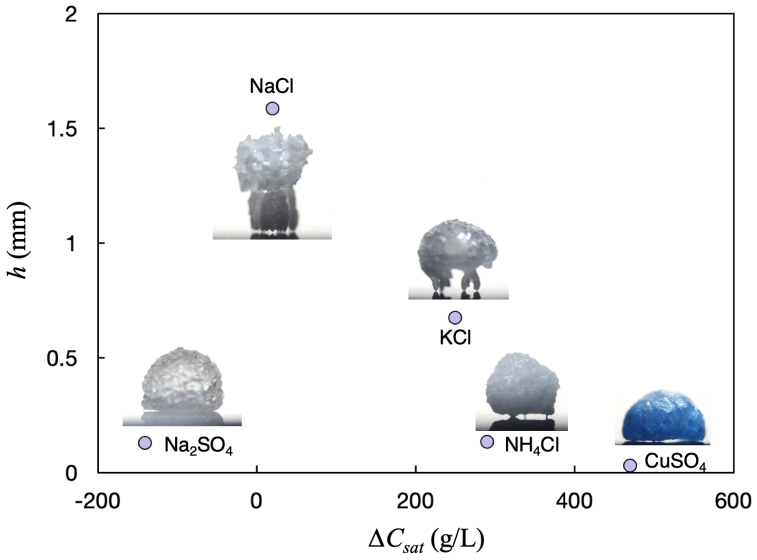

FIGURE 9.5. Other salts and the Critter effect. Leg growth is plotted against the difference in solubility concentrations for five different salts between room temperature and 90°C. Optical images show resultant critters formed for these salts at 90°C.

9.4 Modelling

Now that the occurrence of the critter effect and how it can be disrupted is understood, I consider how it might be applied and controlled. Before proceeding, I quickly summarize the evidence presented thus far regarding the critter effect. First, the legs begin to grow after an initial evaporation phase, are hollow, and always grow perpendicular to the substrate. The number of legs depends on the position of the drop on the surface and grow at locations where fluid has impinged within the Nanograss texture. If a second drop is placed at a location where a critter has previously grown, this second critter will grow legs at the same positions as the first because fluid impinges at these locations. The growth velocity of the legs is uniform across a given example regardless of leg thickness and/or number of legs. In other words, increasing the number of legs does not change the growth rate. Finally, higher temperatures results in higher growth rates and longer legs overall, as shown in Figure 9.1e.

I seek to model how evaporative flow results in growth of the crystalline tubule legs that constitute the crystal critter effect. Volumetric losses due to evaporation are proportional to the evaporative flow multiplied by the line over which evaporation occurs. Assuming that all evaporation occurs at the contact line between the legs and the substrates, this mass balance takes the form:

$$\frac{dV}{dt} = -(2\pi N R_o) J_o \qquad 9.1$$

$$J_o = \frac{D_{vap}\Delta C_{vap}}{\rho}$$

Where R_o is outer radius of a leg, N is the number of legs, and J_o is the evaporative flux (see Figure 5a for geometry). The evaporative flux is a function of the diffusion of water vapor in air (D_{vap}) and the concentration gradient of vapor in air between the vicinity of the air/water interface and the bulk air (ΔC_{vap}). Both of these components are strong functions of the vapor temperature; which can be approximated as the substrate temperature in the immediate vicinity of evaporation. For simplicity, we have assumed in equation 1 that all N legs have the same outer radius; though we know from experimental evidence (Figure 9.2f) that there is wide variability across leg diameters.

Next, I consider a mass balance of the salt by assuming that the salt concentration within the drop remains approximately constant at the saturation concentration. This assumption should be valid for sodium chloride, as precipitation occurs very quickly following changes to volume. Thus, the rate of change of mass within the solution is equal to the saturation concentration multiplied by the volumetric evaporation rate. This is balanced by the rate of mass precipitation, which here will be the rate mass growing into the legs. I approximate the legs as cylindrical tubes with an inner diameter R_i to find:

$$N\rho_{salt}\pi(R_o^2 - R_i^2)\frac{dh}{dt} = -C_{sat}\frac{dV}{dt} \qquad 9.2$$

Where dh/dt is the growth rate of the crystalline tubules (see Figure 9.5a). I set the volumetric evaporation rate in equation 9.2 equal to the expression in equation 9.1 and rearrange to find the growth rate of the legs:

$$\frac{dh}{dt} = \left(\frac{2R_O}{R_o^2 - R_i^2}\right)\frac{C_{sat}J_o}{\rho_{salt}} \qquad 9.3$$

The relationship of equation 9.3 has several features that are observed experimentally, including that dh/dt is independent from number of legs and increases with increasing temperature (J_o). Finally, I test this prediction against experimental data. Taking the geometry from the deposit shown in Figure 9.2h as an example of the typical deposit size so that R_o=15 μm, and R_i=12.5 μm. The density of the salt and saturation concentration are constant, leaving dh/dt as a function of temperature via the evaporative flux. This model is plotted against experimental data in Figure 9.5b with very good agreement.

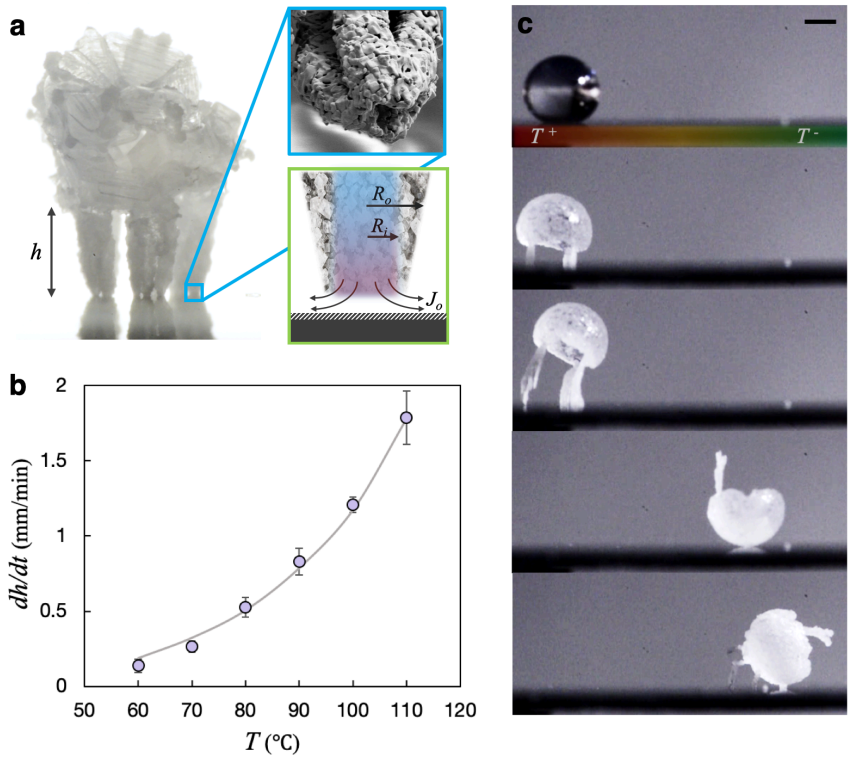

FIGURE 9.6. Growth mechanism and temperature dependence. (a) Images defining model parameters including h (length of the legs), J_o (evaporation rate), R_o, and R_i (outer and inner diameter of a given leg). (b) Average leg growth rate (mm/min) as a function of temperature, where purple circles indicate experimental values averaged from 5-6 trials, error bars show standard deviation, and solid line is model from equation 3 (where R_o=15 μm and R_i=12.5 μm). (c) Experiment showing critter growth on a substrate with an imposed temperature gradient. Legs grow longer on the side with a higher temperature, causing the crystal critter to become more and more unstable until it eventually tips over and rolls in the direction of the lower temperature. New legs begin to grow at the new position until evaporation is complete.

Because leg growth rate increases with temperature, it is possible to induce directional rolling by applying a temperature gradient across the substrate. This is shown in Figure 9.5c, where a drop is deposited on a superhydrophobic Nanograss substrate with an imposed temperature gradient. Legs grow shorter on the side of the drop with a lower temperature, and longer on the side with the higher temperature. Because of this, the resulting crystal structure eventually tips over and rolls towards the direction of lower temperature. At this point, the water hasn't fully evaporated, and remaining water continues to evaporate via formation of new legs at the second location. Using this technique, it is possible to obtain structures that roll two or even three times before complete evaporation. Thus, temperature gradients can be used as a method for encouraging complete detachment of the critter and for controlling the direction of crystal expulsion.

Conclusions

I have introduced and explained the unusual wetting behavior of evaporating drops of saturated sodium chloride on heated, superhydrophobic Nanograss surfaces, and name this behavior the crystal critter effect. Water preferentially wets sodium chloride crystals which form at the air/water interface during the first phase of evaporation and dewet from the superhydrophobic substrate. This then focuses evaporation at limited contact points where liquid has impinged within the nano texture, enabling growth of crystalline tubule legs that eject the entire structure from the surface following complete evaporation. This effect is not disrupted by presence of surfactants (which create mushroom-like structures rather than creature-like structures); but can be disrupted by chemistries which induce contact line pinning during the first phase of evaporation. This limitation can be reduced by increasing the sodium chloride concentration so that halite crystals are the first to precipitate. I also develop and test a simple mass balance model predicting the rate of leg growth as a function of temperature and show how temperature-dependent growth can be used to induce ejection and rolling of the crystal critters.

In addition to being innately interesting, the crystal critter effect also has potential application for improving sustainability in spray cooling heat exchange due its dependence on very high salt concentrations. For example, if ocean water could be directly used as a working fluid without expensive pre-treatment, one could imagine a new type of co-generation plant in which desalinated seawater is produced as a by-product of energy production. This phenomenon also has potential for use in zero liquid discharge (ZLD) systems, where complete recovery of water from very salty reverse osmosis reject water is challenging due to the difficulties in working with high-salt concentration brines. Using waste brine rather than fresh water for thermoelectric cooling applications simultaneously reduces costs associated with water treatment while also preserving fresh water for use in other vital functions.

References

1. Averyt, K. *et al.* Water use for electricity in the United States: an analysis of reported and calculated water use information for 2008. *Environ. Res. Lett.* **8**, 015001 (2013).
2. Pan, S.-Y., Snyder, S. W., Packman, A. I., Lin, Y. J. & Chiang, P.-C. Cooling water use in thermoelectric power generation and its associated challenges for addressing water-energy nexus. *Water-Energy Nexus* **1**, 26–41 (2018).
3. Zhao, X. & Chen, X. D. A Critical Review of Basic Crystallography to Salt Crystallization Fouling in Heat Exchangers. *Heat Transf. Eng.* **34**, 719–732 (2013).
4. Sastri, V. S. CORROSION COSTS. in *Challenges in Corrosion* 95–126 (John Wiley & Sons, Inc, 2015).
5. Feeley, T. J. *et al.* Water: A critical resource in the thermoelectric power industry. *Energy* **33**, 1–11 (2008).
6. Zhang, C., Zhong, L. & Wang, J. Decoupling between water use and thermoelectric power generation growth in China. *Nat. Energy* **3**, 792–799 (2018).
7. Deegan, R. D. *et al.* Capillary flow as the cause of ring stains from dried liquid drops. *Nature* **389**, 827–829 (1997).
8. Deegan, R. D. *et al.* Contact line deposits in an evaporating drop. *Phys. Rev, E* **62,** 756-765 (2000).
9. Shahidzadeh, N., Schut, M. F. L., Desarnaud, J., Prat, M. & Bonn, D. Salt stains from evaporating droplets. *Sci. Rep.* **5**, 10335 (2015).
10. Desarnaud, J., Bonn, D. & Shahidzadeh, N. The Pressure induced by salt crystallization in confinement. *Sci. Rep.* **6**, 30856 (2016).
11. Shahidzadeh-Bonn, N., Rafai, S., Bonn, D. & Wegdam, G. Salt Crystallization during Evaporation: Impact of Interfacial Properties. *Langmuir* **24**, 8599–8605 (2008).
12. Shin, B., Moon, M.-W. & Kim, H.-Y. Rings, Igloos, and Pebbles of Salt Formed by Drying Saline Drops. *Langmuir* **30**, 12837–12842 (2014).
13. Dorrer, C. & Rühe, J. Wetting of Silicon Nanograss: From Superhydrophilic to Superhydrophobic Surfaces. *Adv. Mater.* **20**, 159–163 (2008).
14. Dash, S. & Garimella, S. V. Droplet Evaporation on Heated Hydrophobic and Superhydrophobic Surfaces Droplet evaporation on heated hydrophobic and superhydrophobic surfaces. *Phys. Rev. E* **8910**, (2014).
15. McBride, S. A., Dash, S. & Varanasi, K. K. Evaporative Crystallization in Drops on Superhydrophobic and Liquid-Impregnated Surfaces. *Langmuir* **34**, (2018).
16. Bengaluru Subramanyam, S., Kondrashov, V., Rühe, J. & Varanasi, K. K. Low Ice Adhesion on Nano-Textured Superhydrophobic Surfaces under Supersaturated Conditions. *ACS Appl. Mater. Interfaces* **8**, 12583–12587 (2016).

Chapter 10.

Final Comments

In this thesis, interfacial engineering has been extensively applied to control substrate texture, wettability properties (including the advancing and receding contact angles), and chemistry to explore the influence of interfacial properties on salt crystallization for applications in water treatment and sustainability.

This final chapter discusses some of the common themes which arise throughout the experiments presented in Chapters 3-9. First, I develop a merged phase diagram predicting pattern formation from an evaporating drop of calcium sulfate as a function of the substrate dynamic contact angles using results from Chapters 5-9. Because the pattern morphology for an evaporating drop of calcium sulfate is a function of the salt solubility and the temperature of the substrate, this phase diagram only describes patterns for gypsum evaporated at 60°C. The next discussion topic is how the different crystal properties (including saturation concentration, solubility-temperature relationship, surface energy, and crystal lattice) of the different salts influence their crystallization behavior at interfaces.

The second part of this chapter expands on possible future directions for the work presented here. This section is organized by the three central applications described by previous chapters: fouling inhibition, nutrient recovery, and patterning. I discuss issues of industrial scale up for anti-fouling technologies and for using crystalline patterns as masks for sustainable fabrication. This section concludes with additional ideas for potential applications in the area of crystallization and interfacial engineering beyond those presented in the current work.

10.1 Recurring Themes

Patterning using $CaSO_4$

I have used calcium sulfate as a model salt throughout almost all of the investigations presented in this thesis. Calcium sulfate is an ideal model salt for crystallization induced by evaporation, as altered temperatures do not substantially alter its solubility or crystallization. Calcium sulfate also crystallizes readily and has an ideal solubility concentration in the upper end of the sparingly soluble category. In the experiments presented in Chapters 5-8, 5 μL drops of water with calcium sulfate dissolved to its saturated limit were evaporated. Because I used the same experimental conditions for each of the substrates across projects, it is possible to compile a phase diagram predicting patterning from evaporating drops calcium sulfate in water, as shown in Figure 10.1.

In Figure 10.1, results from Chapters 5-8 are combined in a semi-quantitative (estimated) phase diagram predicting the different regimes of gypsum patterning on surfaces heated to 60°C. These predictions are made by a combination of the water-substrate advancing contact angle (x-axis), and the by the ratio between the receding and advancing angles (y-axis). The different patterns are represented by the different color shadings within this phase diagram, where purple represents spiral/concentric ring patterns presented in Chapter 7, grey represents "clumped" deposits from Chapter 6, blue is the periodic arrays formed from Marangoni instabilities in Chapter 8, and yellow represents triangular patterns also from Chapter 8.

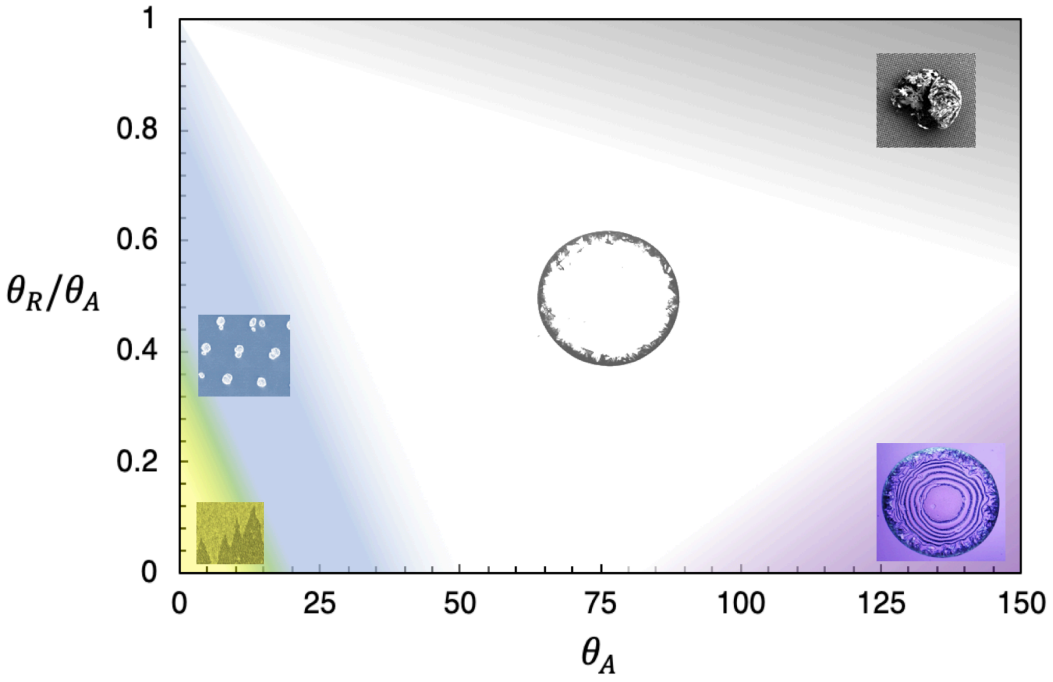

FIGURE 10.1. Merged phase diagram of calcium sulfate evaporative deposition patterns as a function of the substrate advancing and receding contact angles heated to 60°C.

For a vast majority of wetting properties shown in Figure 10.1, calcium sulfate forms the simple, single ring morphology first analyzed by Deegan for an evaporating drop of a colloidal solution.[1] The size of this ring will decrease with increased advancing contact angles and increase with lower advancing contact angles; but will always be ring-like for moderate contact angles with some amount of contact angle hysteresis. This is because gypsum will begin to precipitate at the contact line after some amount of evaporation, which will then pin the contact line. In contrast, if the drop recedes before precipitation occurs, it may form a clumped deposit instead. Clumped deposits (grey region of Figure 10.1) will form on superhydrophobic surfaces with minimal contact angle hysteresis as shown in Chapter 6. Clumped deposits are also able to form on hydrophobic surfaces so long as there is little contact angle hysteresis.

The observation of pattern formation on the deposit interior on hydrophilic substrates presented in chapter 8 was surprising for a number of reasons. First, the experiments presented in Chapter 6 included a hydrophilic control and were some of the earliest experiments performed. Thus, it was unusual that I did not observe the patterns previously. By re-examining some of those samples from that work, I discovered that patterns actually had formed on some of the samples. I did not observe them at the time of performing the study simply because I was not looking for them. Likewise, I have found a handful of examples of other investigations in which patterns form at the interior of evaporative deposits where the authors make no mention of the patterning in their studies. It is likely that these authors either did not notice the patterns or did not wish to detract from the primary message of their manuscripts by pointing out this mysterious result. Another reason why I did not observe patterns in early investigations is between the patterns (shown in the yellow and blue regions of Figure 10.1) won't form on silica substrates that were not recently plasma cleaned, regardless of how clean the sample is. The generation of radicals during plasma cleaning is essential for reducing the contact angle to the required values for the onset of thin film instabilities. This is why no patterns are observed in the hydrophilic example shown in Figure 6.1, where the contact angle (24° at 60°C) was sufficiently high enough to be on the phase boundary between the array and single ring regimes for the phase map of Figure 8.1.

The final regime shown in Figure 10.1 is the purple shaded spiral/concentric ring regime on hydrophobic surfaces with extremely high hysteresis. In Chapter 7, I show that the large initial contact angle of the drop allows for a three-dimensional outer crystalline ring, while the hydrophilic receding angle results in a thin film forming at the drop interior in the later stages of evaporation. When the thin film eventually ruptures, patterning occurs at the newly formed mobile contact line. The patterning behavior shown in Chapter 7 was highly temperature dependent, with uniform patterns only occurring at intermediate substrate temperatures (i.e., 60°C).

Phase diagrams for other temperatures could also be developed. For 20°C, the yellow triangle patterning region would disappear into the corner of the phase diagram at the low end of contact angle, and the blue array regime would occupy the area covered by the yellow regime on the 60°C diagram. Likewise, the purple spiral regime would disappear entirely and be replaced by the single

ring regime (as discussed extensively in Chapter 7). In contrast, the grey clumping regime for a room temperature diagram would remain very similar to that of the 60°C phase map. This was shown in Figure 6.4 in Chapter 6, which found that temperature differences made little difference in deposit morphologies on superhydrophobic surfaces. This is because both the rate of gypsum crystallization and the rate of contact angle recession are directly dependent on the rate of change of drop volume. This would not be the case for other salts with altered solubilities across temperatures, as the rate of crystallization would then depend on both the temperature and the rate of volume change.

A high temperature phase diagram (~90°C) would introduce two new "chaotic" patterning regimes to the catalogue of possible patterns. The first would replace the area currently occupied by the purple spiral regime on the 90°C phase diagram and would be characterized by an outer crystalline ring with randomly deposited crystal structures at the drop interior, as shown in the high temperature samples in Figure 7.6. The second new regime would replace the yellow triangular region and would have a concentric ring deposit morphology. This concentric ring morphology is briefly discussed in Chapter 8 and differs from the concentric rings/spirals found in Chapter 7. These concentric rings are formed from re-wetting of thin films during evaporation due to thermocapillarity. Similarly to the room temperature case, changes to the area occupied by the clumped regime between the 90°C and 60°C diagrams would be minor.

Influence of Salt Chemistry

Another recurrent theme throughout this thesis is how different salts are influenced by various interfacial engineering processes. In many cases, it was possible to attribute these differences to changes in solubility properties and the concentration of the salt. For example, in Chapter 5, I find that the resulting crystalline deposit can be correlated to the solubility-temperature relationship for a given salt and use this to explain why the physics controlling colloidal and crystalline deposits vary. Another example is the crystal critter effect presented in Chapter 10, in which I show that salt solubility is critical in the effect. The critter phenomenon works for a number of salts so long as they fall into a rather narrow range of saturation concentrations. In addition, the temperature-solubility relationship is an important factor in controlling the length of critter "legs," with shorter legs forming for salts that increase solubility at higher temperatures. In Chapter 7, I show that other salts including sodium chloride can also exhibit the same patterning effect so long as the concentration is such that the height of the three-dimensional outer crystalline ring allows it to fall into the patterning regime predicted by equation 7.21.

Differences in salt concentrations, solubility, and solubility-temperature relationships are sufficient to explain most of the differences observed across the salts used here. However, the surface energy of the crystals and the crystal-substrate surface energy also play a role. This is discussed in Chapter 3, where different morphologies of calcium sulfate are observed across smooth substrates of different surface energies (Figure 3.2). The influence is also discussed in

Chapter 5, where individual crystals within evaporative deposits exhibit different morphologies across the surfaces (Figure 5.4). There, it was difficult to decouple the influence of evaporation rate and the influence of surface energy. The role of crystal surface energy is most important for the crystal critter effect presented in Chapter 9. Previous work comparing evaporative deposition of sodium chloride and calcium sulfate crystals found that sodium chloride crystals so not pin the contact line while calcium sulfate does.[2] The authors attribute this difference to the different interfacial interactions of the two crystals, where sodium chloride crystals form at the air/water interface and calcium sulfate crystals form at the triple phase contact line. A similar effect is shown in Figure 9.4, where calcium carbonate pins the drop contact line and disrupts the crystal critter effect when it is able to crystallize before sodium chloride.

The interior crystal lattice of a given salt and the associated salt morphologies are also important in patterning phenomena. The ways in which the crystal lattice of a given salt influences the morphology of ta macroscopic crystal was discussed in Chapter 2 but has not been given much attention in the individual chapters. This influence is seen in each of the experiments in which multiple salts are used (Chapter 3, 5-8). Chapter 3 has the obvious result that sodium chloride and potassium chloride crystals form cubic structures while calcium sulfate forms needle-like crystals.

A more interesting result comes from the patterning work of Chapter 8 (Figure 8.5), where evaporation of silver sulfate and calcium iodate solutions on hydrophilic substrates both form triangular patterns but with morphologies that strongly differ from the dendritic structure of calcium sulfate. In general, dendritic structures form as a result of diffusion-limited growth,[3] which is the result of the extremely fast rate of crystallization occurring at the thin, mobile contact line. In contrast, the silver sulfate crystals form lines rather than dendrites, and the calcium iodate pattern is composed of small circular clusters.

Crystal-Texture Interactions

Micro- and nano-scale substrate textures have a strong influence on crystallization.[4,5] Some effects of this influence are explored in Chapters 3,4, 6, and 9. In Chapter 3, I show that salt scaling on superhydrophobic surfaces is actually greater than scaling on smooth hydrophobic surfaces. This highlights that superhydrophobic surfaces are not the gold-standard in anti-fouling interfaces, and that the texture may do more harm than good for resisting crystallization fouling.

Chapter 4 makes extensive use of the influence of texture on crystallization and shows how crystallization kinetics of struvite are strongly enhanced by the presence of nanoscale pores. The first part of Chapter 4 explores this influence by comparing crystallization kinetics and final structure across three different pore sizes using anodisc membranes of controlled porosity. Next, nanoporous zeolite crystals were tested as a method of enhancing crystallization kinetics and were found to increase the nucleation induction time by a factor of 2-3. In Figure 4.7, needle-like struvite crystals are observed to be adhered to the outer texture of nanoporous zeolite crystals.

Chapters 6 and 9 dealt with crystallization from evaporating drops on superhydrophobic textures. In these studies, it was found that both sodium chloride and calcium sulfate crystals will intrude into a micro-scale texture and induce a Cassie-Wenzel transition. For the calcium sulfate system of Chapter 6, whether or not the crystals would intrude into the texture was a function of both the spacing of the micro-posts and a function of temperature. Increased distance between the micro-posts was associated with an increased likelihood of the Cassie-Wenzel transition. This transition occurred much sooner in the evaporation process than it did for drops of DI water on the same surfaces (Figure 6.3). Crystal intrusion of calcium sulfate into the textures increased the overall surface energy of the solid/liquid interface, which enabled the transition. Likewise, in Chapter 9 (Figure 9.3) it is observed that the critter effect does not occur on superhydrophobic surfaces with micro-scale features due to crystal intrusion of sodium chloride.

10.2 Perspectives & Future Directions

Fouling Inhibition

Mineral fouling is a recalcitrant problem across industries with no simple solution. I have shown that liquid impregnated surfaces (LIS) are able to resist multiple salt foulants due to the physical barrier that the lubricating layer provides between the underlying surface and crystallizing materials. In addition, a collaborative project not described in this thesis has successfully used the same surfaces for eliminating bacterial biofilms.[6] Thus, these surfaces present a promising solution for anti-fouling. However, the lubricating layer method cannot be universally applied. For example, lubricant impregnated surfaces cannot be easily applied to membrane modification, as the oil layer would block pores. Membrane fouling is a critical problem in desalination and in other forms of water treatment, where fouling is often the limiting factor in membrane performance and operation.[7] One investigation attempted an LIS approach for membrane modification, and showed that the material successfully resisted fouling, but also required additional pressure application in order to displace the oil from the pores during operation.[8] The LIS approach is also limited in applications operating under high shear, as shearing flows can entrain the lubricating layer and deplete the oil.[9] While LIS may not be an ideal anti-fouling strategy for pipe flow (where velocities are necessarily large in order to minimize frictional losses), it could be applied to scenarios that are quiescent or have low velocity flows. One such application for fouling prevention in fluid sumps of wastewater treatment plants, where untreated water is stored. These sumps require regular maintenance due to fouling build-up at the air water interface, and plant operators could therefore benefit greatly from fouling resistant coatings. Future work could investigate anti-fouling mechanisms which are applicable to high shear conditions, or methods of improving LIS stability in flows.

Additional work should also be done to explore simultaneous fouling by multiple fouling mechanisms including biofouling. This is particularly important for applications in desalination and waste water treatment, where multiple fouling mechanisms are likely to exist at once. Biological fouling is a mechanism in which organisms (usually bacteria or fungi in industrial systems; but also barnacles, mussels, and algae in aquatic environments) accumulate and form colonies. Biological fouling is problematic in membrane-based desalination where bacterial biofilms severely limits membrane lifetime and performance.[7] Other categories of fouling include corrosion from chemical reactions in harsh environments, adsorption of organics, and particulate accumulation.

In this work, I tested mineral fouling of multiple salts and salt combinations and found that fouling of one salt is altered by the presence of another. Likewise, the presence of multiple fouling mechanisms will have impacts on others. For example, mineral scaling generates surface defects that facilitate corrosion, and soft bio-deposits can facilitate crystal nucleation. Designing surfaces that simultaneously reduce the risk of all contaminants is challenging due to the different mechanisms of adhesion. Hydrophobic surfaces reduce crystal-fouling,[10] while hydrophilic surfaces reduce organic absorption;[11] and biofilm growth has a complex relationship with surface properties.[12] Thus, modification of substrate wettability is not sufficient to address fouling across multiple mechanisms since interfaces which successfully resist one form of fouling become vulnerable to another. This is a self-defeating cycle in which accumulation of a single foulant induces fouling of others.

In chapter 10, I introduce the critter phenomena in which salt crystals are ejected from heated, superhydrophobic surfaces. Additional work in this area could be the scale-up of this process for the application in anti-fouling for spray cooling heat exchange. I have argued that this effect is perfect for this application, as heating of the solid is inherent and because it could enable the use of waste brine as an alternative water source. I have shown that the contamination from other salts and even surfactants of the brine does not prevent the effect so long as the sodium chloride concentration is high enough. However, before this can be implemented in heat exchange, work will need to be done to determine how one can create the specific nanotexture required for the critter effect on industrially relevant material (aka, metals). The scale up of nanoengineering approaches on metallic surfaces is a persistent problem across fields of interfacial engineering.[13] A related challenge is the temperature stability of many hydrophobic functional groups. In bench-scale experiments, samples are typically rendered hydrophobic by the addition of an organic polymer. Such polymers typically do not hold up well to high temperatures. One possible solution to this challenge is the use of ceramic materials for hydrophobicity.[14]

Nutrient Recovery

In the work presented in Chapter 4, I primarily focused on applying nanoengineering to creating surfaces and particles for application in recovering struvite from waste water. However, there are other nutrient crystals that could be explored. In addition, there are other waste streams containing large amounts of desirable chemistries. One such stream is agricultural run-off, which contains large amounts of phosphate and nitrogen. Struvite could be precipitated in these run-off streams by the addition of magnesium; or other nutrient crystal chemistries could be explored. Other waste streams of interest include industrial waste, waste water produced from fracking, and mining tailings.[15] Mining tailings are a particularly interesting system for future work, as with struvite recovery from waste water, crystallization separations processes from these streams can recover useful products while simultaneously reducing environmental impact.

Another interesting waste stream is run-off of snow melt caused by de-icing salts. Salts (usually sodium chloride) have been used across the US to de-ice our roads. Run-off from these roads have resulted in a continuous accumulation of salt in environmental waters, which has a profound impact on both aquatic life and on the quality of our drinking water sources.[16] The application of interfacial engineering to solve this problem is not immediately obvious, as the high solubility of sodium chloride makes it inherently challenging to remove from water. However, it could be possible to engineer interfaces using electrostatic principles to remove at least some fraction of salt from the run-off before it reaches environmental waters.

Additional work could also be done in the area of scaling the interfacial engineering principles developed in Chapter 4 for on testing the applicability of engineered surfaces to real conditions at a wastewater treatment plants (WWTP) including presence of co-contaminants and fluid flow. Struvite growth is a diffusion limited process,[8] and therefore mixing has a significant influence on growth kinetics.[9] A range of fluid flows within wastewater operating conditions will be explored. The flow geometry(s) for these tests could be (1) a scaled model of the serpentine channels used in aeration basins of WWTPs (2) simple stirring in a beaker to model a CSTR (also used in WWTP for flotation/sedimentation), or (3) a Couette cell for accurate determination of flow Reynold's numbers and shear rates. The influence of co-contaminants could also be explored using other salts common in wastewater, and possibly even by using a solution of actual water taken from an aeration basin at a local WWTP.

Crystal Patterning

I have shown how substrate wettability and evaporation rate can be used to control patterning from an evaporating salt solution. These salt patterns are effective masks in a variety of applications and can be used to fabricate micro-textures. Such micro-textures have immediate application for fabricating superhydrophobic surfaces in a way that cuts the costs, reagents, and time required by an order of magnitude. However, for many microtechnological applications, a higher resolution control over the patterns is required. For some applications, resolution on the scale of 10 nm is

required. While the patterns formed here are highly regular, the resolution is sufficient for such applications. Further work could be done in fine-tuning the processes in order to achieve the exact pattern desired. This would involve fine-tuning of the surface energy of the substrate, which influences the magnitude of the energetics forces; and of the evaporation rate.

A higher degree of control of patterning process could also be accomplished by implementing techniques beyond changing the evaporation rate and surface wettability for precisely defining the contact line velocities and thickness of the evaporating film. These two properties primarily are responsible for the specific pattern that emerges on each sample and are not particularly well-controlled in the experiments presented in Chapters 7 and 8. This could also allow the patterning process to be scaled up into geometries larger than the size of the drops used here.

The discovery of the various ways in which a single drop of evaporating calcium sulfate can form patterns was entirely unexpected. Thus, it is possible that there are more patterns to be discovered by altering additional experimental parameters. One such parameter is the geometry of the surface. While performing the experiments reported in Chapter 6 on evaporative deposits on superhydrophobic surfaces, I performed some controls using hydrophilic micro-post textures. The salt spread through these textures in a geometrical fashion, resulting in hexagonal or square coffee-rings rather than a circular one.

Another property that can be altered include the solute chemistry. A common theme in many chapters has been how calcium sulfate is a model salt for patterning due to its relatively constant solubility over a range of temperatures. However, other salts with different solubility properties may be able to repeat the patterning behavior of calcium sulfate by controlling the temperature at which solutions are prepared and the concentration. This is explored in the spiral patterning effect presented in Chapter 7, where I show that a sodium chloride solution prepared at a very specific concentration can almost replicate the patterning effect. The results presented in Figure 8.5 showing triangular patterning across other salts suggest that there is more work to be done exploring the different ways that solutes with differing properties can contribute to patterning.

Other Applications

I have focused specifically on the above applications (anti-fouling materials, nutrient recovery, and water-soluble patterning/masking) with a focus on sustainability. The other applications in which similar interfacial engineering strategies for control of crystallization can be applied are nearly limitless. One application I find particularly interesting is the formation of mineral stones within the shoulder joint in a painful condition called calcific tendonitis.[17] I find this phenomena interesting because the “cure” for this condition is simply waiting for the crystal to re-dissolve, which begs the question of how the minerals form in undersaturated conditions in the first place. It would be interesting to investigate the formation and re-dissolution of these crystals from an interfacial engineering perspective. For example, do the crystals form due to confinement within

the biological tissue? Or due to the presence of a foreign seeding material? The answers to these questions could inform treatment/prevention of the condition, or possibly inform new materials design for nucleating minerals in undersaturated conditions.

Other projects continuing the exploration of the critter effect (but with less industrial relevance than those mentioned previously in anti-fouling) could be exploring the combined interactions between salt and nanoparticles in the effect. For example, it is possible that the particles would disrupt the effect by providing a surface for crystals to nucleate on, and thereby disrupting critter structures. It is also possible that the particles would be incorporated into the crystalline structure, or that the globes would form around them. Rather than having dissolved particles inside the drop, one could also consider creating a liquid marble (in which hydrophobic particles are coated on the exterior of the drop)[18] using a salt solution, and then depositing the marble onto the heated Nanograss surfaces. While such exploratory studies may not have immediate applications, we can only determine whether or not interesting phenomena will emerge by trying.

Some of the results of the current work may also have implications for preventing ice crystallization. This is particularly important in the airline industry, where de-icing chemicals currently used are not environmentally friendly. In addition, there is significant cost associated with the manual de-icing. For these reasons, interfacial engineering is an ideal strategy for reducing ice adhesion to aircraft.[19] Previous work from the lab has shown that ice crystallization in inhibited within the same nano-scale texture used in the Critter phenomena that inhibits salt crystallization,[20] demonstrating a possible analogy between salt and ice crystallization at interfaces. It would be very interesting to find the limits of this analogy and to what extent lessons from one system can be applied to the other.

Conclusions

There are a large number of interesting research directions to be explored under the theme of interfacial engineering for controlled crystallization. These directions range from practical (exploring crystallization as separation process for pollution prevention, industrial scale-up of different applications, etc.) to fundamental experiments (fine-tuning the explanations for how crystal properties influence patterning from evaporating drops). The work presented in this thesis has found a number of unusual results, including the formation of patterns from evaporating drops and the ejection of salt structures during the crystal critter effect; and I am confident that there are many more interesting effects waiting to be discovered.

References

1. Deegan, R. D. *et al.* Capillary flow as the cause of ring stains from dried liquid drops. *Nature* **389**, 827–829 (1997).
2. Shahidzadeh, N., Schut, M. F. L., Desarnaud, J., Prat, M. & Bonn, D. Salt stains from evaporating droplets. *Sci. Rep.* **5**, 10335 (2015).
3. Ball, P. *Shapes: Nature's patterns: a tapestry in three parts*. (OUP Oxford, 2009).
4. Diao, Y., Harada, T., Myerson, A. S., Alan Hatton, T. & Trout, B. L. The role of nanopore shape in surface-induced crystallization. *Nat. Mater.* **10**, 867–871 (2011).
5. Jiang, Q. & Ward, M. D. Crystallization under nanoscale confinement. *Chem. Soc. Rev.* **43**, 2066–79 (2014).
6. Zea, L. *et al.* Design of a spaceflight biofilm experiment. *Acta Astronaut.* **148**, (2018).
7. Guo, W., Ngo, H.-H. & Li, J. A mini-review on membrane fouling. *Bioresour. Technol.* **122**, 27–34 (2012).
8. Hou, X., Hu, Y., Grinthal, A., Khan, M. & Aizenberg, J. Liquid-based gating mechanism with tunable multiphase selectivity and antifouling behaviour. *Nature* **519**, 70–73 (2015).
9. Kim, J.-H. & Rothstein, J. P. Delayed lubricant depletion on liquid-infused randomly rough surfaces. *Exp. Fluids* **57**, 81 (2016).
10. Ferrari, M. & Benedetti, A. Superhydrophobic surfaces for applications in seawater. *Adv. Colloid Interface Sci.* **222**, 291–304 (2015).
11. Sun, W., Liu, J., Chu, H. & Dong, B. Pretreatment and Membrane Hydrophilic Modification to Reduce Membrane Fouling. *Membranes (Basel).* **3**, 226–241 (2013).
12. Lorite, G. S. *et al.* Surface Physicochemical Properties at the Micro and Nano Length Scales: Role on Bacterial Adhesion and Xylella fastidiosa Biofilm Development. *PLoS One* **8**, (2013).
13. Peng, B. *et al.* Applications of nanotechnology in oil and gas industry: Progress and perspective. *Can. J. Chem. Eng.* **96**, 91–100 (2018).
14. Khan, S., Azimi, G., Yildiz, B. & Varanasi, K. K. Role of surface oxygen-to-metal ratio on the wettability of rare-earth oxides. *Appl. Phys. Lett.* **106**, 061601 (2015).
15. Mohapatra, D. P. & Kirpalani, D. M. Process effluents and mine tailings: sources, effects and management and role of nanotechnology. *Nanotechnol. Environ. Eng.* **2**, 1 (2017).
16. Corsi, S. R., Graczyk, D. J., Geis, S. W., Booth, N. L. & Richards, K. D. A Fresh Look at Road Salt: Aquatic Toxicity and Water-Quality Impacts on Local, Regional, and National Scales. *Environ. Sci. Technol.* **44**, 7376–7382 (2010).
17. DE Carli, A., Pulcinelli, F., Rose, G. D., Pitino, D. & Ferretti, A. Calcific tendinitis of the shoulder. *Joints* **2**, 130–6 (2014).
18. Gennes, P.-G. de., Brochard-Wyart, F. & Quéré, D. *Capillarity and wetting phenomena : drops, bubbles, pearls, waves*. (Springer, 2004).
19. Rykaczewski, K., Anand, S., Subramanyam, S. B. & Varanasi, K. K. Mechanism of frost formation on lubricant-impregnated surfaces. *Langmuir* **29**, 5230–5238 (2013).
20. Bengaluru Subramanyam, S., Kondrashov, V., Rühe, J. & Varanasi, K. K. Low Ice Adhesion on Nano-Textured Superhydrophobic Surfaces under Supersaturated Conditions. *ACS Appl. Mater. Interfaces* **8**, 12583–12587 (2016).